Radical Functionalisation and Partial Oxidation of Graphene Derived from Sulphate Intercalated Graphite Compounds

TIANREN XIE

XIE, TIANREN (2021) Radical Functionalisation and Partial Oxidation of Graphene Derived from Sulphate Intercalated Graphite Compounds. Doctoral thesis, Durham University.

Radical Functionalisation and Partial Oxidation of Graphene Derived from Sulphate Intercalated Graphite Compounds

A thesis submitted for the partial fulfilment of the requirement for the Degree of Doctor of Philosophy

In the faculty of Science of

Durham University

By

Tianren Xie

Durham University

Department of Chemistry

University Science Laboratories

South Road

Durham

2020

Copy Right

Declaration

This work was conducted in the Department of Chemistry at Durham University between October 2016 and January 2020. The work has not been submitted for a degree in this, or any other university. It is my own work, unless otherwise indicated.

Acknowledgement

I would like to take this opportunity to appreciate the help from all the people who have in any way contributed to the work in this thesis. In my own lab group, I would like to express my gratitude to all members past and present for interesting discussions on my work and for their companionship in my PhD life. I would like to express special thanks to Stuart Goldie for his assistance with SEM imaging and Raman spectra fitting, to Shan Jiang for her help in TEM imaging. I would like to extend my gratitude to Stephen Boothroyd for his guidance of rheology study and Marcos Fernando Perez-Pucheta for his tremendous help to get rheology measurements. The work in Chapter 4 was conducted alongside Adam West, so he should be acknowledged for his important contributions to my work. I would also like to acknowledge the valuable contributions from the departmental services team; not only the brilliant departmental analytical services (TGA, MS, and NMR) but also the mechanical and electrical workshops and the glassblowers; who play a vital role in enabling novel research to be undertaken.

I must also thank the Applied Graphene Material and Durham University for my PhD funding. This is an exclusive opportunity to work with an innovated industrial partner and a world-class research institute. Obviously, my sincere thank goes to my supervisor Professor Karl Coleman for his academic support and critical insight, which are paramount to the progress and completion of my work. Finally, I want to acknowledge my family for their constant support, especially my wife, I cannot finish the work without her immeasurable love and companionship during Covid-19 pandemic.

Abstract

Graphene, as a wonder 2D material with excellent properties, sees multitude applications in many crucial areas where includes energy storage, composites making, ink production etc. The application of graphene in those areas is confined significantly by its poor chemical compatibility as graphene would re-aggregate spontaneously to form material with reduced properties. Despite the chemical compatibility of graphene can be improved by covalent functionalisation, the process can also be destructive to the outstanding properties of the graphene. The trade-off between the intrinsic properties of graphene and its chemical compatibility becomes the most intriguing challenge to produce the functionalised graphene. Most of current techniques either can produce dispersible graphene flakes with poor physical properties or produce graphene with poor dispersibility but good physical properties. The challenge becomes even more tremendous when the scale of the process is also considered. As the process, which can find a balance point normally, has low efficiency and is expensive to scale. The major aim of this study was to develop novel synthetic methodologies which can produce the functionalised graphene with controlled functionalisation level and be feasible to be scaled. Syntheses of functionalised graphene involving different strategies were attempted and evaluated.

In the first study, reductive functionalisation was performed where potassium GICs (graphite intercalated compounds) were reacted with three different organic electrophiles (4-iodoaniline, epibromohydrin, and 4-nitrobenzyl tosylate). Reactions with all three electrophiles had produced the corresponding functionalised graphene —EP-G, Aniline-G, and 4-Nitrobenzyl-G. The functionalised graphenes were characterised by TGA, AFM, and statistical Raman spectroscopy. The results demonstrated that the 3.4 at%, 4.4 at%, and 9.5 at% of functionalisation degree had been achieved for Aniline-G, EP-G, and 4-Nitrobenzyl-G correspondingly. Among them, the tosylate was first proven to be a feasible electrophile in the reductive functionalisation, and the epoxy functionalised graphene (EP-G) demonstrated extraordinary dispersibility in a range of volatile solvents, in particular, it formed acetone dispersion with stability up to 7 days. However, the process was not amenable to scale as harsh moisture-free conditions are required to handle the potassium GICs and consequent functionalisation.

In the second study, radical functionalisation was performed with the more manageable sulphate GICs as it could exist in stage 1 in normal atmosphere for relative longer time, and arylboronic acids were used as the radical precursor. The radicals were generated by the reaction between $Mn(OAc)_3$ and arylboronic acids. Three arylboronic acids (4-iodophenyl boronic acid, 4-bromophenyl boronic acid, and 4-nitrophenyl boronic acid) were selected to

perform the functionalisation, and production of 4-iodophenyl graphene (4-IPG), 4-bromophenyl graphene (4-BPG), and 4-nitrophenyl graphene (4-NPG) by this novel strategy was confirmed by XPS and SRS analysis. According to TGA and XPS, 0.6 at%, 1.3 at%, and 1.4 at% of functionalisation degree had been accomplished for 4-IPG, 4-BPG, and 4-NPG correspondingly. Even though, the route could offer aryl functionalised graphene in normal atmosphere by one step, however the process suffered from low functionalisation degree as compared to that of reductive functionalisation. In addition, the reaction showed unstable conversion rate (70%-90%) due to competitive reactions and poor mixing.

In the third study, synthesis route using sulphate GICs and mild oxidant $Mn(OAc)_3$, which allowed the production of water-dispersible graphene with balanced properties, was proposed and developed. As the resulting material had relative high carbon to oxygen ratio (C:O ratio = 6.4) and it demonstrated high dispersibility in the water (0.5 mg mL^{-1}) as it could form stable dispersion up to 30 days. According to AFM analysis, 90% of the flakes were 2-7.2 nm thick and 0.18-0.48 μm large. The material also exhibited electrical conductivity (86 S/m). More importantly, the route had achieved the high C:O ratio with one synthetic step. in comparison, to accomplish similar oxidation level, additional reduction step is required if graphene oxide is used. Meanwhile, this method has enabled the production of such materials in large scale potentially.

In the fourth study, the material was used to fabricate composites with PMMA. The rheologic properties of the composites were investigated via SAOS test (Small Amplitude Oscillatory Shear) and compared with other graphene/PMMA composites to understand the effect of the partially oxidised graphene. It was found that addition of exfoliated GNP or partially oxidised graphene with thick flakes at different loading levels retained the terminal behaviour for storage modulus $G'(\omega)$. On the other hand, 2.3 vol% loading of partially oxidised graphene and 4.3 vol% loading of rGO induced the enhancement of storage modulus $G'(\omega)$ at terminal region and had reinforcing effect on PMMA matrix.

Table of Contents

List of Abbreviations

1,2 DCE	1,2 Dichloroethane
3,5-TBD	3,5-Bis-tert-butylbenzenediazonium tetrafluoroborate
4-BBD	4-bromobenzene diazonium tetrafluoroborate
4-NBD	4-nitrobenzenediazonium tetrafluoroborate
AFM	Atomic Force Microscopy
APTES	(3-Aminopropyl)triethoxysilane
BWF	Breit-Wigner-Fano
CVD	Chemical Vapor Deposition
CNT	Carbon Nanotube
DBT	4-docosyloxy-benzenediazonium salts
DMF	Dimethylformamide
FTIR	Fourier-transform infrared spectroscopy
GIC	Graphite Intercalated Compound
GNP	Graphene Nanoplatelet
GO	Graphene Oxide
hBN	Hexagonal boron nitride
HOPG	Highly Ordered Pyrolytic Graphite
LE	Liquid Exfoliation
NMP	1-Methyl-2-pyrrolidone
ODCB	1,2-Dichlorobenzene
OTS	Octadecyltrichlorosilane
P+Number (i.e. P10)	nth percentile
PGIC	Potassium Graphite Intercalated Compound
PdTPP	Palladium Complexed Tetraporphyrin
PMMA	Poly(methyl methacrylate)
PO-G	Partially Oxidised Graphene
rGO	Reduced Graphene Oxide
SDBS	Sodium Dodecylbenzene Sulfonate
SEM	Scanning Electron Microscopy
SGIC	Sulphate Graphite Intercalated Compound
SRS	Statistical Raman Spectroscopy
TCNE	Tetracyanoethylene
TEM	Transmission Electron Microscopy
TRGO	Thermally Reduced Graphene Oxide
XPS	X-ray Photoelectron Spectroscopy
XRD	X-ray Powder Diffraction

Chapter 1. Synthesis of Functionalised Graphene Material from Pristine Graphite

1.1 Properties of Pristine Graphene

Pristine graphene is famous for its excellent physical properties. As a material with the thickness of one carbon atom, it is the thinnest material known and it is stronger than steel (in terms of Young′s modulus ~ 1TPa [1]); it is also known as the most thermally conductive material at room temperature with thermal conductivity up to ~5000 W/mK. [2] Its single layer structure also grants it good transparency (absorbing 2.3% white light [3]) and high surface area (2630 $m^2 g^{-1}$). Apart from all those properties, its most attractive property is its superior electronic properties. According to studies, the carrier mobilities of a free-standing graphene can be 200 000 $cm^2 V^{-1} s^{-1}$. [4,5] Assembling multitude and remarkable properties has made graphene the most promising material in a broad range of applications such as flexible electronic devices [6], energy storage material [7–9], filler of composite [10–13], transistors [14], sensors [15] etc.

All the outstanding properties of graphene stated above are measured based on a defect-free and single layer graphene which is produced by peeling off HOPG with a scotch tape manually. Yet, the low efficiency of this method makes it impossible to satisfy the demand of industrial scale. Unfortunately, this is the only known strategy to produce graphene with consistent and outstanding properties so far. In the past decades, various methods have been innovated and investigated to produce graphene in large scale and with properties approximating to the best. For example, graphene powder composited 90% single layer graphene can be produced in large quantity by liquid exfoliation (LE) of graphite in some specific solvent (NMP [16,17], ODCB [18] etc.). Continuous and uniform layer of graphene film can be produced by CVD on metal substrates; however, the properties would be deteriorated by the impurity after transferring or irregularities on the substrates and affected by wrinkles. Production of pristine graphene with homogenous composition and consistent properties remains as a significant challenge. The strategy of improving the consistency and homogeneity of pristine graphene is studied and reviewed elsewhere.

1.2 Benefits of Graphene Functionalisation

Though outstanding surface area and other physical properties makes graphene as a promising filler for making composite, coatings, or conductive ink, one critical problem of using pristine graphene in composite is its hydrophilicity. The hydrophobic nature of graphene makes it extremely easy to agglomerate in polymer matrix due to the unfavourable interfacial interaction [19], which can lead to reduced physical properties of the material. Good solvents for graphene include NMP [20,21], ODCB [18], and DMF [21] where stable dispersions with a concentration of 0.01-2 mg mL^{-1} can be obtained. Even higher concentrations, up to 50 mg mL^{-1} , can be achieved if equimolar hexafluorobenzene and benzene are used as a solvent.[22] However, those solvents render difficulty for large scale or commercial processing due to their high boiling point and cost.[23] In low boiling point solvents, the concentration of graphene dispersions is very low, for example in chloroform, IPA, and acetone it is 3.4, 3.1, and 1.2 µg mL^{-1} respectively. With long sonication time (>200 hours), the concentration can be improved to 0.5 mg mL^{-1} in IPA and chloroform.[24] In order to prevent aggregation and improve compatibility during process, two treatments are usually used to improve dispersibility of graphene. Better interaction with solvents can be achieved by non-covalent stabilization of graphene. With stabilisation from ionic surfactant, such as sodium cholate [25], sodium dodecylbenzene sulfonate (SDBS)[26], stable graphene aqueous dispersion with concentration 0.05-0.3 mg mL^{-1} can be obtained. Higher concentration of aqueous graphene dispersion using polysaccharides can be obtained with up to 2.3 mg mL^{-1} in pullulan and 5.5 mg mL^{-1} in chitosan.[27] However, the presence of residual surfactant molecules can impede electrical conductivity of graphene and additional steps are required to remove the surfactants.[26,28] Therefore, non-covalent functionalization of graphene is not appropriate for application such as composite and electronic devices where removal of surfactant is difficult to achieve.

Another treatment is covalent functionalization. By adding appropriate functionalities to the surface of pristine graphene, the compatibility of graphene in different chemical environments can be modified. Graphene oxide is an excellent example as a functionalised graphene. Unlike pristine graphene, GO is very dispersible, as dispersion with concentration of 1 mg mL^{-1} in some organic solvent and up to 7 mg mL^{-1} in water [29] can be made; however, GO demonstrates poor electrical conductivity due to the large amount of defects in the basal plane.[30] Covalent functionalisation can also tune the band gap of pristine graphene which makes it more suitable for fabrication of logic transistors. Since monolayer and bilayer graphene has zero or small bandgap, which makes them unsuitable for application as logic transistors. DFT calculations shows that bandgap of monolayer graphene can be tuned between 1-3 eV by decoration of different functional groups.[31] Several studies have shown that bandgap opening of monolayer graphene or few-layer graphene can be achieved by covalent functionalisation.[32-33] And some of them show wide enough bandgap (> 1 eV) after functionalisation to satisfy 10^6 on/off ratio.[34,35]

1.3 Challenges in Graphene Functionalisation

The challenges of covalent functionalisation of graphene are control of the degree of the functionalization and the scale of the production. As the most known method, the method for production of graphene oxide ‘Hummer’s Method’ can produce oxidised graphene material from graphite in large scale. Those functional groups can be removed to generate graphene or can be modified for further functionalization. However, sp^2 network of graphene is hugely disrupted due to addition of oxygen containing functional groups during the aggressive over-oxidation. Consequently, GO is very dispersible in a range of polar solvents. As a trade-off, GO is electrically insulated and thermally unstable. According to relevant studies, GO is metastable at room temperature, it favours spontaneous chemical modification and reduction.[36] It will become unstable from 50 ℃, with further heating GO will degrade. [37] The extensive oxidation will also degrade the mechanical property, Jeffrey T. Paci et al. calculated that the fracture stress decreases from 115 GPa to 63 GPa.[38] Even though reduction can restore the properties of GO to be closer to graphene, the dispersibility of the material is often lost which leads to re-aggregation of the rGO.[30] The defects created during the oxidation are also only partially recoverable.[39,40] The most preliminary principle of producing chemically modified graphene is minimising the deterioration of properties of graphene while enhancing the degree of functionalisation to achieve appropriate dispersibility. Likewise, whatever strategies involved resulting in over-functionalization are not suitable for production of functionalised graphene.

Another challenge is the scale. According to research from the past decades, controllable functionalisation of graphene is achievable, however the scale is always a problem. The problem arises because of the limited dispersibility of the starting material in solvents. Most syntheses start from using few layer or monolayer graphene, which can be obtained by large quantity from liquid exfoliation, however because of their poor dispersibility in the solvents, limited amount of functionalised graphene can be obtained after the syntheses. The yield can be enhanced relatively by using GICs (graphite intercalated compounds) as starting material, which can be obtained by intercalating graphite with guest molecules. The introduction of the guest molecules can expand the interlayer spacing of the graphite, which will facilitate the later exfoliation, and improve the reactivity of the graphene by charge transfer process. More importantly, since the synthesis starts from the graphite, the yield can be significantly improved. The most outstanding example is sulphate GICs, which are important precursors for large - scale production of GO. Successful production of aryl or allyl functionalised graphene by using stage-1 potassium GICs and reactive radicals has been frequently reported. All these works can control the homogeneity of the functionality on the graphene, most importantly, it minimises the adverse effect, which is extensive breakdown of the sp^2 bonding, on π network of graphene from the reaction. However, they are not scalable due to the sensitivity and reactivity of the reagents involved. [41–48]

The aim of this review is to summarise the most important achievements in synthesis of functionalised graphene from graphite recently and shed light on the strategy of synthesis so that a more controllable, versatile, and scalable process can be innovated.

1.4 Reactivity of Graphite and Graphene

The first challenge to produce functionalised graphene from the graphite is to overcome the energy barrier of the functionalisation as pure graphite with high crystallinity is well known for its chemical inertness and stability. Its chemical inertness comes from its bonding and structure. In terms of bonding, single layer graphene has sigma bonds in plane and π-π bonding above and below the plane, which makes basal plane unfavourable for functionalisation energetically. Indeed, numerous studies observe the superior reactivity of the edges experimentally.[44,49,50] Graphite can be treated as an assemble of infinite layers of graphene. Because of the existence of layers, graphite is less reactive than graphene as the interlayer space of graphite is less accessible for reactive species to diffuse in.

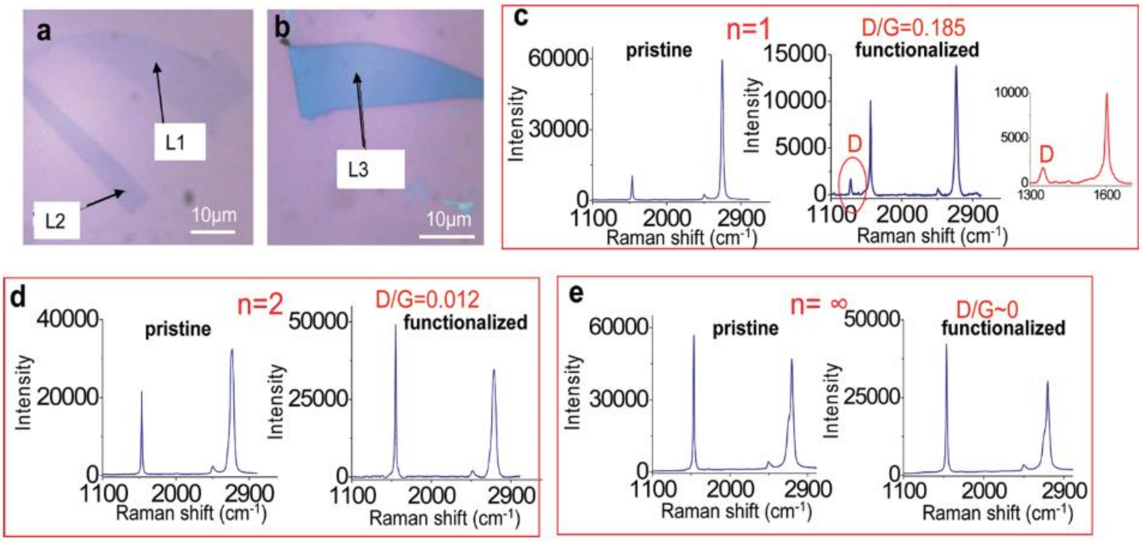

Figure 1.1 (a) and (b) optical image of monolayer, bilayer, and trilayer graphene. (c)-(e) Raman spectra of unfunctionalised graphene and graphene functionalised by 4-NBD with different layers.[44] Reprinted with permission from R. Sharma, J. H. Baik, C. J. Perera and M. S. Strano, Nano Lett., 2010, 10, 398–405 . Copyright 2010 American Chemical Society.

The reactivity of graphene with different number of layers and graphite towards diazonium salts were studied to illustrate the different reactivity due to the number of layers. According to experimental observations (Figure 1.1), crystalline graphite is the least reactive species, and graphene's reactivity decreases with increasing layers. Bilayer graphene generally has been found to be less reactive or inert towards the same functionalisation comparing to monolayer graphene and requires more energy than monolayer graphene to achieve the same functionalisation level.[1,33,45-16] Monolayer graphene has been found to be significantly more reactive than the bilayer graphene when graphene is activated by [K(15-crown-5)$_2$]Na and reacted with 4-iodopyrdine according to study by Mandakini Biswal et al. Reaction rates of monolayer and bilayer graphene on edge and basal plane were calculated based on monitoring the change of I_D/I_G regarding to reaction time. $k_{SLG\text{-}edge}$, $k_{SLG\text{-}interior}$, $k_{BLG\text{-}edge}$ and $k_{BLG\text{-}interior}$ can be estimated to be 0.73, 0.59, 0.054, and 0.029 min^{-1}, respectively.[48] R. Sharma et al. studied the degree of functionalisation when graphene with different layer number is reacted with 4-NBD (4-nitrobenzenediazonium tetrafluoroborate). It turns out monolayer graphene is 10 times more reactive than bilayer and multi-layer graphene (Figure 1.1). R. Sharma et al. attributed this to local puddles of electrons and holes induced by SiO_2 substrate.[51] This induction is more effective for monolayer graphene than graphene with more layers, since top layer of the multi-layer graphene is distant from the substrate.[44] The electro-hole puddles induced by substrate can be used for explaining reactivity of different p-doped graphene. More recently, Ricarda A. Schäfer et al. attributed the superior reactivity of monolayer graphene over bilayer graphene to the reactive substrate, which can stabilise initial adducts by saturating dangling bonds antaratopic to external addends. This pathway is impossible for bilayer graphene since the underlying substrate for bilayer graphene is graphene.[52] It was observed that graphene with different degrees of functionalisation (4-NBD) can be achieved on different substrates (Figure 1.2). Graphene with higher functionalisation level was realised on Al_2O_3 and SiO_2, as both substrates have higher p-doping and higher electron-hole puddle amplitude than hBN and OTS-SiO_2 (Octadecyltrichlorosilane).[53] A similar phenomenon was observed when the monolayer graphene was functionalised with heat-derived radical, where graphene on SiO_2 showed higher reactivity than graphene on hBN and copper.[54] This study was extended to mask CVD-grown monolayer graphene with different chemicals so that reactivity of graphene with different doping can be examined (Figure 1.3). The researchers compared reactivity of graphene with deposition of APTES, OTS, and graphene on the clean substrate Si/SiO_2 against 4-NBD and gold chloride anions. They found n-doped graphene (APTES) exhibits the highest reactivity. This means when graphene becomes n-doped, graphene with higher Fermi level favours electron transfer reaction. Dandan Liu et al. investigated the effect of Fermi level of graphene on its reactivity against benzyl peroxide. The Fermi level of graphene was tuned by applying a gate voltage through the Si/SiO_2 substrate. As the gate voltage was changed from -80 V to +80 V, Fermi level of graphene was changed from -172 meV to 63 meV, the functionalisation degree I_D/I_G ratio, also increased from 0.83 to 1.69.[55] Those studies indicate that the reactivity of graphene can be tuned by tuning Fermi level.

Apart from the doping effect of the substrate to the graphene, other factors from the substrate can also contribute to the reactivity of graphene. According to study from Xu Zhang et al.[56], crystal orientation of the substrate can influence the graphene reactivity. As only the graphene on the Cu (111) substrate exhibits the efficient and fast functionalisation after being reductive activation, whereas graphene on Cu (100) shows slow and ununiform functionalisation. The researchers attribute this phenomenon to the compressive strain created by Cu(111) substrate, which will be relieved after functionalisation.

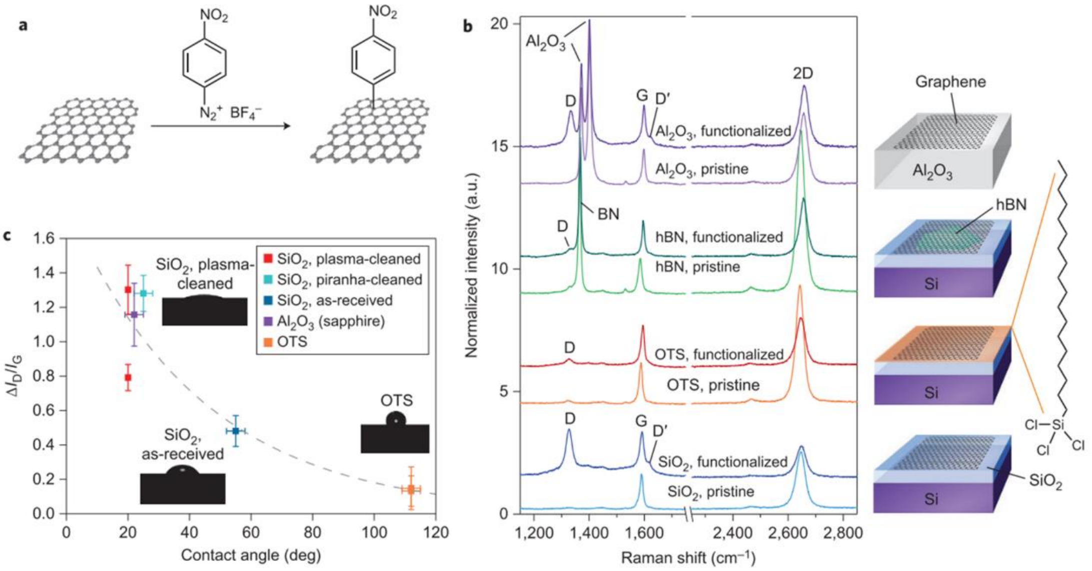

Figure 1.2 (a) Reaction scheme of 4-nitrobenzene diazonium salt with monolayer graphene; (b) Raman spectra of pristine graphene and functionalised graphene derived from different substrates; (c) Difference of I_D/I_G ratio between the functionalised and unfunctionalised graphene plots as function of water contact angle of substrates treated by different approaches.[51] Reprinted with permission from X. Fan, R. Nouchi and K. Tanigaki, J. Phys. Chem. C, 2011, 115, 12960–12964. Copyright 2011 American Chemical Society.

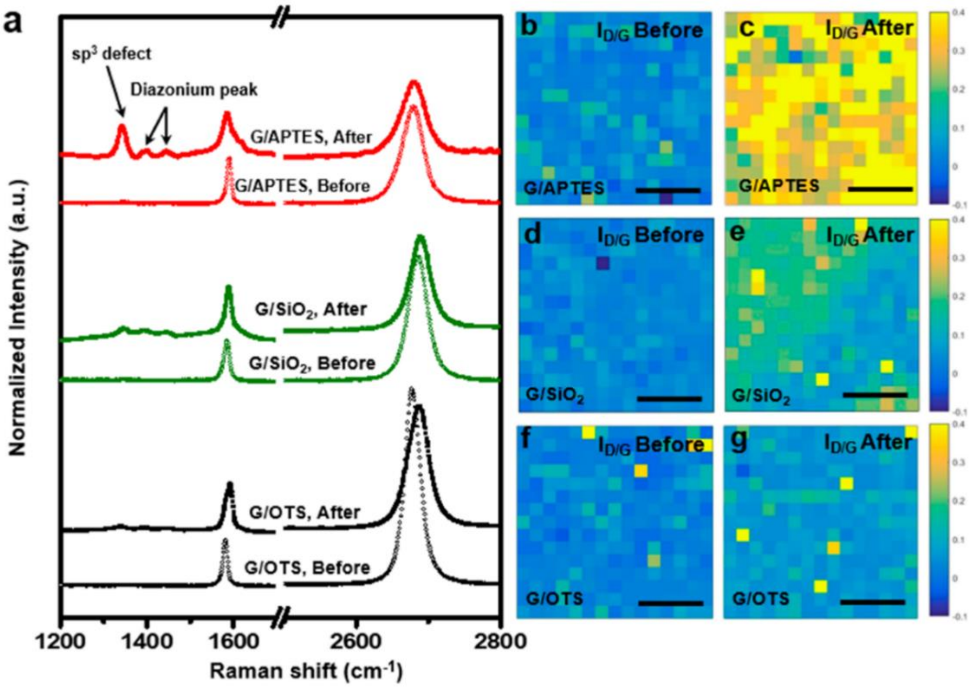

Figure 1.3 Raman spectra (a) and mapping (b-g) before and after functionalisation by 4-nitrobenzene diazonium salt on different substrates.[57] *Reprinted with permission from M. J. Park, H.-H. Choi, B. Park, J. Y. Lee, C.-H. Lee, Y. S. Choi, Y. Kim, J. M. Yoo, H. Lee and B. H. Hong, Chem. Mater., 2018, acs.chemmater.8b01614. Copyright 2018 American Chemical Society.*

Without changing Fermi level of graphene or graphite, graphene or graphite can also be covalently functionalised by reactive radicals. Common techniques used are plasma and diazonium chemistry [58], which is employed to modify the surface of graphite, glassy carbon, HOPG etc. Jörg F. Friedrich et al. have reported bromination of HOPG surface and monolayer graphene by using bromine plasma. The resulted brominated graphene is further reacted with KOH to give hydroxylated graphene, and with NaN_3 to give CN_3 groups.[59] W. Huang et al. achieved oxidation of monolayer graphene by using atmospheric pressure plasma. Depending on the exposure time to the plasma, 20-40% oxygen groups can be attained.[41] Graphite and graphene can also perform Diels-Alder chemistry. Santanu Sarkar et al. [60] demonstrated that HOPG, solution processed graphene, and epitaxial graphene can act as diene or dienophile. For example (as shown in Figure 1.4), graphene and graphite can react with tetracyanoethylene (TCNE) with mild heating. Graphene can also be functionalised by 1,3 dipolar cycloaddition. The other common strategy is using free radical addition, such as diazonium derived radicals.[10,14,17,20–24] Even though those methods become less effective when layers of graphene increased and even difficult to make modification in between the layers of graphite, but they are especially effective for functionalisation of monolayer graphene.

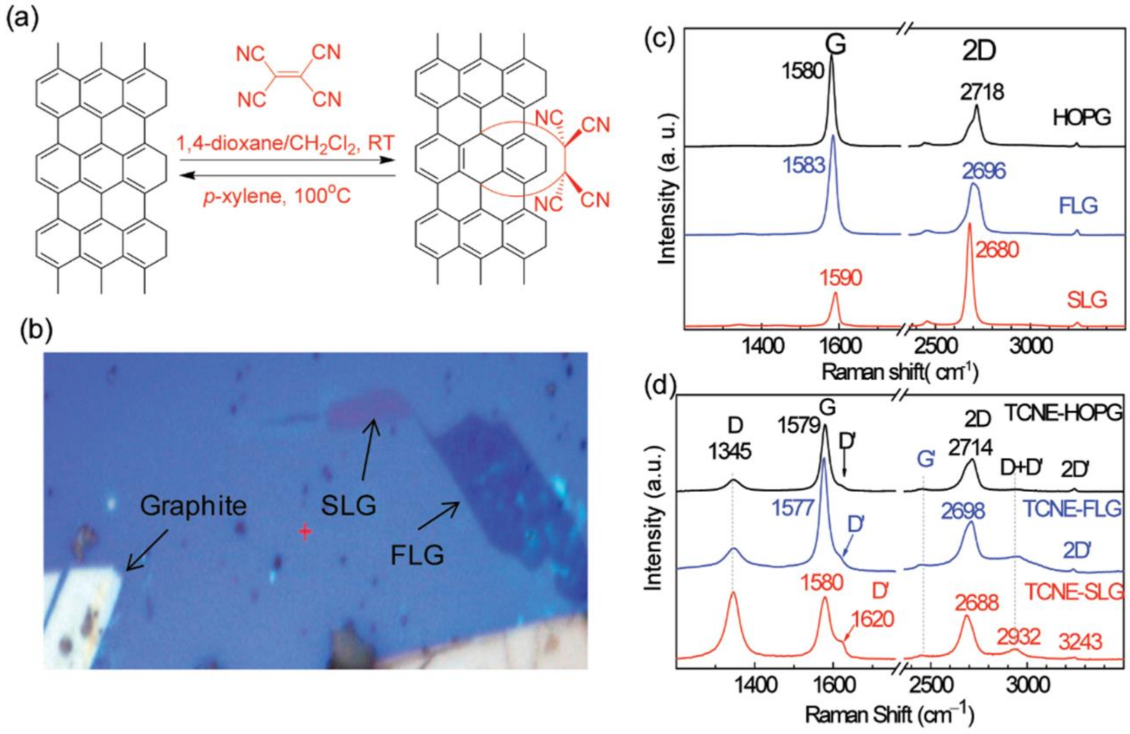

Figure 1.4 (a) Reaction scheme, (c) Raman spectra of Diels-Alder reaction between graphene with different layers and TCNE at room temperature; (b) optical images of HOPG, monolayer graphene, and few-layer graphene.[60] *Reprinted with permission from S. Sarkar, E. Bekyarova, S. Niyogi and R. C. Haddon, J. Am. Chem. Soc., 2011, 133, 3324–3327. Copyright 2011 American Chemical Society.*

Exfoliation and functionalisation of graphite can be done via formation of GICs (graphite intercalation compounds) since Fermi level of graphite will be changed noticeably by charge transfer between intercalants and graphene layers.[63,64] For example, production of graphite oxide by using strong oxidants such as Brodie[65] (potassium chlorate and fuming nitric acid), Hummers (concentrated sulphuric acid and potassium permanganate), Staudenmeir (fuming nitric acid, concentrated sulphuric acid, and potassium chlorate) etc. are well established. The principle of this series of reactions are similar and defined by two steps. The first step is formation of acceptor-type GICs, where layers of graphene are separated by the intercalated molecules and charge transfer happens between them. The second step is addition of functional groups to the graphene layer by redox reaction with an oxidant. As a result, the intercalation will not only make the graphite more reactive by separation and charge transfer but also increase the interlayer space of the graphite which makes consequent exfoliation of graphite into graphene easier.

The other strategy for production of functionalised graphene from graphite is implementing exfoliation and functionalisation separately. Since few-layer graphene can be easily obtained by using techniques such as liquid-phase exfoliation via shear mixing or sonication, thermal or chemical reduction of GO etc. These materials can be good starting point for synthesis of functionalised graphene, as more reactivity is granted by reducing the number of graphene layers. In addition, defects created during those process can be perfect sites for functionalisation. X. You et al. have reported successful mild oxidation by using thermally reduced graphene oxide (T) as starting material. By treating T with $MnSO_4$ and H_2O_2, mildly oxidised graphene with average lateral size 5.2 μm^2 and average 3 layers can be prepared (Figure 1.5). The material is extremely dispersible in water, zeta potential measurement showed that the dispersion has −49.0 mV, which is consistent with the observation that the dispersion can be stable over 2 months storage. UV-Vis study further suggested the absorbance loss of 1.5 mg mL^{-1} dispersion is only 2%. Thermal stability of the dispersion was also investigated, concentration of approximately 6% was lost during 120 h of standing at 80 °C. XPS survey scan indicates that oxygen atomic content increase from 8.3% to 15.8% after oxidation.[66] Heather Au et al. used sodium-naphthalide solution to mix with few-layer graphene so that few-layer graphene becomes more nucleophilic from charge transfer of naphthalide. The activated graphene was reacted with liquid bromine at 0 ℃ for 1 day in an argon filled glovebox to afford brominated few-layer graphene Br-FLG. XPS survey showed that there is 0.9 at% of Br covalently bonded to 95.6 at% carbon. Br-FLG begin thermal decomposition after 100 ℃ in helium. The group further demonstrated that Br-FLG is a good electrophile to perform polymer functionalisation as PMMA-FLG and PEG-FLG were successfully prepared.[67]

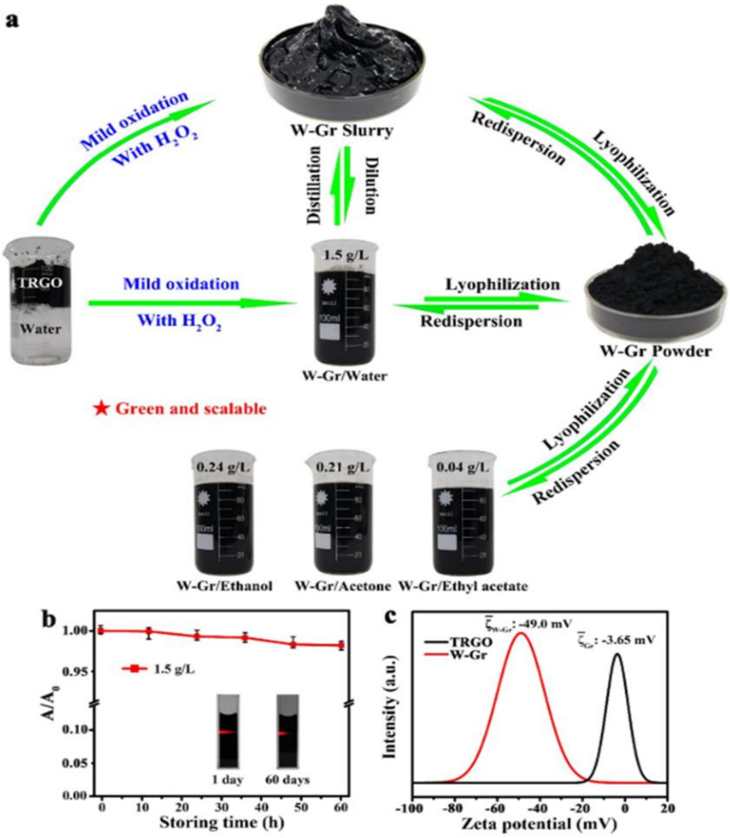

Figure 1.5 (a) Reaction scheme of water dispersible graphene via mild oxidation; (b) Absorbance monitoring over 60 hours by UV-Vis spectrometer; (c) Zeta potential of the water dispersible material and the starting material.[66] *Reprinted with permission from X. You, S. Yang, J. Li, Y. Deng, L. Dai, X. Peng, H. Huang, J. Sun, G. Wang, P. He, G. Ding and X. Xie, ACS Appl. Mater. Interfaces, 2017, 9, 2856–2866.Copyright 2017 American Chemical Society.*

To summarise, monolayer graphene exhibits highest reactivity since it can be functionalised by using either very aggressive conditions or very reactive species. For graphene with layers >1, activation of graphene is required to achieve higher level of functionalisation and the yield of functionalisation is generally in milligram scale. This implies high energy barrier required for making graphene functionalised. It is even more challenging to make functionalised graphene from graphite. Since most of modifications are only surface orientated if one of intercalation, exfoliation, and reactive species is absent. This addresses two prerequisites for preparation of functionalised graphene from graphite: functionalisation, which implies overcoming the energy barrier of changing sp^2 to sp^3 hybridization; and exfoliation, which implies overcoming Van der Waal interaction between graphite layers (exfoliation energy of graphite= 23.8 meV/Å^2).[68]

1.5 Functionalisation of Graphene by Free Radical Addition

1.5.1 Diazonium Chemistry

The most common and well-studied free radical addition reaction for functionalisation of graphene is the reaction involved using diazonium chemistry. Diazonium salts are reactive species which can be converted into radicals easily when contacting with graphene via a spontaneous redox reaction (Scheme 1.1), as graphene has standard potential of+22 mV vs. SCE.[69] Among those diazonium salts, reaction of 4-NBD with monolayer graphene is the most studied and cases of successful functionalisation have been achieved by heating. For example, 4-NBD functionalised monolayer graphene was prepared by heating graphene in dispersion of SDS and NBD at 30 ℃ for 4 hours.[10,14,17,20–24] Syntheses of functionalised graphene by using few-layer graphene dispersion and diazonium chemistry have also been reported, where the stable few-layer graphene dispersion was obtained by dispersing sonicated graphene, PVP, and SDS in NMP. Diazonium salts, such as (phenyl carboxylic, nitrobenzene, benzenesulfonic acid), were added to the dispersion. Corresponding functionalised graphene (PCFG, NBFG, BSFG) were prepared consequently. Electrical conductivity of each functionalised graphene was measured, the value is 5.5×10^{-2} S/cm (PCFG), 8.3×10^{-2} S/cm (BSFG), and 6.8×10^{-2} S/cm (NB-FG). The electrical conductivity decreased by 2 orders compared to that of the starting material (5 S/cm).[62] The time required for the completion of reaction is usually several hours to several days, and there is study indicating some type of diazonium salt will only be physiosorbed after several hours heating.[70]

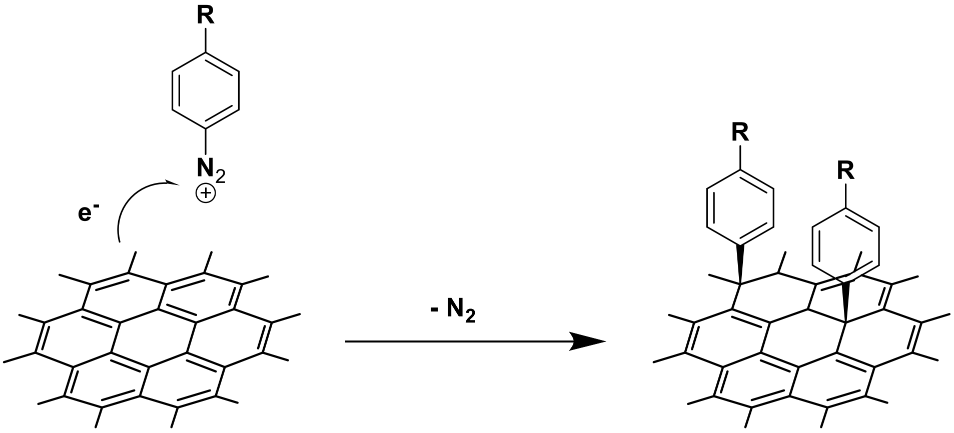

Scheme 1.1 Spontaneous reaction between graphene and diazonium salts

Reactivity of graphene against aryl diazonium salts can be improved significantly by electrochemical bias since the Fermi level of graphene would be increased by anodic potential. The surface of graphite (Figure 1.6) and glassy carbon can be modified by aryldiazonium salts with help of current.[71] Consequently, an electrochemical approach involved of functionalising graphene with aryl diazonium salts has been developed. John Greenwood et al. reported successfully grafted different functional groups, such as 3,5-Bis-tert-butylbenzenediazonium (3,5-TBD), and 4-NBD from their diazonium salt onto CVD grown monolayer graphene by electrochemical bias in several minutes. Although applying electrical bias accelerated the functionalisation process, but it also led to polymerisation of the aryl species as polyaryl species were found to be grafted on the surface of graphene.[72,73] This multi-layer functionalisation could be excluded by using radical precursors with bulkier groups, as monolayer functional groups were predominantly found for 3,5-TBD.[74] The uniform layer of functionalisation for 4-docosyloxy-benzenediazonium salts (DBT) on graphene could be done by pre-formation of physiosorbed self-assembled monolayer of DBT. It was found that sheet resistance of the functionalised graphene increases from 600 ± 90 (pristine graphene) to 3000 ± 300 Ω/□. The sheet resistance could decrease to 2000 ± 200 Ω/□, if only monolayer of functional groups was grafted. The surface potential is lifted from 245 ± 10 mV to 305 ± 15 mV after the modification, because the p-alkoxyphenyl groups are electron donors.[75] More recently, the steric and electronic effects of substituents on functionalisation of graphite surface were investigated.[58] The results show that formation of multi-layered functional groups is suppressed when 3,4,5 positions tri-substituted diazonium salts are used and the effect is independent on the electronic property of the substituents. The degree of functionalisation increases with increasing electron-donating property of the aryl radical.

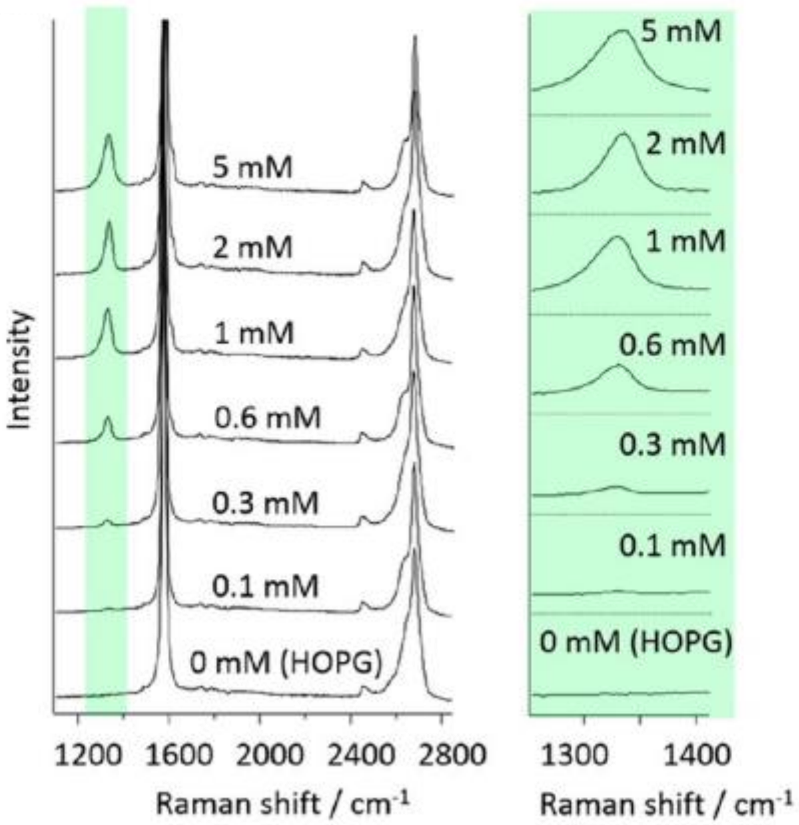

Figure 1.6 Raman Spectra of electrochemical functionalisation of HOPG by using different concentration of 3,5-TBD.[74] *Reprinted with permission from Z. Xia, F. Leonardi, M. Gobbi, Y. Liu, V. Bellani, A. Liscio, A. Kovtun, R. Li, X. Feng, E. Orgiu, P. Samorì, E. Treossi and V. Palermo, ACS Nano, 2016, 10, 7125–7134.Copyright 2016 American Chemical Society.*

Due to the high reactivity of the approach, electrochemical assisted diazonium modification can be applied to the functionalisation where graphene > 1 layer and less reactive diazonium salts are involved. Chih-Jen Shih et al.[76] demonstrated that monolayer graphene could be functionalised by 4-NBD and 4-BBD (4-bromobenzene diazonium), as according to result of another study [70], heating monolayer graphene with 4-BBD will only result in physisorption of diazonium salts onto graphene. Moreover, bilayer graphene could be functionalised to a significant degree, which is in stark contrast to the observation of other study where limited degree of functionalisation was resulted without electrochemical bias.[44] As a consequence of functionalisation, band gap opening of both monolayer and bi-layer graphene was achieved.

1.5.2 Other Radicals

More recently, azide anion in aqueous buffer solution can also be converted to azide free radical under electrochemical potential. The generated azide radicals were reacted with a monolayer graphene, where the graphene is used as anode (Figure 1.7). The successful addition of azide groups was confirmed by XPS, since 4.7 at% of nitrogen was found and the nitrogen 1s region of the azidated sample showed two peaks at 400.6 and 404.4 eV at a ~ 2:1ratio, which is consistent with those typically found in sodium azide. The azidated graphene becomes an important intermediate as various functional groups can be added through the azides groups, these include nucleophilic reactions, copper catalysed conjugate addition, and 1,3 dipolar addition etc.[77]

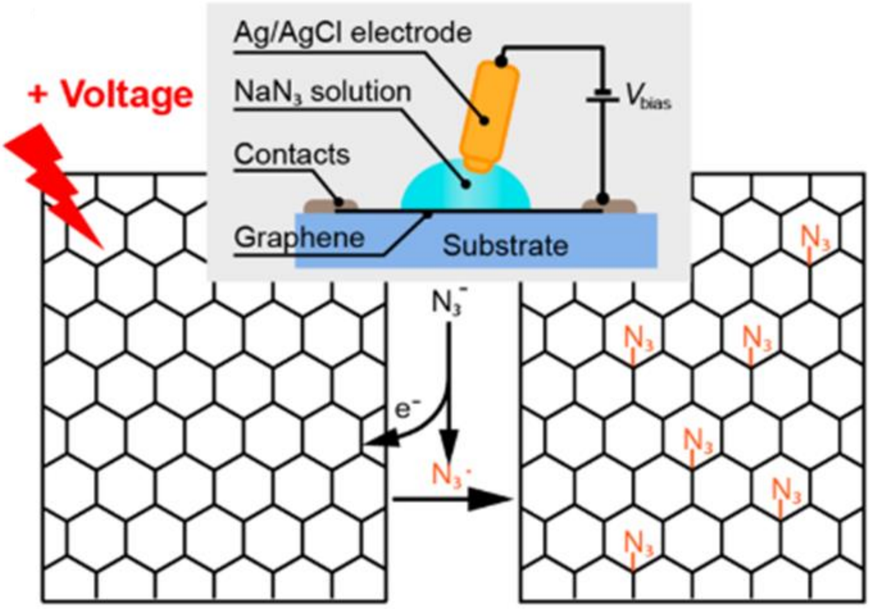

Figure 1.7 Experimental set-up and scheme of graphene functionalisation via sodium azide.[77] Reprinted with permission from W. Li, Y. Li and K. Xu, Nano Lett., 2020, 20, 534–539. Copyright 2020 American Chemical Society.

Some conventional polymerisation initiators are also found to be effective as free radical for graphene functionalisation. Xiaoyong Zhang et al. demonstrated isobutyronitrile functionalised graphene by heating 2,2'-azobisisobutyronitrile with liquid phase exfoliated graphene in NMP at 75℃ for 7 hours. Increase of I_D/I_G ratio after reaction confirmed the successful addition. TGA shows 10% weight loss in the region 220-550 ℃, this is equivalent to functionalisation degree of 1 isobutyronitrile group substituent per 50 carbon atoms, which is consistent with XPS measurement.[78] Benzoyl peroxide is another species having been proved to be effective for radical addition for graphene.

1.5.3 Summary

Diazonium chemistry is an efficient approach to functionalise monolayer graphene (especially those on the substrates) and few- layer graphene with help of electrochemical bias. It becomes mainly surface orientated when it reacts with graphite. However, two major problems need resolving so that diazonium chemistry could become a common methodology for functionalisation of graphene in industrial scale. The first problem is the high hazardous profile (explosive) of diazonium salts, which may pose safety concern in handling, especially when used in large scale. The other problem is their tendency to self-polymerise, which makes functionalisation less controllable and efficient. The latter is an inevitable problem for other free radical functionalisation.

1.6 Cycloaddition Reactions

1.6.1 Diels-Alder Cycloaddition

Graphene's reactivity towards Diels-Alder reaction can be attributed to its unique electronic structure—gapless bandgap [79] (touch of conduction band and valence band). —which grants graphene a lot of canonical structures. This also means HOMO and LUMO of graphene are the same at Dirac point. They can be represented by nonbonding molecular orbital, and its energy level corresponds to work function of graphene, which is about 4.6 eV and varies with number of layers of graphene. Theories [60] suggest an ambiguous role of graphene during Diels-Alder reaction and whether it behaves as a diene or dienophile depending on the reaction conditions. It is worthy to note that the electronic structure of graphene>1 layer is more complicated as a small band gap exists for bilayer graphene and band overlaps for tri-layer graphene and for graphite,[79] the bandwidth becomes 1.5 eV with band overlap of 0.1 eV. However, epitaxial grown graphene exhibits extra reactivity. These mean the reactivity of graphene materials may change significantly with change of layer number. Indeed, Santanu et al. indicated that the most degree of functionalisation after Diels-alder reaction has been achieved to monolayer graphene and the degree decreases with increasing number of layers. The defects and edge of graphene also play a vital part for reactivity of graphene towards cycloaddition, as it was found that the reaction between graphene and TCNE would only proceed if graphene is defective. In addition, energy barrier of Diels-Alder reaction on graphene may decrease with increasing size of aromaticity of graphene.[80]

Experimentally, as expected from theoretical prediction, researchers observed that graphene exhibits extraordinary affinity to dienophile and diene. Graphene with different origins can be functionalised by dienophiles such as TCNE,[60] maleic anhydride (MA),[60] N-(2,2,6,6-tetramethyl-piperidinyl)-maleimide (TEMP-MI),[81] or other maleimide derivatives. For the reactions with TCNE and maleimide derivatives, functionalisation can be done by immersing graphene in reactant solution at room temperature for a certain duration. For the reactions with MA and TEMP-MI, heating over 100 ℃ is required. Graphene can also be functionalised by diene 2,3-dimethoxy-1,3-butadiene (DMBD) and 9-methylanthracene (9-MA). The reactions require heating to accomplish.[60]

1.6.2 1,3 Dipolar Cycloaddition

1.6.2.1 Reactions Proceed from Azomethine Ylides

Azomethine ylides have been a common intermediate for 1,3 dipolar cycloaddition of graphene. By using the condensation reaction between α-amino acid and aldehyde (Scheme 1.2), different substituted azomethine ylides can be easily made, hence differently substituted pyrrolidine rings can be formed on graphene. Vasilios Georgakilas et al. synthesised catechol substituted graphene, which has good dispersibility in ethanol.[82] Mildred Quintana et al. synthesised amine functionalised graphene [43,49] through a three-step reaction. In the first instance, carboxylic acid substituted pyrrolidine is formed on graphene via 1,3 dipolar cycloaddition, and then triamine or diamine with protection groups were added to graphene by peptide formation. Finally, the amine groups are freed by deprotection. The confirmation of functionalisation is directly visual under TEM, since gold nanorod can selectively bind to acidified amine groups. Xiaoyan Zhang et al. [83] and Aijian Wang et al. [84] demonstrated that porphyrin can be added to rGO and LPE-G via 1,3 dipolar addition via azomethine ylides. The ylides was prepared by condensation of sarcosine with aldehyde group on tetraporphyrin, in which the aldehyde group was grafted onto porphyrin beforehand. The same functionalisation can be done to palladium complexed tetraporphyrin (PdTPP). The functionalised material was characterised by several techniques. Besides I_D/I_G ratio increased after the reaction, UV-Vis spectra of the hybrid material also showed strong absorption bands at 419 and 525 nm, which originated from the covalently bonded PdTPP. Pd 3d core level was measured to be 338.5 eV by XPS, which is assigned to Pd-N. TGA suggested the degree of functionalisation is 0.41% which is equivalent to one PdTPP group per 240 carbon atoms. The fluorescence and phosphorescence of the hybrid material was studied by fluorescence spectroscopy. It turned out the fluorescence and phosphorescence of PdTPP are quenched after being functionalised with graphene. The PdTPP/graphene could have potential applications in sensors and catalysis. Eunice Cunha et al. [85] performed a solvent free 1,3 dipolar cycloaddition using GNP and azomethine ylides produced by iminodiacetic acid (IDA) and paraformaldehyde (PFA). The functionalisation was confirmed by emergence of nitrogen and oxygen signal in XPS spectra after reaction. And the functionalised material was more dispersible in water after the carboxylic groups are deprotonated by NaOH.

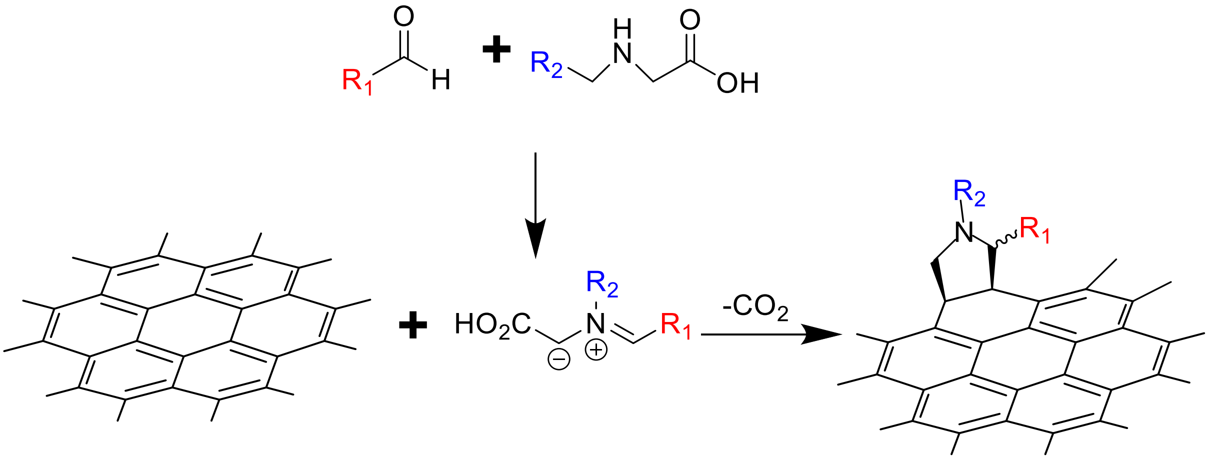

Scheme 1.2 A general process illustrates the generation of azomethine ylides from aldehyde and α-amino acid and 1,3 dipolar cycloaddition of graphene. R_1 and R_2 can be any functional group which can affect dispersibility of graphene.

1.6.2.2 Nitrile imine & Nitrile Oxide

It has been found that microwave can enhance the rate of 1,3 dipolar cycloadditions. Myriam Barrejo´n and co-workers reported cycloaddition via nitrile imines (Scheme 1.2). Nitrile imine with different substituents formed *in situ* with presence of N-chlorosuccinimide (NCS) and triethylamine (NEt_3) and could be added to graphene under heating for several days to afford corresponding pyrazoline functionalised graphene (Scheme 1.3).[86] The process can be shortened to 1 hour by microwave heating. In addition, the microwave heating is effective to accelerate cycloaddition with azomethine ylides as well since a typical reaction duration for cycloaddition to finish is several days. Ultraviolet photoelectron spectroscopy was employed to investigate the band structure and calculate work function of all the functionalised graphene. Generally, functionalisation decreases work function of the material and if there is electron donating groups, work function will be reduced further. Among them, remarkable 4.46 eV work function and 1.7 eV band gap has been obtained by one functionalised graphene. Likewise, Helena Uceta et al. used another imine derivative oxime to perform 1,3 dipolar cycloaddition, as oxime (Scheme 2) can be converted into nitrile oxide in presence of NCS and NEt_3.[86] The nitrile oxide was synthesised *in situ* and microwave heated with graphene dispersion to give isoxazoline functionalised graphene. Again, the microwave speeds up the addition process.

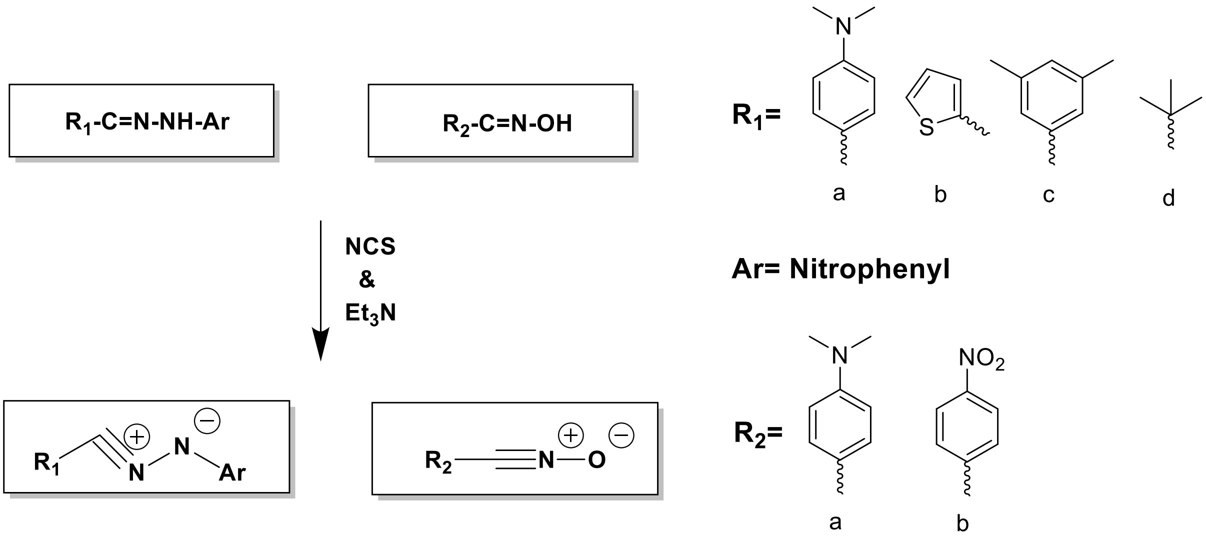

Scheme 1.3 Generation of nitrileimine [87] and nitrile oxide [86].

1.6.2.3 Zwitterionic Compounds

Xiaoyan Zhang et al. performed an unusual 1,3 dipolar cycloaddition by using zwitterionic compounds.[88] The zwitterionic compounds were prepared by reaction between acetylene dicarboxylates based on the mechanism below. Two derivatives were functionalised to the graphene. And the resulted functionalised graphene demonstrated different dispersibility compared to the starting graphene, as they are dispersible and stable in chloroform (2 months) or water (1 month). More importantly, the lateral size of graphene is not changed after the functionalisation. The standard four-point probe method was applied to measure the electrical conductivity of the graphene films. The conductivity decreases from 3269 ± 132 S m^{-1} to 6.88 ± 0.36 S m^{-1} (1) and 665 ± 20 S m^{-1} (2).

1.6.3 Cycloaddition with Benzyne

Based on computational studies, cycloaddition of benzyne to graphene has been found to proceed either via [4+2] or [2+2] concerted mechanisms to give 6 membered or 4 membered pericyclic rings.[89,90] Experimentally, aryne functionalised graphene can be prepared in one hour with mild heating.[61–93] Same as other reactive intermediate, benzyne is usually synthesised *in situ* from its precursor under heat. Substituted benzene compounds with two leaving groups at ortho positions are used as precursor for benzyne generation. There are two common approaches to generate benzyne. The first one is using substituted anthranilic acid, benzyne is produced by elimination of carboxylate and diazonium groups by heating. The other method involves fluorination of trimethylsilylaryl triflates, in which the fluoride (from a fluoride source) replaces the trimethylsilyl group (Scheme 1.4). Following by elimination of fluoride and triflates, benzyne is produced.

Xing Zhong et al. demonstrated aryne-graphene by using trimethylsilylaryl triflates derivatives with high level of functionalisation (5.6%). With different substituents on benzyne, good dispersibility and stability in a range of solvents have been realised.[91] By showing that benzyne can be used as a coupling agent, D. García et al. explored the synthesis of nano-conjugated compounds. Tetrasubstituted benzene was used so that a two-step cycloaddition can be performed. In the first step, benzyne was added to fullerene (Figure 1.8). In the second step, graphene was conjugated to the fullerene from the other benzyne active site. The formation of covalent benzene skeleton between fullerene and graphene was supported by increase of I_D/I_G ratio and increase of flake thickness after the reaction.[90] In another work, Xing Zhong functionalised graphene with pyridine equivalent benzyne, pyridyne. The pyridyne was produced *in situ* from trialkylsilyl and triflates substituted pyridine in presence of CsF. Functionalisation level of 1 pyridine group 29 carbon atoms has been achieved. The electrochemical activity of the pyridine functionalised graphene was investigated, and results indicated that the material is potential to apply as oxygen reduction reaction electrocatalysts.[92]

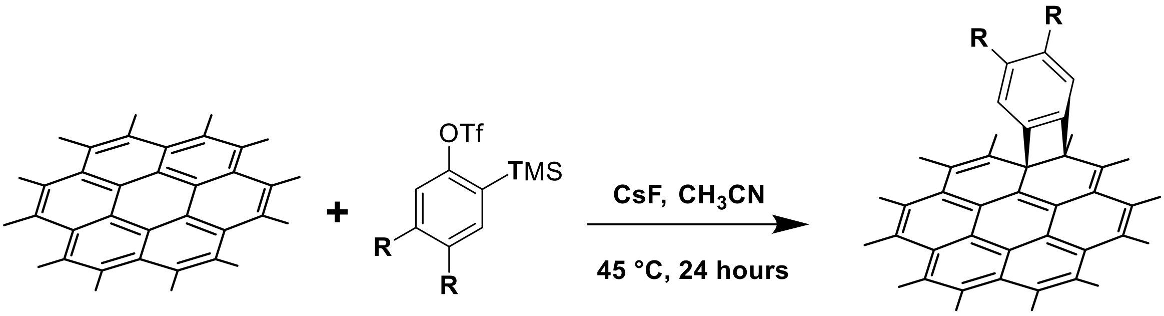

Scheme 1.4 Functionalisation of graphene by benzyne.

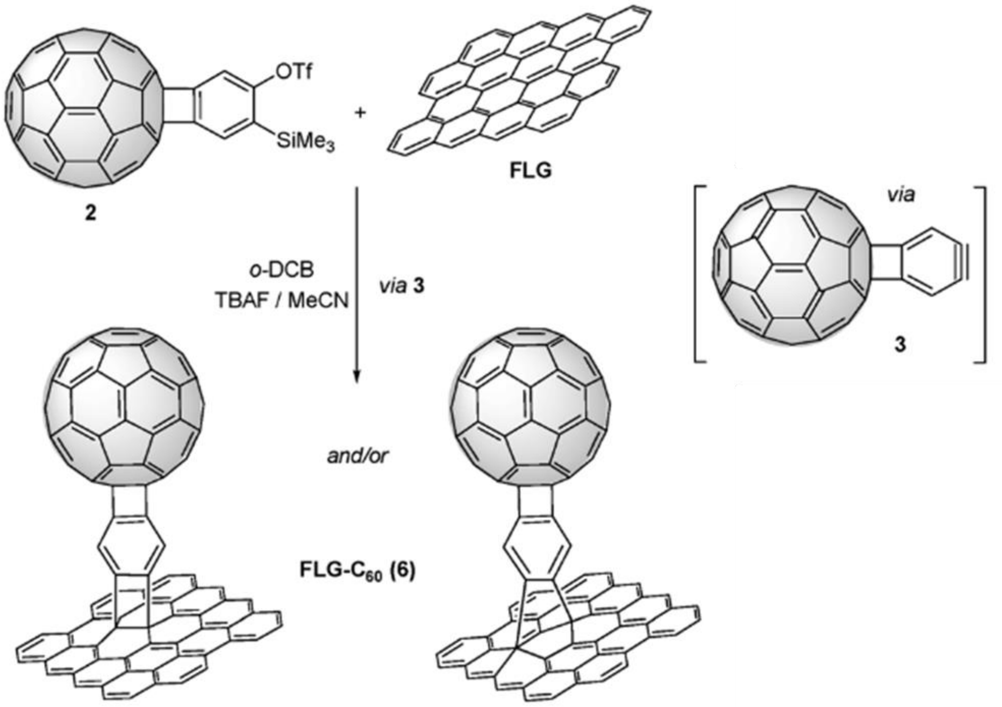

Figure 1.8 Fullerene conjugated graphene, the fullerene is grafted onto the graphene by benzyne.[91] *Reprinted with permission from X. Zhong, J. Jin, S. Li, Z. Niu, W. Hu, R. Li and J. Ma, Chem. Commun., 2010, 46, 7340–7342. Copyright 2010 Royal Society of Chemistry.*

1.6.4 Cycloaddition of Nitrene and Carbene

Carbene, as a highly reactive intermediate, has been used for carbon-carbon bond formation in organic chemistry. It is also widely applied in functionalisation of other carbon allotropes CNT and fullerene. Wenyan Zan studied reactivity of carbene derivatives CR_2 with different substituents (R= H, Cl, F, CH_3, CN, NO_2, OCH_3, CCH, C_6H_5) towards graphene by DFT calculations. The calculations turn out the carbene is reactive for covalent functionalisation when R= H, Cl, CH_3, NO_2, and band gap can be tuned by the same amount 0.2 eV.[94] Experimentally, Chun Kiang Chua et al. used a traditionally derived carbene from reaction of NaOH, chloroform, and phase transfer catalyst. This was reacted with the dichlorocarbene to give the functionalised graphene. The product was characterised by Raman, FTIR, XPS, and TEM, and from FTIR and XPS the emergence of C-Cl bonds was noticed after the reaction. TEM showed that graphene was more wrinkled after the reaction.[95] Zhen Hu et al. used diarylcarbene, in which the two aryl groups were decorated by one epoxy group respectively. Reaction of this modified diarylcarbene with results in functionalised graphene with good dispersibility in organic solvents acetone, and in epoxy resin matrices. After the reaction: oxygen weight percentage increased from 8.43% to 15.74% in XPS; emergency of new band at 910 cm^{-1}in FTIR spectra; shift of G band from 1570 cm^{-1} to 1580 cm^{-1}, these changes indicate the successful functionalisation. The material demonstrated reinforcing effect for epoxy resin, since with 0.2 wt% blending the resulted composite has significant improvements in tensile strength (56.6%) and modulus strength (26.2%).[96] Toby Sainsbury et al. reported synthesis of dibromocarbene functionalised few-layer graphene from bromoform. The functionalisation was confirmed by the presence of bromine signal in XPS survey scan of the product and C-Br stretch in FTIR. Thermal gravimetric analysis reveals the level of functionalisation of the product is c.a. 5%. The electrical conductivity of the functionalised graphene is 5.13×10^{-2} S/cm, which is two orders of magnitude lower than the 7.14 S/cm pristine graphene. Terahertz time-domain spectroscopy was employed to explore the electronic property of the nanocomposite derived from the functionalised graphene and PTFE, the result shows that the behaviour of this functionalised graphene is midway between the GO and graphene.[97]

Similarly, the ability of adapting to different electron configurations has made nitrene a powerful intermediate for functionalisation of graphene. It was reported that modification of EG by azidotrimethylsilane, and 1.9% level of functionalisation had been achieved.[98] Normally, the nitrene radicals are produced in situ from azide groups by heating or irradiation, and the azido compounds used in the synthesis are prepared by nucleophilic substitution of organic halides from sodium azide due to their limited commercial availability. The most frequent used azido compounds are perfluorophenylazide (PFPA).[99–102] PFPA is the name of compounds which have a six substituted benzene compound with azide group and another functional group at *para* position and the rest of carbons are attached by fluorine atoms. In graphene functionalisation, aziridines will be formed via cycloaddition of azide groups and the other group on the benzene is responsible for modifying properties of graphene. The use of PFPA was first reported to immobilise graphene on Si/SiO_2 so that graphene will firmly attach to the substrate during various processing. The PFPA links Si surface via formation of siloxane, here PFPA was applied as coupling agents. The resistance of the PFPA functionalised single layer graphene was found to be 1.62kΩ, and the thickness increase to 0.84 nm after functionalisation.[103] The PFPA can also be coupling agent to link graphene with nanoparticles (Figure 1.9). Jaehyeung Park et al. demonstrated that graphene can be coupled to silica nanoparticles and gold nanoparticles with PFPA-silane and PFPA-disulphide by UV irradiation (Figure 1.10). More PFPA analogues were synthesised to modify the dispersibility of graphene as shown in another work by Li-Hong Liu and co-workers, the PFPA functionalised graphene may show affinity to water or organic solvents depending on the nature of the functional groups.[99] 2,4,6-Trichloro-1,3,5-triazine is another major precursor for nitrene production because it is a cheap, commercially available.[104,105] In addition, since chlorines have different reactivity, stepwise nucleophilic substitution can be performed. For example, azide group can replace the chlorine at 2 position easily at low temperature. The other chlorines can be active sites for further modification. Abbas Faghani et al. demonstrated L- and D-cysteine (L-Cys and D-Cys) can replace the second chlorine and the third chlorine can be replaced by rhodamine 6G, polyglycerol amine, amino-β-cyclodextrin via nucleophilic addition to triazine-graphene. In another work, Mohammad Fardin Gholami demonstrated addition of polymer via triazine to graphene. Both cases exhibit the possibility of fabricating nanohybrid materials via covalent chemistry and their potential in biological application.

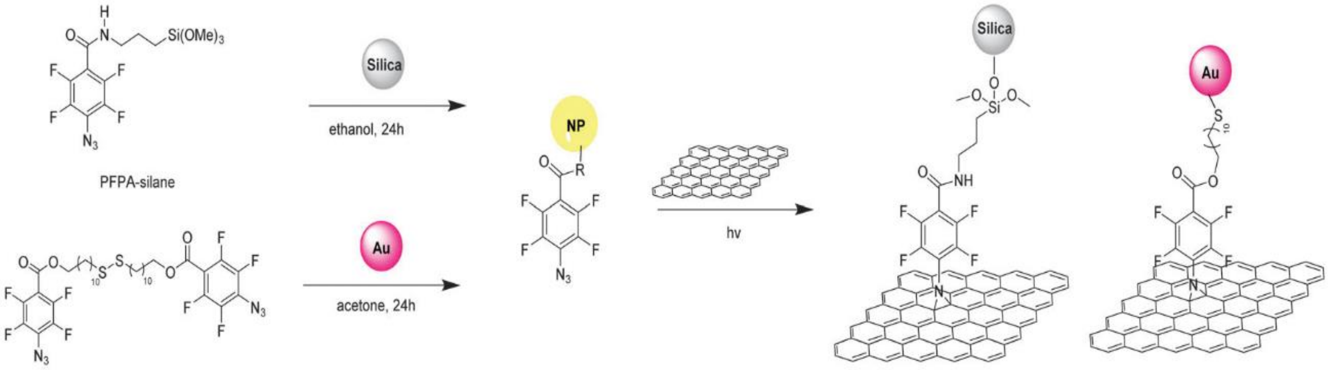

Figure 1.9 Conjugation of nanoparticle and graphene via PFPA.[106] *Reprinted with permission from J. Park, H. S. N. Jayawardena, X. Chen, K. W. Jayawardana, M. Sundhoro, E. Ada and M. Yan, Chem. Commun., 2015, 51, 2882–2885. Copyright 2010 Royal Society of Chemistry.*

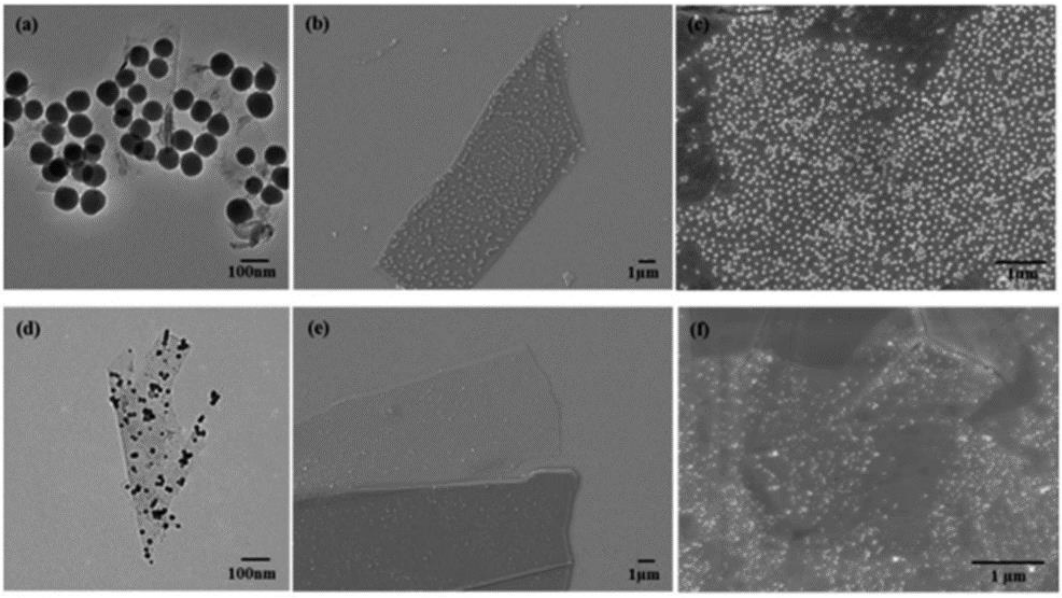

Figure 1.10 ESEM images of silica nanoparticles conjugated on (a) few layer graphene, (b)mechanically exfoliated graphene, (c) CVD graphene; and gold nanoparticles on (d) few layer graphene, (e)mechanically exfoliated graphene, (f) CVD graphene.[106] *Reprinted with permission from J. Park, H. S. N. Jayawardena, X. Chen, K. W. Jayawardana, M. Sundhoro, E. Ada and M. Yan, Chem. Commun., 2015, 51, 2882–2885. Copyright 2010 Royal Society of Chemistry.*

The application of functionalised graphene in Li battery had also been explored. The rGO was functionalised by anthraquinone (AQ) via nitrene chemistry. Degree of functionalisation can be enhanced by increasing load of AQ based on TGA and XPS measurement. The electrical conductivity, as expected, decreased from 2016 S/m (0% AQ) to 316 S/m with increasing extent of functionalisation.[107]

The advantages of nitrene cycloaddition are its efficiency, as the reaction can be done very fast and reactivity towards graphene since most of the reactions can be done in one day and the reactions can proceed without heating or with irradiation. Besides, it demonstrates unique coupling ability which make it stands out from other functionalisation reagents. However, multiple steps are required to functionalise graphene, because most of azido compounds are not commercially available. In addition, most of azides are labelled as toxins and explosophores. This means using them in large scale may address significant safety problem.

1.7 Exfoliation and Functionalisation from GICs

It is known that the layer structure of graphite is maintained by the Van der Waal forces between the graphene layers; the scale of the Van der Waal forces proportions with r^{-6}, where r is the interlayer distance. The binding is weakened upon the intercalation of neutral intercalants and formation of functional groups as the interlayer distance increases. For example, the d-spacings of graphite oxide increases from 0.34 nm (pristine graphite) to 0.7 nm and graphite oxide can be converted into graphene oxide easily by mild exfoliation.[108] However, the interaction may be reinforced via the intercalation, as the computational simulation indicated that the ionic intercalants would increase the exfoliation energy via the electrostatic interactions by 1.5 to 5-fold.[109]

1.7.1 Reductive Functionalisation

In reductive functionalisation, graphite is converted into a chemically reactive species ‘graphenide’. In general, graphenide is prepared by graphite intercalation with alkali metal, where a charge transfer process takes place to make individual graphene of graphite reduced. The most used GIC is potassium GICs, which is usually prepared by heating potassium with graphite at 250℃ under an atmosphere in an evacuated glass tube. Depending on the molar ratio of graphite and potassium, GICs with different stages can be synthesised.[110] Typically, stage-1 potassium GICs are desired as the starting material for the subsequent functionalisation and the successful preparation is indicated by colour change from black to golden. The potassium GICs were then readily dissolved in a series of aprotic polar solvents to offer graphenide salts solutions. The solution was left still overnight or centrifuged to remove any large undissolved material. The supernatant was probe-sonicated to reduce number of layers of graphenide. The sonicated solution was then treated with electrophile or oxidant to produce corresponding functionalised graphene. There are two other approaches to generate reduced graphene: (1) by dissolving eutectic Na/K alloy and mixing them with graphite in 1,2 DME, graphenide can be generated after 3 days stirring; (b) by using Birch reaction, where sodium or lithium is dissolved in THF and condensed ammonia at -78 ℃, graphite will be charged by the mixture in 1 hour.[111]

The earliest functionalisation of graphene by using potassium GICs was reported by Soma Chakraborty et al. in 2007. In this study, solid potassium GICs was reacted with 1-iodododecane, the functionalised material is 7-9 nm thick in average with lateral size 0.1-1.4 μm and exhibits solubility in chloroform, benzene, and 1,2,4-trichlorobenzene.[112] Later on, studies show that potassium GICs can be dissolved in NMP, THF, DMF, DMSO, and 1,2 DME.[113] The dissolved, solvated, exfoliated, and extremely reducing graphenide is a perfect nucleophile for nucleophilic reactions. Jan M. Englert et al. prepared graphenide by dissolving Na/K alloy activated potassium GICs in 1,2 DME and treated the graphenide with 4-tert-butylphenyldiazonium tetrafluoroborate (4-tBPD) and 4-sulfonylphenyldiazonium chloride (4-SPD) to produce arylated graphene (Figure 1.12 Raman Spectra, AFM image and measurement of potassium GICs (a)-(c), exfoliated graphene (d)-(f), less functionalised graphene (g)-(i), and highly functionalised graphene (j)-(l).[47]). This is the first systemic and comprehensive study on functionalisation of graphene by using graphenide solution and electrophiles. TGA study suggests the functionalised material will be stable until 480 ℃, where C-C bond between functional group and graphene is broken. AFM confirmed the thickness of monolayer functionalised material is c.a. 2 nm, much thicker than the pristine graphene. Re-dispersibility test was done and arylated graphene can stay dispersible in chloroform with concentration of 27 μg mL^{-1}.[47]

Besides organic diazonium salts, reactions between organic molecules with other good leaving group and potassium GICs are studied extensively. Iodonium salts [114] are the other reactive species which can be precursors for functionality of graphene. Several studies have demonstrated the synthesis of functionalised few-layer graphene or monolayer graphene from GICs or activated CVD-graphene by using corresponding organic iodonium salts. Ferdinand Hof et al. reported functionalisation of potassium activated SWCNT and graphite by using para-functionalised λ^3-iodane (Figure 1.11 A-C). A correlation between the ratio of potassium: graphite and degree of functionalisation was found in this study: graphene exhibits the most functionalisation when (K:C=1:8) stage-1 potassium GICs are used, which is consistent with the reactivity trend of graphene.[115] Ricarda A. Schäfer et al. used λ^3-iodane to functionalise graphene on SiO_2 substrate, where graphene is reduced by Na/K alloy in 1,2 DME.[52]

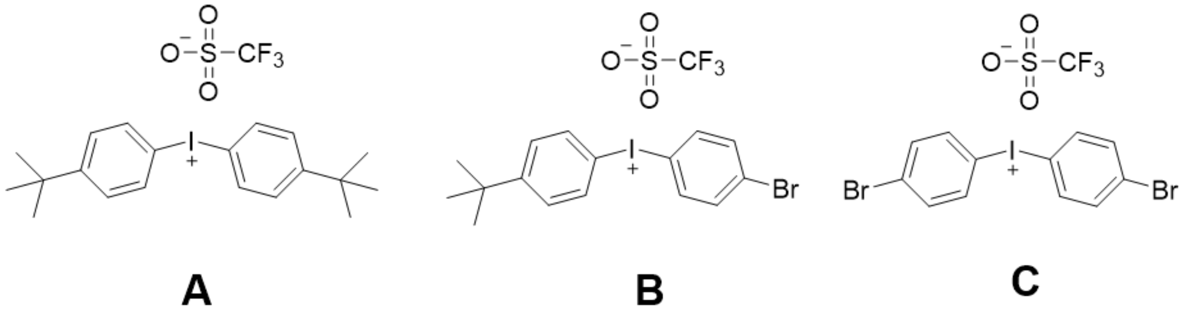

Figure 1.11 Para-functionalised λ^3-iodane bis-(4-(tert-butyl)phenyl)iodonium trifluoromethane-sulfonate (A), (4-bromophenyl)(4-(tert-butyl)phenyl iodonium trifluoro-methanesulfonate (B), and bis-(4-bromophenyl) iodonium trifluoro-methanesulfonate (C)

Kathrin C. Knirsch et al. [116] reported silylation of graphene by using graphenide dissolved in 1,2 DME. In this study, silylation with different precursors trimethylsilyl chloride, trihexylsilyl chloride, and dodecyl(dimethyl)silyl chloride (THS-Cl, TMS-Cl, DDMS-Cl) were carried out. The graphene functionalised by different silyl groups was obtained through nucleophilic substitution. Significant change of I_D/I_G distribution has been realised after the reaction. The functionalisation is further confirmed by TGA-MS since corresponding fragments of functionalities can be identified. Functionalisation degrees of 0.7%, 0.4%, and 1.6% were determined for each electrophile based on the TGA results. Also, it turns out that different bulkiness of precursors does not influence the degree of functionalisation for graphene. The easiest functionalisation that can be achieved by using graphenide is oxidation, hydrogenation, and hydroxylation, where graphenide is spontaneously oxidised out of inert atmosphere. Successful synthesis of hydrogen and hydroxyl grafted graphene has been reported by Philipp Vecera [117,118] et al. The synthesis is done by depositing drops of KC_8/DMSO solution on a silicon wafer and exposing it in ambient atmosphere. According to TG-MS study, the resulted degree of functionalisation is c.a. < 9% at%. The AFM shows that the resulted functionalise graphene are monolayer.

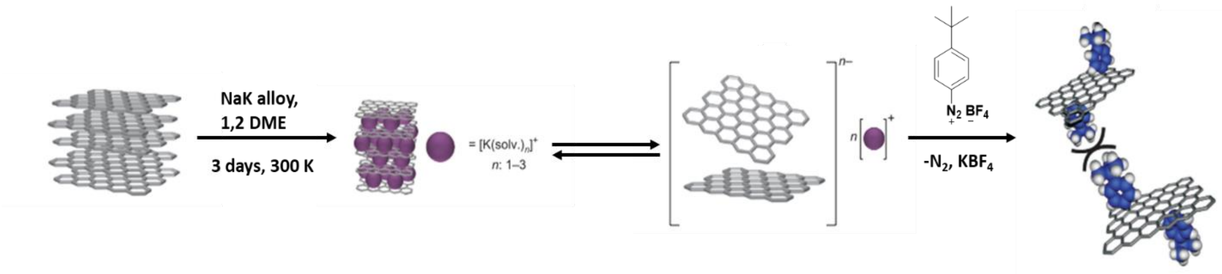

Scheme 1.5 Functionalisation and exfoliation of graphene by using potassium GICs and diazonium salts. Reprinted with permission from J. M. Englert, C. Dotzer, G. Yang, M. Schmid, C. Papp, J. M. Gottfried, H. P. Steinrück, E. Spiecker, F. Hauke and A. Hirsch, Nat. Chem., 2011, 3, 279–286. Copyright 2011 Springer Nature.

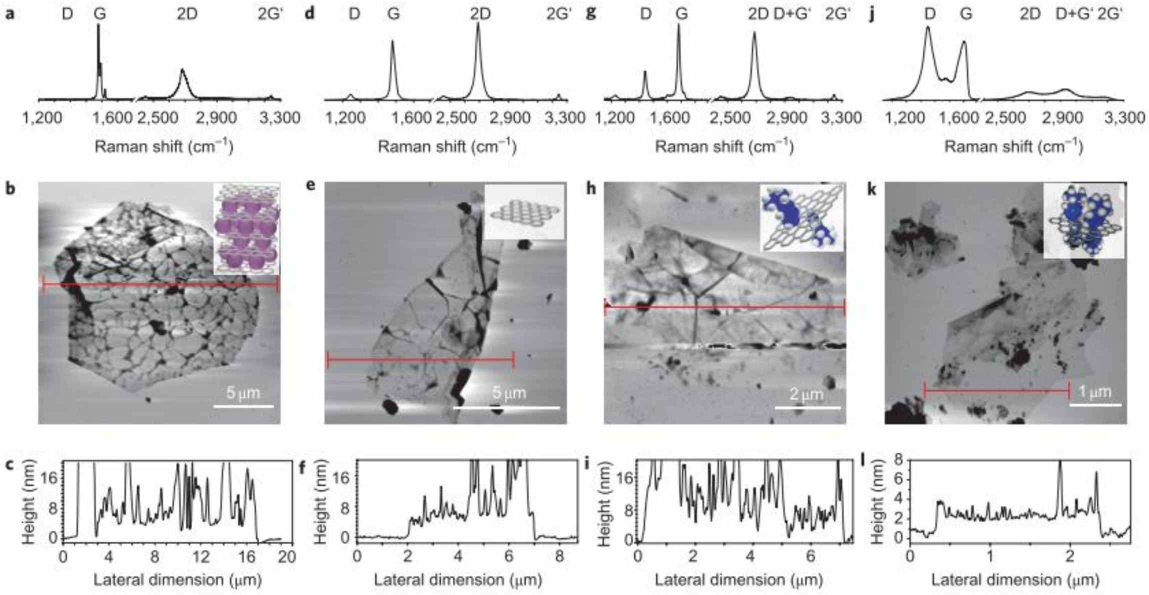

Figure 1.12 Raman Spectra, AFM image and measurement of potassium GICs (a)-(c), exfoliated graphene (d)-(f), less functionalised graphene (g)-(i), and highly functionalised graphene (j)-(l).[47] *Reprinted with permission from J. M. Englert, C. Dotzer, G. Yang, M. Schmid, C. Papp, J. M. Gottfried, H. P. Steinrück, E. Spiecker, F. Hauke and A. Hirsch, Nat. Chem., 2011, 3, 279–286. Copyright 2011 Springer Nature.*

Following the same principle of potassium activated graphenide, Jan M. Englert et al. [42] reported successful alkylation of graphene by using eutectic alloy Na/K activated graphite (Scheme 1.5). The liquid alloy dissolved in 1,2 DME can diffuse into interlayer spaces of graphite to form the GICs and activate the graphite after long time mixing (7 days) without any heating. After formation of GICs, hexyl-iodide was introduced into the mixture, and hexyl-graphene was produced. Statistical Raman Spectroscopy (SRS) indicates that very high overall I_D/I_G ratio (Figure 1.13), which suggests high extent of sp^3 after new C-C bonds formation from the functionalisation; and very high overall I_{2D}/I_G ratio, which is indicative of few-layer and monolayer graphene. Results of TGA-MS shows that the degree of functionalisation is 1.2% for every carbon atom. Enhancement of dispersibility in organic solvents was observed for the hexylated graphene.

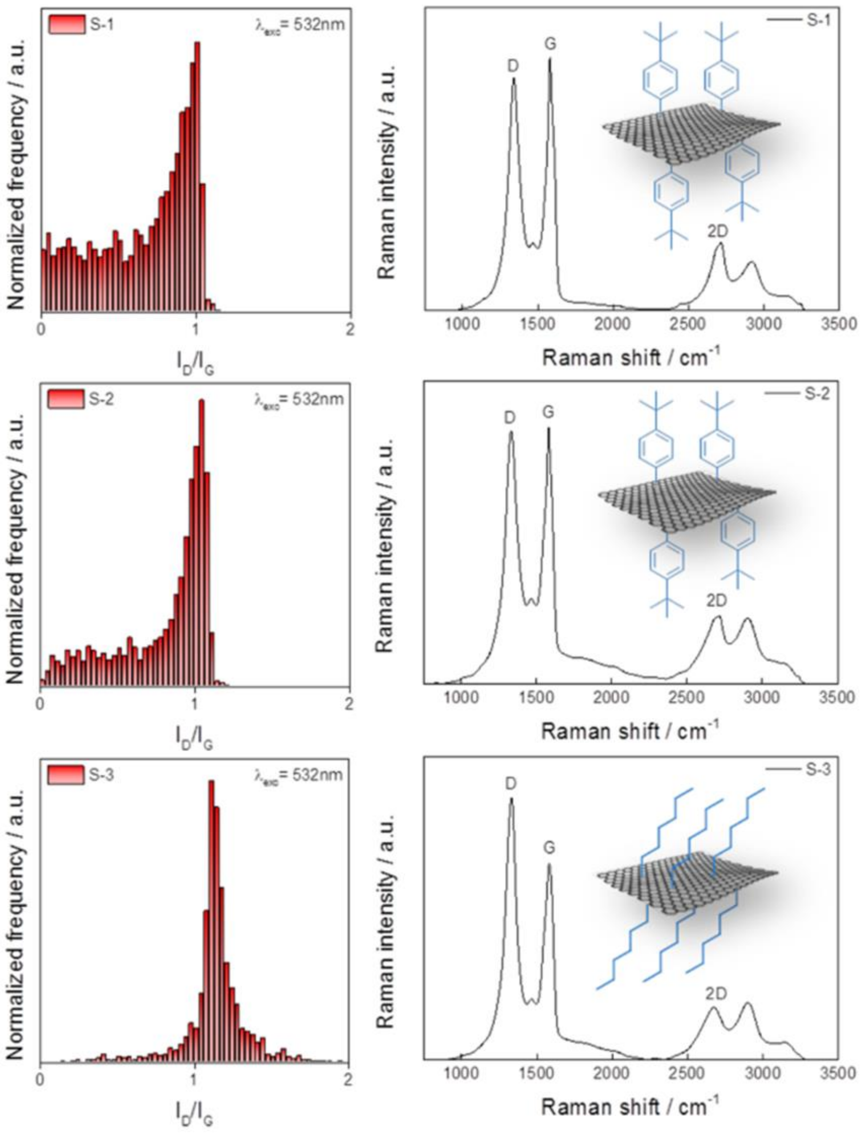

Figure 1.13 SRS and Raman spectrum of graphene functionalised by 4-tert-butylphenyldiazonium (S-1), bis(4-(tert-butyl)phenyl)iodonium salts (S-2), and hexyl iodide (S3).[114] Reprinted with permission from G. Abellán, M. Schirowski, K. F. Edelthalhammer, M. Fickert, K. Werbach, H. Peterlik, F. Hauke and A. Hirsch, J. Am. Chem. Soc., 2017, 139, 5175–5182. Copyright 2017 American Chemistry Society.

When crown ether (15-crown-5) is added to the alloy, the dissolution of alloy into THF can be faster. After dissolution, mixed metal salt [K(15-crown-5)$_2$]Na can be made, and sodium will have an unusual oxidation state -1.[56] Mandakini Biswal et al. [48] used this mixture to activate single layer graphene or bilayer graphene derived from mechanical exfoliation and test them against different organic halides. According to their studies, reactivity of alkyl, aryl, pyridyl, and aniline halides follows the trend I>Br and for the corresponding fluorides and chloride no functionalisation was observed after reaction at room temperature. Crown ether has also been explored to increase the maximum concentration of graphenide in NMP. Chengmin Jiang et al. employed 18-crown-6 to coordinate with potassium cation so that better solubility in organic solvent can be achieved. Noticeably, the maximum concentration increases from 0.9 mg mL^{-1}

to 1.5 mg mL^{-1} in NMP with appropriate concentration of 18-crown-6 additive, further addition would result in aggregation.[119] However, this is more significant for stabilising graphene in solvent, as pointed out by Hui-Lei Hou et al. [120] in another study, excessive solvation of potassium cation would decrease the reactivity of graphenide. The solvation effect of different solvents on the functionalisation level is also investigated and the reactivity of graphenide in solvent follows the order of 1,2 DME > THF > NMP > DMF. Appropriate degree of solvation of graphenide is found to be beneficial to the final degree of functionalisation since solvation of graphenide can prevent graphenide from flocculation before reaction. Kathrin C. Knirsch et al. [116] demonstrated that reaction between the liquid electrophile and solid potassium GICs would result in product with 26% lower degree of functionalisation compared to the product reacted from graphenide solution.

By utilising the nucleophilic property of potassium GICs, different organic moieties can be conjugated onto graphene and properties of graphene can be hence modified. Hui-Lei Hou and Andreas Hirsch [121] demonstrated covalent attachment of a nickel complex (nickel tetraphenylporphyrin) to graphene surface by using diazonium group on the complex, which has been achieved before by cycloaddition. The resulted hybrid demonstrates different absorption behaviour compared to pristine NiTPP. Aryl diazonium salts, such as methoxyphenyl, are found particularly efficient on covalent functionalisation of graphenide.

To summarise, the first advantage of using graphenide is easy control of functionality on the graphene, as the reaction condition is rigidly controlled, consistent and the same functionalities can be resulted. Utilising this property, researcher [46] reported the successful mono- and ditopic bifunctionalisation of graphene where two different functionalities are added to one-side or both sides of graphene through a multiple activation process. The second advantage is control of functionalisation degree, as the reaction is thermodynamically favourable, no further treatment is required, thus no over-functionalisation will happen, and structure of graphene will be retained for the most part. The third advantage is the nucleophilic nature of graphenide opens various possible functional groups for functionalisation.

However, the disadvantages of reductive functionalisation are obvious too. One major issue is the limited scalability of the process. The first problem comes from the condition of the reaction. Since inert atmosphere is required through the whole process, in addition, all the starting material needs special dehydration and degas, the cost of scaling such a process is massive. The second problem is related with the low solubility of graphenide in organic solvents. According to relevant studies, graphenide is most soluble in NMP, where it can achieve a concentration of 0.9 mg mL^{-1} .[69] Other solvents, such as THF etc. the maximum concentration that can be achieved is below this value. The low solubility of graphenide suggests that even though the conversion of graphenide to functionalised graphene is 100%, the yield for every batch is still low. The reaction time is another potential issue, as most of studies report that days of reaction are required to complete the reaction. Overall, reductive functionalisation is an excellent strategy to produce high quality functionalised few layer to monolayer graphene, however, its characteristics make it unfavourable as a feasible industrial process.

1.7.2 Oxidation of Graphene

In contrast to induce negative charges on graphene in reductive functionalisation, positive charges are induced during oxidative functionalisation. Generally, a more electronegative molecule or atom can be intercalated into interlayer of graphite, for example, bromine, fluorine, perchlorate, bisulphate etc. Among them the most studied GICs is the sulphate GICs. Compared to formation of potassium GICs, though oxidants are required for the formation of sulphate GICs[64], however, the condition for formation is not as harsh as that of potassium GICs. Sulphate GICs can not only be prepared at atmospheric condition, but also be relatively stable to be stored. The stability of sulphate GICs originates from the protection of excessive sulphuric acid. According to relevant study, stage 1 sulphate GICs start its transition to higher stage GICs when the concentration of surrounding sulphuric acid is diluted to 10M. This means stage 1 sulphate GICs will stay stable when sulphuric acid is concentrated enough.

A typical oxidative functionalisation using sulphate GICs as starting material is the method for GO production (Hummers, Brodie[65], and Staudenmaier[122] method). Due to evolution of ClO_2 during reaction, Staudenmaier and Brodie method are less favourable nowadays since its accumulation leads to risk of explosion. The original Hummers method was also modified and has become the most popular approach for graphene oxide preparation for research.

Generally, the oxidation of graphite starts with the intercalation of graphite by sulphuric acid by stirring graphite in a strongly oxidised and acidic medium (for example by using con. H_2SO_4 and $KMnO_4$).[123] The successful intercalation is indicated by the presence of deep blue colour of the graphite.[64,123] Oxidants, such as potassium permanganate, sodium perchlorate etc., are added afterwards so that functionalities can be added to the graphene of graphite through oxidation reactions. The graphite oxide after the purification, is then exfoliated by sonication or other techniques to form graphene oxide. From this point, the graphene oxide can be reduced to reduced graphene oxide (rGO) or partially oxidised graphene. Graphene oxide is an important precursor for graphene and functionalised graphene.

However, unlike functionalisation derived from potassium GICs, due to addition of strong oxidants during reaction, the graphene produced is over-oxidised, as a result, the resulted carbon lattice is extensively damaged and oxygen content is high, the typical C/O ratio range is 1.8-3. The other difference comparing to the reductive functionalisation is the functionality is less controllable. A plethora of relevant studies have shown GO is graphene material functionalised by epoxy, hydroxyl, carbonyl, and organosulphur groups. In addition, over-functionalisation will leave defective sites on graphene domain. K.A. Mkhoyan et al. employed AFM and EELS techniques to study the structure of GO, they found GO flake is rough and distorted due to sp^3 from oxygenated functionalities on the basal plane. And when C/O = 5, it is enough to make this structural change.[124] Those defects may remain after reduction. C Gómez-Navarro et al. observed topological defects in Hummers method derived and hydrogen plasma reduced sample, which are created due to removal of oxygen groups after reduction. From their observation on TEM images (Figure 1.15), they also deduced that oxidation happens on isolated area since c.a. 60% area is intact. In comparison, graphene produced by mechanically cleavage, however, has no such defects.[125] In addition, relevant TEM study also indicates the presence of holes in GO flakes. K.Erickson et al. suggests the size of those holes are no more than 5 nm^2.[39] For the origin of those holes on the basal plane of GO, there are several assumptions. They can be the intrinsic defects in graphite. They can also be created during oxidation where C-C bonds are broken due to the aggressive condition.[39] Based on computational results from Jeffrey T. Paci et al., occasional broken of C-C bonds will leave holes in graphene lattice and become sites for carbonyl and alcohol groups. At elevated temperature, holes can also be created in GO.[38] S. Eilger ascribed the formation of those holes to elimination of CO_2 or CO during the reduction. As they found CO_2 and water are intercalated or adsorbed in GO, intercalated CO_2 would be realised with water and CO to cause bursting of GO film upon heating to 130 ℃, according to AFM and SEM study, the size of these blisters is 20-30 nm (Figure 1.14).[37]

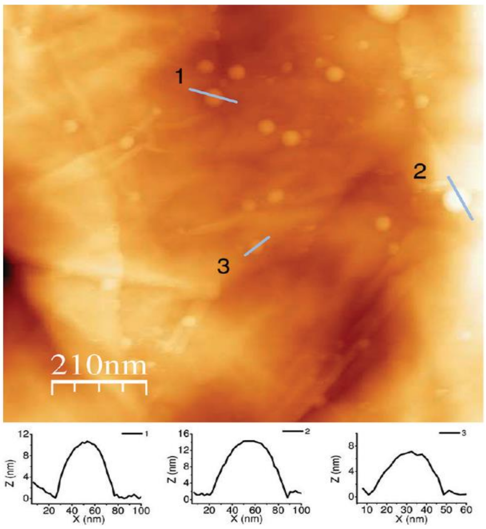

Figure 1.14 AFM image and measurements of blisters created after heating GO film to 180 ℃.[37] *Reprinted with permission from S. Eigler, C. Dotzer, A. Hirsch, M. Enzelberger and P. Müller, Chem. Mater., 2012, 24, 1276–1282. Copyright 2012 American Chemistry Society.*

Therefore, researchers have been focusing on controlling the degree of the oxidation, so that the structure of the produced graphene oxide can be retained to the most extent. Generally, researchers approach this problem by two angles, one is to enhance the effect of reduction so that the damaged structure can be restored, which will not be discussed in this review. And the other is to modify the conditions during oxidation.

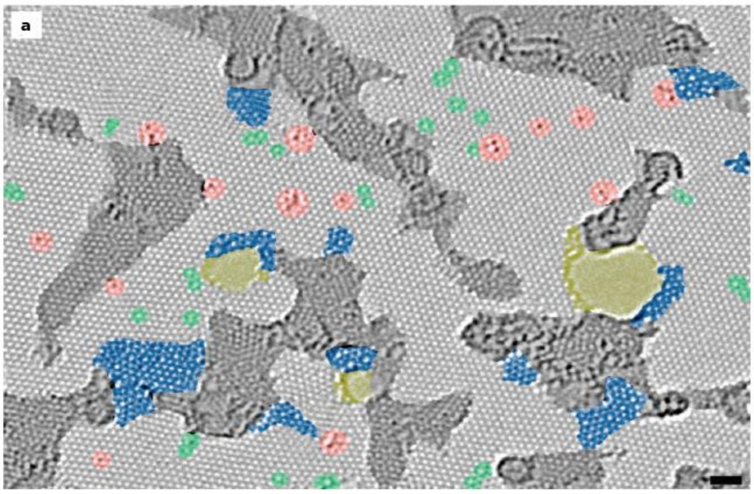

Figure 1.15. Atomic resolution, aberration-corrected TEM image of a single layer reduced-graphene oxide membrane. The defect free crystalline graphene area is displayed in the light grey colour. Contaminated regions are shaded in dark grey. Blue regions are the disordered single-layer carbon networks, or extended topological defects, which are results of the oxidation reduction process. Red areas highlight individual ad-atoms or substitutions. Green areas indicate isolated topological defects, that is, single bond rotations or dislocation cores. Holes and their edge reconstructions are coloured in yellow. Scale bar 1 nm.[125] *Reprinted with permission from C. Gómez-Navarro, J. C. Meyer, R. S. Sundaram, A. Chuvilin, S. Kurasch, M. Burghard, K. Kern and U. Kaiser, Nano Lett., 2010, 10, 1144–1148. Copyright 2012 American Chemistry Society.*

The attempts of producing mildly oxidised graphene or partially oxidised graphene start from modifying Hummers Method. By changing the original conditions of Hummers Method such as the amount of $KMnO_4$, temperature of oxidation, starting material of oxidation, or duration of oxidation, numerous studies report the successful preparation of graphene oxide with different degree of oxidation, though the control of oxidation degree is very limited for most of cases. G. Shao [126] studied the effect of using shorter reaction time and lower oxidation temperature in the step 3 of Hummers method. The statistical AFM measurements shows that graphene oxide with larger average size can be produced by shorter reaction time and lower temperature in the final step. However, the effect on C/O ratio is not significant comparing to GO produced by Hummers method.

Higher C/O ratio can be achieved by decreasing the amount of $KMnO_4$ during oxidation. Y. Xu et al.[127] has investigated the effect of decreasing $KMnO_4$:grahite ratio from 3:1 to 1:1. They found C/O ratio has increased from 2.1 to 3.1 consequentially according to XPS study. By comparing peaks of UV-Vis spectra, π-π domain was more preserved for GO with less oxidant. Even higher C/O ratio can be achieved by overall modification of Hummers Method. Suyun Tian et al. [128] and S. Kim et al. [129] reported the synthesis of graphene oxide with relative low oxygen by using less potassium permanganate (mass ratio 1:1 to graphite), lower temperature, and shorter reaction time. In S. Tian’s work, they also found that the mild condition facilitates the edge oxidation and leaves basal plane of graphene oxide intact. S. Kim et al. have also studied the effect of various reaction time. By varying reaction time (30 mins, 60 mins, 90 mins, 120 mins), graphite with different degree of oxidation were obtained.

Without changing the starting materials of Hummers reaction, S.Eigler et al. have demonstrated that less defective GO can be prepared by controlling micro-macro kinetics of the oxidation. Instead of reducing oxidation time, S.Eigler increased oxidation time to 16 hours and maintained the oxidation temperature below 10℃. Though, the XPS survey indicated that the resulted material (n-GO) contains 52% carbon, which is slightly more oxidised compared to the c-GO (GO prepared by standard Hummers method, carbon content: 59%). The n-GO displayed a sharper peak at 230 nm than that of c-GO. This means n-GO has more ordered structure. The fact of n-GO having less defects than c-GO was corroborated by Raman study of corresponding derived from the same method. By calculating the distance between defects, rGO-n has longer average distance between defects. This proves that less defects were created during the oxidation for production of n-GO.[130]

Table 1.1 Variations in conditions of the Hummers method to produce GO with more C:O ratio.

	Oxidant	Amount of Oxidant	Step 1	Step 2	Step 3	C/O Achieved
Hummers Method [65,126]	$KMnO_4/NaNO_3$	1:3 to 1-6	1 hour stirring < 5 ℃	2 hours stirring @ 35 ℃	Water added 15 mins @ 98℃	2.33
Modified Hummers Method (1) [126]	$KMnO_4/NaNO_3$	1:3	1 hour stirring < 5 ℃	0.5 hour stirring @ 60 ℃	0.5 hour stirring @ 60℃	2.28
	$KMnO_4/NaNO_3$	1:3	1 hour stirring < 5 ℃	15 mins stirring @ 60 ℃	No	No
	$KMnO_4/NaNO_3$	1:3	1 hour stirring < 5 ℃	1 hour stirring @ 45 ℃	No	No
	$KMnO_4/NaNO_3$	1:3	1 hour stirring < 5 ℃	1 hour stirring @ 30 ℃	No	2.25
Modified Hummers Method (2) [129]	$KMnO_4$	1:1	stirring @20 ℃	0.5-2 hour stirring @ 20 ℃	No	4.1 to 2.8
Modified Hummers Method (3) [127]	$KMnO_4$	1:1	stirring @50 ℃	Water added 15 mins @ 98℃	no	3.1

More recently, S.Eigler [131] found a way to produce mildly functionalised graphene from sulphate GICs without presence of conventional oxidants. Firstly, sulphate GICs were prepared by a method suggested by Dimiev et al.[64], where graphite is added to con. H_2SO_4/ persulphate mixture, unlike sulphate GICs prepared by nitric acid and potassium permanganate, no C-O bonds are formed during the synthesis. High quality functionalised graphene is then prepared by treating as-synthesised stage-1 sulphate GICs water directly and purified by repeated centrifugation and re-dispersion (Figure 1.16). The elemental analysis shows that this material (oxo-G) contains 86% carbons. Further TGA-MS results suggested the mildly oxidised graphene has low degree of oxidation as only 11.8% weight loss is realised between 200-500 ℃. Degree of functionalisation 4% was calculated based on TGA and elemental analysis. The defect density of derived by this material was analysed by SRS to understand the damage from functionalisation to the carbon backbone of graphene. It turned out the resulted has only 0.04% defects, which means the condition of functionalisation is very mild. However, just as the problems in reductive functionalisation by using potassium GICs, the yield of oxo-G is not great. Moreover, there are contradictory reports regarding to the same reaction, as some groups observed the sulphate intercalation is reversible upon addition of water [64] (sulphate GICs will turn into graphite again upon water addition), S. Seiler et al. [132] suggested that grade of graphite might play a critical role in this contradiction. As S. Seiler et al. compared formation and hydrolysis of sulphate GIC prepared by three different graphite, they found the only sulphate GIC reverts to starting graphite upon addition of water is the turbostratic graphite which lacks stacking order. Successful synthesis of oxo-G was realised for the other two natural graphite.

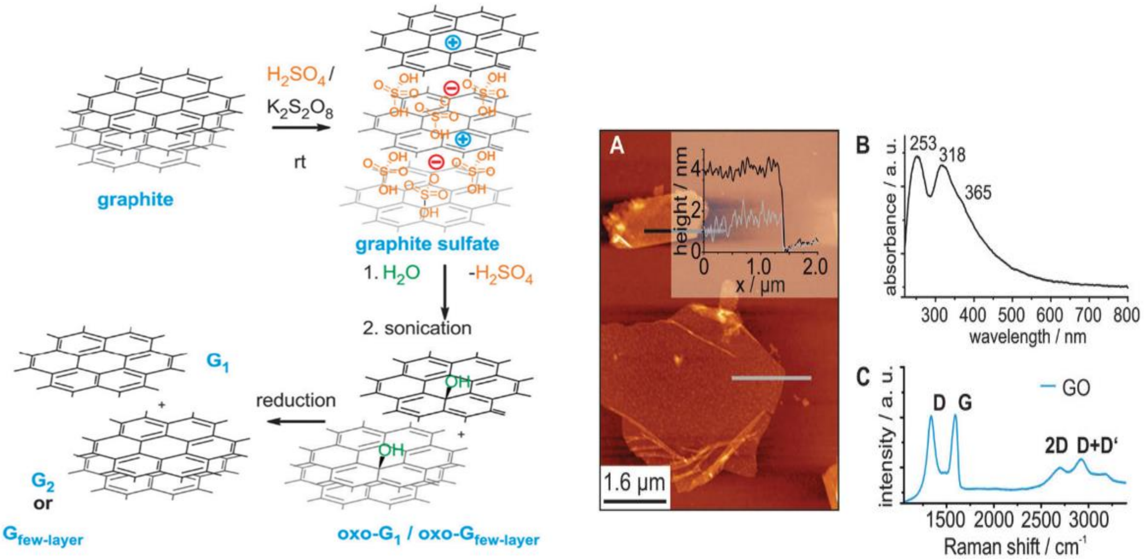

Figure 1.16 Left: preparation of sulphate GICs and production of oxo-G through water quenching process. Right: (A) AFM image and measurement of oxo-G flakes, (B) UV-Vis spectrum of oxo-G in water, (C) Raman spectrum if oxo-G.[131] Reproduced from S. Eigler, Chem. Commun., 2015, 51, 3162–3165 with permission from the Royal Society of Chemistry..

It is worthy to note that the aim of many studies on mild oxidation is to explore a versatile approach of producing exfoliated graphene with less damage to sp^2 domain of graphene, so that graphene with comparable properties to that of pristine graphene can be prepared after reduction. In this sense, graphene derived from mild oxidation is a precursor for production of graphene. Therefore, properties of these intermediates, such as dispersibility, electrical conductivity etc., have been rarely investigated.

1.7.3 Electrochemical Exfoliation and Functionalisation

Electrochemical methods of preparing GICs have been extensively studied before the discovery of graphene, until recently electrochemical exfoliation and functionalisation of graphite has been realised as a methodology to produce functionalised graphene. The same as the reductive and oxidative functionalisation, electrochemical functionalisation & exfoliation of graphite starts from the formation of GICs. By applying biased current/electrical potential, migration of electrolytic anions or cations into interspace of graphite will happen. The functionalisation happens through the radicals which is formed due to the transformation of electrolyte by current and electrical potential. As the edge and boundary of graphite is functionalised, expansion of graphite on c-axis happens and then exfoliation is achieved. Depending on the polarity of graphite during the electrochemical process, the process can be anodic or cathodic. When graphite is anode, graphite will undergo oxidative functionalisation; however, when graphite is cathode, graphite will undergo reductive exfoliation. In addition, depending on the electrolyte used, the process can also be categorised into aqueous and non-aqueous.[133]

Functionalised graphene might be prepared by adapting anodic process, where intercalation of anions into graphite will be assisted by current flow. The most common anion used for the process is sulphate anions since production of different stage sulphate GICs from concentrated sulphuric acid and HOPG under different electrochemical conditions is well established. Recently, exfoliation and functionalisation of graphite using diluted sulphuric acid are developed. Although most of these studies focus on production of exfoliated non-functionalised graphene, but theirs XPS analysis indicate the exfoliated graphene was not intact but oxidised after electrochemical treatment. This is because the inevitable generation of free radicals at anode during the process. Suyun Tian et al. reported synthesis of water dispersible few-layer graphene by using electrochemical method. Oxone (($KHSO_5 \cdot 0.5\ KHSO_4 \cdot 0.5\ K_2SO_4$) was used as electrolyte and oxidants, with 50 V anodic potential, the dissolved SO_4^{2-} will be active for intercalation and HSO_5^-, HSO_4^- will be activated to radicals $SO\cdot^-$ or $OH\cdot$ (Figure 1.17). Those strongly oxidising radicals are responsible for oxidation of graphene. The resulted graphene demonstrated excellent re-dispersibility as absorbance of a 0.2 mg mL^{-1} water dispersion did not show any change after 10 days sediment. The material could contain 13.37 at% or 16.37 at% of oxygen if anodic potential during synthesis was changed. In addition, UV-Vis spectrum of the dispersion shows a strong absorption at 266 nm. This means graphene was mildly oxidised during the electrochemical process. AFM (31 flakes) and SEM (45 flakes) study suggested c.a. 60% of flakes are 2-5 layers graphene, and the lateral size of the flake is ranged from 1-5 μm. The electrical conductivity of the material was measured by fabricating the graphene into thin paper. The flexible paper was very conductive as smooth, as the conductivity is 11,415.5 S/m.[134]

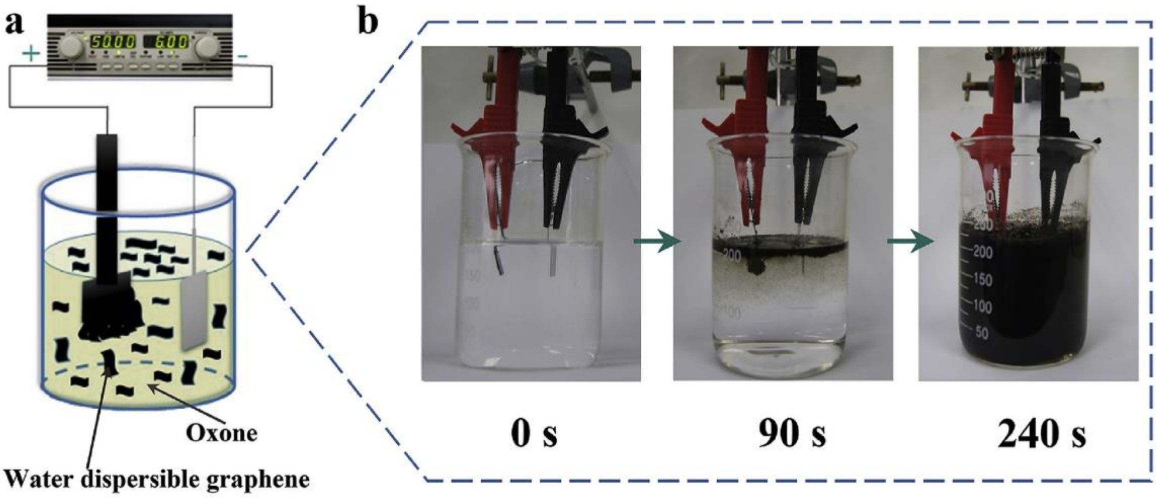

Figure 1.17 (a) Experimental set-up of electrochemical exfoliation and oxidation of graphene by using oxone. (b) exfoliation at different reaction time.[134] *Reprinted with permission from S. Tian, S. Yang, T. Huang, J. Sun, H. Wang, X. Pu, L. Tian, P. He, G. Ding and X. Xie, Carbon N. Y., 2017, 111, 617–621. Copyright 2016 Elsevier Ltd.*

As functionalisation governed by one-electron process can be hugely enhanced by the electrochemical bias, other species with similar behaviour are also explored to functionalise graphene. Santanu Sarkar et al. discovered that Kolbe reaction can be used to functionalise graphene. In detail, carboxylate groups of a benzyl carboxylic acid can unde anodic oxidation to give benzyl radical; α-naphthylacetate was selected as precursor for α-naphthylmethyl radical to produce α-naphthylmethyl functionalised epitaxial graphene. They further found the modification is reversible under electrochemical condition.[135]

Hui Shan Wang devised a different methodology to exfoliate and functionalise bulk graphite. Instead of facilitating formation of GICs, they focused on oxidation to weaken Van der Waal interaction between graphite layers, so that a second step of exfoliation can be easily done by sonication. They used p-phthalic acid and NaOH as electrolyte, the oxidation originates from hydroxyl radicals generated during the anodic process. The p-phthalic acid would precipitate out during the process and cover the surface of graphite. The masked graphite anode would undergo less bubble generation and hence prolonged oxidation. It was found that other aromatic molecules with pH-dependent solubility in water have the similar outcomes. After processing, water dispersible graphene of 1–6 atomic layers in thickness with 11.7 at% oxygen and 1.0–2.5 μm was produced. Its water dispersion was found to be stable up to 2 months by UV-Vis study.[136]

1.8 Concluding Remarks and Outlook

Functionalised graphene with retained sp^2 structure would not only demonstrate enhanced dispersibility in solvents with respect to pristine graphene but also exhibit improved thermal stability with respect to graphene oxide. In addition, the less disrupted sp^2 network can mitigate the impact of functionalisation on the intrinsic properties of graphene such as electrical conductivity or thermal conductivity. The high-quality functionalised graphene will show great potential in improving the interfacial interaction between the graphene and the polymer for fabrication of composite. Over the extensive research in the past twenty years, the methodologies and strategies of graphene functionalisation have been evolving significantly and significant achievements have been made as functionalised graphene with various functionality can be synthesised via different chemistry. In addition, the resulting material also demonstrates good control on the extent of the functionalisation and the identity of the functionalisation. However, most of the methods are difficult to be scaled-up. In parallel, the development of large-scale production of functionalised graphene have exhibited encouraging results. For example, electrochemical routes and using sulphate GICs show great potential to produce water-dispersible graphene in large scale, though the control of identity of functionalities is problematic. Overall, the emerging functionalisation methods all have their advantages and disadvantages, and the production of high-quality functionalised graphene with controlled dimensions and functionalities in large scale remains as major challenges.

The aim of this PhD project is to explore novel strategies and methods which can produce functionalised graphene with controlled degree of functionalisation and are also amenable for large scale production. Although there are various methods to produce functionalised graphene, this project will focus on the methods which involves using GICs for its higher reactivity and greater potential of scalability. In Chapter 2, reduction functionalisation has been performed by using potassium GICs and organic halides. In Chapter 3, a novel methodology which achieved aryl functionalisation by using *in situ* generated radicals and sulphate GICs was studied and investigated. In Chapter 4, production of the mildly oxidised graphene from SGICs, which was catalysed by $Mn(OAc)_3$, was explored and investigated. In Chapter 5, the mildly oxidised graphene derived in the Chapter 4 was applied to PMMA, the rheological properties of the resulting nanocomposite were studied and compared with those of composites with other types of graphene fillers.

Chapter 2. Synthesis of Functionalised Graphene from Na/K alloy activated Potassium GICs

2.1 Introduction

Insertion or intercalation of potassium atoms into the interlayer of graphite leads to formation of the lamellar compounds: potassium graphite, which can be denoted as C_nK^+. Depending on the conditions during intercalation, potassium graphite with different stages (indicated by n, where n=8 is stage 1, n=24 is stage 2 etc.) can be prepared. A stage 1 GIC means the layers of guest atoms and layers of graphene alternate. Indeed, the stage 1 potassium graphite or potassium GICs KC_8 suspending in THF, have been investigated in a range of organic reactions as a reducing agent.[137–139]

The fate and the role of the counter anion graphenide during organic reactions has only been of interest since the discovery of graphene and the subsequent demand for functionalised graphene. Numerous studies have suggested that few-layer graphene can be produced by probe-sonicating KC_8 dispersion.[47,114,121,140–142] KC_8 is ready for exfoliation because the distance of interlayer space of graphite has increased from 0.335 nm to 0.54 nm upon intercalation [143] and the interlayer interaction graphite has been weakened by the intercalants. The exfoliated KC_8 can be further centrifuged to remove any insoluble material to give graphenide solution, which has been proved to be extremely reactive nucleophile for production of functionalised graphene. Successful functionalisation of graphene from this GICs derived graphenide have been shown by using diazonium salts,[47,140] iodonium salts, and organic halides [24,116,81] based on relevant studies. Similarly, the formation of nucleophilic graphene sheets can be achieved directly by treating monolayer graphene with a eutectic alloy of sodium and potassium Na/K and reaction with organic halides.[42,47,48,111]

Surprisingly, very few studies have tested the dispersibility of the functionalised material in volatile organic solvents and the role of the functional group. One possible reason is the limited amount of material that can be produced. In this work, an epoxy group functionalised graphene (**EP-G**) is prepared by using epibromohydrin and Na/K alloy derived potassium GICs. The dispersibility of this **EP-G** is tested in THF, acetone, IPA, methanol, and ethanol. **EP-G** demonstrates excellent stability and dispersibility in those solvents, which make it a promising filler for composites fabrication. In addition, 4-iodoaniline and 4-nitrobenzyl tosylates were used as aryl groups precursors to react with the potassium graphenide. Corresponding 4-aminobenzene (**Aniline-G**) and 4-nitrobenzene functionalised graphene (**4-Nitrobenzyl-G**) were obtained.

2.2 Preparation and Characterisation of Potassium GICs from Na/K Alloy

There are several existing ways for potassium GICs preparation: (i) electrochemical intercalation developed by Eichinger et al. [144], (ii) two-zone vapour transportation developed by Dresselhaus et al.[110] in 1980s, (iii) melting potassium over graphite under an atmosphere used first by J.-M. Lalancet in 1970s [139], (iv) liquid phase intercalation via formation of Na/K alloy in 1,2 DME reported more recently by Jan M. Englert and co-workers [47]. In this work, the vacuum dried graphite was mixed with eutectic mixture of sodium and potassium in a N_2 filled glovebox. The mixture was then heated to 160-200 ℃. The reaction completed after 4 hours' heating with the appearance of golden colour of the mixture. After cooling to room temperature and before dispersing into THF to produce potassium graphenide, the golden material was characterised by Raman spectroscopy and powder XRD to confirm the existence of stage-1 potassium GICs.

To investigate if stage-1 potassium GICs can be prepared successfully by using graphite with different thickness and lateral sizes, two sources of graphite were used. Two sources of graphite were selected—the mesh 325 graphite flakes (**F325**), which is natural graphite flakes with lateral size <44 μm; and the P40 graphene nanoplatelet (**P40 GNP**), which is commercial graphene material with average lateral size 10 μm and thinner thickness 50-200 nm. Both starting materials were characterised by Raman spectroscopy. The Raman spectrum (Figure 2.1-d) of **F325** demonstrated three peaks D band (1350 cm^{-1}), G band (1580 cm^{-1}), and 2D band (2709 cm^{-1}), which are typically attributed to graphite. Identically, **P40 GNP** (Figure 2.2-d) exhibited the same peaks with the same peak positions. I_D/I_G ratio was calculated to evaluate the defects level and I_{2D}/I_G ratio was calculated to evaluate the thickness in the graphite and graphene materials. In this study, I_D/I_G can be useful to indicate the degree of functionalisation. The position of 2D band *Pos* (2D) is another parameter which can qualitatively reveal the exfoliation level of graphene. Statistical Raman spectroscopy (SRS) was further employed to check the homogeneity of both materials. At least 225 spectra were acquired from a 80×80 μm sample area. As the histogram shown (Figure 2.1 a-c and Figure 2.2 a-c), the narrow distribution of I_D/I_G ratios and the low average I_D/I_G ratios (**F325**= 0.11; **P40 GNP**= 0.11) suggests both starting materials have low level of defects. The narrow distribution of I_{2D}/I_G ratios and the low average I_{2D}/I_G ratios (**F325**= 0.32; **P40 GNP**= 0.33) indicate both starting materials are thick graphite rather than graphene materials. These results are consistent with the results derived from the I_{2D}/I_G vs *Pos* (2D) plot, where the I_{2D}/I_G ratios are correlated with the other thickness indicator position of 2D peaks—material with lower *Pos* (2D) is thinner.

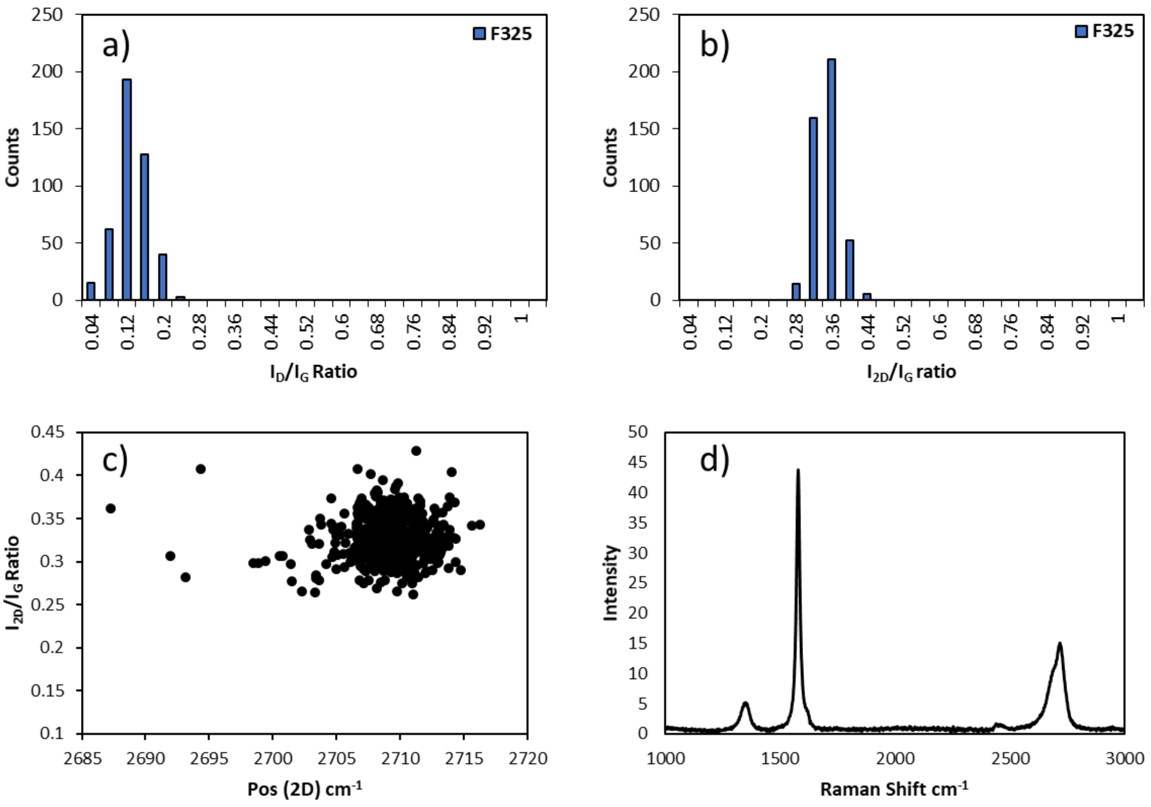

*Figure 2.1 (a) I_D/I_G and (b) I_{2D}/I_G histograms, (c) I_{2D}/I_G vs Pos (2D) plot, and (d) Raman spectrum of **F325**.*

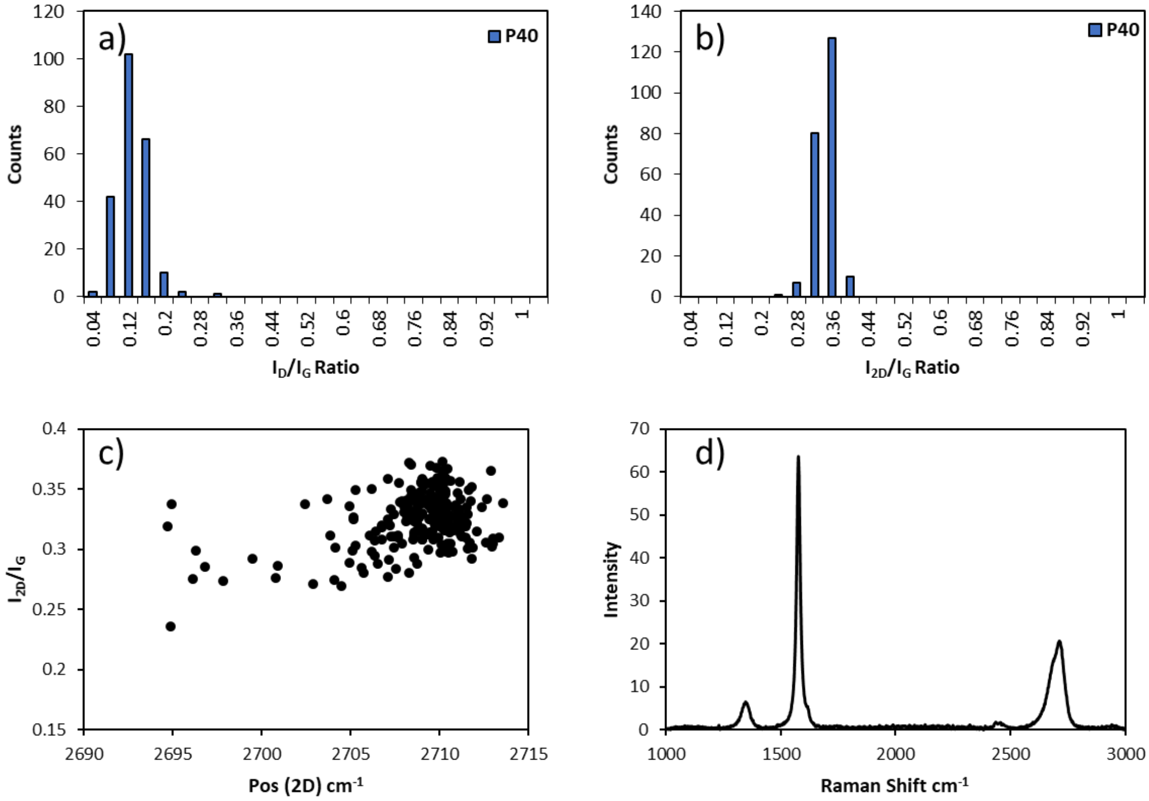

*Figure 2.2 (a) I_D/I_G and (b) I_{2D}/I_G histograms, (c) I_{2D}/I_G vs Pos (2D) plot, and (d) Raman spectrum of **P40 GNP**.*

After intercalation, Raman spectrum of graphite material demonstrates significant differences due to charge-transfer between graphene layer and potassium. SRS was not employed to study the homogeneity of the potassium GICs due to the air sensitivity of the material. Four noticeable vibrational modes can be identified from the Raman spectra of the potassium GICs (Figure 2.3). The first mode is C_z at 560 cm^{-1}, this mode corresponds to carbon atoms out of plane motion and only be visible when high intercalation levels are achieved. The intensity of C_z mode is the highest when potassium GIC of the study shows the most golden colour. The next signature region is from 1140 to 1260 cm^{-1}. It is called D mode as it arises from the defects or edge of the graphite. The G band becomes very complicated for the first stage potassium GICs. It has Breit-Wigner-Fano (BWF) line-shape and it is composed by 3 different modes E_{2g2} mode (1510 cm^{-1}), E_{2g1} mode (1547 cm^{-1}), and GD mode (1563 cm^{-1}). The contribution of each mode can be deconvoluted by BWF line shape analysis. Same as the D mode, the GD mode originates from the intrinsic defects on the starting material rather than the potassium GICs, in other words they are not related with level of intercalation. The more defective of the sample, the more contribution from those two components. E_{2g1} mode will increase with increase of D and GD mode and E_{2g2} mode follows a reverse trend. E_{2g2} mode contributes the most when the sample is defect-free and highly intercalated. Composition of G band will become less complicated for potassium GICs with lower intercalation level. For the second stage potassium GIC, the Fano feature is reduced, however the position of G band is shifted to 1610 cm^{-1}. For GICs with stage>2, a second G band, which is close to that of graphite and graphene, will show up at 1580 cm^{-1}, and 2D band starts to appear.[107,147]

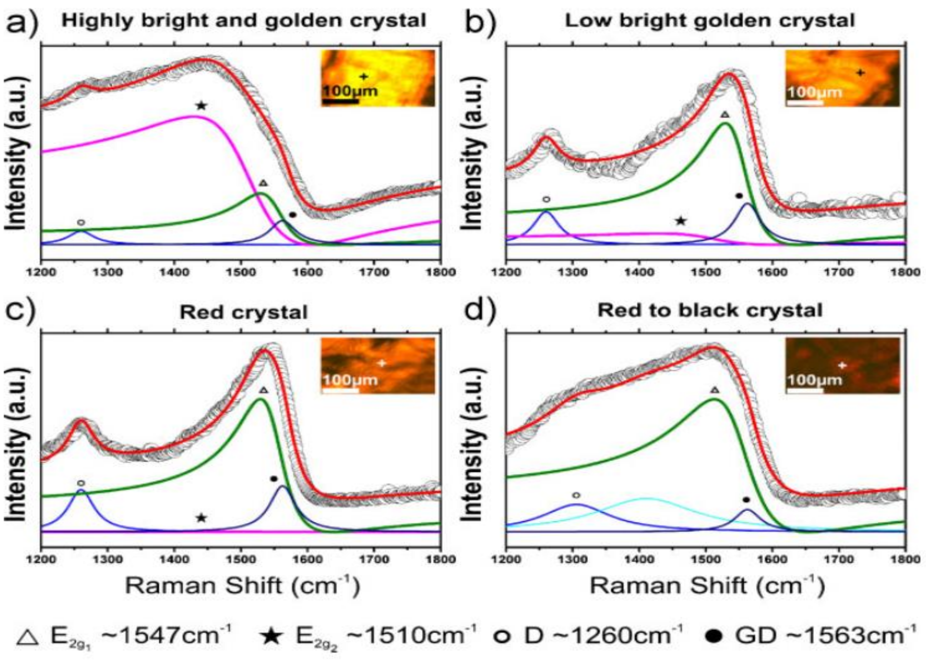

Figure 2.3 Crystal of KC$_8$ with different colours are analysed by Raman spectrometer. The Breit-Wigner-Fano (BWF) line-shape is deconvolved to each component. The solid lines represent fits with BWF lines corresponding to the D and GD modes (blue curve), the E$_{2g1}$ mode (green curve) and E$_{2g2}$ mode (pink curve).[147] *Reprinted with permission from J. C. Chacón-Torres and T. Pichler, Phys. Status Solidi Basic Res., 2011, 248, 2744–2747. Copyright 2011 John Wiley and Sons.*

The production of stage-1 GICs from each graphite is confirmed by powder XRD (Figure 2.4). The disappearance of (002) at 26.9 ° indicates that the interlayer distance has increased after potassium intercalation. Instead, peaks at $2\theta = 15.3°$ and $33.2°$ emerge and they come from the stage one potassium GICs — KC$_8$. Raman spectroscopy study demonstrates more differences between the two GICs. As shown from the Raman spectra of both GICs (Figure 2.5), first stage potassium GICs have been obtained due to appearances of BWF line-shaped G band and C$_z$ mode. The only difference between the two is **P40** GICs is more defective than the **F325** GICs as stage 1 PGICs of **P40 GNP** exhibited GD peak (1563 cm^{-1}) and D peak (1260 cm^{-1}). However, this contradicts to the low I$_D$/I$_G$ ratio (0.08) from the SRS analysis. The mystery is unveiled when SEM images and XRD spectra of the two graphites are compared. Though **P40 GNP** demonstrated small intensity of defects in Raman spectroscopy, stacking and size of **P40 GNP** is less ordered and smaller than **F325** graphite as the (101) XRD pattern (Figure 2.4) of **F325** is sharper than that of **P40 GNP** which indicates presence of increased parallel carbon layers and more orderly arranged aromatic carbon grid layer.[148] The different stacking of the two materials can be visualised by their SEM images (Figure 2.6). The **P40 GNP** exhibits distinct feature of re-aggregation as flakes of graphene are crumpled up, whereas **F325** graphite is more crystalline. The observation from Raman spectra of potassium GICs was consistent with XRD results (Figure 2.5). Potassium GICs prepared from **P40 GNP** exhibited characteristic defects peaks at ~1563 cm^{-1} and 1266 cm^{-1}. Therefore, **F325** graphite flake was selected as the starting material for the preparation of potassium GICs due to its lower defects.

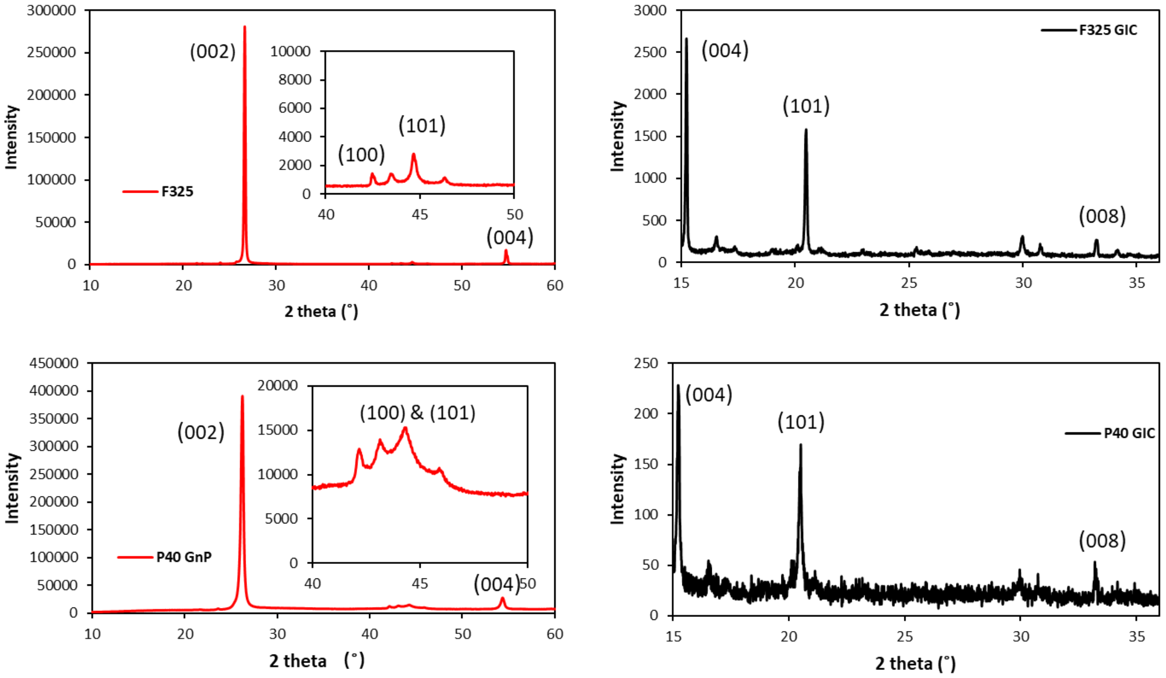

*Figure 2.4 XRD patterns of pristine **F325** graphite (a) and **P40 GNP** (c) with (101) peak shown in the inset and their corresponding Stage-1 potassium GICs (b), (d) after intercalation. Diffraction patterns of the graphite were acquired by using Cu Kα1 X-ray source (λ = 1.5406 Å); XRD patterns of Potassium GICs were acquired by using Mo-Ka1 X-ray source (λ = 0.7093 Å).*

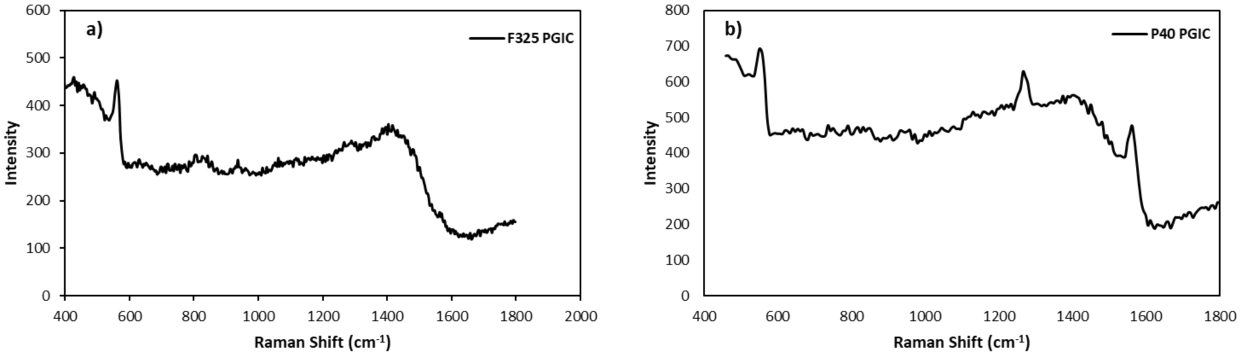

*Figure 2.5 Raman spectrum of Stage-1 (a) **F325** and (b) **P40** Potassium GICs*

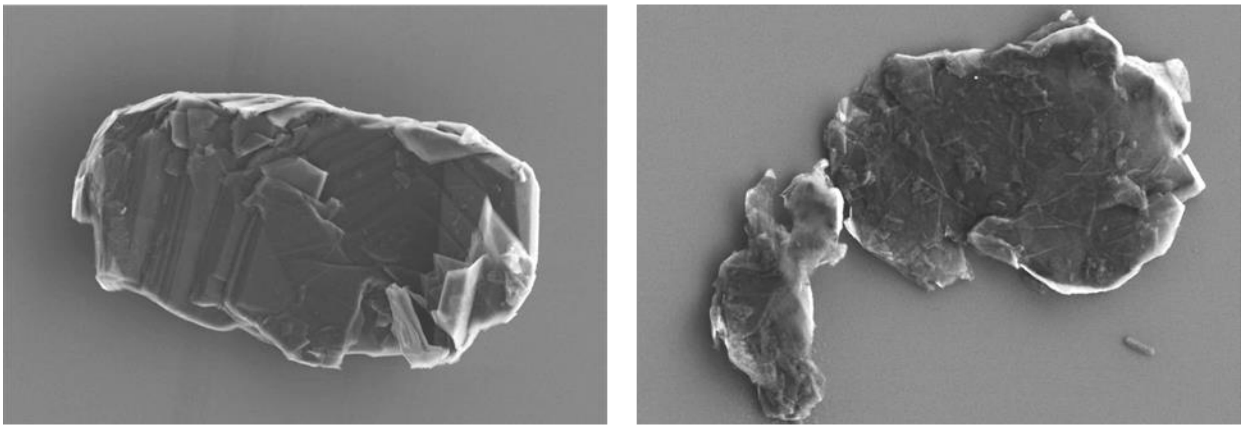

Figure 2.6 SEM images of ***F325*** *graphite (left) and* ***P40*** *GNP (right).*

2.2.1 Preparation and Characterisation of Graphenide

The potassium GICs were dispersed into THF by magnetic stirring and 20 mL dispersion was probe sonicated at 250 W for 0.5 hour. The sonicated dispersion was centrifuged to remove any big particles and the supernatant was kept for UV-Vis analysis. The potassium graphenide in THF exhibited two distinctive bands at 297 nm and 244 nm (Figure 2.7). The peak at 296 nm represents the charge transfer on the graphene n-π *, its intensity is reduced when the graphenide was slowly oxidised in the atmosphere. The peak at 244 nm represents π-π * transition of the graphenide, it became less distinctive as the oxidation progressed due to precipitation of the oxidised graphene and it will merge with UV cut-off of THF (212 nm).

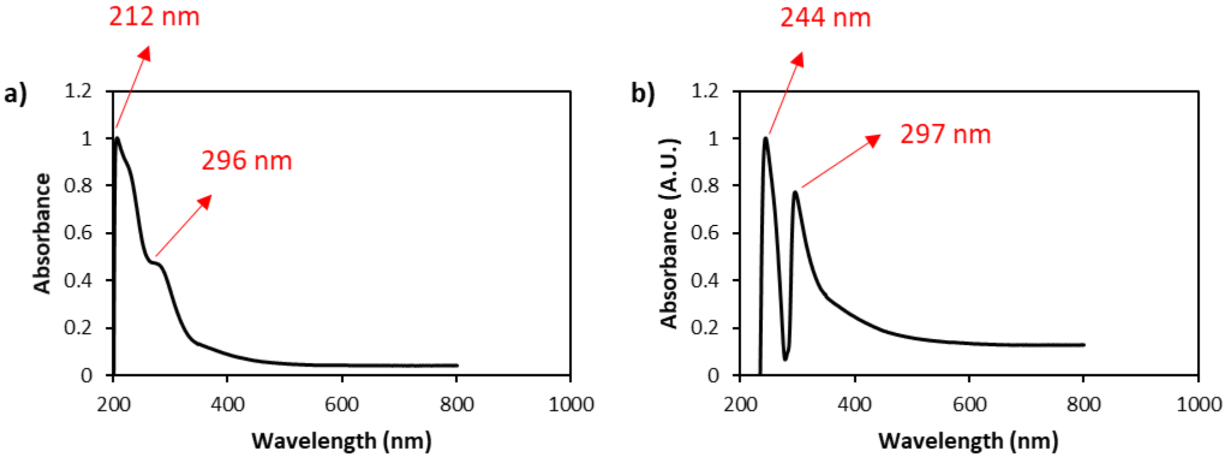

Figure 2.7 UV-vis spectrum of (a) oxidised graphenide and (b) graphenide in THF.

2.3 Preparation and Characterisation of Epoxide Functionalised Graphene

Graphenide solution can be obtained by exfoliation of potassium GICs. The thickness of the graphenide can be controlled by applying different speed of centrifuge during the separation.

The graphenide is very nucleophilic, and it was used to react with the organic halides by nucleophilic substitution on epibromohydrin so that a C-C bond with the graphene layer will be formed (Scheme 2.1). The blue colour of the graphenide solution changed to a homogenous black immediately upon the addition of epibromohydrin. The mixture was left to react overnight and the solid was collected by vacuum filtration. The crude black solids were washed to remove any salts and by-products. The **EP-G** was dried at 100 ℃ *in vacuo* thereafter and ready for the characterisations.

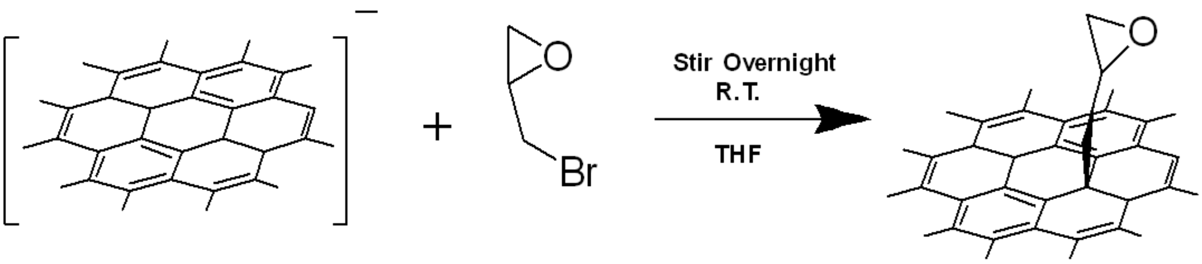

Scheme 2.1 Reaction between graphenide and epibromohydrin.

The **EP-G** was characterised by TGA-MS and XPS (Figure 2.8). The fragments with m/z=57, which is the mass of methylepoxide group, cleaved from the graphene during the heating, are detected. This evidence indicates the successful addition of epoxy groups to graphene. The **EP-G** exhibits 21.3% weight loss within the range 100-600 ℃. If all the weight loss was contributed by epoxy group, then a degree of functionalisation 5.6% can be obtained (equivalent to 17.7 carbon atoms for 1 epoxy group and 4.5% oxygen content). The corresponding oxygen content is c.a. 4.4 at% which is measured by XPS, which is consistent with the TGA result. The sample demonstrated three element peaks in XPS survey scan (Figure 2.9), which are oxygen, carbon, and fluorine. The emergence of fluorine peak is because of using PTFE membrane during separation. High resolution carbon 1s was also acquired. The deconvolution (details in Section 6.1.1) of C 1s core-level spectrum results in three major components: sp^2 carbons at 284.5 eV, C-O-C at 285.9 eV, and π-π^* at 290 eV. The presence of π-π^* shake up satellite indicates the maintenance of graphene sp^2 structure after the functionalisation.

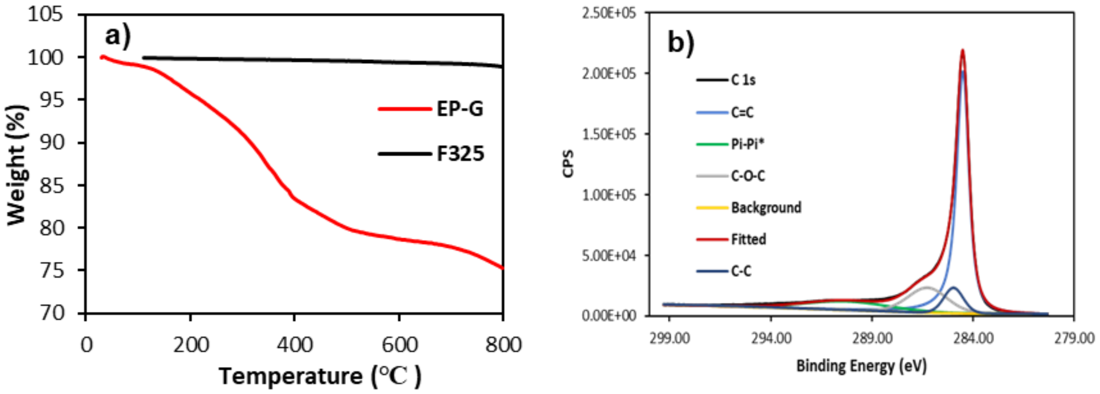

Figure 2.8 TGA (a) of ***EP-G*** *and* ***F325****, and deconvolution of XPS C1s (b) for* ***EP-G****.*

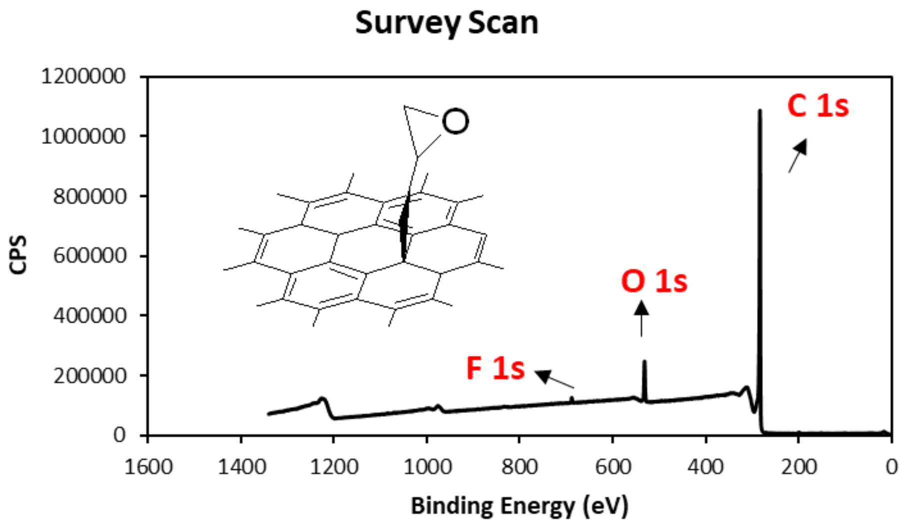

Figure 2.9 XPS survey scan of ***EP-G****.*

SRS was employed to determine the extent of the functionalisation by comparing to the starting pristine graphite flakes (Figure 2.10). Before functionalisation, the pristine graphite exhibits narrow distribution of I_D/I_G ratio at low I_D/I_G ratio region (0-0.2). This indicates the starting material is a homogenous graphite with few defects in the basal plane. The 2D band is positioned at 2723 cm^{-1} and has asymmetrical shape. Both characters belong to Bernal AB stacked crystalline graphite. As expected, a significant shift of the histogram of I_D/I_G ratio from low value to high value I_D/I_G region was achieved after the functionalisation as the average of I_D/I_G ratio increased from 0.11 to 0.65. The increase of I_D/I_G ratio generally represents formation of sp^3 defects, which confirms the addition of functionality to graphene. By comparing the I_D/I_G distribution of the **EP-G** with that of the starting material, the conversion of the functionalisation is 100% as no starting material is left after the reaction. Besides, the reaction gives a rather homogenous mixture.

2D band changes too after the exfoliation from the potassium GICs. The stacking order of the graphite has been lost as the 2D band shows a symmetric shape instead of an antisymmetric shape after the reaction. A noticeable blue shift of *Pos* (2D) from 2723 to 2690 cm^{-1} and increase of I_{2D}/I_G ratio from 0.32 to 0.56 indicates the exfoliation has produced few-layer graphene from graphite (Figure 2.11). AFM offers direct evidence to the morphology and thickness of graphene after the exfoliation and functionalisation. Statistical AFM (at least 100 flakes) was constructed to analyse the thickness and the lateral size of the **EP-G** (Figure 2.12). As can be seen from the lateral distribution, most of the flakes are 0.1-0.3 μm, and those flakes have round-edge (Figure 8.6). The thickness of **EP-G** is more widely distributed since the thickness can be ranged from 1 nm to more than 10 nm. The average thickness is 8 nm and 75% of the sample are flakes are less than 8.7 nm thick. The distribution analysis indicates **EP-G** has wide distribution of flake thickness and relative uniform lateral size (Table 2.1 & Table 2.2). The results of statistical AFM show good consistency with the results obtained from SRS.

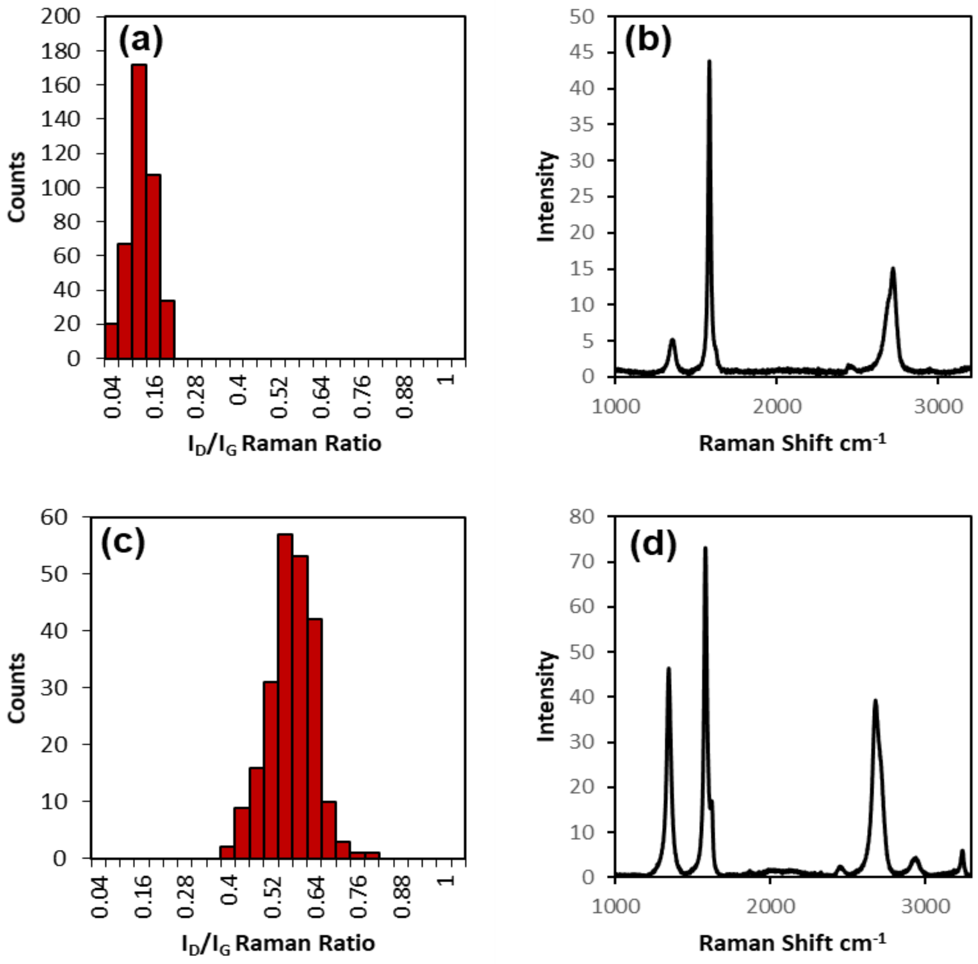

*Figure 2.10 I_D/I_G histograms of **F325** graphite (a) and **EP-G** (c); Raman spectrum of **F325 graphite** (b) and **EP-G** (d).*

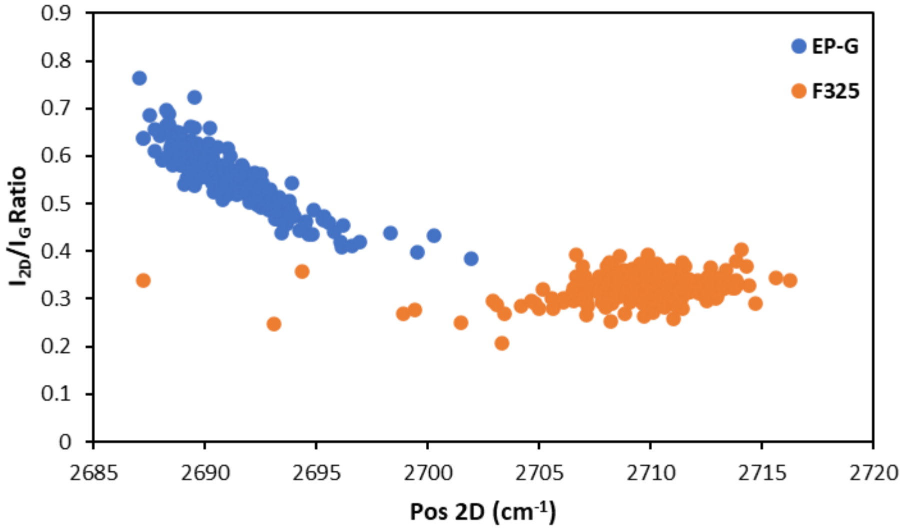

*Figure 2.11 I_{2D}/I_G and 2D position plot of **EP-G** and **F325** graphite.*

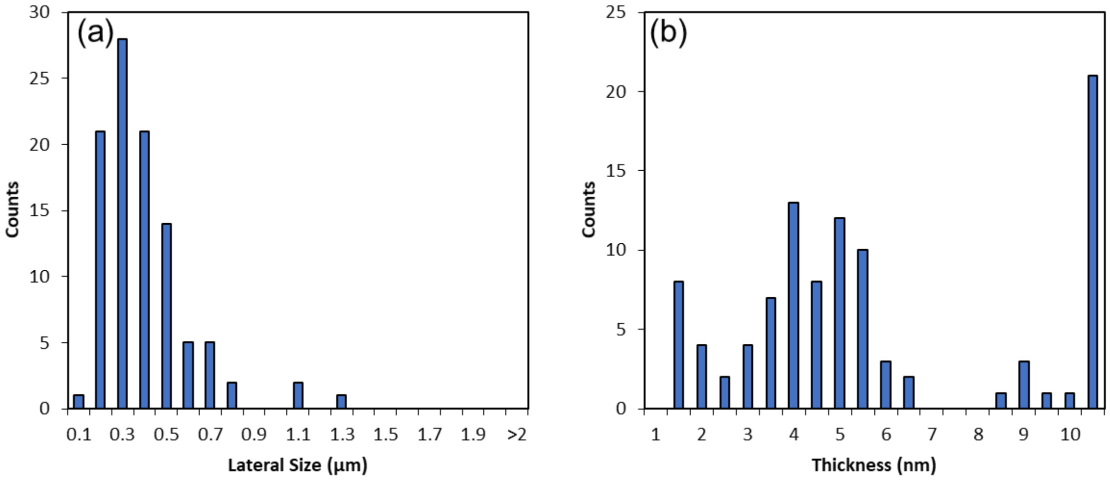

*Figure 2.12 Lateral size (a) and thickness (b) histograms of **EP-G** obtained from AFM.*

The dispersibility of **EP-G** was tested in several solvents after the confirmation of the functionalisation. A movie over a period of 24 hours (Figure 8.37-Figure 8.39) was recorded to compare the resulted dispersion with that of the pristine graphite. The results show that **EP-G** can form stable dispersion (1 mg mL^{-1}) in IPA, acetone, methanol, ethanol, THF, and chloroform. To allow direct comparison of concentration between different dispersions, the extinction coefficient of **EP-G** in methanol (Figure 2.13), ethanol, and IPA were calibrated and calculated by Beer Lambert Law (see details in section 6.1.4) and using the absorbance at 660 nm. The **EP-G** exhibits different extinction coefficient (Ɛ) in different solvents. In methanol Ɛ=1543 $L{\cdot}g^{-1}m^{-1}$, in ethanol Ɛ=951.9 $L{\cdot}g^{-1}m^{-1}$, in acetone Ɛ=101.9 $L{\cdot}g^{-1}m^{-1}$ and in IPA Ɛ=1367 $L{\cdot}g^{-1}m^{-1}$. In contrast, pristine graphene was reported to have unique extinction coefficient in various solvents. In addition, the peak positions of **EP-G** in different solvents are different too.

In methanol, the peak is located at 272 nm; the position of the peak red-shifts to 291 nm when the solvent was changed to ethanol; the band peak with similar peak position 291 nm was observed when the **EP-G** was in IPA; though a peak was observed for acetone at 330 nm, however, the peak position is difficult to be identified as acetone also absorbs at 330 nm (Figure 2.13). Overall, the shift of peak position implies the epoxy group on the **EP-G** influences the interaction between the **EP-G** and the solvents.

The stability of the **EP-G**/acetone dispersion was monitored by UV-Vis spectrometer (Figure 2.14), the concentration of the dispersion was halved (starting concentration was 0.4 mg mL^{-1}) after 6-days sediment. And the trend indicates the concentration of the dispersion had become stable after 72 hours, which suggests the **EP-G** can form 0.2 mg mL^{-1} stable dispersion in acetone. The dispersibility of the **EP-G** has been significantly improved comparing to that of the GNP and graphite since GNP or graphite/acetone dispersion will precipitate out completely in one hour.

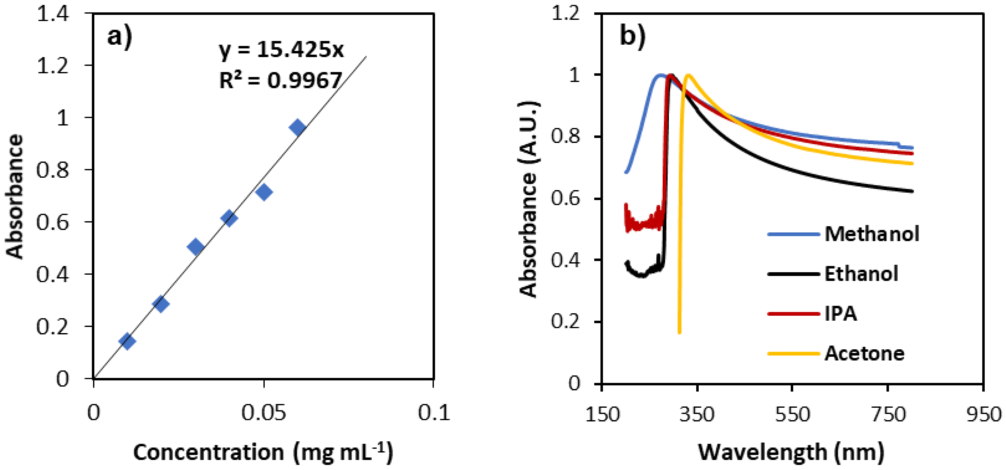

*Figure 2.13 (a) UV-Vis calibration plot of **EP-G** in methanol; (b) UV-Vis spectrum of **EP-G** in different low-boiling point solvents.*

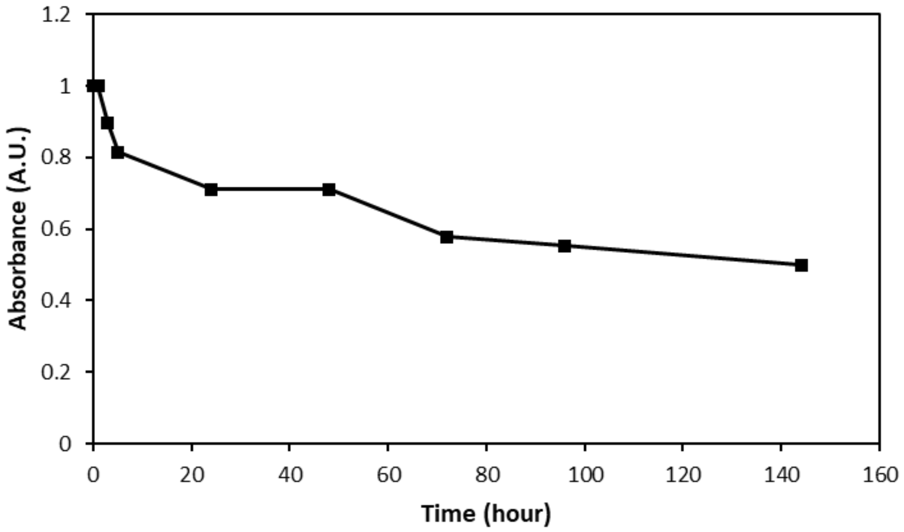

*Figure 2.14 Stability monitoring of the **EP-G**/Acetone dispersion*

*Table 2.1 Flake Thickness distribution analysis of **EP-G**, **Aniline-G**, and **4-Nitrobenzyl-G***

Sample	10th Percentile nm	50th Percentile nm	90th Percentile nm	<Average Thickness> nm
EP-G	1.9	4.7	14.3	8.0
Aniline-G	3	4	5.2	6.5
4-Nitrobenzyl-G	2.4	4.3	8.7	5.2

*Table 2.2 Flake size distribution analysis of **EP-G**, **Aniline-G**, and **4-Nitrobenzyl-G***

Sample	10th Percentile μm	50th Percentile μm	90th Percentile μm	<Average Lateral Size> μm
EP-G	0.17	0.31	0.58	0.35
Aniline-G	0.24	0.43	1.29	0.63
4-Nitrobenzyl-G	0.13	0.15	0.2	0.16

2.4 Preparation and Characterisation of Aniline Functionalised Graphene

The aniline functionalised graphene can be obtained by mixing the graphenide solution with 4-iodoaniline overnight at room temperature (Scheme 2.2).

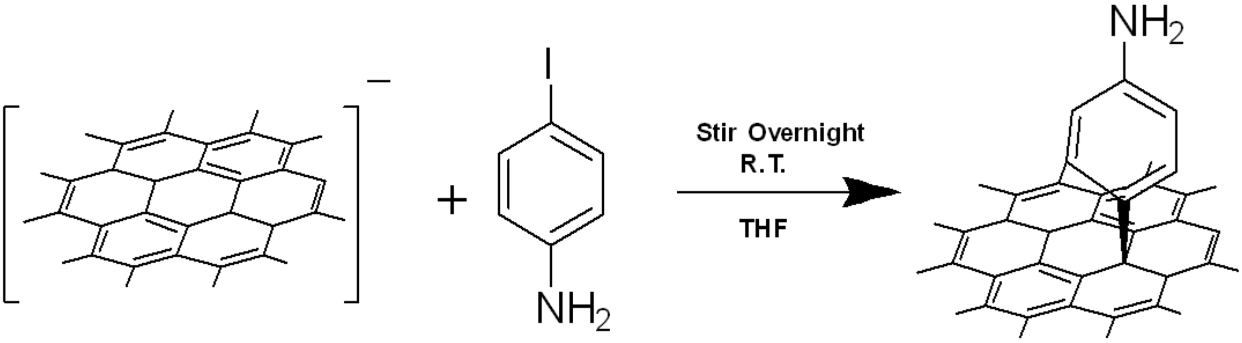

Scheme 2.2 Reaction between graphenide and 4-iodo-aniline.

The SRS (Figure 2.15) shows that the average of I_D/I_G ratio of the **Aniline-G** has been improved and the entire distribution has been shifted to higher values generally after the functionalisation, which are the signs of successful functionalisation. 21% weight loss was realised for the **Aniline-G** within 100-600 ℃, this corresponds to a degree of functionalisation 3.4% (equivalent to one aniline group for every 28.8 carbon atoms), if aniline group contributed to all the weight loss (Figure 2.18).

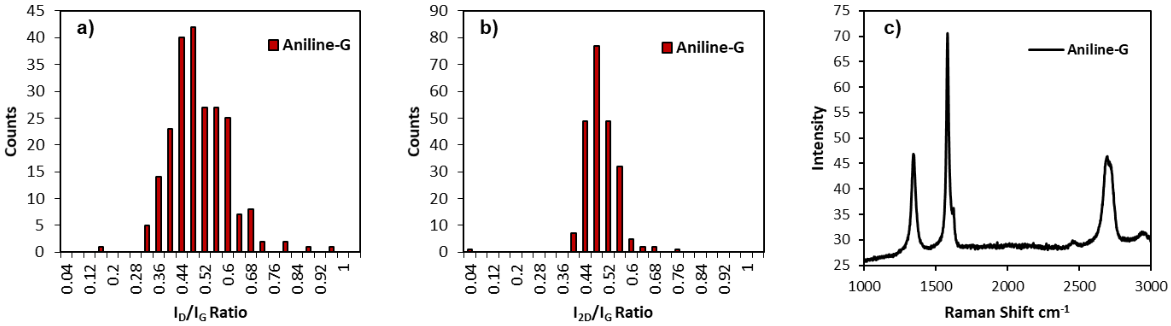

Figure 2.15 I_D/I_G ratios histograms (a), I_{2D}/I_G ratios histograms (b), and average Raman spectrum (c) of ***Aniline-G***

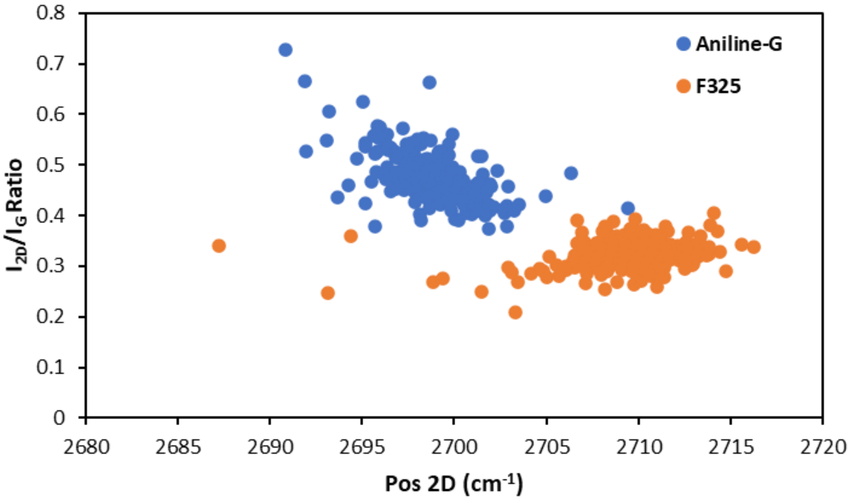

Figure 2.16 I_{2D}/I_G *and 2D position plot of* ***Aniline-G*** *and* ***F325*** *graphite.*

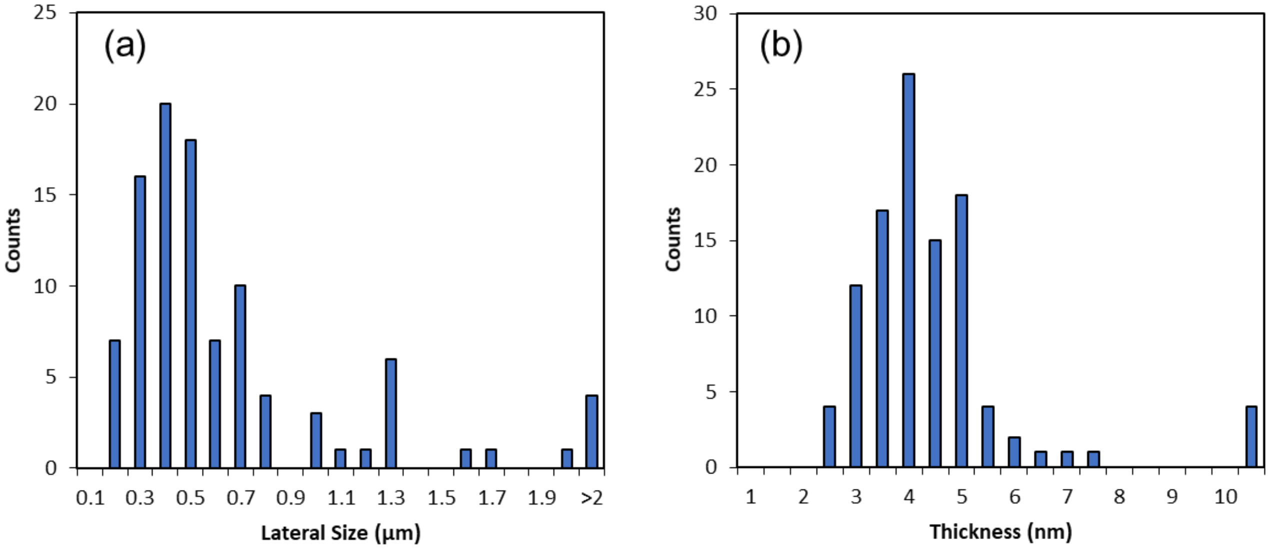

Figure 2.17 Statistical AFM lateral size (a) and thickness (b) histograms of ***Aniline-G***

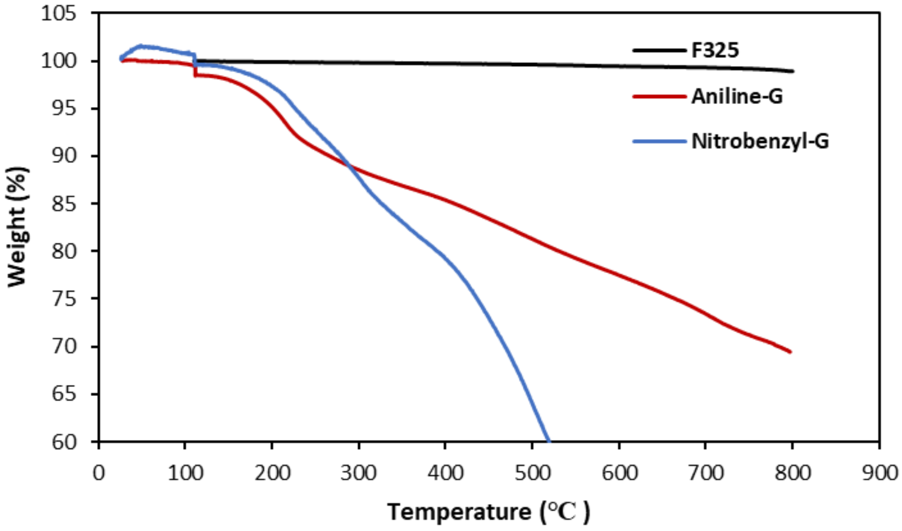

*Figure 2.18 TGA profile of **F325**, **Aniline-G** and **4-Nitrobenzyl-G***

According to the statistical AFM (Figure 2.17), the lateral size of most of **Aniline-G** is ranged from 0.1 to 1.9 μm, and 82% of the sample has lateral size less than 0.9 μm (Table 2.1 & Table 2.2). In comparison, the distribution of thickness of the **Aniline-G** is narrower, since 90% of the analysed samples are less than 5.2 nm thick and difference between the 10th percentile and 90th percentile is only 2.2 nm. The results of statistical AFM are consistent with the result of I_{2D}/I_G and 2D position plot of **Aniline-G** and **F325** graphite, as the 2D positions indicates most of **Aniline-G** are few-layer graphene (Figure 2.16).

2.5 Preparation and Characterisation of 4-Nitrobenzyl Graphene

The 4-nitrobenzyl tosylates was synthesised according to a known method. 0.03 mmol of 4-nitrobenzyl tosylates were added to the centrifuged graphenide (Scheme 2.3). The mixture was left to stir overnight at room temperature in the glovebox.

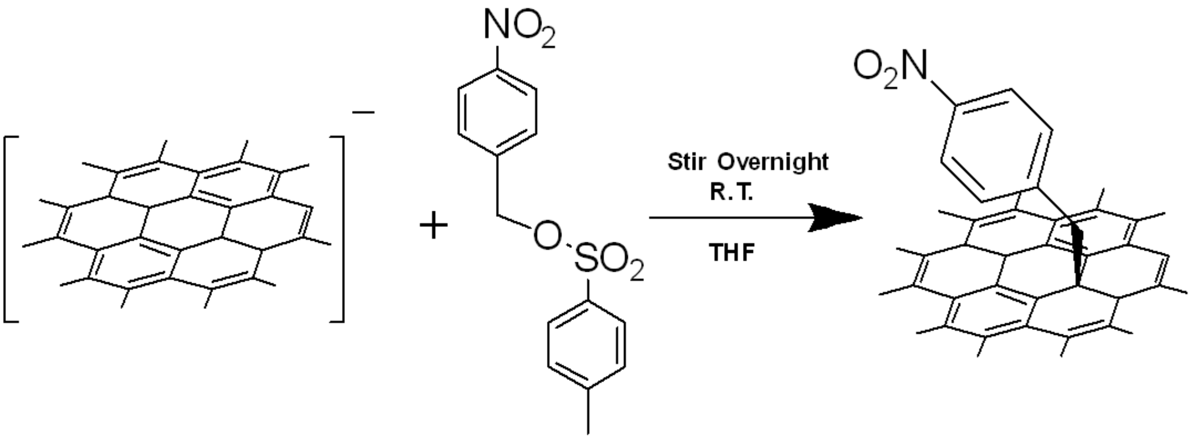

Scheme 2.3 Reaction between graphenide and 4-nitrobenzyl tosylates.

The SRS results (Figure 2.19) show that the average of I_D/I_G ratio had been increased after the reaction. The characteristic C-N symmetric stretch at ~ 1128 cm^{-1} and N-O antisymmetric stretch at ~1398 cm^{-1} and 1440 cm^{-1} can be identified from the Raman spectrum of the **4-Nitrobenzyl-G**. [50] The distribution of I_D/I_G ratio suggests the reaction proceeded less uniformly than the reactions with the other two organic halides, as graphene without functionalisation (with low I_D/I_G ratio) can be spotted in the histogram. This could be originated from the bulkiness of the tosylate species, which hinders it from reaching the basal plane of the graphenide. While the possibility of edge functionalisation cannot be ruled out, as more weight loss than expected were observed from the TGA. The TGA (Figure 2.18) of **4-Nitrobenzyl-G** demonstrated dramatic weight loss (54.5%) within 250-600 ℃. The weight loss is equivalent to 9.5% degree of functionalisation (equivalent to 1 nitrobenzyl group for every 9.5 carbon atoms), if all the weight loss was due to decomposition of 4-nitrobenzyl groups.

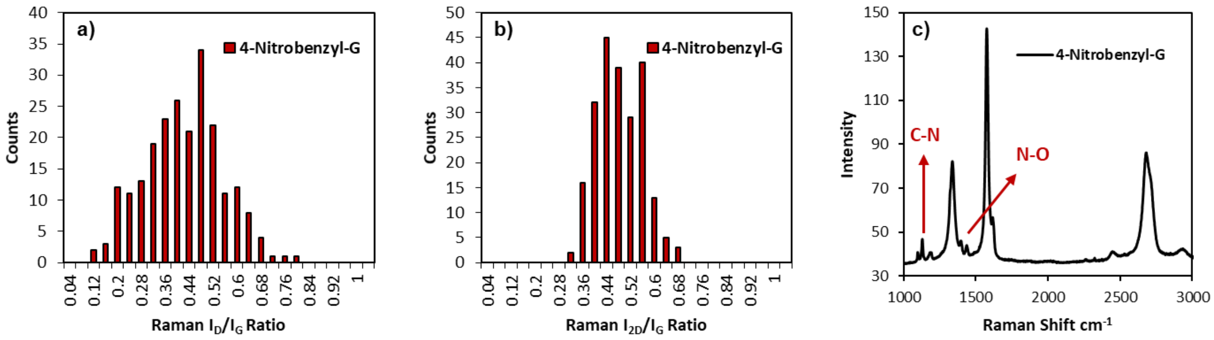

*Figure 2.19 I_D/I_G ratios histograms (a), I_{2D}/I_G ratios histograms (b), and average Raman spectrum (c) of **4-Nitrobenzyl-G***

Results of statistical AFM (Figure 2.21) show that 90% of the **4-Nitrobenzyl-G** have lateral size of c.a. 0.2 μm and 75% of the sample are 6.5 nm thick, though no monolayer graphene had been found (Table 2.1 & Table 2.2). Since I_{2D}/I_G and 2D position plot of **4-Nitrobenzyl-G** (Figure 2.20) shows that 2D positions of the functionalised graphene shifted to lower wavenumber and higher average I_{2D}/I_G ratio comparing to those of graphite, the successful synthesis of few-layer functionalised graphene from the exfoliation of potassium GICs is confirmed.

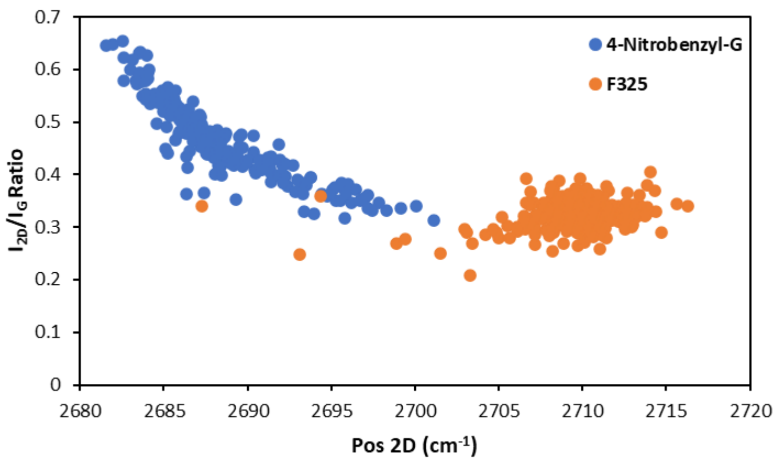

*Figure 2.20 I_{2D}/I_G and 2D position plot of **4-Nitrobenzyl-G** and **F325** graphite.*

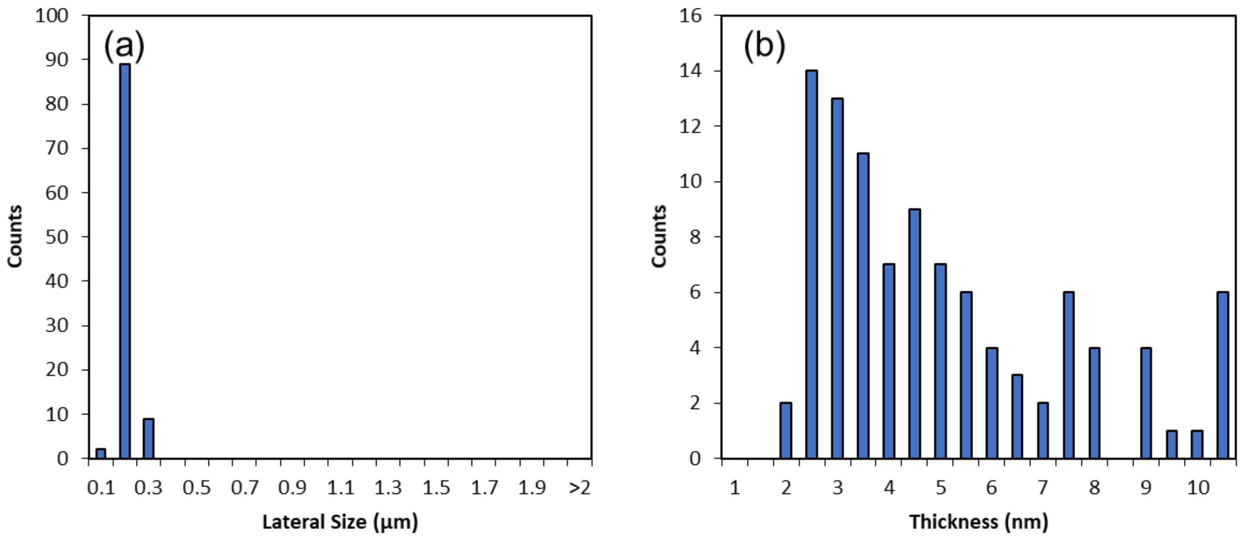

Figure 2.21 Statistical AFM lateral size (a) and thickness (b) histograms of 4-Nitrobenzyl -G

2.6 Conclusion

In this chapter, graphene exfoliation and functionalisation have been achieved by using potassium GICs. Addition of epoxide, 4-nitrobenzyl, and 4-aminophenyl functional groups from corresponding electrophiles to the potassium activated graphene has been successfully performed. The SRS study shows that the reaction between the charged nucleophilic graphenide and electrophiles is very efficient in terms of functionalisation level and homogeneity. The use of tosylate as electrophile in graphenide functionalisation was first investigated in this study, the SRS results show that the reaction proceeds less homogenously as compared to the other two reactions using organic halides, as areas without functionalisation and with low functionalisation could be found. By considering the unusual high weight loss in TGA and relative low I_D/I_G ratio from SRS, it is worthy to investigate the reaction with ostensible edges to see if the bulkiness of the tosylate groups will determine the sites (edge or basal plane) for functionalisation. Nevertheless, the study provides additional series of electrophiles to the arsenal of the graphenide functionalisation by using tosylate chemistry.

The epoxy functionalised materials (**EP-G**,) have been characterised by SRS, TGA-MS, XPS, and AFM. The functionalisation grants graphene good dispersibility in a range of solvents with good concentration and good stability, which includes volatile solvents such as methanol, ethanol, IPA, and DCM. For 1 mg mL^{-1} dispersion, stability over 25 hours can be achieved. In acetone, dispersion with initial concentration of 0.4 mg mL^{-1} gradually sedimented and final concentration of 0.2 mg mL^{-1} was achieved after 6 days, which is much higher than the reported 1.2 mg mL^{-1} dispersibility of graphene in acetone. [24] The exceptional dispersibility can reduce the difficulty when formulating the graphene-based composites. More importantly, the good dispersibility and compatibility of **EP-G** means it could be a promising filler material for composite fabrication. However, the yield of the procedure would be a huge obstacle in front of any further investigation regarding to properties or application of the functionalised materials. Although the conversion of reaction is 100% from the result of SRS, however, the yield for every batch is limited, only 20 mg functionalised material can be obtained from every 50 mL graphenide solution as calculated. The solubility of potassium graphenide in THF is the yield determining factor. Relevant research indicates solubility of graphenide can be increased (0.7 mg mL^{-1}) by using NMP [149] as solvent and can be further enhanced by adding crown ether. [119] However, the NMP is difficult to be removed and the residual NMP will deteriorate the properties of graphene. [21] Exploring methodologies to enhance the solubility of graphenide in volatile solvent would be crucial to improve the efficiency of the process. Requiring harsh handling conditions is the other problem for the functionalisation using potassium graphenide, as presence of any moisture would lead to the deactivation of the graphenide and its precursor. Huge difficulty and cost would be associated to make it a feasible industrial process.

Chapter 3. Functionalisation of Graphite or GNP via Sulphate Graphite Intercalation Compounds and Arylboronic Acid Derived Free Radicals

3.1 Introduction

Despite covalent functionalisation of graphene being achieved with various methodologies such as free radical addition,[45,47,57,74,77] Diels-alder Chemistry,[60,150,151] 1,3 dipolar cycloaddition,[43,82,85–87,152] or plasma treatment [41,59,153] the reductive functionalisation from potassium GICs is potentially the most efficient to produce graphene with controlled degree of functionalisation and functionality [114]. The reductive functionalisation has been used in silyllation,[116] alkylation,[42,112,114] and arylation [47,114] functionalisation reactions. However, rigid moisture and air free environment are required for the generation of the reactive graphenide and consequent reaction, which limits the scalability of the method. Recently sulphate GICs have attracted attention from researchers with a positive charge induced upon the sulphate intercalation.[131,132,154] Importantly, it exhibits higher stability compared to that of potassium GICs towards moisture and oxygen. As S. Eigler demonstrated, high quality functionalised and aqueous-dispersible monolayer graphene and few-layer graphene can be produced simply by treating the sulphate GICs with water.[131,132] Since no strong oxidants are included during the formation of the sulphate GICs and consequent functionalisation, over-oxidation, which usually happened in Hummers method, does not happen in this reaction. However, unlike potassium GICs which have various electrophiles for functionalisation, the sulphate GICs has very limited numbers of nucleophiles to react with. Indeed, the functionalisation with water is the only reported example so far. As a consequence, study of exploring more nucleophiles for functionalisation of sulphate GICs is highly desirable.

In this chapter, I will present an *in situ* and one-pot arylation of GNP from sulphate GICs by using arylboronic acid derived free radicals (Figure 3.1). Similar to its analogue aryl diazonium salts, arylboronic acids are a common aryl radical precursor, which is developed in organic chemistry for production of biaryl organic compounds. [155–157] The generation of aryl radical is mediated by manganese (III) acetate $Mn(OAc)_3$, which is an important one-electron oxidising agent in organic synthesis.[158] Comparing to the hazards of using unstable and potentially explosive diazonium salts to generate aryl radicals, arylboronic acid is considered much safer. Arylboronic acids with different substituents were used for the functionalisation. The generation of the radical was checked by TEMPO radical quenching reaction. The resulted graphene material from the reaction is fully characterised by SRS to understand the extent of the functionalisation and exfoliation of this reaction. Dimensions and functionalities of the functionalised graphene were characterised by UV-Vis, SRS, TGA, XPS, and AFM.

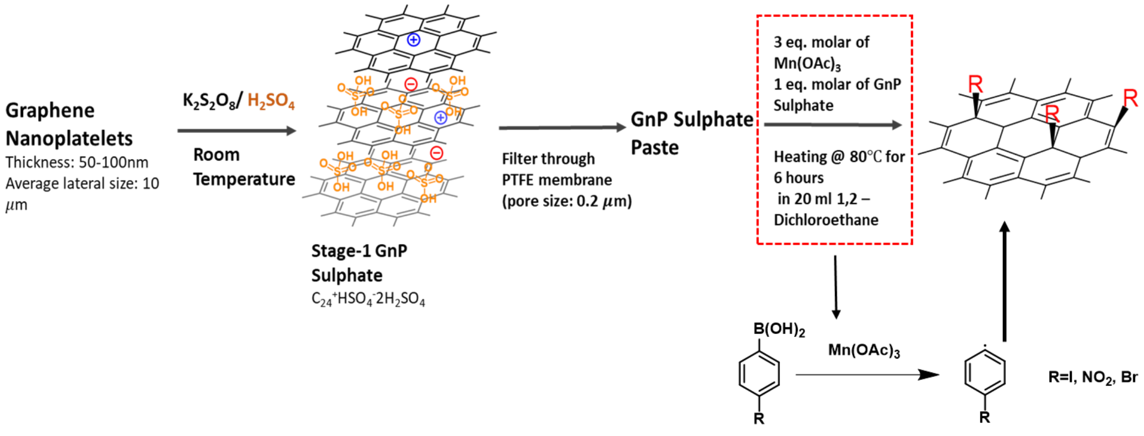

Figure 3.1 Reaction Scheme of $Mn(OAc)_3 \cdot 2H_2O$ mediated radical functionalisation of sulphate GICs

3.2 Results and Discussion

3.2.1 Synthesis and Characterisation of Sulphate GICs

The sulphate GICs was prepared by exposing graphite to a mixture of oxidants persulphate and sulphuric acid. Unlike the traditionally employed electrochemical method for sulphate GICs production, which requires continually current supply, this method can produce sulphate GICs spontaneously in few hours. In addition, differentiating from methods involving use of strong oxidant (concentrated nitric acid or potassium permanganate), this approach does not oxidise the graphite irreversibly.

Two different graphite, **P40 GNP** and Mesh 80 Graphite (**M80**) have been used for the synthesis. **P40 GNP** is graphene nanoplatelet with 50-100 nm thickness and average lateral size 10 µm, and **M80** is graphite with average lateral size 117 µm. The intention of using two different graphite is to see if making stage 1 SGIC with graphite having different flake size and thickness is possible. The production of stage-1 sulphate GICs is confirmed by the colour change of both graphite, which is from black to deep blue (Figure 3.2). The blue colour is an indication for charge transfer from graphene layers to sulphate anions. The Raman spectrum of stage-1 sulphate GICs derived from both graphite were characterised by disappearance of 2D band and D band. the G band of **P40** SGIC is selectively intensified, and blue shifted from 1578 cm^{-1} to 1633 cm^{-1}, which corroborates the charge transfer in this compound. Blue shift of G band for **M80** SGIC is observed which as well is from 1578 to 1638 cm^{-1}. However, no enhancement of the G band intensity has been observed for **M80** SGIC. The origin of G band enhancement and 2D band suppression can be explained by the suppression- enhancement mechanism which was proposed by Chen et al.[159] According to the theory and experimental observation[154], the higher the doping level, the more deconstructive interference is eliminated, which will lead to stronger G band intensity. Therefore, Raman spectroscopy study suggests first stage SGIC can be produced from both graphite starting materials.

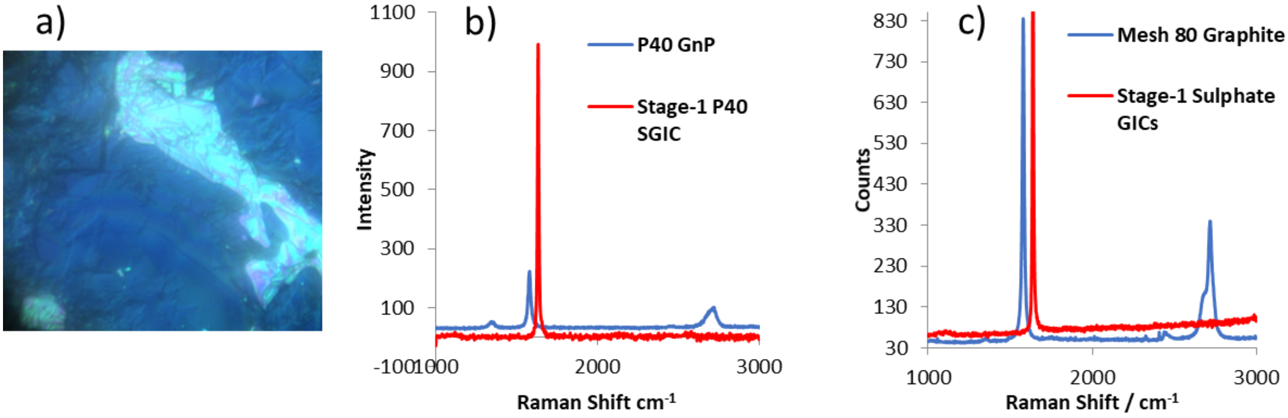

Figure 3.2 (a) optical image of stage-1 sulphate GICs; Raman spectra of pristine GNP and stage-1 GNP sulphate GICs (b) and Mesh 80 graphite and stage-1 ***M80*** *GICs.*

3.2.2 Functionalisation of Graphite with 4-Iodo-Phenylboronic Acid Derived Free Radical

To analyse the reaction more comprehensively, a Raman spectra map containing 225 points was acquired for the crude product of each reaction. A histogram was constructed based on the I_D/I_G and I_{2D}/I_G ratios. In order to analyse each reaction more quantitatively, the standard deviation, mean, and percentile for each set of data were calculated, and those values were employed to estimate the homogeneity, functionalised degree, and conversion rate for each reaction. Therefore, more light can be shed to understand if the radical addition takes place or not.

For the reaction with **P40 GNP**, the average of I_D/I_G ratio increased from 0.10 to 0.24 (Table 3.1), the product after the reaction was found to be significantly different from the starting material since after the reaction. However, the standard deviation also increased from 0.03 for the pristine **P40 GNP** to 0.33, this means the sample has become more heterogeneous after the reaction due to the coexistence of unreacted and reacted GNP. The same conclusion can be drawn by looking at the distribution directly, as 96% of the sample is in the I_D/I_G ratio range 0-0.2 for the pristine **P40 GNP**, only 63% of the sample (Table 3.1) is in the same range after the reaction. This indicates that more than half of the GNP stayed intact after the reaction, and a small amount of sample underwent the reaction (Figure 3.3).

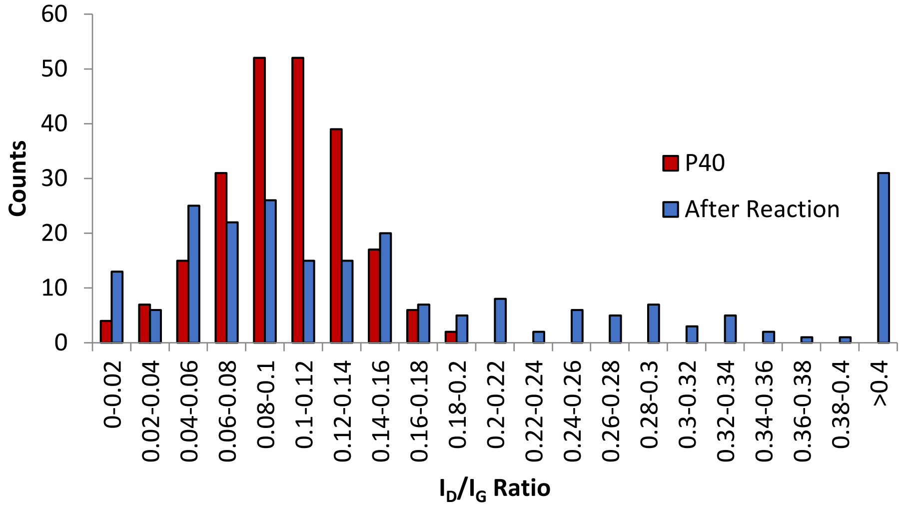

*Figure 3.3 I_D/I_G histogram of pristine **P40** GNP (red) and crude product (blue) which has reacted with 4-iodophenyl radical.*

The same reaction condition was applied to **F325** graphite (Figure 3.4 ID/IG histogram of pristine **F325** graphite (red) and crude product (blue) which has reacted with the 4-iodophenyl radical.), the average of I_D/I_G ratio increased from 0.11 to 0.16 after the reaction (Table 3.1), which means the sample was functionalised after the reaction. This is corroborated by the shift of the whole distribution to higher I_D/I_G ratio after the reaction. In addition, the standard deviation of I_D/I_G ratio stayed almost the same (0.04 before the reaction vs. 0.05 after the reaction); this means the reaction is uniform. By calculating the percentage of $I_D/I_G > 0.2$, the conversion rate of the radical reaction can be estimated, it can be found that a small amount of sample (ca. 10%) was converted to functionalised graphite (Table 3.1).

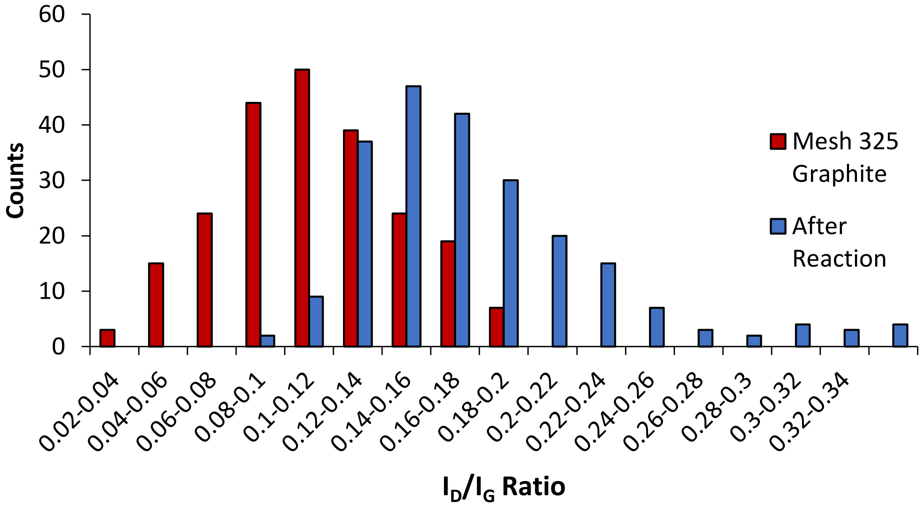

*Figure 3.4 I_D/I_G histogram of pristine **F325** graphite (red) and crude product (blue) which has reacted with the 4-iodophenyl radical.*

The outcome of the radical reaction with **M80** graphite (Figure 3.5) was different from the previous graphite. The change of the I_D/I_G distribution of **M80** graphite was ignorable and the average of I_D/I_G ratio stayed the same after the reaction. According to the SRS analysis only 1% of the sample I_D/I_G ratios were found to be >0.2, which is similar to the value of pristine **M80** graphite 2%. (Table 3.1).

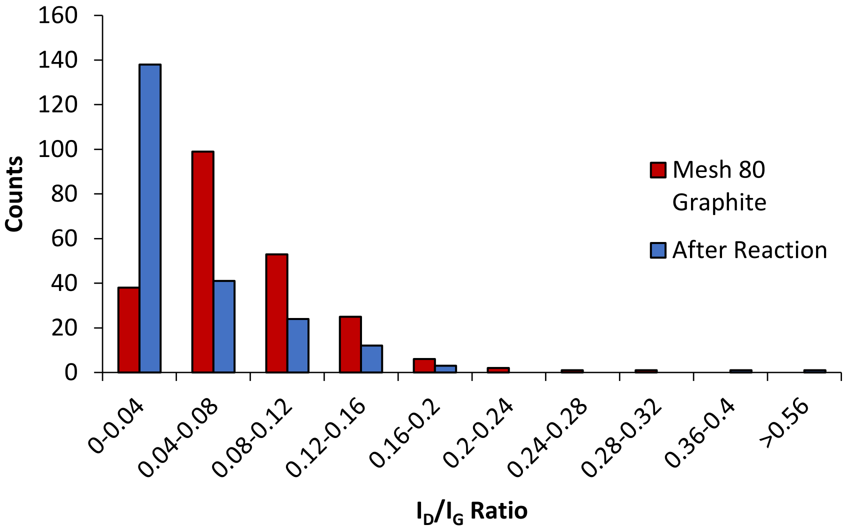

*Figure 3.5 I_D/I_G histogram of pristine **M80** graphite (red) and crude product (blue) which has reacted with 4-iodophenyl radical.*

Table 3.1 The mean and standard deviation of I_D/I_G and I_{2D}/I_G of the product and pristine graphite

	Average		Standard Deviation		Percentage of I_D/I_G >0.2
	I_D/I_G	I_{2D}/I_G	I_D/I_G	I_{2D}/I_G	
M80 Graphite	0.08	0.32	0.05	0.02	2%
P40 GNP	0.10	0.30	0.03	0.03	4%
F325 Graphite	0.11	-	0.04	-	0%
Reaction with P40	0.23	-	0.33	-	37%
Reaction with F325	0.16	-	0.05	-	10%
Reaction with M80	0.04	0.33	0.07	0.07	1%

3.2.2.1 Summary

The feasibility of the radical reaction with graphite can be judged by looking at the distribution of I_D/I_G ratio and comparing the means. Based on those results, free radical reacted differently with different kinds of graphite. In terms of reactivity, the order is **M80** graphite< **F325** graphite < **P40 GNP** and no reaction had been realised for **M80** graphite. This trend of reactivity follows inverse relationship with the size of those starting material, as the smallest **P40** GNP exhibited the highest reactivity and the biggest **M80** graphite had the lowest reactivity. As the structure study in the Chapter 2, the **P40 GNP** has less crystalline structure, the smaller flake sizes which is result of processing during its manufacture, has more defective sites than those of **M80** and **F325**. Those defective sites are more susceptible to radical attack. For **P40 GNP** and **F325** graphite, even though some of the starting material had been functionalised, most of the starting materials stayed intact after the reaction. This means the free radical alone can react with the graphite yet with a limited extent. For further degree of functionalisation, activation of graphite would be required.

3.2.3 Functionalisation of Sulphate GICs with Phenylboronic Acids Derived Free Radical

3.2.3.1 Control Experiments

Before the radical reaction with the sulphate GICs, three control reactions were performed with SGIC to understand the mechanism of the reaction. The first reaction was conducted without using any radical mediator $Mn(OAc)_3{\cdot}2H_2O$. The assumption was that there should be little or no functionalisation without the mediator, as no free radicals would be generated with (4-iodophenyl boronic acid) 4-IPB. By comparing the average (0.08) of I_D/I_G ratios (Figure 3.6) and the percentage (2%) of $I_D/I_G>0.2$ of the pristine **M80** graphite, it can be seen that the average (0.12) of I_D/I_G ratios and the percentage (16%) of $I_D/I_G>0.2$ suggests that little functionalisation occurred. The very small change in the I_D/I_G ratio may originate from the reaction of boronic acid and the positive charge on the sulphate GICs or oxidation of graphite after heating with the moisture in the starting material. In terms of exfoliation (Figure 3.6), it can be seen that some degree of exfoliation occurred during the reaction as the percentage of $I_{2D}/I_G>0.38$ ratio increased from 0% for the pristine graphite to 28% after the reaction (Table 3.2). This is more apparent when the position of the 2D peak is plotted against the I_{2D}/I_G ratio, as the position of 2D is clearly blue shifted from 2711.5 cm^{-1} to 2706.3 cm^{-1} after the reaction, which is indicative of exfoliation. This may suggest that the presence of 4-IPB may aid the exfoliation of the graphite.

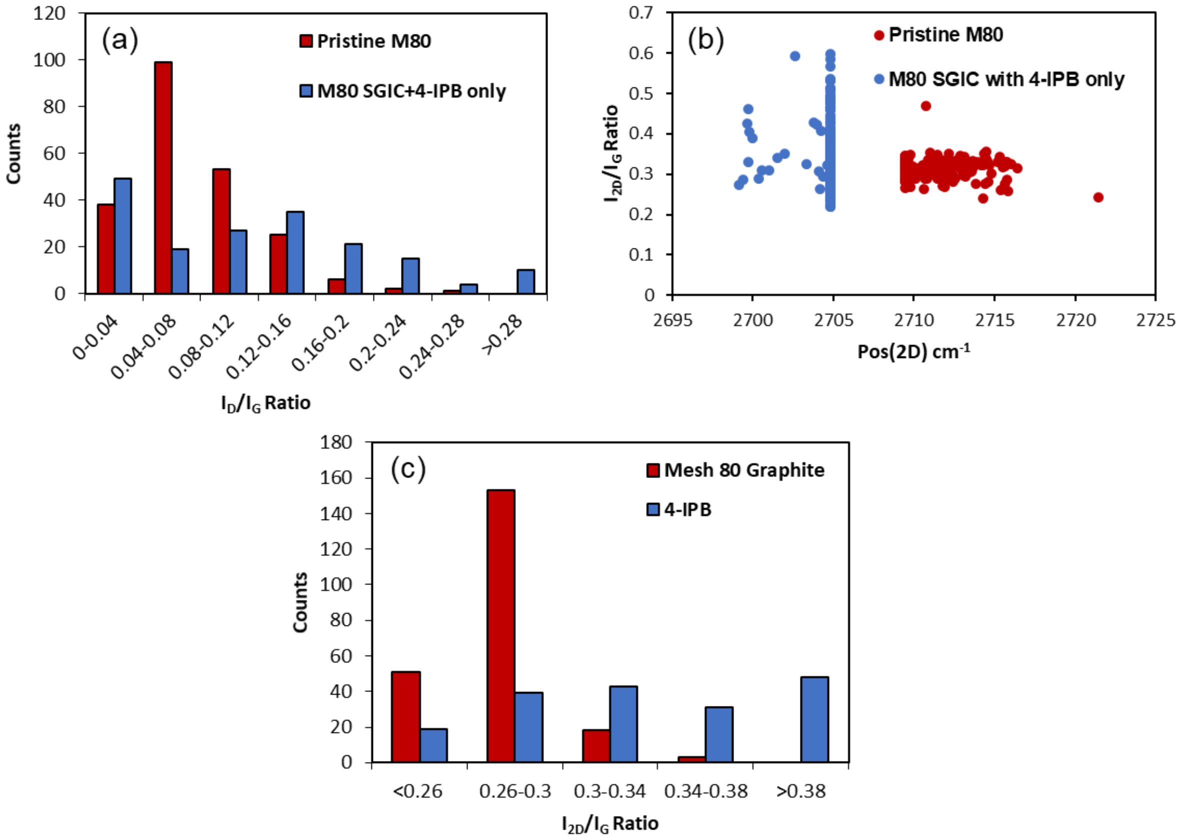

*Figure 3.6 I_D/I_G histograms (a), I_{2D}/I_G (c) and 2D position plot (b) of **M80** graphite and product derived from **M80** SGICs and 4-IPB.*

The second reaction was conducted with the catalyst $Mn(OAc)_3{\cdot}2H_2O$ only. Similar to the last reaction, no changes on I_{2D}/I_G and I_D/I_G ratio histograms (Figure 3.7) would be expected after the reaction, as presumably, no radicals would be generated without the precursors present. Surprisingly, the average of I_D/I_G ratio increased from 0.08 to 0.30 with a small change of standard deviation (0.03 before the reaction vs. 0.04 after the reaction), this means that the graphite was functionalised uniformly after the reaction. By looking at the percentage of $I_D/I_G>0.2$, a 100% conversion rate has been achieved after the reaction compared to 0% before the reaction. The I_{2D}/I_G ratio histogram stayed almost the same after the reaction, as the average of I_{2D}/I_G ratios only changed from 0.32 to 0.35 and the percentage of $I_{2D}/I_G > 0.42$ was still 0 after the reaction (Table 3.2). The I_{2D}/I_G ratio analysis gives tenable results about the exfoliation of this reaction as the formation of defects or functionalisation could reduce the I_{2D}. The 2D position shifts from 2711.5 to 2708.6 cm^{-1}, which indicates exfoliation had happened during the reaction. Overall, the Raman analysis indicates that the graphite had been functionalised and exfoliated by manganese (III) acetate, this would be an important side reaction, a proposed oxidation mechanism may be the redox reaction between Mn(III) and sulphuric acid. This reaction will be discussed in more details in the next chapter.

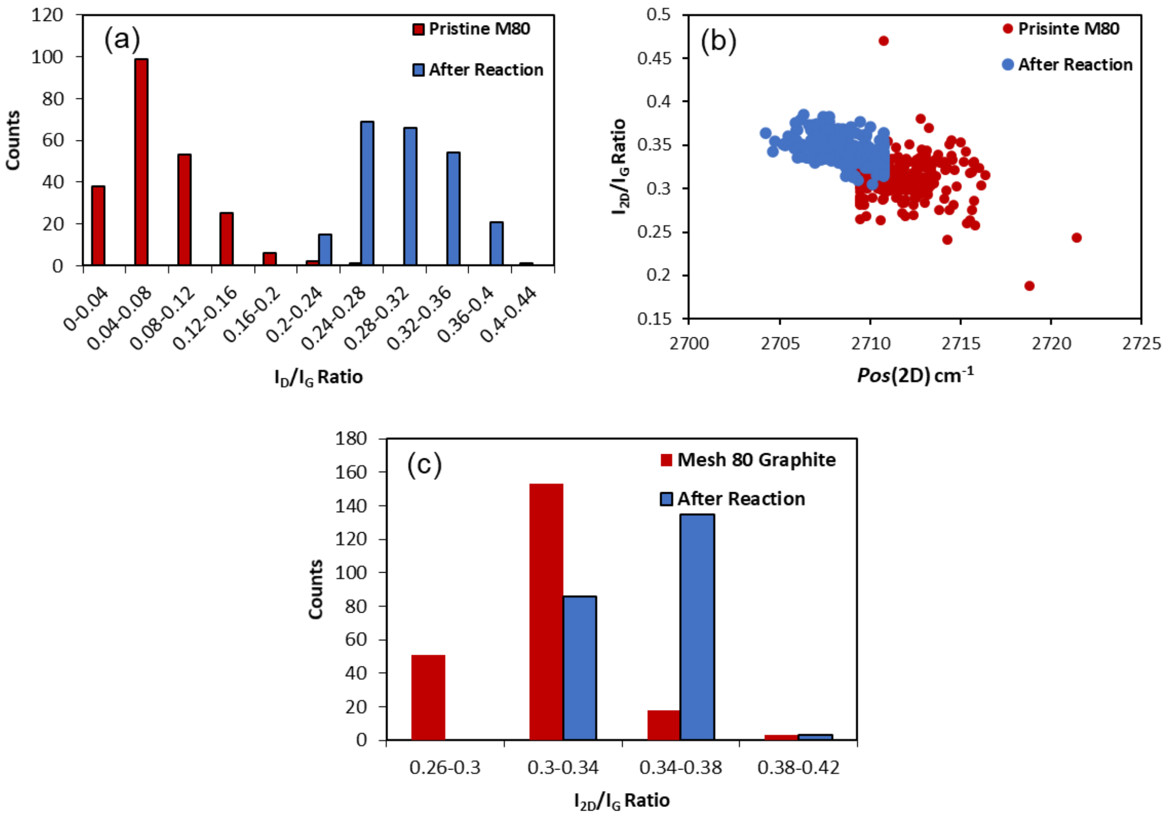

Figure 3.7 I_D/I_G *(a) and* I_{2D}/I_G *(c) histograms, and 2D position plot (b) of* ***M80*** *graphite and product derived from M80 SGICs and the catalyst only (after the oxidation).*

The third experiment was conducted by adding the TEMPO radical to the mixture of SGIC, radical precursor, and $Mn(OAc)_3 \cdot 2H_2O$ (Table 3.2). The presence of the TEMPO radical will quench the *in situ* generated radicals, which means the addition of TEMPO radical will stop the functionalisation and exfoliation of the graphite, if the reaction proceeds via the free radicals.[160] According to the statistical Raman analysis (Figure 3.8), the proportion of I_D/I_G >0.2 of the products has reduced significantly (89% vs.15%) as comparing to that of the control reaction after the addition of the TEMPO radical. The average of I_D/I_G ratio changed to 0.15 after the addition of the TEMPO radical, whilst this value increased to 0.23 when TEMPO radical was absent. Therefore, the addition of the TEMPO radical suppresses the free radical reaction as expected. The percentage of I_{2D}/I_G ratio >0.4 has dropped from 62% to 10% after the addition of the TEMPO radical (Table 3.2). The average of I_{2D}/I_G ratio changed from 0.44 to 0.34 after the addition of the TEMPO radical.

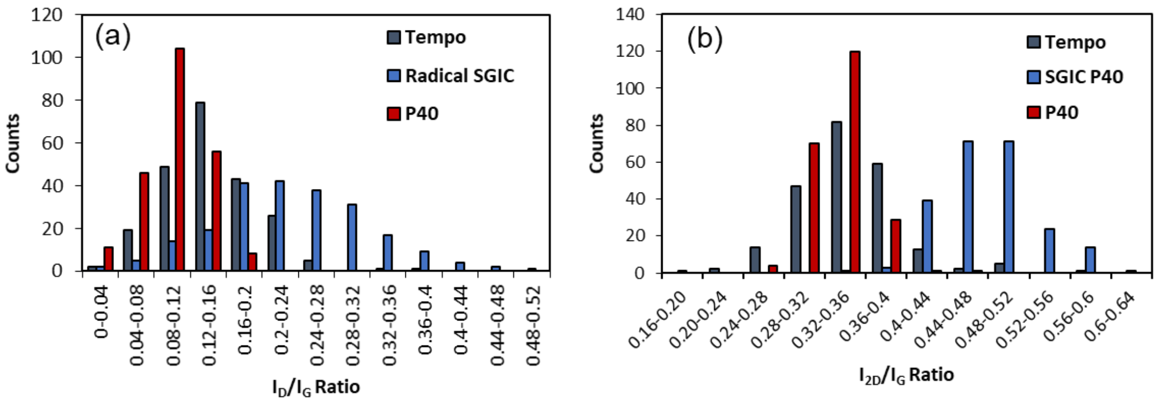

*Figure 3.8 I_D/I_G (a) and I_{2D}/I_G (b) histograms of **P40 GNP**, product derived from SGIC and 4-IPB radical, and product derived by quenching the radical reaction with TEMPO radical.*

From these three control experiments, it can be concluded that the sulphate GICs could be used to produce mildly functionalised graphite or GNP with $Mn(OAc)_3·2H_2O$ alone, the reaction may proceed via oxidation mediated by $Mn(OAc)_3·2H_2O$. This oxidation reaction could be a strong competitive reaction for the functionalisation of the sulphate GICs, which will be discussed in Chapter 4. On the other hand, the functionalisation of sulphate GICs and graphite proceeds via free radical pathway as the functionalisation and exfoliation of graphite would be suppressed if radical quenchers were used in the reaction.

Table 3.2 The mean and standard deviation of I_D/I_G and I_{2D}/I_G of the product derived from different control experiments and pristine graphite.

	Average		Standard Deviation		Percentage	
	I_D/I_G	I_{2D}/I_G	I_D/I_G	I_{2D}/I_G	$I_D/I_G>0.2$	I_{2D}/I_G
Pristine M80 Graphite	0.08	0.32	0.05	0.02	2%	0
Pristine P40 GNP	0.10	0.33	0.03	0.03	4%	1%
P40 Sulphate GICs with 4-IPB	0.23	0.44	0.09	0.07	64%	72%
P40 Sulphate GICs with 4-IPB, Catalyst, and TEMPO	0.15	0.34	0.05	0.07	15%	10%
M80 Sulphate GICs with Catalyst Only	0.30	0.35	0.04	0.02	100%	0
M80 Sulphate GICs with 4-IPB	0.21	0.35	0.27	0.08	16%	28%

*Note: Percentage of I_{2D}/I_G >0.38 is calculated for Mesh 80 Graphite and >0.4 for **P40 GNP** to evaluate the degree of exfoliation.*

3.2.3.2 Reactions with Mesh 80 Graphite Sulphate GIC

In the following series of reactions, the effect of using sulphate GICs on degree of functionalisation is compared to that of radical reaction using pristine graphite. The aim of this comparison is to confirm the activation effect of the intercalated sulphate anions. In addition, the effect of using different boronic acids on reaction of sulphate GICs was also investigated in this section.

By comparing the percentage of I_{2D}/I_G ratio>0.38 (Table 3.3), **M80** sulphate GIC reaction has the largest exfoliation rate, which is 52% and the exfoliation rate of the other two samples are 0% and 1%. This difference indicated the radical reaction of SGICs could lead to production of thinner GNPs, it also implied while small amount of sulphate GICs became graphite again, most of the GICs became exfoliated after the radical reaction. The exfoliation can be attributed to the deintercalation of the SGICs during the reaction. Based on the standard deviation of I_{2D}/I_G ratio, the distribution of products derived from the **M80** sulphate GICs is significantly different from the ratios of the pristine graphite and the reacted graphite, as the standard deviation changed from 0.02 for the pristine graphite and 0.06 for the reacted graphite to 0.15 for the reaction with the sulphate GIC; the broad distribution (Figure 3.9) implies that the SGICs did not undergo the same exfoliation during the reaction, which can be related to the heterogenous reaction conditions.

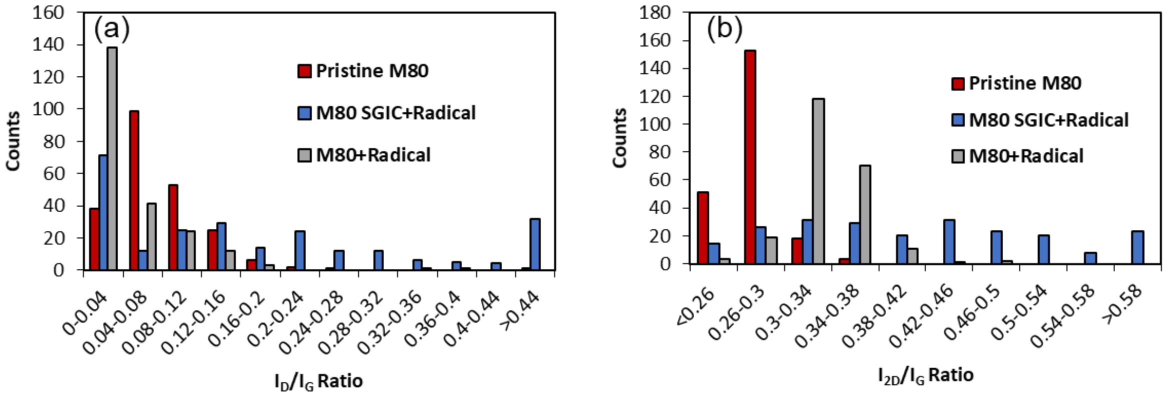

*Figure 3.9 I_D/I_G (a) and I_{2D}/I_G (b) histograms of pristine **M80** graphite, M80 reacted with 4-iodophenyl radical, and M80 SGICs reacted with 4-iodophenyl radical.*

The I_D/I_G ratio analysis (Table 3.3) of the reaction showed that the graphite had become more reactive after intercalating by sulphate ions clearly, as the average of I_D/I_G ratio had increased from 0.08 to 0.21. The same conclusion can be obtained by looking at the percentage of I_D/I_G ratio>0.2, as almost 100% samples are in the I_D/I_G ratio range 0-0.2 for the pristine **M80** graphite and **M80** graphite undergoing reaction, 32% of the sample became more functionalised when the sulphate GICs were used as the starting material. A heterogeneous trend was also observed by analysing the I_D/I_G histogram of the reaction with the sulphate GICs, as the standard deviation of the I_D/I_G ratio increased from 0.05 (pristine graphite) and 0.06 (reaction with pristine graphite) to 0.26 (sulphate GICs). Those results mean that the I_D/I_G ratios of graphite change more significantly after being activated by sulphate intercalation after the same reaction. Though there is still a portion of sulphate GICs remaining as graphite after the reaction, the number has been reduced. The statistical analysis of I_{2D}/I_G and I_D/I_G ratios gives direct evidence that the free radical reaction can give more functionalised and exfoliated graphene material by using sulphate intercalated graphite than by using the pristine graphite. However, the functionalisation and exfoliation are not homogenous.

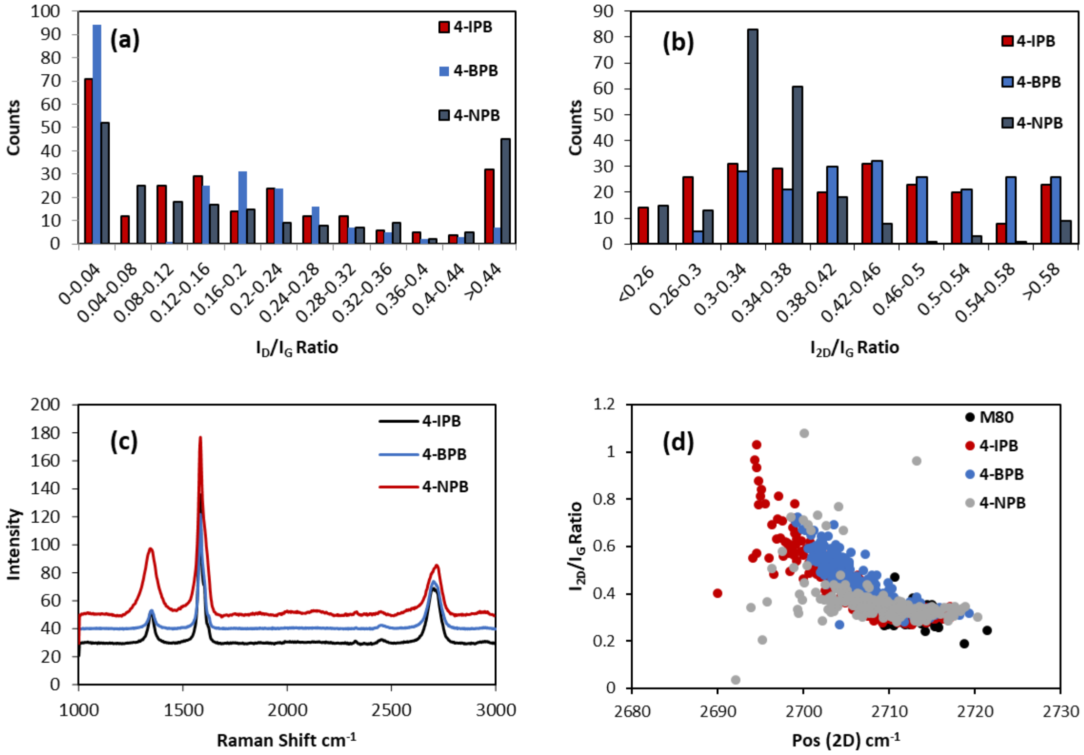

Figure 3.10 I_D/I_G (a) and I_{2D}/I_G (b) histograms Raman spectra (c), and I_{2D}/I_G and 2D position plot (d) of functionalised ***M80*** *graphite derived from different arylboronic acid. The Raman spectra are averaged based on the SRS mapping.*

Radical reactions with 4-BPB (4-bromophenyl boronic acid) and 4-NPB (4-nitrophenyl boronic acid) had also been done. The I_D/I_G ratio histogram (Figure 3.10) shows that graphite reacted with 4-NPB gave similar functionalised graphite as comparing to that which reacted with 4-IPB, as the average of I_D/I_G ratio was 0.25 (Table 3.3). The level of functionalisation for the products varied significantly due to the inefficient mixing of the reactants. For example, reactions with 4-IPB and 4-NPB exhibited high I_D/I_G standard deviation, which were 0.27 and 0.31; the product derived from 4-BPB had the lowest standard deviation 0.14, the value still indicated widespread of the functionalisation degree. Nevertheless, reactions with three different arylboronic acids had shown very close conversion rate as the percentage of products with I_D/I_G ratio >0.2 for each reaction was 32% (4-IPB), 30% (4-BPB), and 38% for (4-NPB). The percentages of I_{2D}/I_G ratio>0.38 shows that products derived from 4-IPB (56%) and 4-BPB (58%) gave material with similar degree of exfoliation. The low percentage of 4-NPB reaction can be attributed to the high level of functionalisation which will reduce the I_{2D}. Therefore, I_{2D}/I_G and 2D position plot was employed to analyse the exfoliation qualitatively. A clear red-shift of *Pos (2D)* had been observed for 4-IPB (2706.3 cm^{-1}), 4-BPB (2706.6 cm^{-1}), and 4-NPB (2708.5 cm^{-1}) as comparing to that of M80 (2711.5 cm^{-1}). The lower wavenumber of 2D positions is indicative of production of thinner GNP. The identity of the grafted functional groups on the product becomes more ambiguous due to the existence of the by-product from the oxidation.

In summary, SRS had been applied to analyse the reactions between arylboronic acid and **M80** SGICs, and all the products derived from radical reaction exhibited higher level of functionalisation (higher I_D/I_G ratio) than the starting material. Nevertheless, features of unreacted graphite were recognised from the histograms of reactions with all tested arylboronic acids. Moreover, the conversion rate of the reaction is only around 35% and the functionalisation level of the products varied significantly, which can be ascribed to the heterogenous reaction profile. Afterall, **M80** graphite has become more reactive towards the free radical after intercalating with sulphate anions. The intercalation and radical reaction also improved the exfoliation as more thinner GNPs could be produced. Same as the functionalisation, only part of the materials underwent exfoliation as the efficiency of the exfoliation was also governed by the solubility of reactants in the solvent. Overall, besides the intact graphite, products (I_D/I_G ratio between 0.28-0.36) derived from oxidation of sulphate GICs by $Mn(OAc)_3{\cdot}2H_2O$ can also be spotted in I_D/I_G histograms of those reactions.

Table 3.3 The mean and standard deviation of I_D/I_G and I_{2D}/I_G of the product functionalised by different arylboronic acid and pristine graphite

	Average		Standard Deviation		Percentage	
	I_D/I_G	I_{2D}/I_G	I_D/I_G	I_{2D}/I_G	$I_D/I_G>0.2$	I_{2D}/I_G
M80 Graphite	0.08	0.32	0.05	0.02	2%	0%
M80 Graphite with Radical	0.12	0.33	0.09	0.07	4%	1%
M80 SGICs + 4-IPB	0.21	0.43	0.27	0.15	32%	52%
M80 SGICs + 4-BPB	0.13	0.46	0.14	0.10	30%	58%
M80 SGICs + 4-NPB	0.25	0.35	0.31	0.15	38%	10%

*Note: Percentage of I_{2D}/I_G >0.38 is calculated for Mesh 80 Graphite and >0.4 for **P40 GNP***

3.2.3.3 Reactions with **P40 GNP** Sulphate GIC

The same series of reactions were done by using **P40** SGICs as well. The reactivity of **P40 GNP** was found to be improved towards the free radical after the intercalation.

When the radical precursor is 4-IPB, significant shifts of I_D/I_G and I_{2D}/I_G distribution (Figure 3.11) have been observed after the reaction: as the percentage of I_D/I_G >0.2 (Table 3.4 **&** Table 3.5) for the sulphate GIC reaction has changed from 0% to 70%; the percentage of I_{2D}/I_G> 0.4 has increased to 81% from 1% comparing to that of the pristine **P40** GNP. The average value of I_D/I_G ratio of sulphate GIC reaction increases from 0.10 to 0.24 comparing to I_D/I_G of reaction using pristine **P40 GNP**. In addition, unlike the product which derived from the pristine **P40 GNP**, which was a mixture of unreacted GNP and functionalised material, the product derived from the sulphate GICs was more homogeneous, as the standard deviation of the distribution decreased from 0.33 to 0.09. The products have also become more exfoliated, as the average I_{2D}/I_G ratio also improved from 0.33 (pristine **P40 GNP**) to 0.45 when sulphate GIC was used as reactant. Further evidence of exfoliation can be extracted from the *Pos* (2D) and $I_{2D}/_G$ ratio plot (Figure 3.13 **c**). Comparing to that of **P40 GNP**, despite the *Pos* (2D) does not shift significantly, I_{2D}/I_G ratio increased apparently after the reaction. This means functionalisation and exfoliation of graphite were both achieved by using **P40** sulphate GICs when the radical precursor is 4-iodophenylboronic acid.

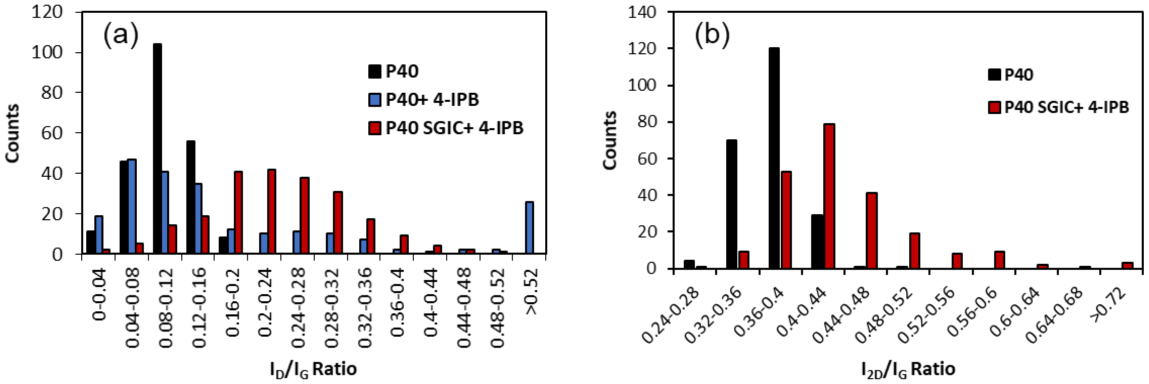

*Figure 3.11 I_D/I_G (a) and I_{2D}/I_G (b) histograms of pristine **P40 GNP**, **P40 GNP** reacted with 4-iodophenyl radical, and **P40** SGICs reacted with 4-iodophenyl radical.(I_{2D}/I_G ratios of **P40 GNP** which had reacted with 4-iodophenyl radical were not examined as it was irrelevant.)*

A very similar exfoliation effect (Figure 3.12) has been observed when the **P40** sulphate GICs reacted with 4-BPB, as the average I_{2D}/I_G ratio for 4-IPB is 0.45 and the average I_{2D}/I_G ratio for 4-BPB is 0.46 (Table 3.4 **&** Table 3.5). An improved functionalisation degree has been observed by using 4-BPB, as the average I_D/I_G ratio is 0.33 and the average I_D/I_G ratio for 4-IPB is 0.24. By looking at the percentage of I_D/I_G >0.2 and I_{2D}/I_G> 0.4, it can be seen very high values have been achieved by using 4-BPB (89% for I_D/I_G >0.2, 89% I_{2D}/I_G> 0.4). By looking at the *Pos* (2D) and $I_{2D}/_G$ ratio plot of reaction of **P40** SGIC with 4-BPB (Figure 3.13 **c**), the position of the 2D band shifts to lower wavenumber and the I_{2D}/I_G ratios increase significantly after the reaction comparing to the 4-IPB reaction. This indicates that the 4-BPB is a more reactive radical precursor than 4-IPB.

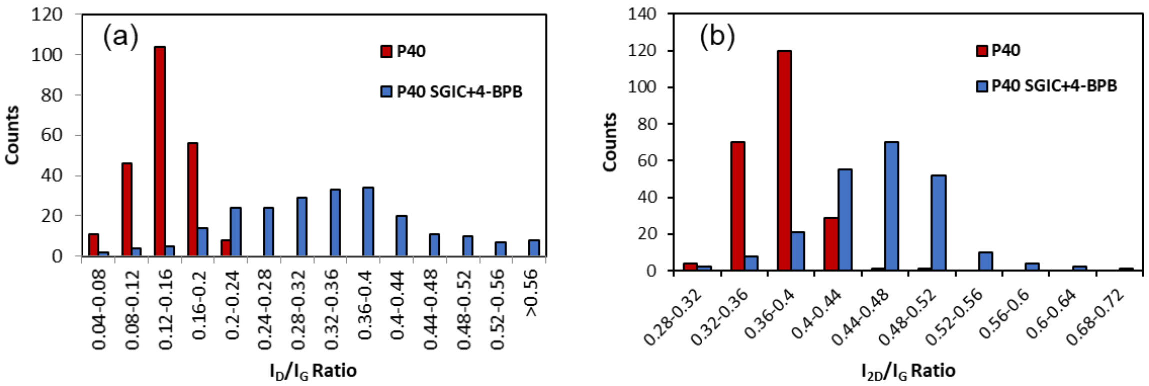

*Figure 3.12 I_D/I_G (a) and I_{2D}/I_G (b) histograms of pristine **P40 GNP** and **P40** SGICs reacted with 4-bromophenyl radical.*

The 4-NPB (Figure 3.13 ***a & b***) was also employed to react with the **P40** sulphate GICs. The product derived from this reaction was not homogenous, as besides the reacted GNP region (I_D/I_G ratio>0.2), an apparent unreacted GNP region can be recognised from the I_D/I_G histogram (I_D/I_G: ratio 0-0.2). In addition, the standard deviation of I_D/I_G ratio has increased from 0.05 to 0.18 (Table 3.4 **&** Table 3.5) after the reaction, which confirms the wide distribution of the products. In terms of exfoliation, it was found that a small portion of the sulphate GICs became un-exfoliated after reacting with 4-nitrophenylboronic acid, as I_{2D}/I_G distribution of the product overlapped with that of pristine **P40 GNP** for the range0.24-0.4, also the average of I_{2D}/I_G ratio changes compared to that of pristine **P40 GNP** (0.41 vs. 0.33). By looking at the percentage of I_D/I_G >0.2 and I_{2D}/I_G> 0.4, it can be seen relative low conversions have been achieved by using 4-NPB (72% for I_D/I_G >0.2, 79% I_{2D}/I_G> 0.4). By looking at the *Pos* (2D) and $I_{2D}/_G$ ratio plot of reaction of **P40** SGIC with 4-NPB, the average position of the 2D band shifts from 2709.3 cm^{-1} (**P40 GNP)** to lower wavenumber 2707.2 cm^{-1} and a large portion of the flakes exhibited higher I_{2D}/I_G values after the reaction comparing to those of **P40 GNP**.

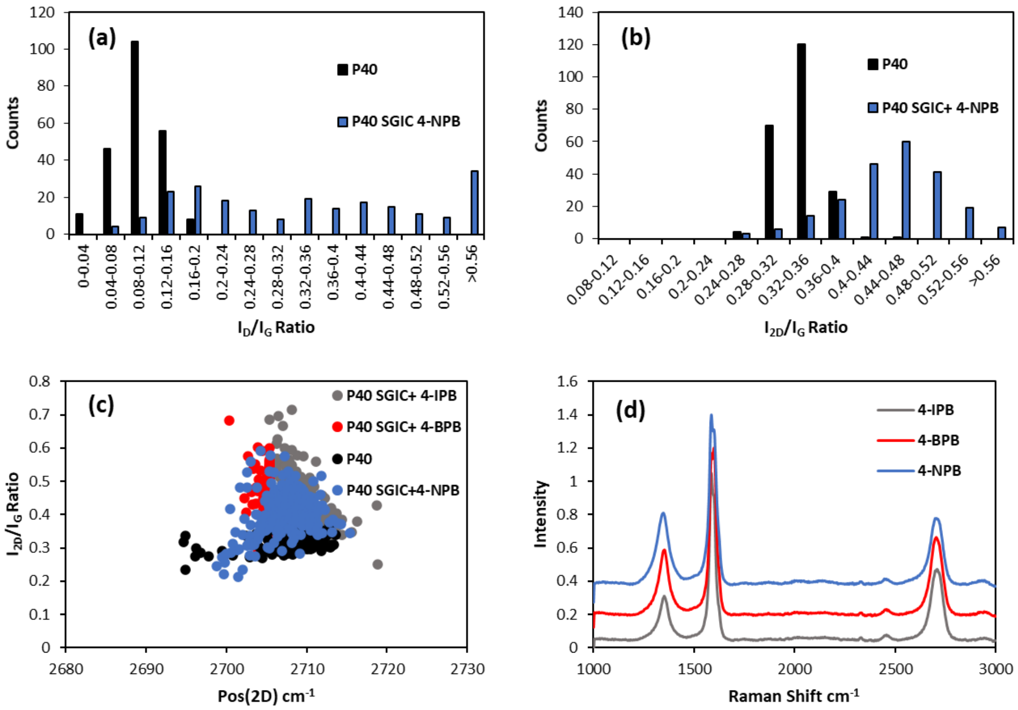

*Figure 3.13 I_D/I_G (a) and I_{2D}/I_G (b) histograms of pristine **P40 GNP** and **4-NPG**; I_{2D}/I_G and position of 2D band plot (c) of GNP GICs reacted with different arylboronic acid; average Raman spectra of **4-IPG**, **4-BPG**, and **4-NPG**.*

The effects of using boronic acids with different functionalities (Figure 3.14) on the degree of functionalisation and exfoliation were compared. In terms of functionalisation (Table 3.4 **&** Table 3.5), all the products **4-IPG** (0.24), **4-BPG** (0.34), and **4-NPG** (0.35) showed increased average I_D/I_G ratio than that (0.08) of **P40 GNP**, which indicated functionalisation of the GNP after the reaction of SGIC and radicals. It is noticeable that the **4-NPG** had the highest I_D/I_G standard deviation among the three (0.18), which suggested the wide-spread functionalisation level and the heterogeneous nature of the reaction. The **4-IPG** and **4- BPG,** on the other hand, looked less heterogeneous as their I_D/I_G standard deviation were only 0.08 and 0.11, however they were still almost doubled as comparing to the standard deviation (0.05) of **P40 GNP**. The wide distribution of I_D/I_G ratio might imply the presence of unreacted GNPs. This can be corroborated by the percentage of I_D/I_G> 0.2, as for **4-IPG** 70% of the sample was converted into functionalised GNP after the radical reaction, this percentage was increased marginally to 72% when **4-NPG** was used. Among the three arylboronic acids, reaction using 4-BPB had the highest conversion rate which was 89%. In terms of exfoliation, all three arylboronic acids can afford the material with similar exfoliation level as the resulting products had very similar average I_{2D}/I_G ratio and I_{2D}/I_G standard deviation. The **4-IPG** and **4-NPG** had the similar exfoliation conversion rates as percentage of I_{2D}/I_D>0.4 was 81% and 79% respectively. The I_{2D}/I_G vs *Pos* (2D) plot was employed to further explicate the exfoliation degree of the functionalised GNPs since the I_{2D}/I_G ratio could be reduced (<0.2) if the sample was highly functionalised. According to calculation, the *Pos* (2D) of **4-NPG** shifted to 2707.2 cm^{-1} and the *Pos* (2D) of **4-BPG** shifted to 2705.2 cm^{-1} as comparing to 2709.2 cm^{-1} for pristine GNP. The *Pos* (2D) of **4-IPG**, however, stayed the same, which was 2709.0 cm^{-1}. The smaller *Pos* (2D), higher I_{2D}/I_G ratio, and symmetrical 2D band could indicate the production of thinner GNPs. In terms of completion of the reaction, reaction with 4-BPB seems to be more outstanding than the other two types of phenylboronic acid due to its high values for I_D/I_G >0.2 (89%) and I_{2D}/I_G> 0.4 (89%). Overall, the products derived from reactions involving 4-BPB can achieve more degree of functionalisation and exfoliation.

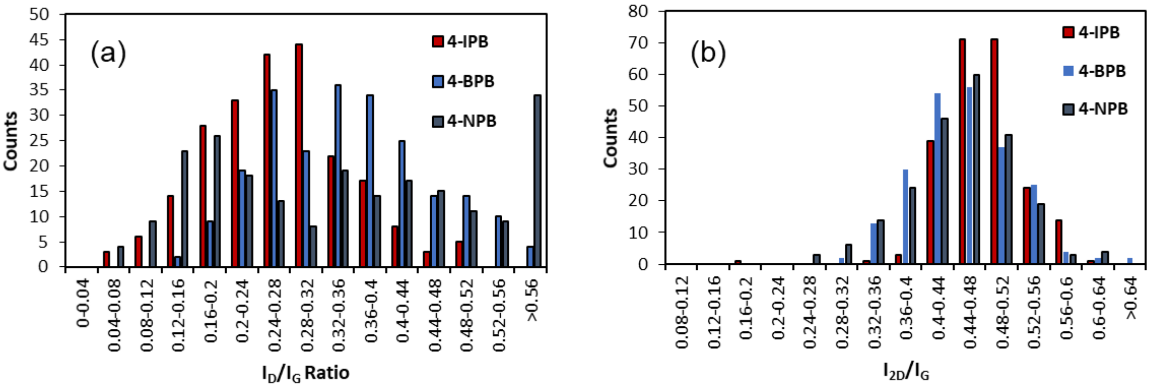

Figure 3.14 I_D/I_G (a) and I_{2D}/I_G (b) histograms of ***P40*** *SGICs reacted with 4-iodophenyl, 4-bromophenyl, and 4-nitrophenyl radical.*

In summary, **P40 GNP** has become more reactive after sulphate intercalation. The reactions of P40 sulphate GICs with arylboronic acid containing different functionalities show that the functionality of the phenylboronic acid will affect the degree of functionalisation and exfoliation of the products, as the 4-BPB had shown the superlative effect in terms of exfoliation and functionalisation conversion rate of the reaction, the 4-NPB on the other hand tended to produce product with much more functionalisation.

Table 3.4 The mean and standard deviation of I_D/I_G and I_{2D}/I_G of the product functionalised by different arylboronic acid and pristine ***P40 GNP***

	Average		Standard Deviation	
	I_D/I_G	I_{2D}/I_G	I_D/I_G	I_{2D}/I_G
Pristine P40 GNP	0.08	0.32	0.05	0.02
Reaction with P40 GNP	0.24	-	0.33	-
P40 SGICs with 4-IPB	0.24	0.45	0.08	0.07
P40 SGICs with 4-BPB	0.34	0.46	0.11	0.05
P40 SGICs with 4-NPB	0.35	0.41	0.18	0.06

Table 3.5 Summary of average I_D/I_G and $I_{2D}/_G$ and percentage of the ***P40*** *and* ***M80 GICS*** *functionalised by different arylboronic acid.*

	P40 SGICs		M80 SGICs		P40 SGICs (Percentage of I_{2D}/I_D>0.4 and I_D/I_G>0.2)		M80 SGICs (Percentage of I_{2D}/I_D>0.42 and I_D/I_G>0.2)	
	I_{2D}/I_D	I_D/I_G	I_{2D}/I_D	I_D/I_G	I_{2D}/I_D	I_D/I_G	I_{2D}/I_D	I_D/I_G
4-IPB	0.45	0.24	0.41	0.15	81%	70%	47%	30%
4-BPB	0.46	0.34	0.46	0.13	89%	89%	58%	30%
4-NPB	0.41	0.35	0.35	0.25	79%	72%	10%	38%

Note: Percentage of I_{2D}/I_G >0.38 is calculated for ***M80*** *SGICs and >0.4 for* ***P40*** *SGICs; percentage of I_D/I_G>0.2 is used for both* ***M80*** *and* ***P40*** *SGICs.*

In general, both **M80** graphite and **P40 GNP** (Table 3.5) have become more reactive after sulphate intercalation. Based on the SRS analysis and XPS, both **M80** graphite and **P40 GNP** have been functionalised successfully by corresponding phenylboronic acids. By comparing the percentage of I_{2D}/I_D>0.4 and I_D/I_G>0.2 of products derived from P40 and **M80** sulphate GICs, it can be seen that while the products derived from using **M80** sulphate GICs has smaller population of functionalised and exfoliated sample, more samples in products derived by using P40 sulphate GICs were functionalised and exfoliated. This indicates that P40 sulphate GICs was more reactive than **M80** sulphate GICs. In addition, the reaction involving P40 sulphate GICs was more complete in terms of exfoliation and functionalisation than the reaction involving the **M80** sulphate GICs. In terms of exfoliation, the products derived from both GICs show apparent exfoliation compared to the pristine graphite/GNP. However, whilst the P40 sulphate GICs gave more homogenous exfoliated material, the **M80** graphite produced material with wide distribution and unreacted starting material. Still, production of thinner material was realised according to the change of the average I_{2D}/I_G ratios after the intercalation and radical interaction. For the radical reaction between the P40 SGICs and different boronic acid, it is shown that phenylboronic acids with specific functionalities may have specific different effect on the products: 4-NPB would make the graphite more functionalised but also more heterogenous, and more functionalised and exfoliated graphite can be achieved by using 4-BPB. Competitive oxidation reaction was confirmed when SGICs were reacted with $Mn(OAc)_3$ only. Indeed, the oxidised product can be identified by comparing the histograms of oxidation reaction and the radical addition reaction. The unfunctionalised region in I_D/I_G histogram of the radical reaction indicates that part of the *in-situ* generated iodophenyl radical acts as radical quencher to stop the reaction between $Mn(OAc)_3 \cdot 2H_2O$ and SGIC. Similarly, the more functionalised region (I_D/I_G>0.4) could arise due to the radical functionalisation or oxidation. Consequently, at least two functionalities are added to the graphite or GNP after the reaction.

Besides competitive oxidation, significant amounts of starting materials might be left intact (no functionalisation or no exfoliation) after the radical reactions, which suggests those reactions undergo incomplete reaction. The problem originated from the poor solubility of radical precursors and SGICs in 1,2 DCE. Despite reaction mixture was stirred constantly during the reaction, most of the reactants stayed suspended in the solvent or the SGIC became stuck to the bottom of the flask due to its high viscosity. Thus, the collisions between the generated radicals and the reactive sites of SGICs happened unevenly, which had led to heterogenous functionalisation. The effect was amplified for the **M80** series reaction, as **M80** graphite was much bigger and thicker than the **P40 GNP** which had aided the inefficient mixing and collision of the radicals. Consequently, the conversion rate of reactions using **M80** was significantly less than that of reactions using **P40 GNP**. The problem varies with the identity of arylboronic acid and is mitigated when 4-BPB was used as precursors. This is arduous to fix, since except concentrated sulphuric acid, no good solvents for first stage SGIC without breaking its intercalation are known. Moreover, it is also difficult to find the replacement for 1,2 DCE because as a chlorinated solvent it will not stop the radical reaction and its boiling point is high enough to sustain the reaction. Ortho-dichlorobenzene (ODCB) is a promising substitute and frequently used in radical reaction, however, our study suggests that GNP will become less functionalised in ODCB (Figure 8.12 in the Supporting Information), as the average I_D/I_G ratio decreased from 0.24 to 0.20 and the I_D/I_G distribution also shifted to lower region which represented less functionalised. One of the possible reasons might be that the ODCB reacted with the radical.

3.3 Characterisation of the Aryl Functionalised Graphene

The functionalised graphene derived from the **P40 GNP SGIC** was further probe sonicated in NMP to achieve better exfoliation, separated to remove unreacted graphite and thick flakes, and then characterised by AFM and TGA.

Since SRS analysis is not able to differentiate the identities of functional groups grafted onto the GNP, XPS is adapted to investigate if aryl groups are added with interference of oxidation reaction. Corresponding heteroatom signal can be identified from the XPS survey spectrum. For the **4-IPG**, iodine 3d doublet can be located at 620.5 eV and 632 eV, 3p signal can be located at 875 eV and 933 eV, 4d signal at 62 eV, and 4s at 186 eV in the survey scan (Figure 3.15). High resolution iodine 3d spectrum (Figure 3.18 a) indicates each 3d singlet splits into doublet further due to C-I bond. Four major peaks contribute to the composition of C 1s core level peak of **4-IPG**: they are sp^2 carbon at 284.5 eV, C-I/C-O at 285.49 eV, COO- at 288 eV, and π-π^* at 290 eV. The presence of C-O bond signal confirms the competitive oxidation reaction (Figure 3.19 a). For the **4-BPG**, bromine 3d signal can be detected at 71 eV (3d), 184 eV and 190 eV (3p1/2 and 3p3/2), and 257 eV (3s) in XPS survey spectrum (Figure 3.16). The high-resolution Br 3d peak (Figure 3.18 b) can be deconvolved into two peaks (70.8 eV and 71.9 eV) which correspond to covalently bonded bromine. The C 1s (Figure 3.19 b) of **4-BPG** can be deconvolved into 3 components: sp^2 carbon at 284.8 eV, C-Br/C-O at 285.9 eV, and π-π^* at 290 eV. For the **4-NPG**, doublet nitrogen signal can be spotted from 399- 408 eV (Figure 3.18 c). The peak at 406 eV indicates nitro groups, and the peak at 401 eV indicates amine groups which are the by-product during the diazotisation reaction. Similarly, the C 1s of **4-NPG** can be fitted by three components: sp^2 carbon at 284.8 eV, C-N/C-O at 285.9 eV, and π-π^* at 290 eV (Figure 3.19 c). Therefore, the successful functionalisation by corresponding boronic acid is confirmed by the presence of the corresponding heteroatoms signal. On the other hand, the competitive oxidation reaction is also confirmed due to presence of relevant oxygen and C-O peaks. For all the samples, no manganese and no boron signals have been identified which indicates efficient cleaning and thorough conversion had been done.

The TGA profiles (Figure 3.20) of the separated functionalised graphene are shown below. The **4-IPG** demonstrates the smallest weight loss (9.5%) over 150-600 ℃, which is consistent with its lowest average I_D/I_G ratio. The weight loss is significantly lower than the iodine concentration calculated from XPS (2 at% iodine is equivalent to 26.5 % weight percentage of iodophenyl groups in the **4-IPG**), which indicates the presence of excessive iodine after the reaction. The deconvolution of iodine 3d 5/2 spectrum results in two major peaks, the peak at 620.6 eV can be attributed to molecular iodine, the emergence of peak at 622.4 eV is contributed by C-I covalent bond. Since C-I bond contributes to the 30.5 % of the iodine 3d peak, iodophenyl group weight% is c.a. 8.1%, which is more consistent to the TGA result.[161,162] The **4-BPG** loses 14.3 % overall weight over 150-600 ℃, this corresponds to every 77.6 carbon atoms having one 4-bromophenyl group (equivalent to 1.3 at% degree of functionalisation), if all the weight loss is from 4-bromophenyl group. The calculation based on XPS survey scan results indicate the 4-bromophenyl contributes to 11.9 % of the total weight (eq. 1 at%). The deconvolution of Br 3d peak suggests it is an overestimation since two C-Br peaks can be fitted in and the peak at 71.9 eV can be attributed to oxybrominated derivatives.[7,59,67] Hence, 9.2 wt% of 4-bromophenyl was found for **4-BPG**. The TGA profile of **4-NPG** indicates 17.6 wt% loss over 150-600 ℃ interval. The XPS survey scan shows that there was 1.4 at% of nitrogen in the sample which is equivalent to 13.2 wt% of 4-nitrophenyl groups, if all the nitrogen signals were from NO_2. However, the deconvolution of N 1s signal suggests besides nitro groups (405.9 eV), there was the presence of amnio groups (400.3 eV),[163,164] which is the impurities from the starting material. Taking this into account, 1.4 at% of nitrogen is equivalent to 8.7 wt% of 4-nitrophenyl and 4-aminophenyl groups. Oxygenated functionalities contribute to the rest of the weight loss.

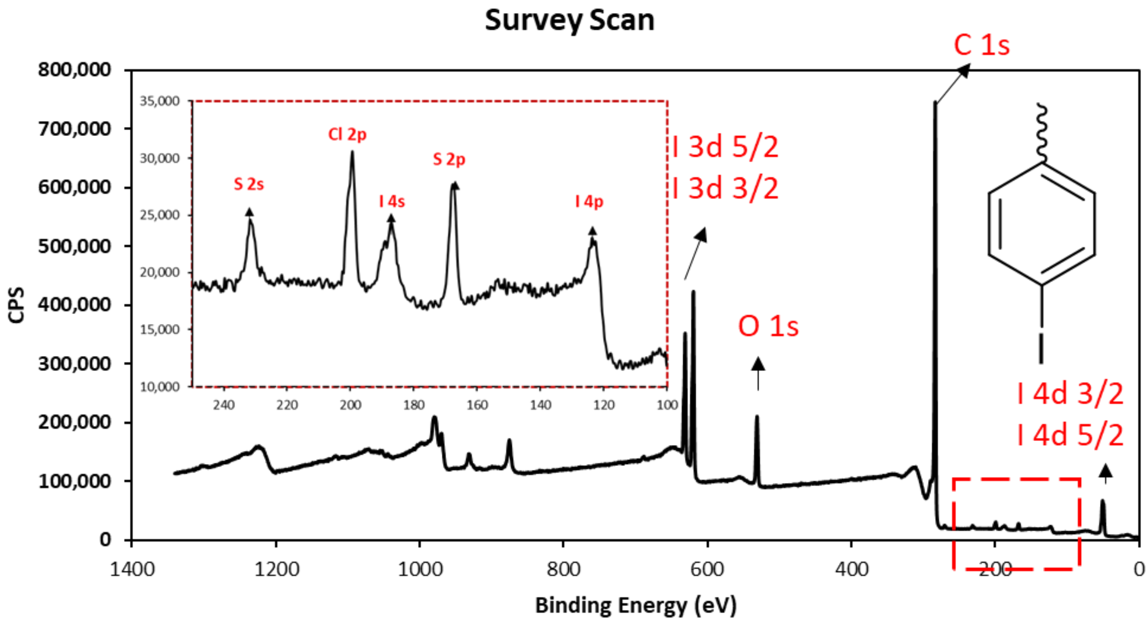

*Figure 3.15 XPS survey scan of the graphene functionalised with 4-IPB (**4-IPG**).*

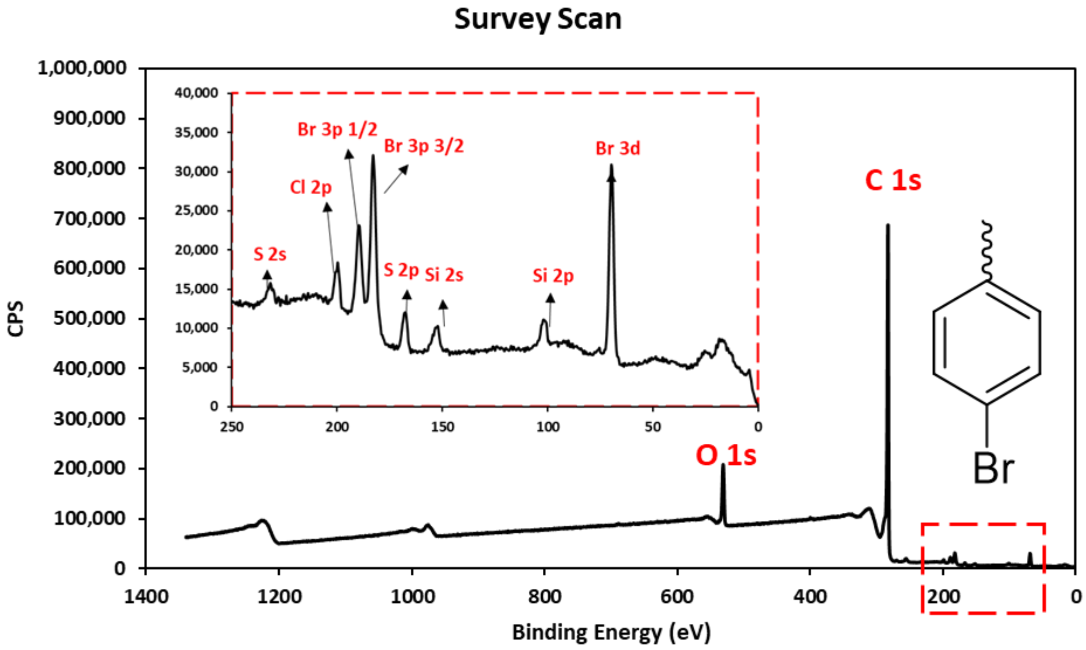

*Figure 3.16 XPS survey scan of the graphene functionalised with 4-BPB (**4-BPG**).*

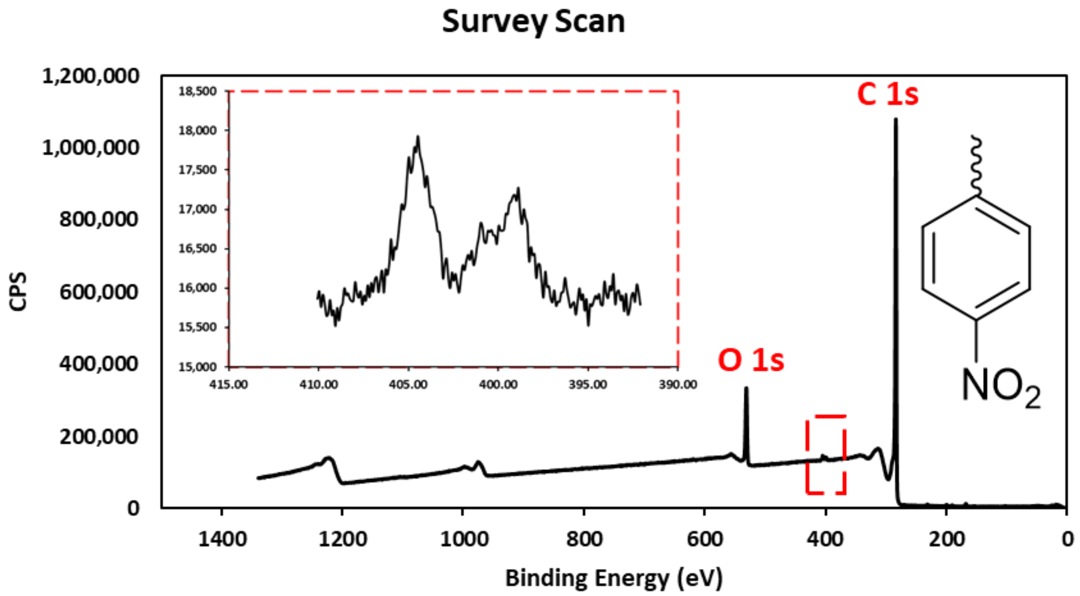

*Figure 3.17 XPS survey scan of the graphene functionalised with 4-NPB (**4-NPG**). The inlet shows the nitrogen peak.*

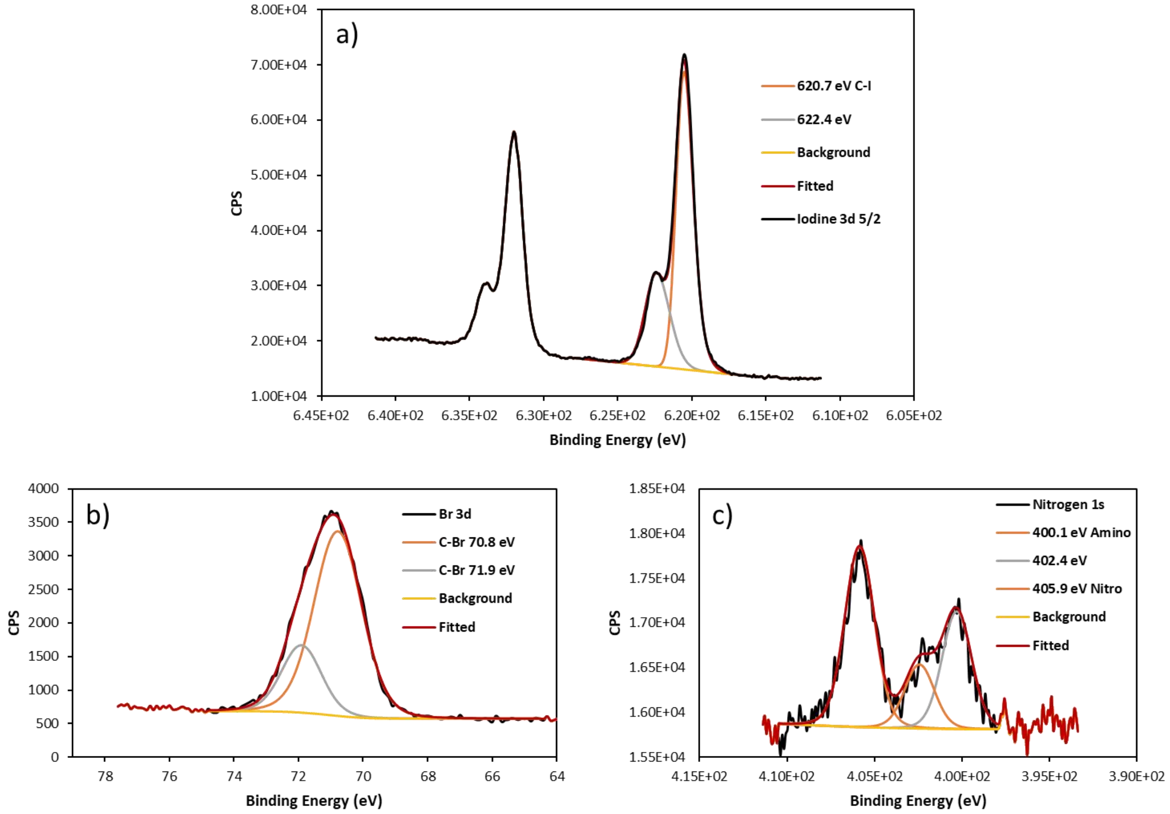

Figure 3.18 High resolution scan and deconvolution of a) iodine 4d, b) bromine 3d, and c) nitrogen 1s.

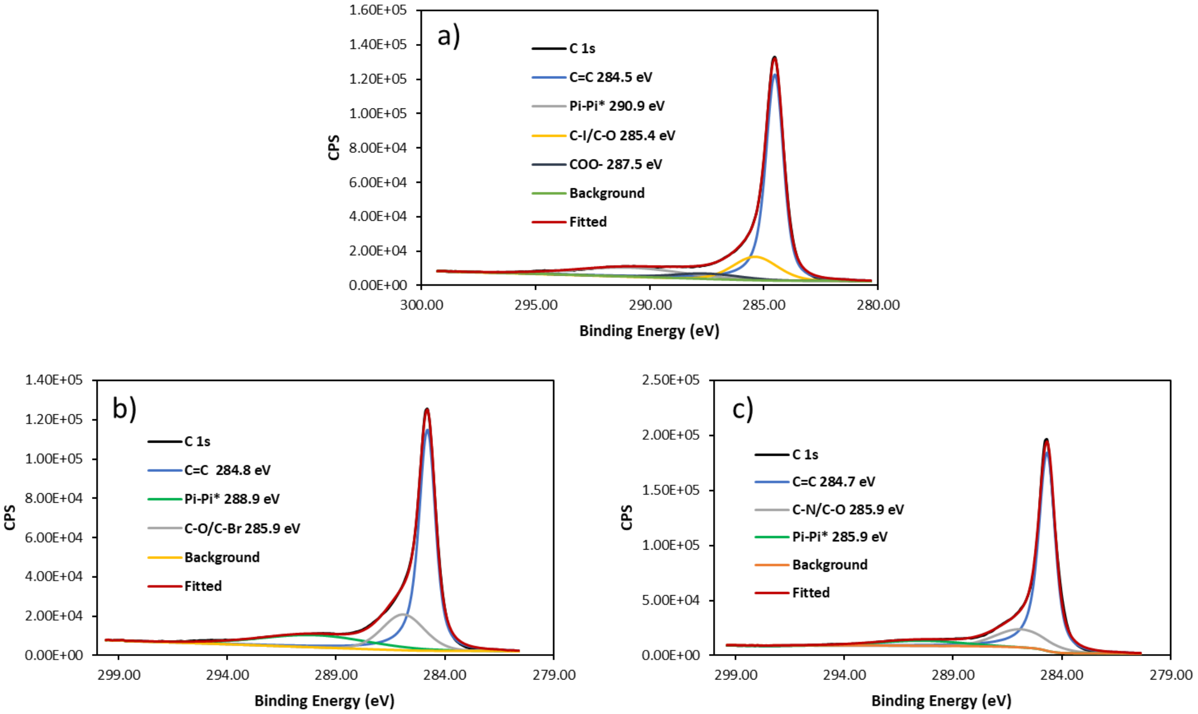

Figure 3.19 Deconvolution of C 1s peak for a) ***4-IPG****, b)* ***4-BPG****, and c)* ***4-NPG***

The lateral size and the thickness of the functionalised graphene was obtained directly by statistical AFM analysis (Figure 3.21). P10, P50, P90, and average values of thickness and lateral size of each sample were calculated to help understand the distribution of the dimensions of the samples (Table 3.6 & Table 3.7). In case of lateral size, all the functionalised GNP demonstrate wider distribution, where larger differences between P10 and P90, the $\Delta_{ls}\ for$ **4-IPG**, **4-BPG**, and **4-NPG** were 0.42, 0.47, and 0.4 μm, can be observed. In comparison, the probe sonicated pristine GNP (**EX-P40**) possessed the most uniform size distribution as very small difference existed among the P10 (0.16 μm), P50 (0.2 μm), P90 (0.27 μm), and the $\Delta_{ls}\ for$ **EX-P40** was only 0.11 μm. In addition, the average lateral size of **EX-P40** is 0.22 μm, which is the smallest comparing to the graphene functionalised with 4-BPB (0.43 μm), 4-NPB (0.64 μm), and 4-IPB (0.30 μm). The wider distributions of the lateral size of the functionalised GNP indicate the intercalation and the consequent radical reaction were more heterogenous, which could be related to the biphasic nature of the functionalisation. The distributions of the thickness demonstrated diverging distribution due to the same reason, however thinner flakes were produced due to the intercalation effect. Due to incomplete exfoliation during the reaction and the post-processing, a limited portion of thin functionalised graphene was obtained for **4-IPG**. As the thickness distribution (Figure 3.22) of the **4-IPG** shows, 10% of the sample were 60 nm or ≥ 60 nm thick. The P10 value of **4-IPG** (3.5 nm) is almost the same as that of the **EX-P40** (3.7 nm). In comparison, the **4-BPG** and **4-NPG** were more exfoliated, in which the **4-BPG** was the most exfoliated, as 90% of the sample were ≤

5.2 nm with average thickness of 8.8 nm. 90% of **4-NPG** sample were ≤ 14.3 nm with average thickness of 9.1 nm. In addition, the P10 values of those two samples were only 1.7 and 1.8 nm. The smaller P10 values suggest the radical reaction did facilitate the exfoliation. The **4-BPG** also exhibited the most uniform thickness distribution as its Δ_{ls} wis only 3.5 nm, indicating 4-BPB had the best exfoliation effect among the three tested arylboronic acids. Although the average thickness and the distribution of all the functionalised graphene and exfoliated GNP are very similar, except for the **4-IPG** (**4-IPG**: 22.7 nm, **4-BPG**: 8.8 nm, **4-NPG**: 9.1 nm, and **EX-P40**: 7.5 nm), **EX-P40** demonstrated the thickest flakes if the thickness were converted to number of layers as the thickness of pristine graphene is 0.33 nm and the thickness of the functionalised graphene could be 1-1.5 nm. This reflects the intercalation could enhance the exfoliation comparing to the liquid phase probe-sonication of the pristine GNP.

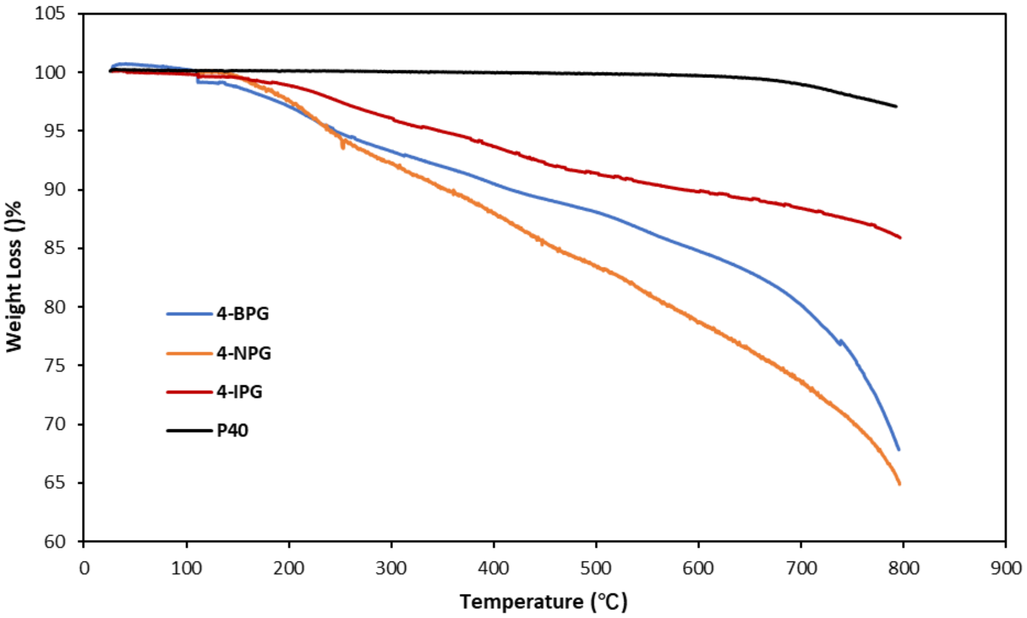

*Figure 3.20 TGA of the probe-sonicated and centrifuged radical functionalised graphene and pristine **P40 GNP***

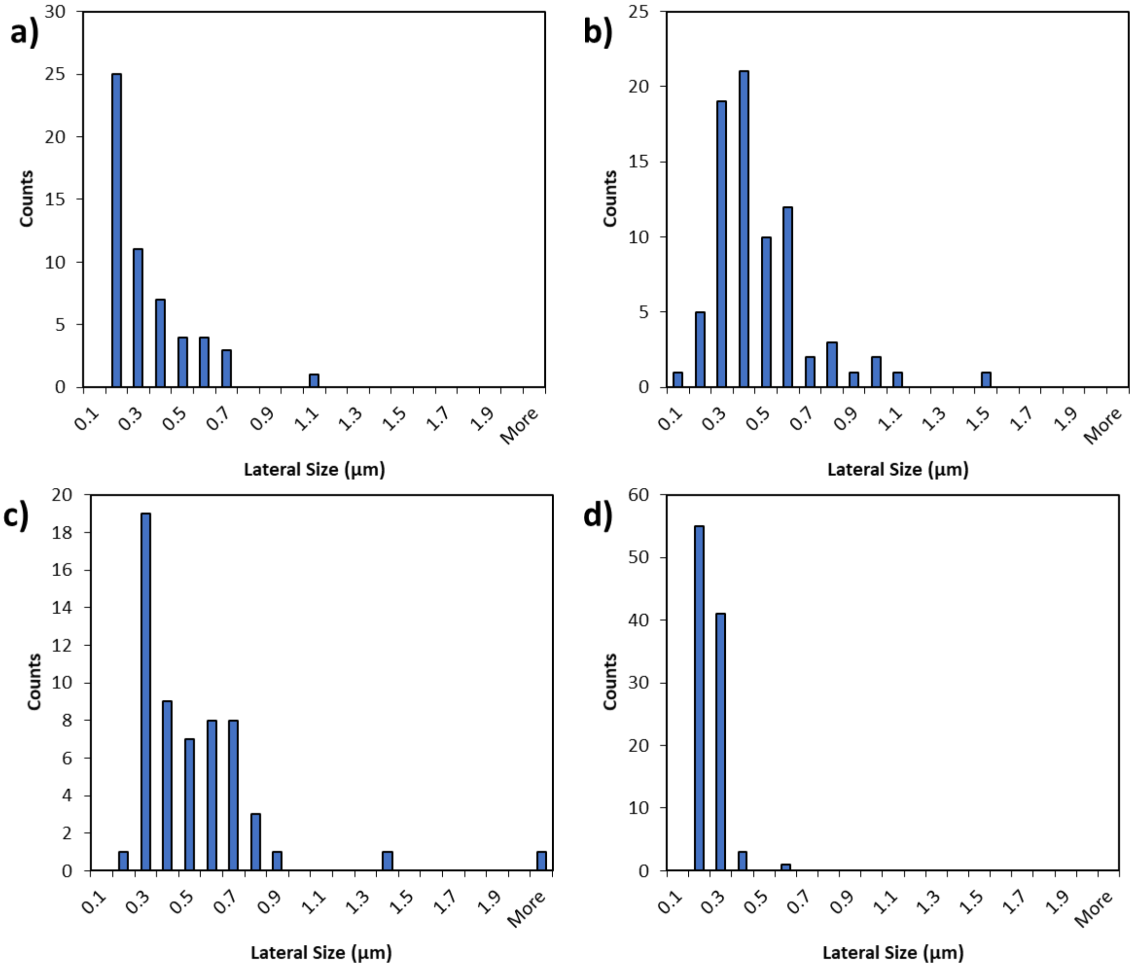

Figure 3.21 Flake size distribution of a) ***4-IPG****, b)* ***4-BPG****, c)* ***4-NPG****, and d)* ***EX-P40*** *(Exfoliated P40 GNP).*

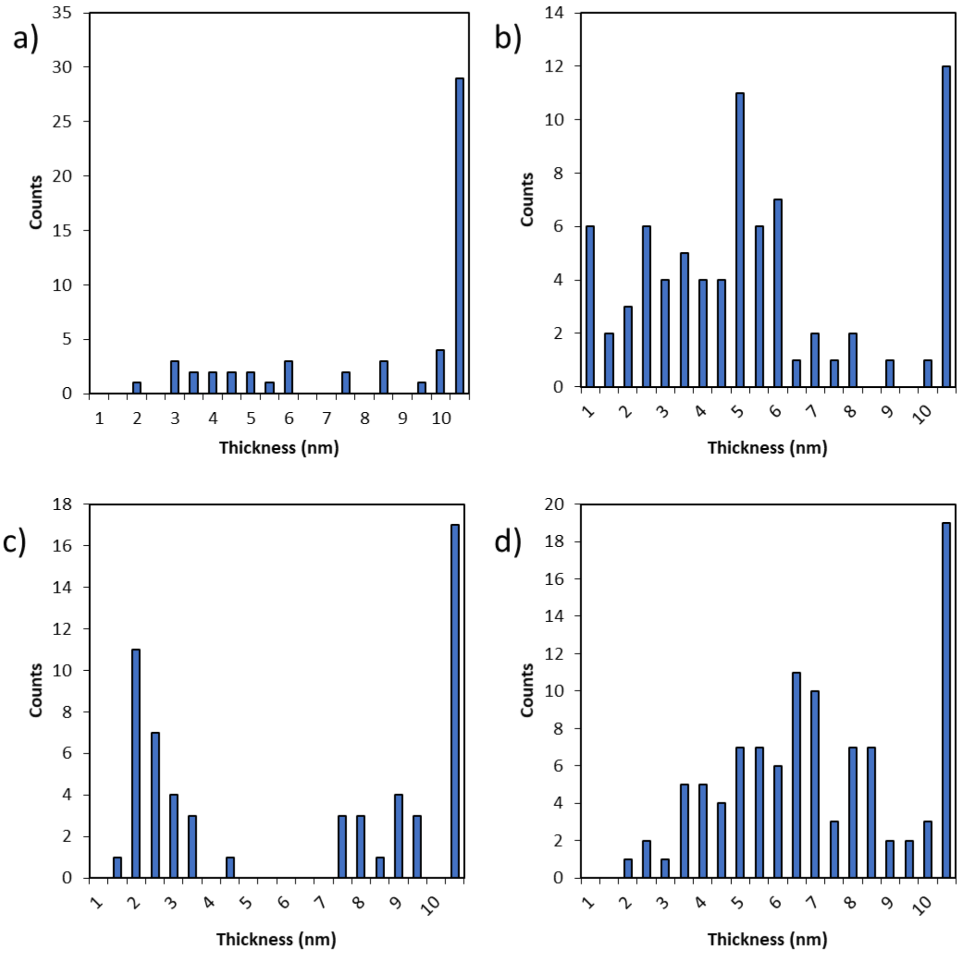

Figure 3.22 Histograms of flake thickness for a) ***4-IPG****, b)* ***4-BPG****, c)* ***4-NPG****, and d)* ***EX-P40*** *(Exfoliated P40 GNP).*

0.1 mg mL^{-1} NMP dispersions were prepared by using **4-IPG**, **4-BPG**, and **4-NPG** (Figure 3.23). The stability of those dispersions was compared with that of the **EX-P40** NMP dispersion by using the UV-Vis spectrometer. Absorbance of dispersions at 660 nm with known concentration was recorded with a specific time interval up to 7 days. The absorbance plot shows that EX**-P40** had the highest stability over the test, though 50 wt% of the material was lost after 6 days. The **4-NPG** exhibited consistent sediment and lowest stability over the test duration. **4-BPG**, however, showed the highest stability in the first 48 hours among the functionalised materials, and sedimented completely after 6 days. **4-IPG** exhibited gradual precipitation over 6 days observation and retained 1/5 of the starting material in the NMP. The impact of thickness on the stability of dispersion can be excluded as the average thickness of three kinds of graphene material are very similar (**4-BPG**: 8.8 nm, **4-NPG**: 9.1 nm, **EX-P40**: 7.5 nm). The only one exception is **4-IPG** (22.3 nm), which also has wide distribution of thickness and thicker flake due to presence of numerous thick materials (Table 3.6 & Table 3.7). However, **4-IPG** showed higher stability than **4-NPG** and **4-BPG**. In fact, the lateral size of the flakes governed the dispersion stability as the trend of dispersion stability follows the trend of lateral size of the flakes **EX-P40** (0.22 μm)< **4-IPG** (0.30 μm) < **4-BPG** (0.43 μm) < **4-NPG** (0.64 μm).

Table 3.6 Flake thickness distribution analysis of ***4-IPG****,* ***4-BPG****, Exfoliated P40 GNP and* ***4-NPG***

Sample	10th Percentile nm	50th Percentile nm	90th Percentile nm	<Average Thickness> nm
4-IPG	3.5	10.9	60	22.7
4-BPG	1.7	4.8	5.2	8.8
4-NPG	1.8	7.5	14.3	9.1
Exfoliated P40 GNP	3.7	6.7	12.5	7.5

Table 3.7 Flake size distribution analysis of ***4-IPG****,* ***4-BPG****, Exfoliated P40 GNP and* ***4-NPG***

Sample	10th Percentile μm	50th Percentile μm	90th Percentile μm	<Average Lateral Size> μm
4-IPG	0.13	0.24	0.55	0.30
4-BPG	0.23	0.37	0.7	0.43
4-NPG	0.26	0.41	0.69	0.64
Exfoliated P40 GNP	0.16	0.20	0.27	0.22

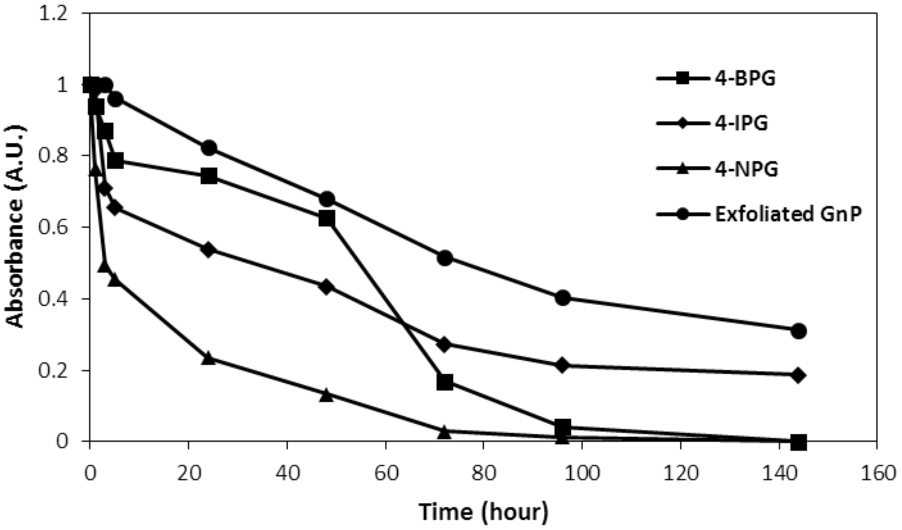

Figure 3.23 Stability of the aryl functionalised graphene and exfoliated GNP dispersions in NMP.

3.4 Conclusion and Future Work

According to our study, aryl radical generated from corresponding arylboronic acid and $Mn(OAc)_3 \cdot 2H_2O$ can be used to produce aryl functionalised graphene materials. The degree of the functionalisation and exfoliation can be further enhanced significantly if the graphite is activated by sulphuric acid intercalation. This study provides an alternative route for aryl groups addition to graphene. Comparing to aryl diazonium salts, arylboronic acid is more stable and safer to use in large scale. Comparing to graphenide which is produced under moisture and oxygen free conditions, the prerequisites to activate graphite by using sulphuric acid graphite intercalated compounds is less harsh. By utilising the chemistry of the arylboronic compounds, more potential functional groups can be grafted to graphene by similar processes. Although this route has been proved to be effective experimentally, but the efficiency of this pathway is impacted by several problems. Unlike the radical precursors, which are soluble and dispersible (the catalyst) in the solvent, the SGIC is neither soluble nor dispersible in 1,2 DCE. The poor solubility and dispersibility of the SGICs make the functionalisation and exfoliation less uniform, which will result in the appearance of non-functionalised graphene or thick non-exfoliation graphene. And due to the necessity of using further exfoliation and separation technique to obtain finer product, the yield is only 15-30 mg per 100 mg **P40 GNP**. The other crucial issue is the competitive reactions. Two competitive reactions can be identified from this process. One is the competitive oxidation which is governed by SGIC and $Mn(OAc)_3{\cdot}2H_2O$. Therefore, besides aryl groups, the product is also functionalised by oxygen containing functional groups C-O etc. The other one is dimerization of the radical, which will deter the efficiency of the reaction. Both problems pose difficulties in the consequent separation of the products.

Comparing to the c.a. 100% conversion rate of the reductive functionalisation which used potassium graphenide and electrophiles (in Chapter 2), the conversion rate of this radical reaction was between 70% to 90%. Finding a way to enhance the homogeneity and the efficiency of the reaction is important to make this synthesis more useful. The most effective way is to make SGIC and the radical precursors in the same phase. However, suitable solvents are very limited due to the limited solubility in solvents and highly oxidising power of SGIC. Though oxygenated solvents are presumably good to disperse SGIC, but the intercalated structure will also be destroyed upon the dispersion, which will cause the deficiency of exfoliation. The other issue of using organic oxygenated solvents is the potential hazard to produce peroxide due to presence of concentrated sulphuric acid. To avoid the risk of peroxide formation, chlorinated solvents are more suitable. Besides 1,2 DCE, ODCB seems to be the other optimal solvent for the reaction for its good compatibility to disperse graphene and relatively high boiling point. However, our rough test showed the functionalisation level was reduced after the reaction.

The dispersibility and stability of the functionalised material was recorded and compared in NMP. Surprisingly, the addition of the functionalities does not improve the dispersibility of the graphene, instead reverse dispersibility and stability had been observed for the functionalised graphene as compared to the exfoliated GNP in the NMP. The reverse dispersion stability seems to be originated from the bigger flake sizes; the role of the tested functionalities seems to have very limited impact on enhancing dispersion stability in NMP when the lateral sizes of the flakes are too big. The relationship between the aspect ratio of the functionalised graphene and the density of functional groups is still unclear and merits systematic studies. This relationship is fundamental to understand the effect of the functionalities.

Chapter 4. Functionalised Graphene Derived from $Mn(OAc)_3$ Mediated Mild Oxidation of Sulphuric Acid Graphite Intercalated Compound

4.1 Introduction

Graphite oxide is an important precursor for production of graphene with large scale and low cost. Derived from the reaction of graphite and mixture of sulphuric acid and potassium permanganate, graphite oxide is heavily functionalised with various oxygen containing functional groups (hydroxyl, carbonyl, carboxylic, epoxy, and other groups). Those groups grant graphite oxide with excellent solvent compatibility as GO is dispersible in a range of polar solvents with low boiling point, those solvents include water, ethanol, methanol etc. Comparing to highly dispersible GO, the extremely hydrophobic graphene powder tends to re-aggregate and is only dispersible in a limited range of solvents with high boiling point. The solvent compatibility of GO makes its consequent application easier. However, the excellent dispersibility of GO is achieved with the cost of significant damage to the sp^2 structure of graphene, which will cause the deterioration of the other properties of graphene. Consequently, graphene oxide is thermally unstable and electrically insulated. To recover those properties, an additional reduction step is always needed for GO to obtain reduced graphene oxide (rGO). Despite a series of reduction methods can remove the functional groups of GO and restore graphene's properties, the defects and damage from the over- oxidation are unrecoverable by reduction. Apart from the defects in the basal plane of structure, the graphene would unavoidably lose its dispersibility due to lose of functional groups. The dispersibility of graphene materials is a crucial property which will also influence their performances in applications as better compatibility between graphene materials and polymer matrices, better interaction/adhesion will be. As Tang et al.[165] studied, with better dispersibility in epoxy resin will enhance the electric conductivity and overall strength of rGO/epoxy resin composite. In addition, as the functional groups are lost after reduction, the reduction condition must be suitable for fabrication to avoid any possible damage or contamination from the reduction. In short, the major challenge of producing chemically modified graphene is minimising the deterioration of properties of graphene while enhancing the degree of functionalisation to achieve appropriate dispersibility.

Regarding to this challenge, several solutions have been proposed. The first solution focuses on using milder condition instead of Hummers method during oxidation process to avoid over-oxidation. In research, this is generally done by modifying the $KMnO_4$ and graphite ratio or reaction time and temperature in Hummers method. The problem of these methods is that the additional reduction is still required. The second solution involves using potassium graphite intercalated compound (GIC) as starting material to achieve controllable functionalisation. The controllable functionalisation is defined as the identity of functional groups is homogenous. As the chemical reactivity of graphene layer will be changed upon intercalation, Andreas Hirsch et al. published representative works, where stage-1 potassium GICs was employed to react with electrophile (organic iodide or bromide) to achieve aryl or alkyl functionalised graphene.[47] However, the condition required for this approach is harsh, and the yield is very low. Relatively large scale of production of partially oxidised graphene can be achieved by using electrochemical method where graphite foil or HOPG is used as anode.

Using sulphate GICs as precursor for functionalised graphene material was first studied by S.Eigler (Scheme 4.1).[131] In his study, few layer and monolayer oxygenated graphene can be produced by adding distilled water directly to the reaction mixture of sulphate GICs (23 mL sulphuric acid, 3 g potassium persulphate, 1 g graphite). By utilising the exothermic nature of diluting the sulphuric acid, the reaction mixture was heated to 60 ℃ spontaneously, the functionalised graphene was separated by centrifugation at 3000 rpm. Without addition of other oxidants, the functionalised graphene was less defective and showed moderate level of functionalisation (13 wt%). However, no efforts have been made to determine the dispersibility and electric conductivity of the separated material due to the low yield of the process. On the other hand, contradictions arise since other studies suggest the formation of SGICs is reversible as graphite can be reobtained by quenching the SGICs mixture with water.[154] A later study from S.Eigler's group suspended the argument by showing that whether the action of water quenching will produce functionalised graphene or graphite depends on the crystallinity of the graphite—graphite with better crystal structural will undergo irreversible oxidation.[132]

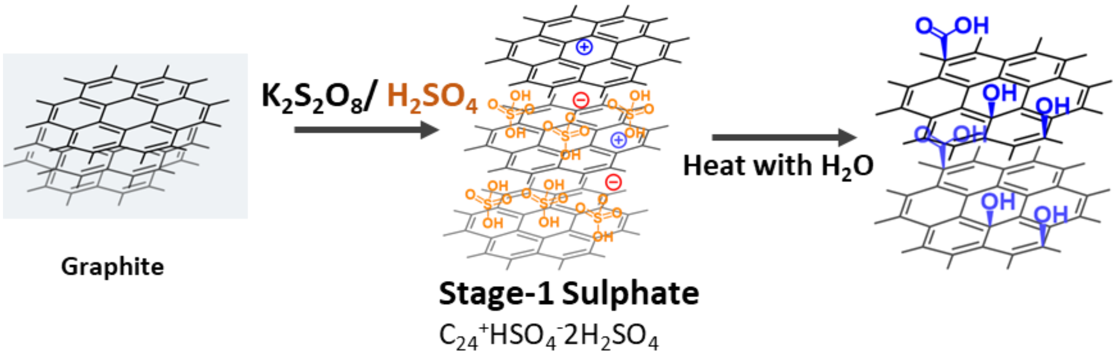

Scheme 4.1 synthetic route of oxidised graphene via nucleophilic attack of water to the sulphate GICs.

In this chapter, the oxidation reaction (Scheme 4.2), which is recognised as a by-reaction in the reaction between radical precursors and SGICs in the last chapter, will be studied. More specifically, the factors which influence the oxidation will be investigated and the conditions for partially oxidised graphene production will be optimised. The comprehensive study will shed light on the mechanism of the oxidation. Comparing to potassium permanganate and other traditional strong oxidants, $Mn(OAc)_3$ is milder, therefore it can be a promising reagent to achieve partial oxidation. In addition, the scheme is more efficient as compared to the nucleophilic reaction proposed by S.Eigler due to the presence of $Mn(OAc)_3$.

4.2 Results & Discussion

4.2.1 Factors Influencing the Partial Oxidation

4.2.1.1 Role of Sulphate GICs

The graphite intercalated compounds are favoured as the starting material for the functionalisation of graphene for two major reasons. The first reason is the charge transfer between graphene layer and the intercalated molecule will make the chemically inert graphite more reactive. In case of sulphate GICs, the intercalated sulphuric acid molecule will make the graphene layer more nucleophilic. On the other hand, it is found that less layered graphene is more reactive than more layered graphene according to the relevant studies. The intercalation process can be considered as a process which changes the chemically inert graphite to the more reactive graphene. The second major reason is the intercalated molecule will facilitate the exfoliation of graphite into graphene. Overall, it is expected that the GIC is more reactive than the pristine graphite.

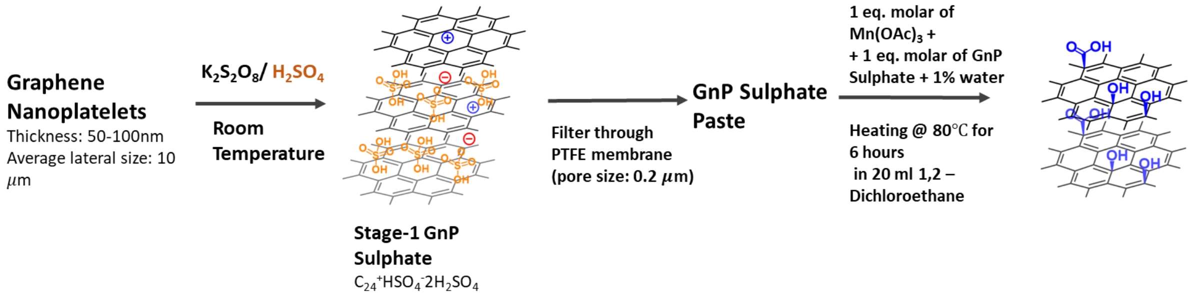

*Scheme 4.2 The synthetic route of partially oxidised graphene using **P40 GNP** as starting material.*

The partial oxidation (Scheme 4.2) was realised when a mixture of 1, 2-dichloroethane, sulphate GICs (1 equivalent mole), and manganese (III) acetate dihydrate (1 equivalent moles with respect to sulphuric acid in the SGICs) or anhydrous manganese acetate with 1% water was heated at 80 ℃ for 6 hours. The crude product was purified by diluted H_2O_2 and HCl solution washing. The purified and unseparated product is called **crude PO-G**. In the last chapter, we have also demonstrated that without intercalation, the pristine **P40 GNP** is less reactive towards the *in situ* generated aryl radicals. For confirmation of role of SGICs, oxidation reaction of pristine **P40 GNP** was conducted (using manganese (III) acetate dihydrate) and the product was analysed by SRS. The SRS results (Figure 4.1) shows marginal change in terms of I_D/I_G distribution. Like the outcome of the radical reaction, the pristine **P40 GNP** exhibited limited reactivity towards $Mn(OAc)_3$ even with heating. This result confirms the irreplaceable role of SGIC in oxidation again.

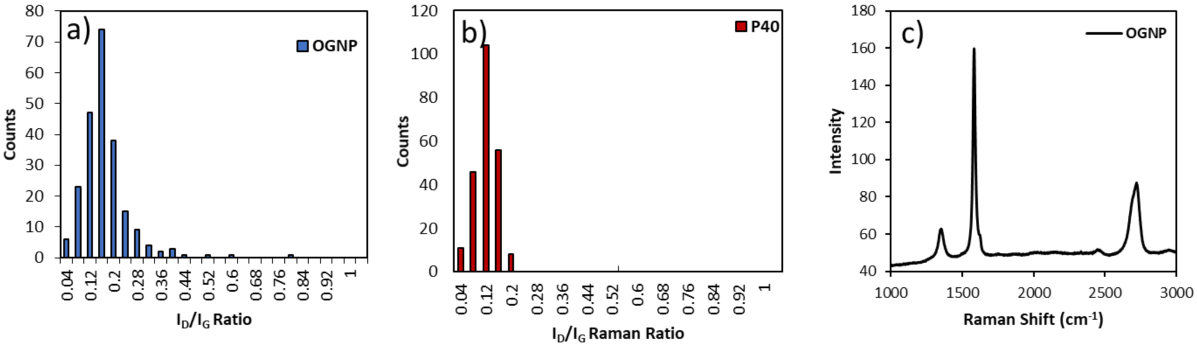

*Figure 4.1 I_D/I_G ratio histograms of the OGNP (a) (derived from reaction between P40 GNP and $Mn(OAc)_3$) and pristine **P40 GNP** (b); the average Raman spectrum of OGNP*

4.2.1.2 Role of Manganese triacetate

Since water can also react with sulphate GICs directly as other studies have suggested, and water was not excluded in this reaction, several control experiments had been conducted to demonstrate the origin of the oxidation was not due to the presence of moisture in atmosphere and reagents. Statistical Raman spectroscopy (SRS) was employed to characterise the corresponding products. The first control experiment was heating the sulphate GIC at 80 ℃ in 1,2 –dichloroethane without the addition of manganese (III) acetate dihydrate. As the average Raman spectrum (Figure 4.2 **G-2**) indicated, the stage-1 sulphate GIC had been converted to a mixture of stage-2 sulphate GIC and higher stage sulphate GIC after heating. This mixture was further washed with copious amounts of water and dried; the resulted sample was labelled **PO-WOM**. The Raman spectrum of the washed sample showed that there was almost no oxidation as the I_D/I_G ratio was essentially unchanged. This suggests the moisture from the solvent, sulphuric acid, and atmosphere during the reaction were not enough to cause the oxidation of the GNP. This also indicates that water as a potential nucleophile is not able to attack the carbocation in the sulphate GIC at room temperature.

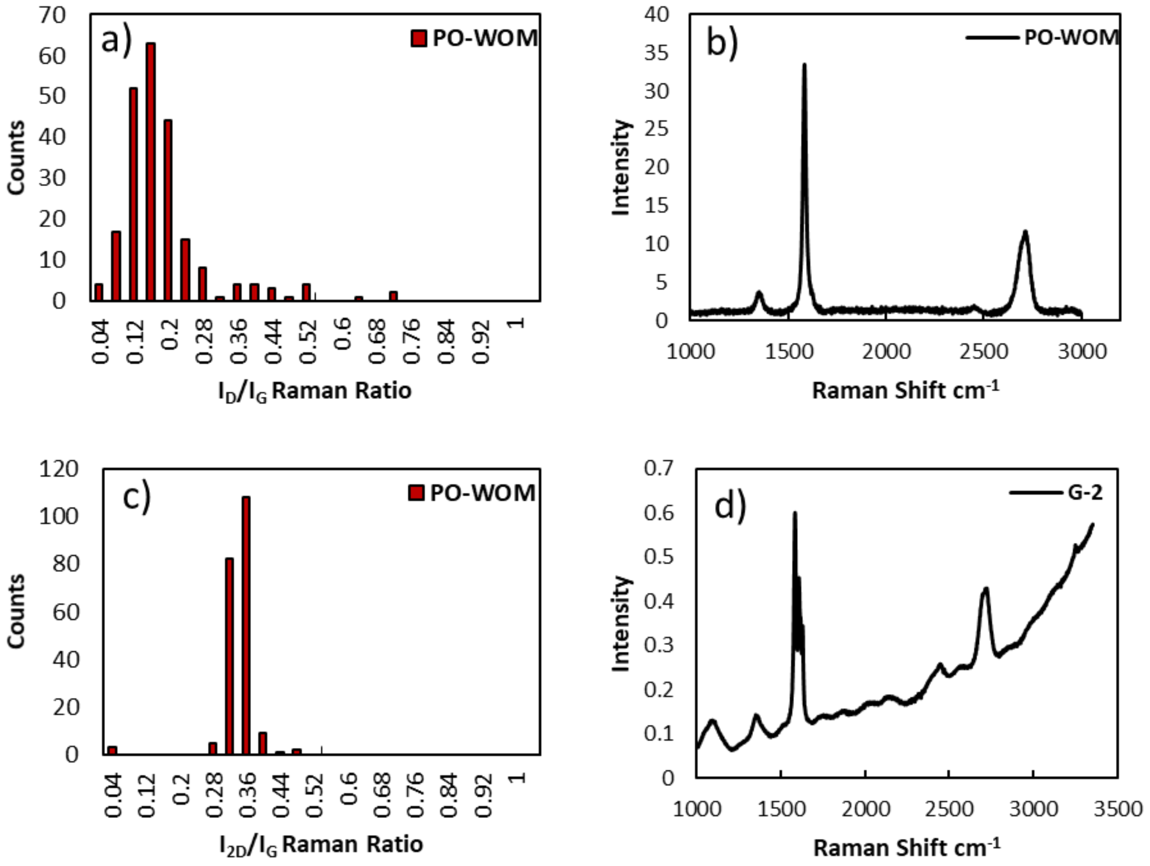

*Figure 4.2 I_D/I_G (a) and I_{2D}/I_G (c) Raman ratio histograms of GNP derived without using oxidant (**PO-WOM**). Raman spectrum of **PO-WOM** (b) and product (d) obtained immediately after heating without any purification (**G-2**).*

If the solvent was changed from 1, 2-dichloroethane to pure water, and the sulphate GIC was heated without the presence of manganese (III) acetate dihydrate, the product (**PO-W**) showed a change in the I_D/I_G ratio compared to that of pristine GNP after heating (Figure 4.3). Furthermore, this I_D/I_G value (0.46) was very close to the value of the **crude PO-G** (0.5) derived from the standard condition. This indicates water could react with the carbocation in the sulphate GICs to oxidise the GNP at 80 ℃, the oxidation degree was comparable to the reaction using manganese (III) acetate dihydrate.

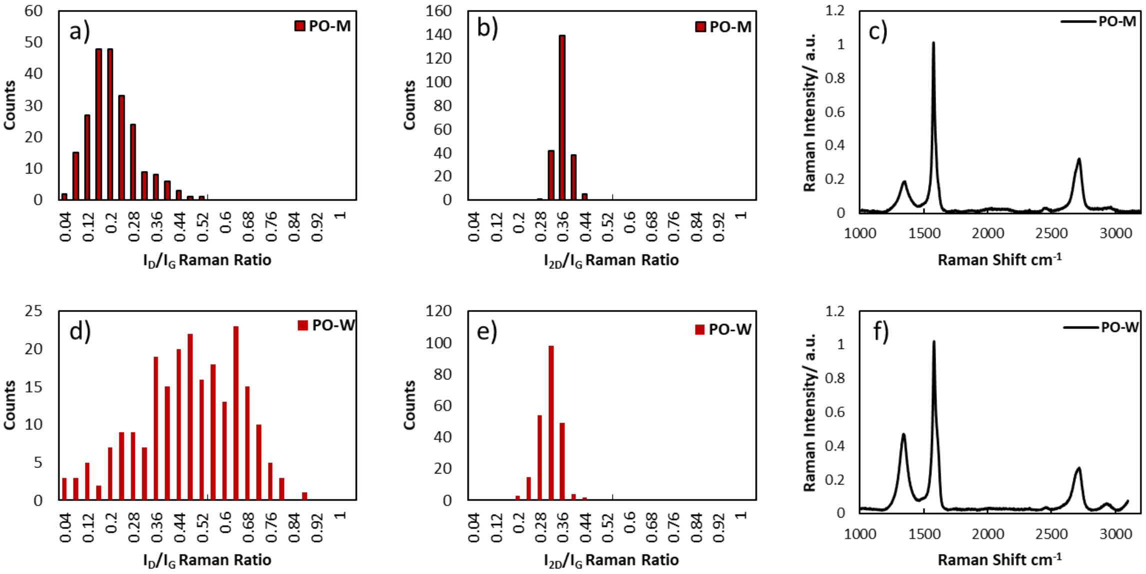

*Figure 4.3 I_D/I_G (a), I_{2D}/I_G (b) histograms, and average Raman spectrum of **PO-M;** I_D/I_G (d), I_{2D}/I_G (e) Raman ratio histograms and average Raman spectrum (f) for **PO-W**.*

Not surprisingly, with the presence of manganese (III) acetate dihydrate, after 6 hours heating at 80 ℃ in water, the product (**PO-M**), is less oxidised than the **crude PO-G (**Figure 4.3**)**. This result showed that manganese (III) acetate dihydrate is deactivated in the presence of large amounts of water, as manganese (III) acetate dihydrate is expected to disproportionate into Mn(II) and Mn(IV).[166]

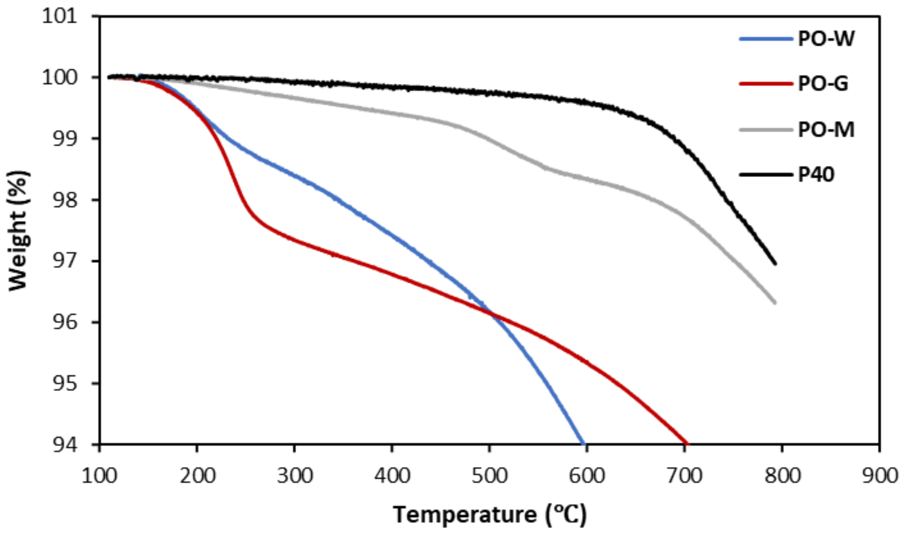

Figure 4.4 TGA of partially oxidised graphene which was derived from different conditions.

The TGA (Figure 4.4) of **PO-W** showed a very similar profile to that of **crude PO-G** and a significant difference to that of P40 GNP. This result was consistent with the high I_D/I_G ratio. However, it can be seen that the weight loss of **PO-W** (1 wt%) was less than that of **crude**

PO-G (2.5 wt%**)** in the temperature range of 200 to 300 ℃ and the weight loss of **crude PO-G** is sharper in the same temperature range indicating **crude PO-G** has more labile oxygen containing groups than **PO-W**. The **PO-W**, however, also undergoes sharp weight loss beyond 500 ℃. The reason that **PO-W** has bigger global weight loss might be the burning off from the residual SGICs. This is possible since most of the loss happens in the high temperature region. This also explained the better dispersibility of **crude PO-G** in water. On the other hand, **PO-M** showed a similar overall weight loss compared to that of pristine GNP before 800 ℃. This was consistent to its low I_D/I_G ratio. **PO-M** demonstrated an additional weight loss from 500 to 600 ℃, indicating **PO-M** may contain some residual SGIC.

Besides examining degree of functionalisation by statistical Raman spectroscopy and TGA, the dispersibility of all the products in water was examined by a white light optical camera. A 1 mg mL^{-1} dispersion in water of each sample was prepared (Figure 8.30). Only **crude PO-G** remained dispersible after 12.5 hours, which was probably expected due to its higher degree of functionalisation. Surprisingly, the **PO-W** sample, which had almost the same I_D/I_G as that of **crude PO-G**, performed badly in the dispersion test and a sediment was formed in 1 hour. The rest of samples— pristine **P40 GNP**, **PO-WOM**, and **PO-M** – their dispersions completely settled out in 3 hours. The results of the dispersibility test and TGA suggested that the high I_D/I_G value of **PO-W** probably arises from the small portion of oxidised graphene/GNP and residual SGIC in the mixture. The absorbance of the supernatant of **PO-W** was measured using UV-Vis spectroscopy, and the concentration of the supernatant was calculated based on a pre-determined extinction coefficient (ε=1105.6 L g^{-1} m^{-1}, for details please see section 7.1.4). The concentration of **PO-W** decreased from 1 mg mL^{-1} to 0.01 mg mL^{-1} , whereas the concentration of **crude PO-G** decreased to 0.65 mg mL^{-1} after 24 hours' standing. The result of different concentration reveals the difference in term of dispersible material.

In summary, it can be concluded that manganese (III) acetate dihydrate is a vital part of the partial oxidation, dispersible GNP can be prepared by its aid. The exclusion of manganese (III) acetate dihydrate will result in products with little degree of oxidation or no oxidation. On the other hand, the presence of excessive water would be detrimental to the process as manganese (III) cation would disproportionate in acidic aqueous solution. Despite the sulphate GIC can react with water, the resulted product is less functionalised and dispersible in water. And due to absence of oxidant, the resulted material might contain residual SGICs.

4.2.1.3 Role of Water in the Oxidation

From the Section 4.2.1.2, the SGIC can be oxidised by pure water with constant heating and the oxidation reaction mediated by $Mn(OAc)_3$ is quenched by excessive water. In this section, the dual role of water in this oxidation reaction is explored further by using anhydrous

Mn(OAc)$_3$ to reduce the possible water source during the reaction. The water content in SGIC is controlled by using the prepared SGIC immediately to avoid further absorption of water. The reactions were carried out by adding water (0%, 1%, 2%, and 6% respect to volume of 1,2 DCE) to the reaction mixture. The crude product for each reaction was analysed by SRS, TGA, and dispersibility monitoring.

The SRS results (Figure 4.5) show that **crude PO-G** derived from 1% water addition exhibited the most level of functionalisation for wider distribution of I_D/I_G ratio and highest average I_D/I_G ratio (0.5). Sample derived from 2% water showed some extent of functionalisation. While samples derived from 0% water and 6% water demonstrated the narrowest I_D/I_G distribution and lowest average I_D/I_G ratio which is comparable to that of pristine P40 GNP. The video dispersibility monitoring indicates dispersible material can be produced by addition of 1% and 2% water, whereas addition of no water or excessive water would lead to formation of non-dispersible material with low level of functionalisation.

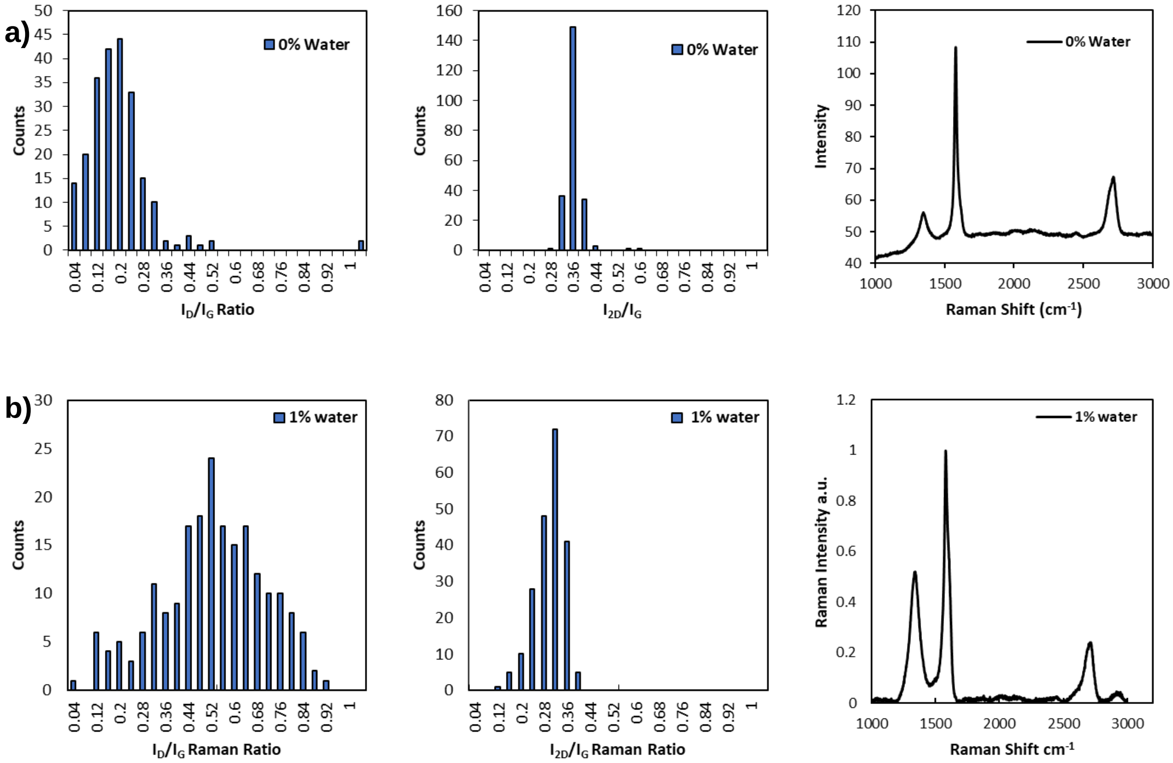

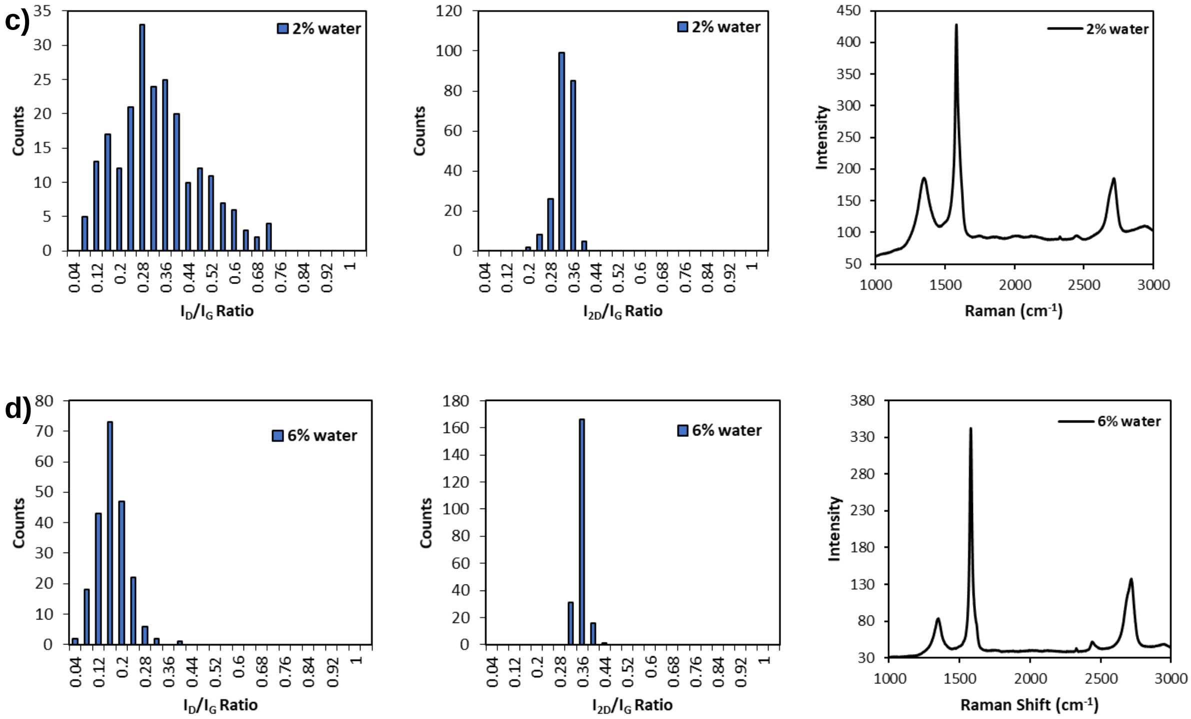

Figure 4.5 I_D/I_G, I_{2D}/I_G histograms, and average Raman spectrum of partially oxidised GNP derived by addition of 0% (a), 1% (b), 2% (c), and 6% (d) of water.

From the TGA profile (Figure 4.6), sample with 1% and 2% water both demonstrates similar and sharp mass loss at 220 ℃, the mass loss in this region represents the thermal cleavage of oxygenated functionalities from the graphene skeleton. In contrast, even less weight losses are identified for the samples with 0% and 6% water, this means less functionalisation have been achieved for these samples. The inconsistency arises when the TGA profile is considered alongside with the SRS results for sample derived from 2% water, higher average and distribution of I_D/I_G ratio should be expected. The origin of the inconsistency could be release of the intercalated water molecules in between the GNP layers at elevated temperature. Nonetheless, the results of partially oxidised graphene derived from 0% water may suggest the synergic action of water and oxidant for the functionalisation. In case of abundant water (6% water), a threshold concentration of water exists for the reaction, as below that concentration the generated hydroxyl radicals may react with the graphene, above that concentration it may be detrimental to the oxidants.

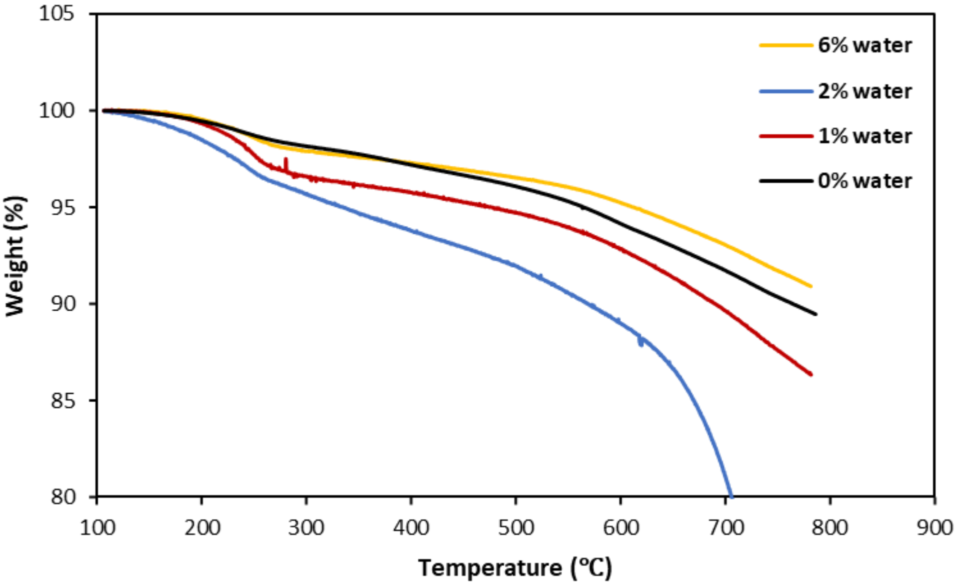

Figure 4.6 TGA of the crude partially oxidised graphene which were produced by using different amount of water.

4.2.1.4 Optimisation of Partially Oxidation Conditions

The optimal condition for partial oxidation was obtained by comparing the average I_D/I_G ratio and the results of video dispersibility test for **crude PO-G** deriving from different conditions. The tested conditions and the corresponding outcomes were summarised in the table below (Table 3.5). It can be seen using less $Mn(OAc)_3 \cdot 2H_2O$ would lead to formation of product with low level of functionalisation and unstable dispersion which would sediment quickly in water. Conducting reaction at lower temperature produced material with similar dispersibility as materials derived from using less oxidant, however the product exhibited higher average I_D/I_G ratio. This contradictory observation could indicate the formation of some non-dispersible product or intermediate at lower temperature. Shortening the length of the reaction will result in non-dispersible product with low I_D/I_G ratio. Doubling the oxidation length will not influence the outcome of the reaction, whereas tripling the oxidation length will result in non-dispersible material. Afterall, oxidation of 6 hours, using of equimolar oxidant $Mn(OAc)_3 \cdot 2H_2O$, addition of 1-2 vol% water (when anhydrous $Mn(OAc)_3$ is used), and heating at 80 ℃ construct the optimal condition for the partial oxidation.

Table 4.1 The average I_D/I_G ratio and video dispersibility outcomes of ***crude PO-G*** *deriving from different conditions. The dispersibility test video can be found in the appendix in chapter 8.*

Conditions	Average I_D/I_G ratio	Results of Dispersibility Test
Molar Ratio of (H_2SO_4: $Mn(OAc)_3 \cdot 2H_2O$)		
2:1	0.17	Sediment quickly
4:1	0.19	Sediment quickly
Temperature		
60 ℃	0.41	Sediment quickly
40 ℃	0.44	Sediment quickly
Time		
3 hours	0.46	Sediment quickly
12 hours	0.42	Stable
18 hours	0.4	Sediment quickly
Water content		
0 vol%	0.17	Sediment quickly
1 vol%	0.5	Stable
2 vol%	0.32	Stable
6 vol%	0.16	Sediment quickly

4.2.2 Proposed Mechanism of the Partial Oxidation

Several key pre-requisites were identified for the process from the results of the controlled experiments in the past sections, which are fundamental to outline the picture of the mechanism for the oxidation.

1. The oxidant anhydrous $Mn(OAc)_3$ cannot oxidise the graphene without sufficient water during the reaction.
2. The oxidation would be compromised (around 2%) or stopped if excessive water (≥ 6 vol%) is present.
3. The oxidation can be quenched by the addition of radical trapper (TEMPO).
4. The oxidation cannot proceed without presence of the intercalated sulphuric acid.

Given that the $Mn(OAc)_3$ normally generates radical species by single electron transfer according to studies, the rough oxidation mechanism of the process could be the generation of hydroxyl or other radical from the electron transfer of manganese (III). The generated hydroxyl or other radicals can react with the carbocation activated by the intercalated sulphuric acid and lead to formation of oxidised graphene.

4.2.3 Separation of the Crude Product from Partial Oxidation

4.2.3.1 Centrifuge without Probe-sonication

Variations in the size and flakes of the graphene material could lead to non-ideal behaviour and limit its performance in the consequent applications. [167] Therefore, the partially oxidised graphene was subjected to separation study so that thinner partially oxidised graphene with more homogenous dimensions can be obtained.

The purified **crude PO-G** has complex composition in terms of size, layers, and degree of functionalisation. This is supported by its I_D/I_G histogram (Figure 4.7), where the low I_D/I_G region showed the sign of unreacted GNP. From the plot of *Pos* (2D) and I_{2D}/I_G ratio, shift of position of 2D band to lower wavenumber can be noticed after the reaction (Figure 4.7). This implies the exfoliation has happened during the oxidation. The functionalisation and exfoliation of the GNP is further supported by the observations from XRD (Figure 4.8), where the intensity of (002) peak at 26.7 ° has decreased significantly and another broad peak (10-14°) appears. AFM study of the **crude PO-G** shows that the oxidation reaction has resulted in flakes with a range of sizes from several microns to sub-microns. The distribution of thickness is wide too as both unexfoliated and exfoliated GNP can be identified. And the exfoliation effect of the oxidation reaction can be spotted too due to the appearance of incompletely exfoliated GNP (Figure 4.9). Those results are consistent with the results from SRS and XRD study.

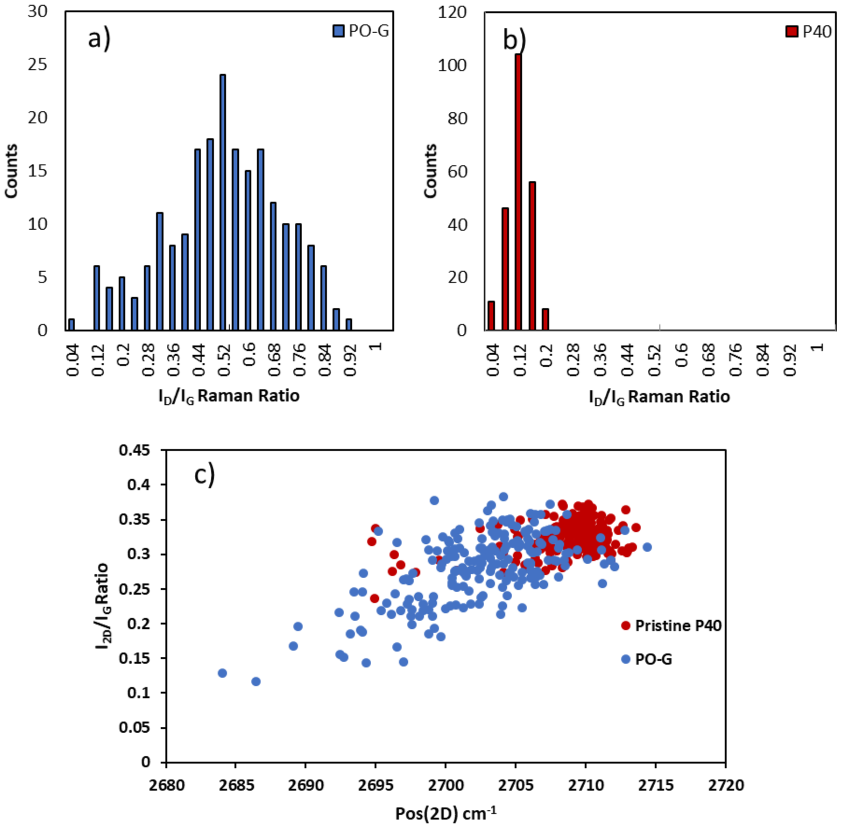

*Figure 4.7 I_D/I_G histograms of **crude PO-G** (a) and **P40 GNP** (b). (c) I_{2D}/I_G ratio and 2D position plot of **P40 GNP** and crude **PO-G**.*

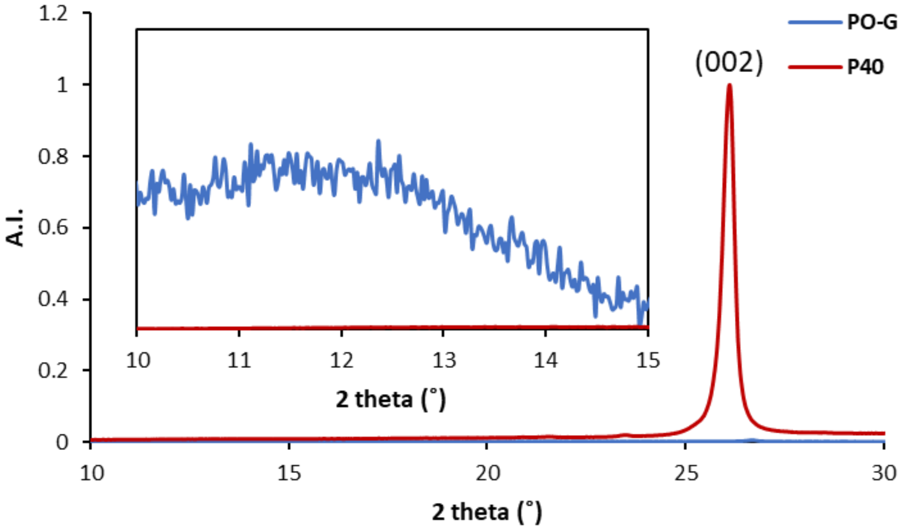

*Figure 4.8 Powder XRD of **P40 GNP** and **PO-G**. All peaks are normalised to **P40 GNP**. Inset: XRD pattern between 10-15°. Cu Kα1 X-ray source (λ = 1.5406 Å)*

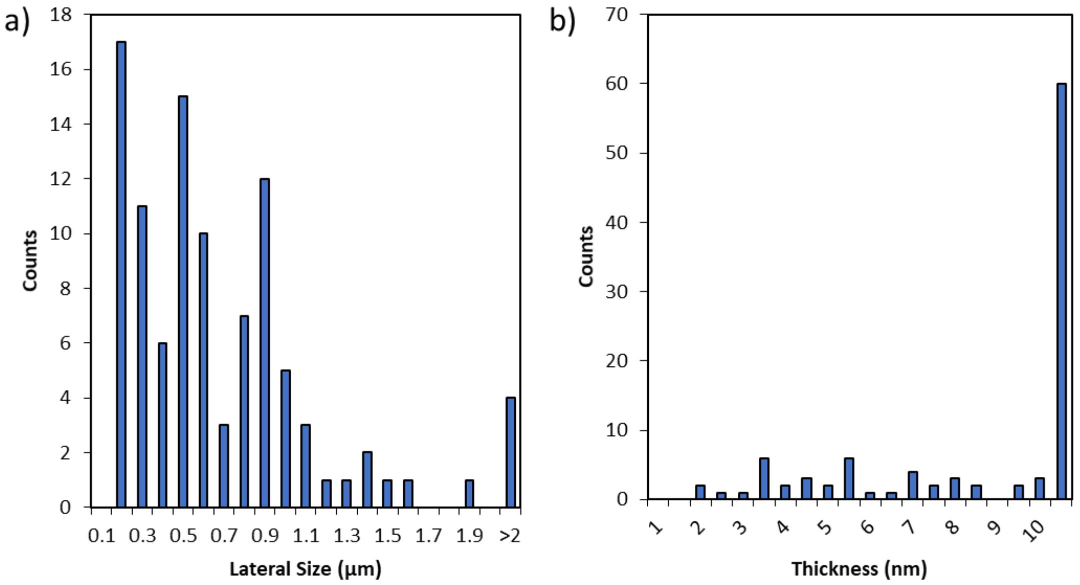

*Figure 4.9 Histograms show the distribution of lateral size (a) and thickness (b) for **crude PO-G**.*

To separate the mixture, 300 rpm centrifugation was applied to the **crude PO-G**. The separated materials were analysed by SRS and TEM. After centrifugation at 300 rpm (11 rcf), the **crude PO-G** were separated into two parts, the sediment was called **300 Sed**, the stable dispersion was called **300 Dis**, both parts were filtered and dried before any analysis. According to the SRS (Figure 4.11), I_D/I_G of **300 Dis** was higher than that of **300 Sed**, which indicates that the **300 Dis** was more functionalised than the **300 Sed**. The I_D/I_G histogram of **300 Dis** also revealed that the heterogeneity still existed in the sample as material with low I_D/I_G value was identified which is the same as the **crude PO-G**. This suggests the composition of the **300 Dis** remains similar after the separation and a higher centrifugal force was required for achieving a more homogenous separation. By comparing the TEM images (Figure 4.12 & Figure 4.13) of **300 Sed** and **300 Dis**, it is shown that the **300 Dis** sample is generally smaller and thinner. Two products were characterised by the Powder XRD (Figure 4.10). As expected, intensity of (002) peak of **300 Dis** is reduced significantly and broad peak appears at 10-14 ° due to exfoliation, whereas **300 Sed** exhibits strong (002) peak, which represents the presence of graphite. The XRD results are in accordance with TEM and SRS study. Consistent results can be obtained from AFM images of **crude PO-G** (Figure 4.14), as exfoliated thin layer material and multilayer material can be spotted. Finally, the dispersibility test of **300 Dis** in water demonstrated at least 12 hours stability, which is comparable to the stability before the separation, whereas the stability of **300 Sed** sample in water was less than 2 hours.

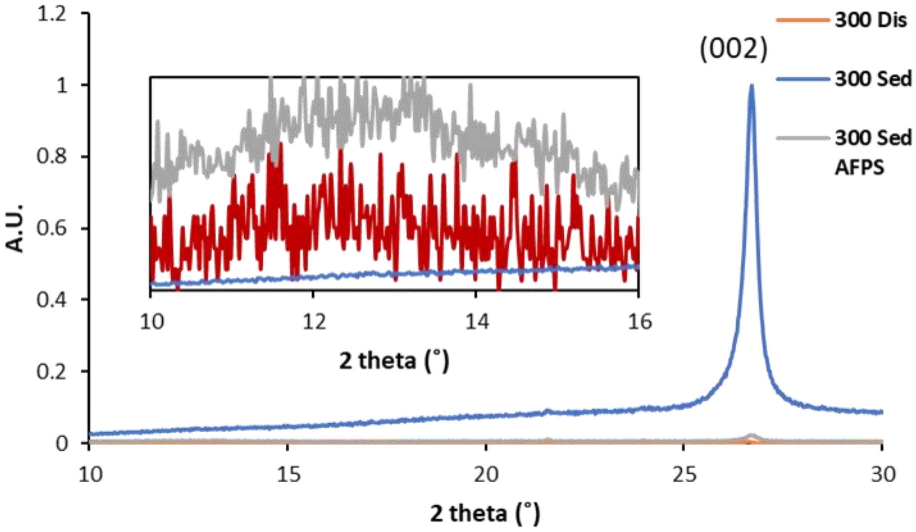

Figure 4.10 XRD pattern of PO-G underwent different processing, all peaks are normalised respect to 300 SeD. Inset: normalised XRD pattern from 10-15°. Cu Kα1 X-ray source (λ = 1.5406 Å)

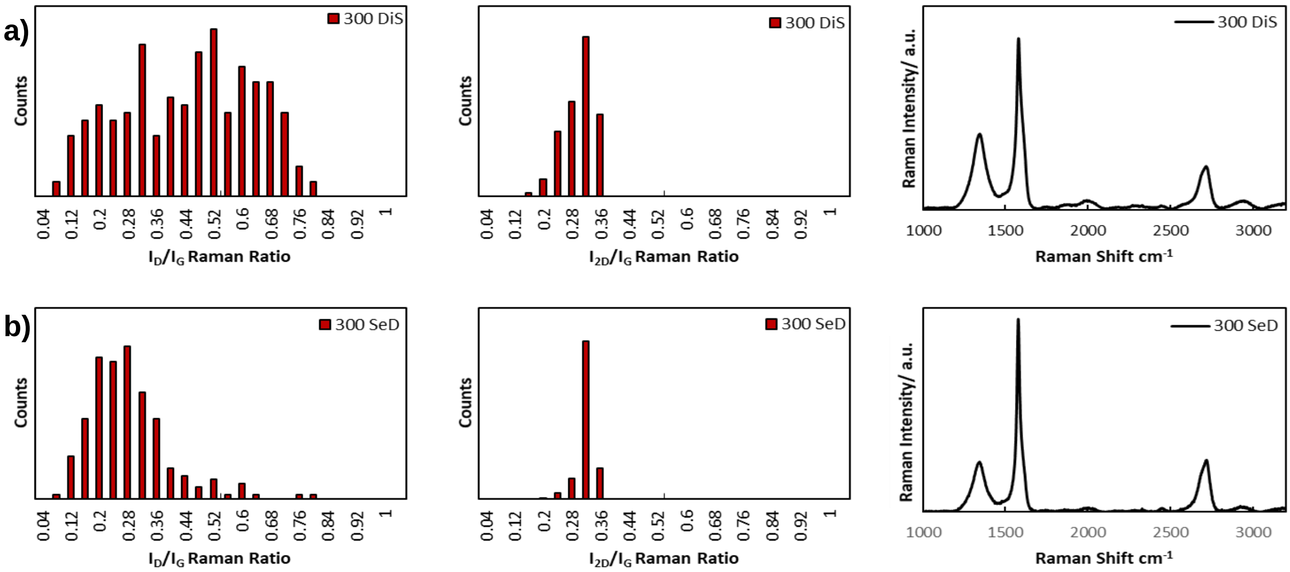

Figure 4.11 I_D/I_G, I_{2D}/I_G histograms, and average Raman spectrum of the supernatant (a) and the sediment (b) separated by 300 rpm centrifugation.

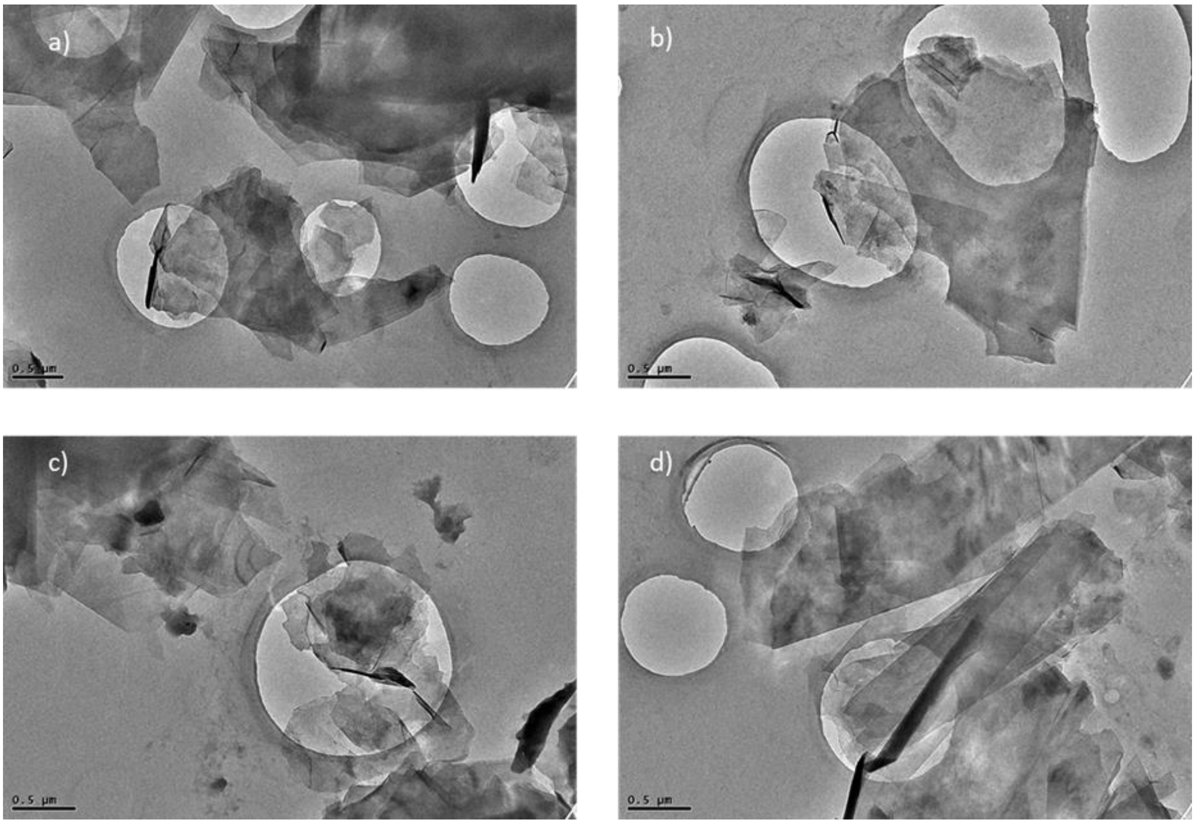

Figure 4.12 TEM images showing flakes (a), (b), (c), and (d) 0f ***300 Dis*** *sample.*

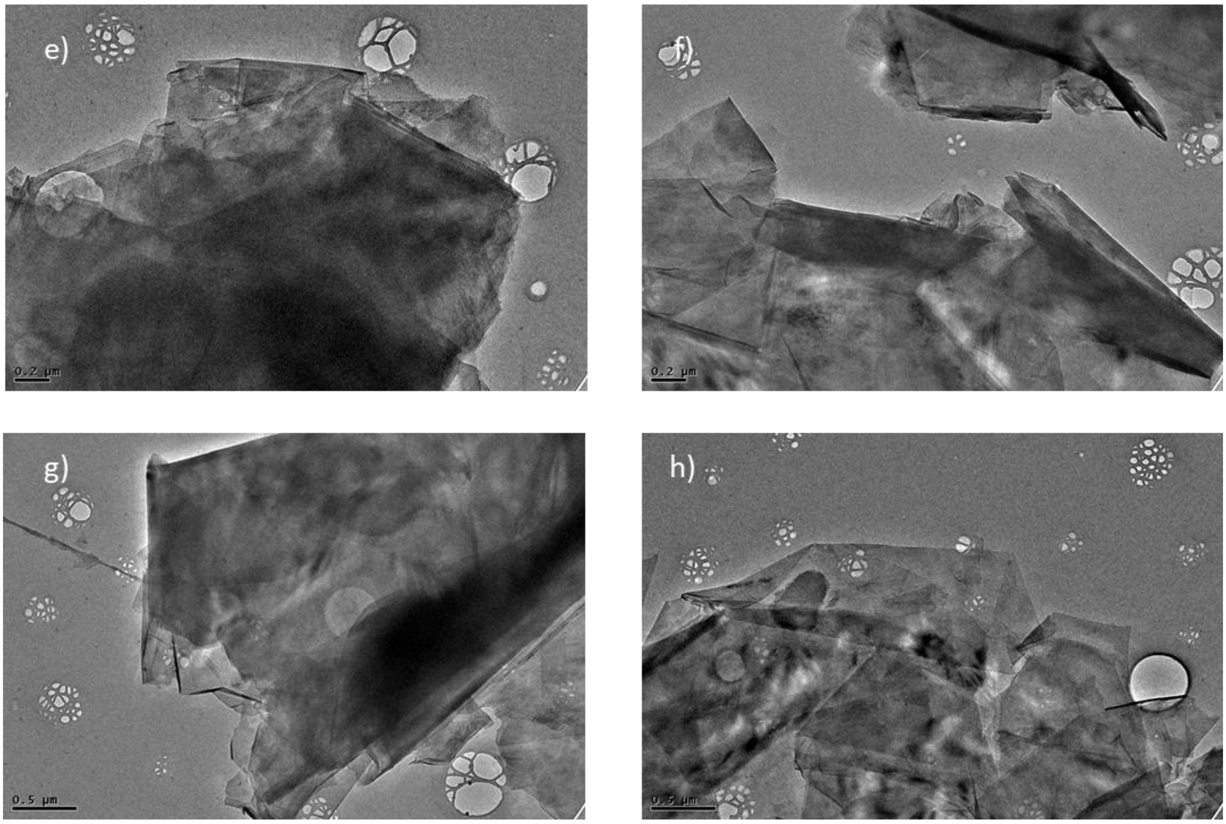

Figure 4.13 TEM images of thick GNP (a), (b), (c), and (d) from ***300 Sed*** *sample.*

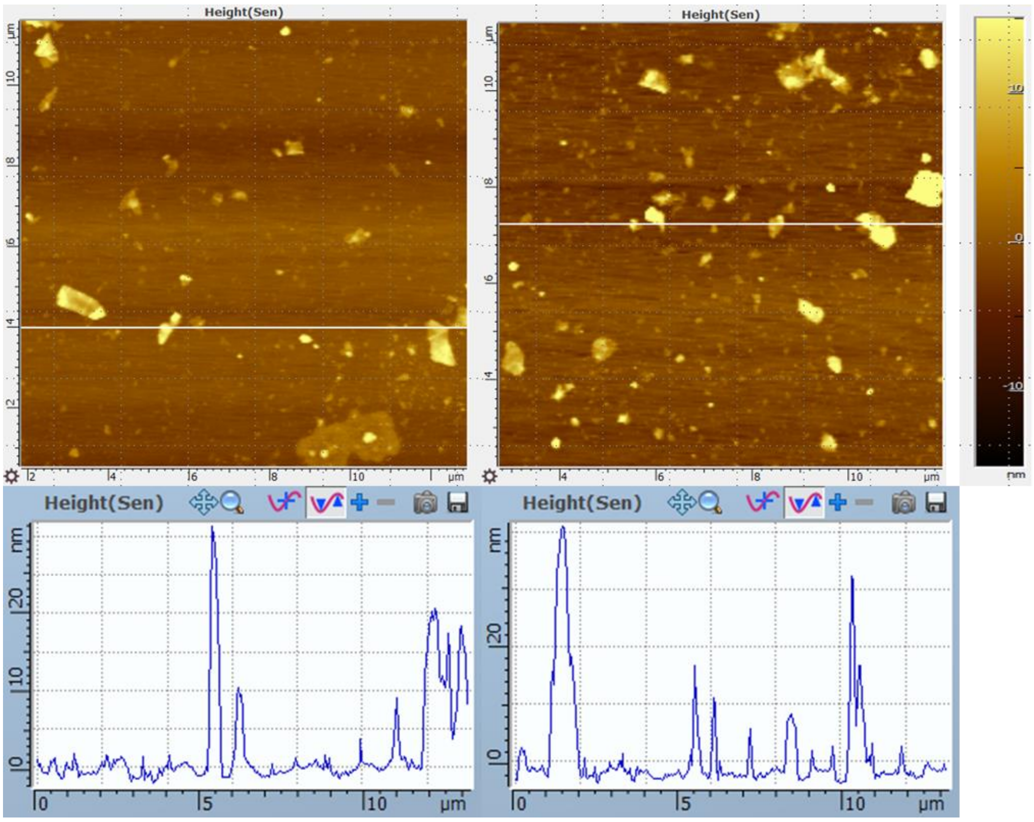

Figure 4.14 AFM images and height profiles of the ***crude PO-G*** *separated with 300 rpm centrifugation (****300 Dis****).*

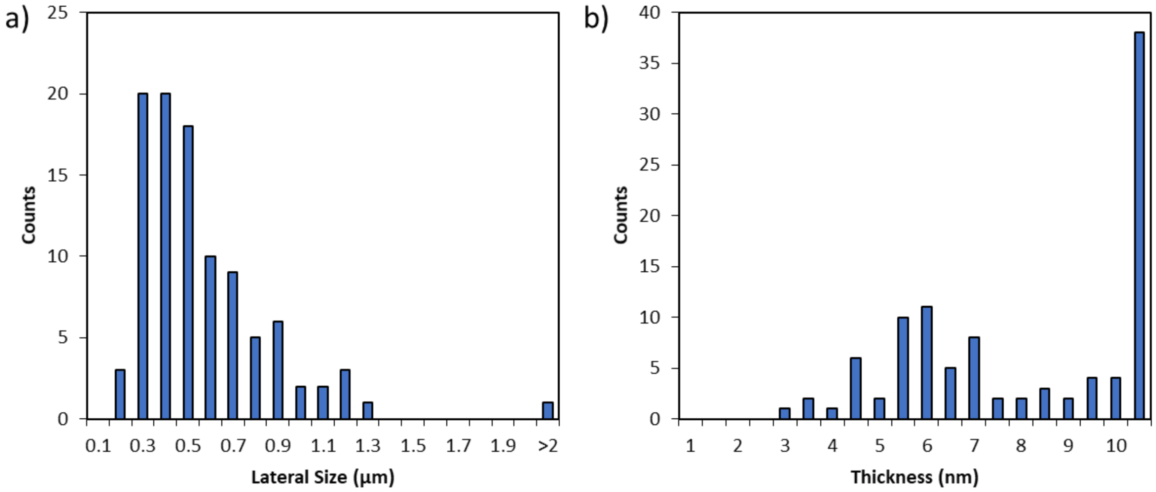

*Figure 4.15 Lateral size (a) and thickness (b) histograms of **300 Dis** sample.*

Overall, the **crude PO-G** was composed of various size and thickness, the average thickness is 18.2 nm and the average size is 0.66 μm. The uniformity of the material was improved significantly after being processed by 300 rpm centrifuge though big dimensions variation remained, as the average thickness was changed from 18.2 to 9.1 nm and the average size was changed marginally from 0.66 to 0.64 μm (Figure 4.15). The difference between the P10 and P90 Δ_{ls} of the thickness reduced from 37.4 nm (**Crude PO-G**) to 12.5 nm (**300 Dis**); the P10 and P90 difference of the lateral size was reduced from 0.97 to 0.4 μm. This suggested that some of the thick and large flakes were removed by the centrifuge (Table 4.3 & Table 4.4). Overall, the results above have shown that a mild separation process can be used to remove part of the unreacted and thick GNP from the **crude PO-G**, however, some of those flakes persisted after the separation. The height and size distributions also indicate the exfoliation extent of the reaction is restricted, and this problem might be originated from heterogenous nature of the reaction. To get better degree of exfoliation, the **crude PO-G** was subjected to probe-sonication.

4.2.3.2 Probe-sonication and Centrifuge

Interestingly, the probe sonication is found to be effective to convert the sediment sample during the separation to the exfoliated sample. As the **300 Sed** was re-dispersed into water, the dispersion was probe-sonicated in ice bath for 0.5 hour. The resulted dispersion was filtered, dried, and labelled as **300 Sed AFPS**. The powder was analysed by SRS, AFM, and TEM. The I_D/I_G histogram of **300 Sed AFPS** revealed there was an apparent shift of the I_D/I_G distribution to higher value (0.26 to 0.57) after probe sonication (Figure 4.17). At the same time, the I_{2D}/I_G ratios reduction (0.3 to 0.23) and small red shift of 2D band position (2707 cm^{-1} to 2706 cm^{-1}) are observed. These can be interpreted as the probe sonication had smashed the bigger and thicker flakes into smaller and thinner flakes. In AFM, except the big and thick flakes (Figure 4.18) which survive through the sonication process, small thin flakes can also be found (Figure 4.19). Moreover, flakes with expanded layered structure can also be spotted, the existence of those flakes suggests the exfoliation effect of sonication (Figure 4.18). The TEM images of **300 Sed AFPS** show that the size and thickness of graphite flake decrease comparing to those of **300 Sed** after the probe sonication (Figure 4.20). Sign of exfoliation has also been noticed by comparing the XRD pattern of the two samples. New peak appears at 10-15 ° after the probe-sonication, which indicates the increase of interlayer distance of the GNP; whereas **300 Sed** exhibits no such peak (Figure 4.10). A dispersibility test was set up for the **300 Sed AFPS** sample. The stability of **300 Sed AFPS** water dispersion was better than that of **300 Sed** and comparable to that of the **crude PO-G**. In short, the bigger, less functionalised, and non-dispersible material can be converted into dispersible material by probe sonication.

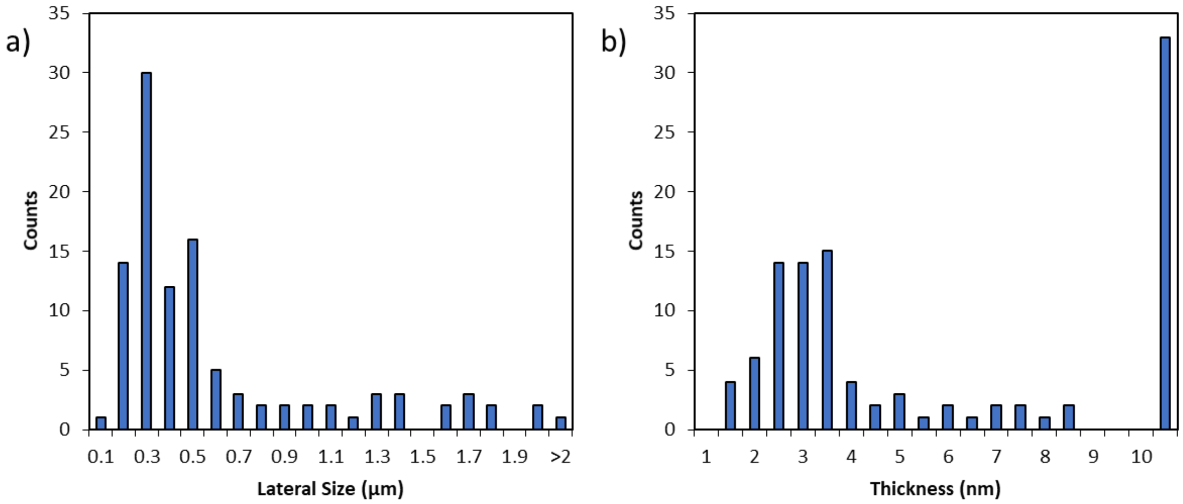

*Figure 4.16 Lateral size (a) and thickness (b) histograms of **300 SeD AFPS sample**.*

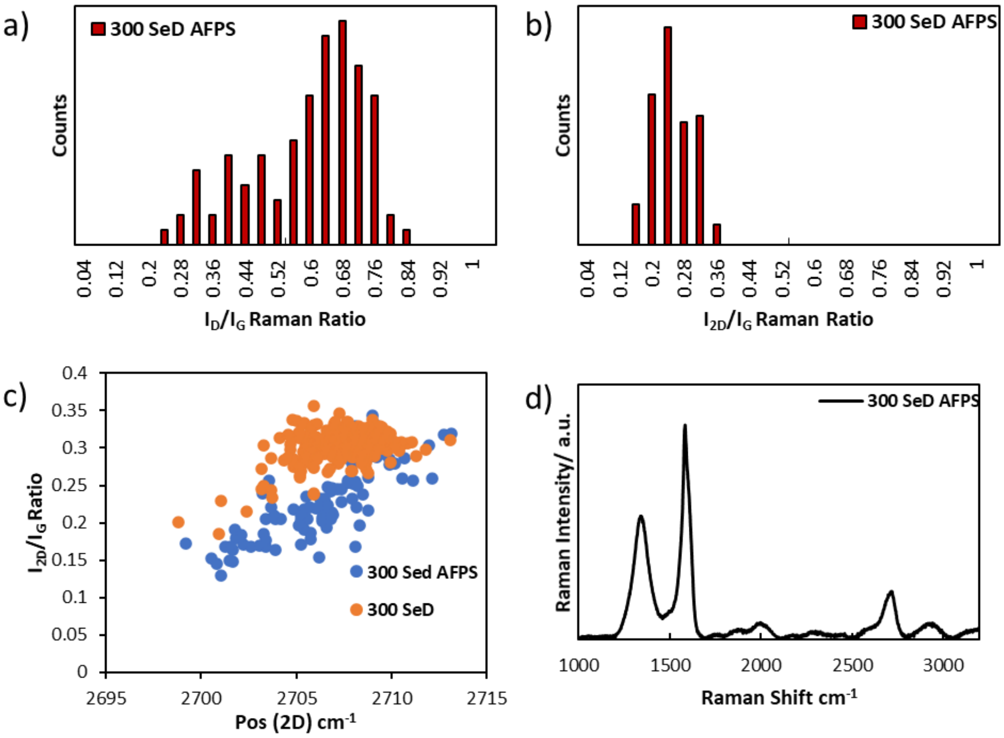

*Figure 4.17 I_D/I_G (a), I_{2D}/I_G (b) histograms , I_{2D}/I_G ratio vs 2D position plot (c), and average Raman spectrum (d) of **300 Sed AFPS**.*

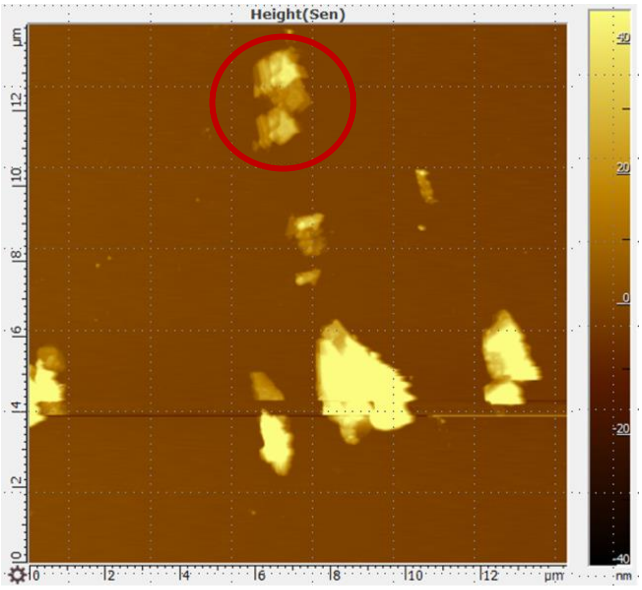

*Figure 4.18 AFM images of intermediate exfoliated flakes from **300 Sed AFPS**. The expansion of interlayer spacing of the flakes along c-axis can be seen, which is indicated by red circle.*

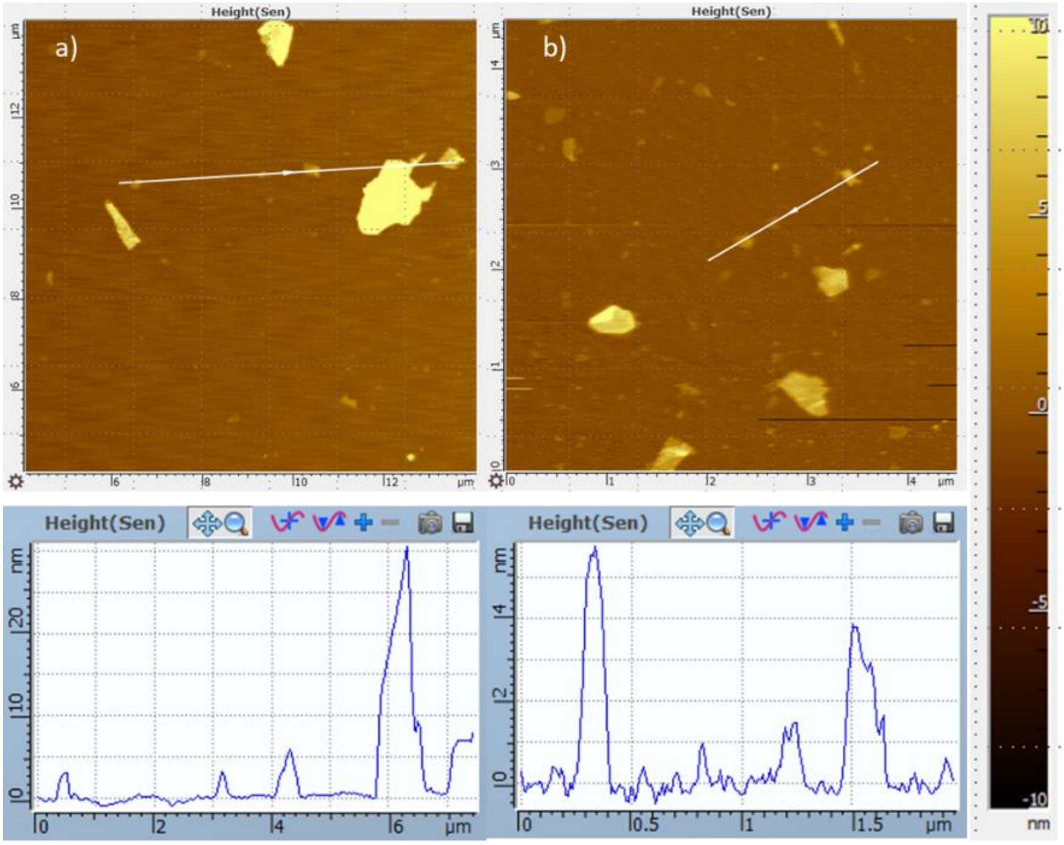

Figure 4.19 AFM images and height profiles of thick flakes (a) and exfoliated flakes (b) from ***300 Sed AFPS***

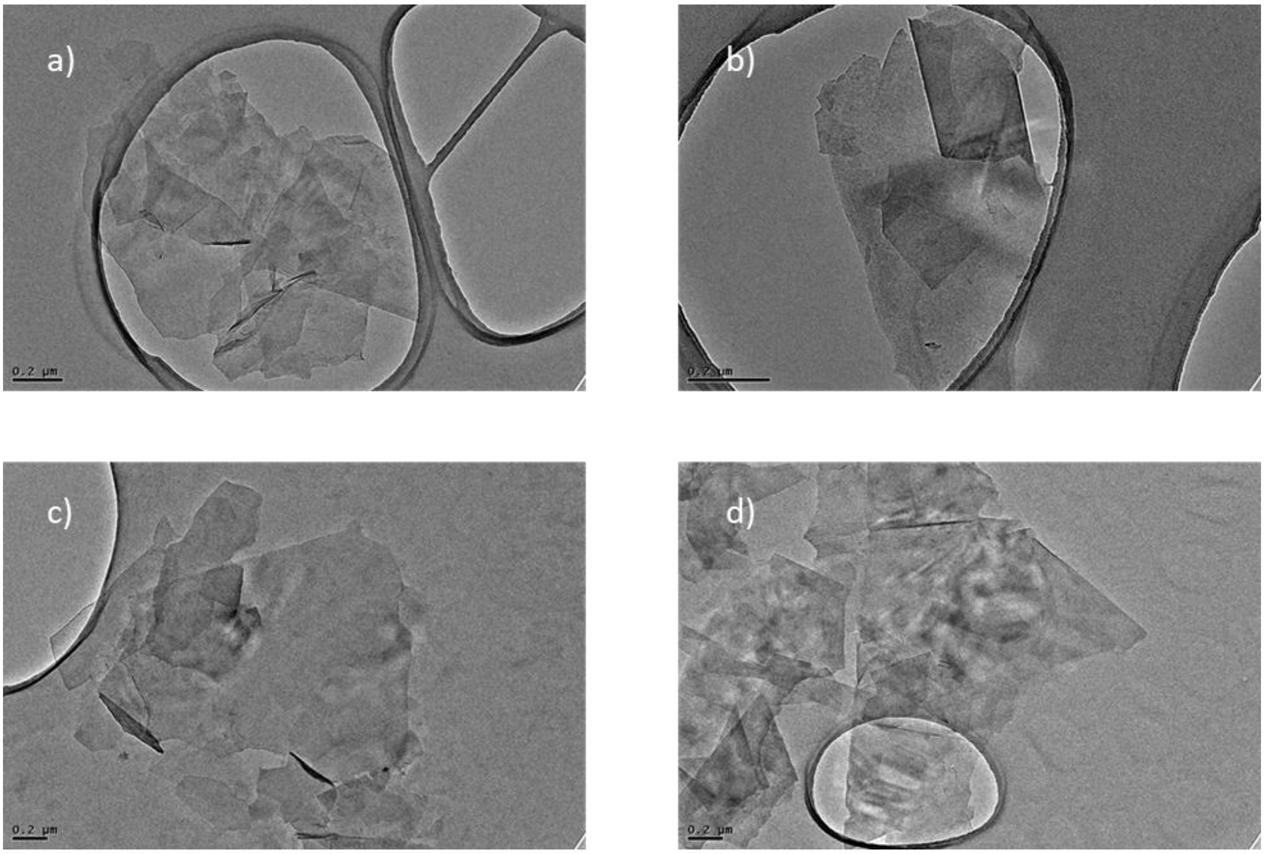

Figure 4.20 TEM images of flakes from ***300 Sed AFPS****.*

As more exfoliated material can be obtained by probe-sonication, the **crude PO-G** was probe-sonicated at 250 W and 33% amplitude for 30 minutes. The sonicated sample was centrifuged at 700 rpm to remove the thick and unfunctionalised GNP. The supernatant was collected by filtration and dried for further characterisation by SRS, TEM, AFM, and TGA. The **crude PO-G** separated by this approach is called **700 Dis**. The I_D/I_G histogram of the **700 Dis** has a narrow distribution at high I_D/I_G region (Figure 4.22). The absence of low I_D/I_G region (0-0.2) indicates the successful removal of the unreacted and less oxidised material. The 2D position of **700 Dis** was plotted against I_{2D}/I_G ratio to check the thickness of the sample. As the plot shows, a significant shift of position of 2D band is observed with reduction of I_{2D}/I_G ratio comparing to that of **P40 GNP**. The red shift of 2D position (from 2709 cm^{-1} to 2694 cm^{-1}) is indicative of production of thinner graphene. The decrease of I_{2D}/I_G ratio represents high level of functionalisation. However, *Pos* (2D) would become tentative to determine the thickness of the functionalised material as 2D band would deform due with increasing level of functionalisation. Therefore, TEM and AFM were adapted to confirm the size and structure of **700 Dis**. The TEM images (Figure 4.24) show the sample after centrifugation possesses smaller size and fewer layers, and the flake structure has been retained after the oxidation. The effect of probe-sonication is revealed by characterising **700 Dis** via AFM (Figure 4.26). Thicker graphene flake with incomplete broken flake structure is indicative of samples with incomplete exfoliation after probe-sonication. Monolayer, bilayer, and few-layer graphene, which are rarely found in **300 Dis** sample with various lateral sizes can be identified with AFM scanning (Figure 4.25). Histograms (Figure 4.21) were constructed to show the distribution of the lateral size and thickness for **700 Dis**. The results show the thickness of **700 Dis** is more homogeneous, whereas the distribution of size is still widespread. The percentiles were calculated to analyse the distribution of the flakes more quantitatively (Table 4.3 & Table 4.4). The average thickness was 4 nm and the average size was 1.0 μm. Most importantly, the uniformity of the thickness of the **PO-G 700 Dis** is enhanced significantly, as the gap between the 10th percentile and the 90th percentile is only 5.2 nm. The uniformity of the lateral size had not been changed too much as compared to that of **crude PO-G**. In perfect accordance with the result of TEM, sub-micron flakes were also found, and majority of those flakes were bilayer graphene and few-layer graphene. The dispersibility of this highly functionalised and exfoliated sample was monitored by camera and its dispersion exhibits extraordinary stability in water over at least 25 hours (Figure 8.35). Informal eye inspection indicated the stability can be over 1 month.

Here, it is also interesting to notice the stabilising effect of the more dispersible flakes sample. The AFM images gives visual evidence on this stabilising effect, where 0.2 μm few-layer (2-4 nm) flakes carry the big (>2 μm) and thick (50-100 nm) flakes (Figure 4.23). The more dispersible flakes act as surfactant through π-π interaction to make big flakes more dispersible in the water.

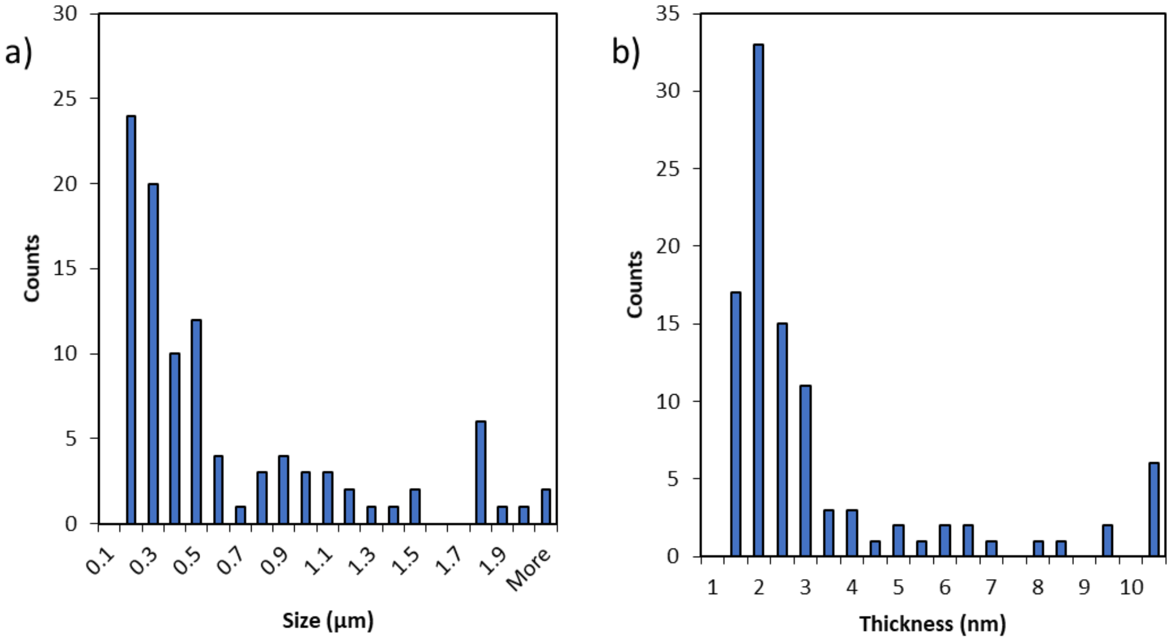

*Figure 4.21 Lateral size (a) and thickness (b) histograms of **PO-G 700 Dis sample**.*

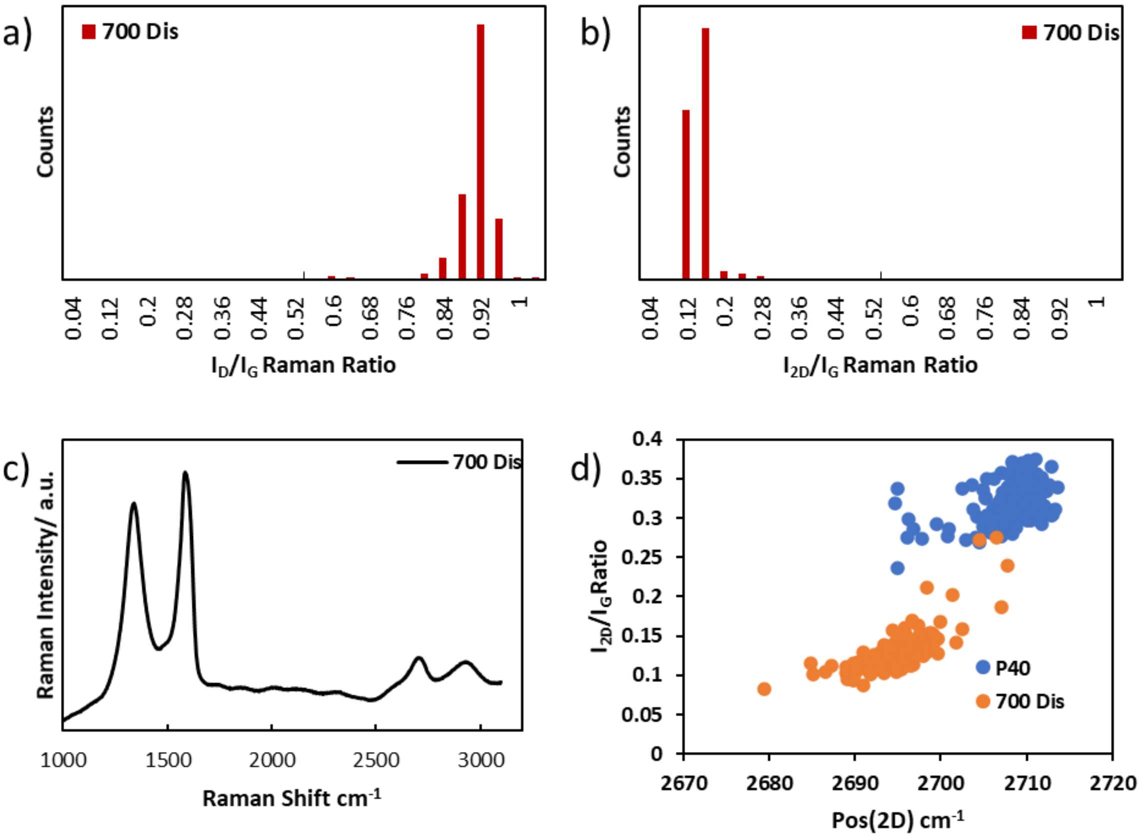

*Figure 4.22 I_D/I_G (a), I_{2D}/I_G (b) histograms, and average Raman spectrum (c) of sample processed by probe-sonication and 700 rpm centrifugation (**PO-G 700 Dis**). I_{2D}/I_G ratio vs 2D position plot (c) of **PO-G 700 Dis** and pristine **P40 GNP**.*

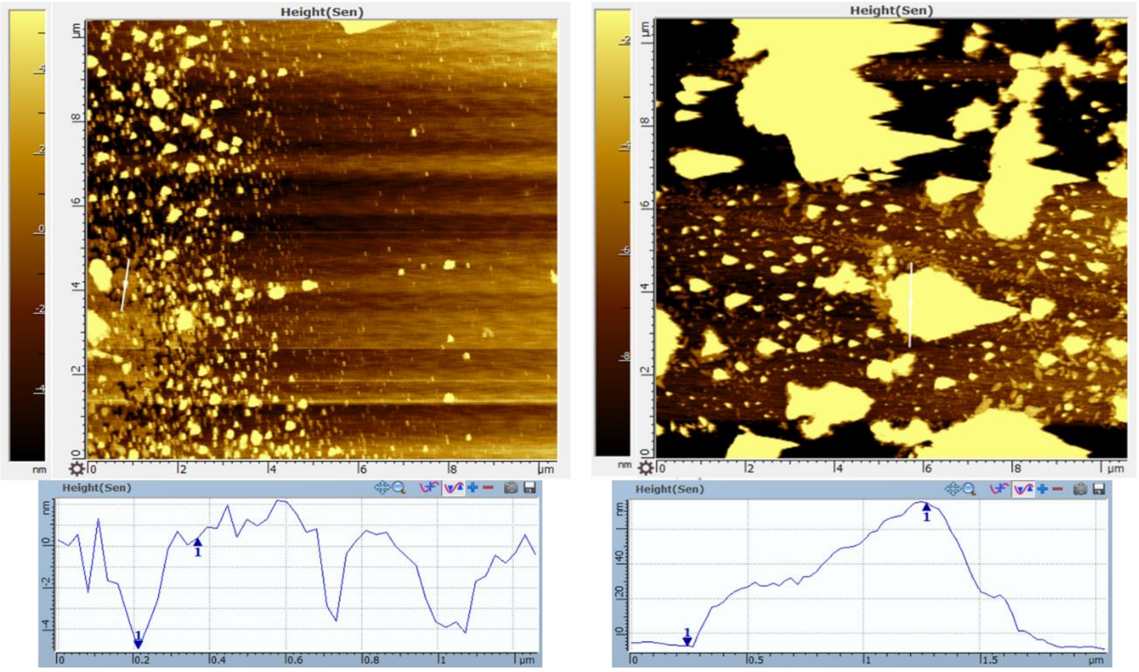

*Figure 4.23 AFM images of graphene flakes in **PO-G 700 Dis**, where the small and thin flakes act as surfactant to carry the big and thick flakes.*

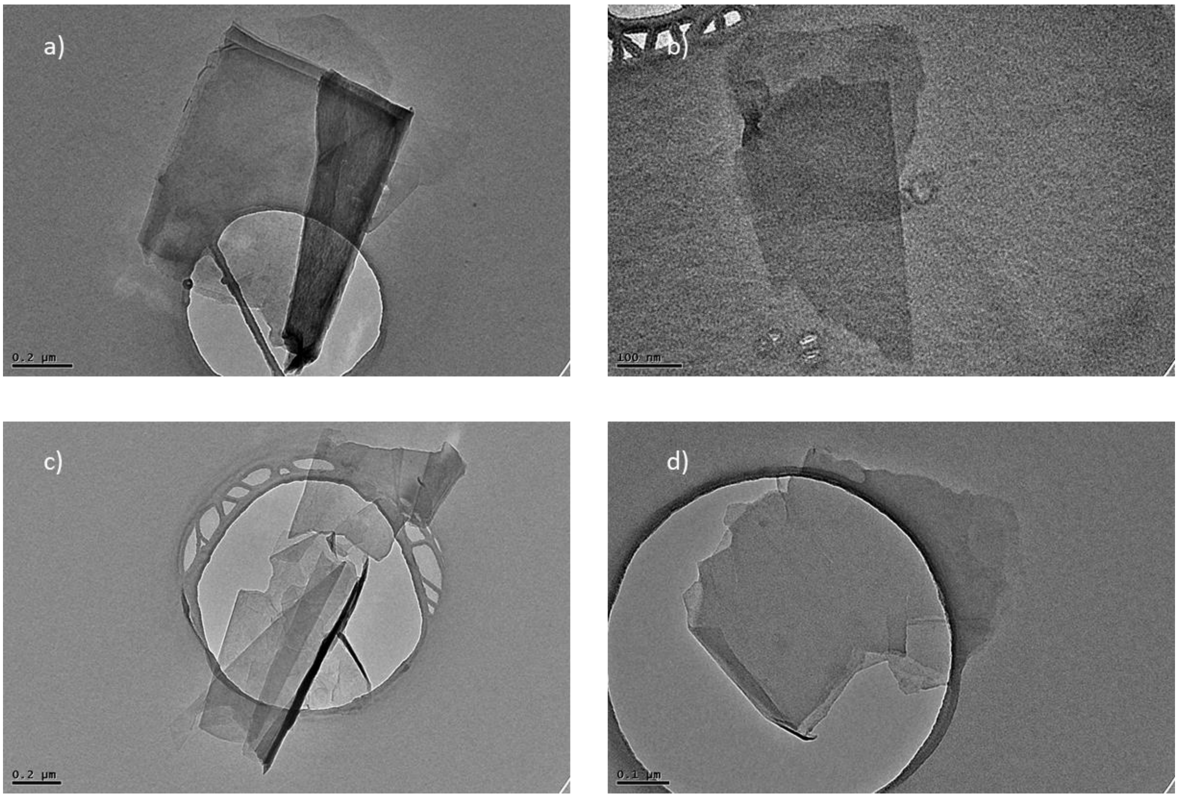

*Figure 4.24 (a), (b), (c), and (d) TEM images of graphene flakes from **PO-G 700 Dis** sample.*

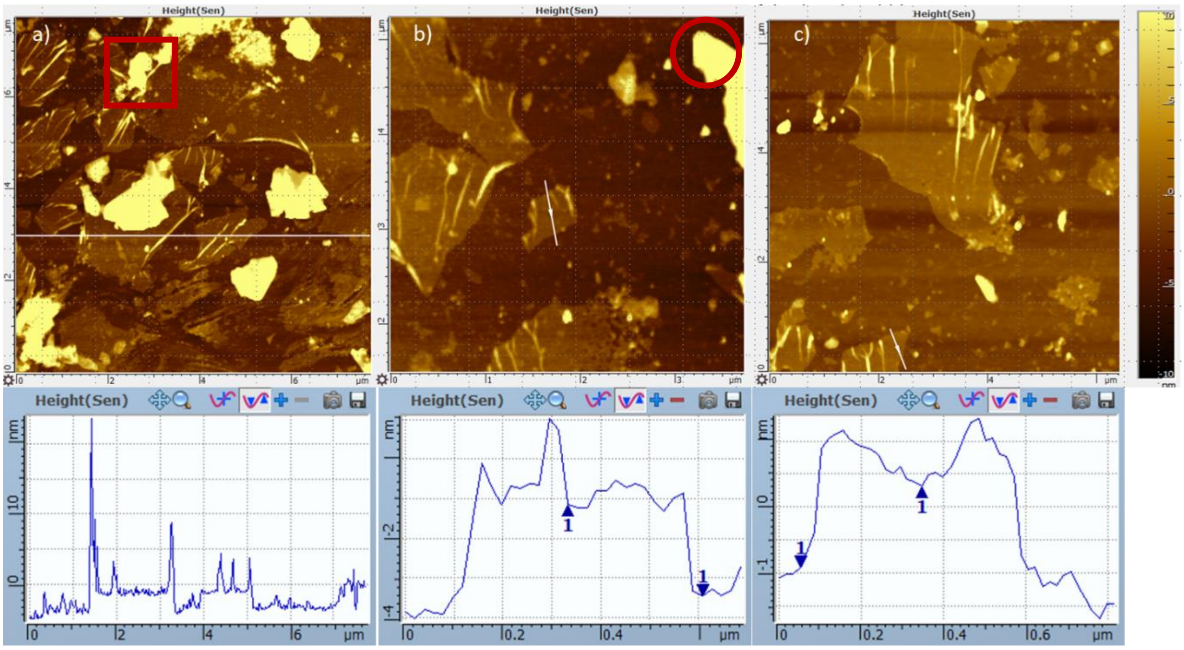

*Figure 4.25 (a), (b), and (c) AFM images and corresponding height profiles of monolayer and bilayer functionalised graphene with large lateral sizes from **PO-G 700 Dis** sample. The bright lines in the flakes represent wrinkles of graphene. Incomplete exfoliation (red square) and thick flakes (red circle) can be spotted.*

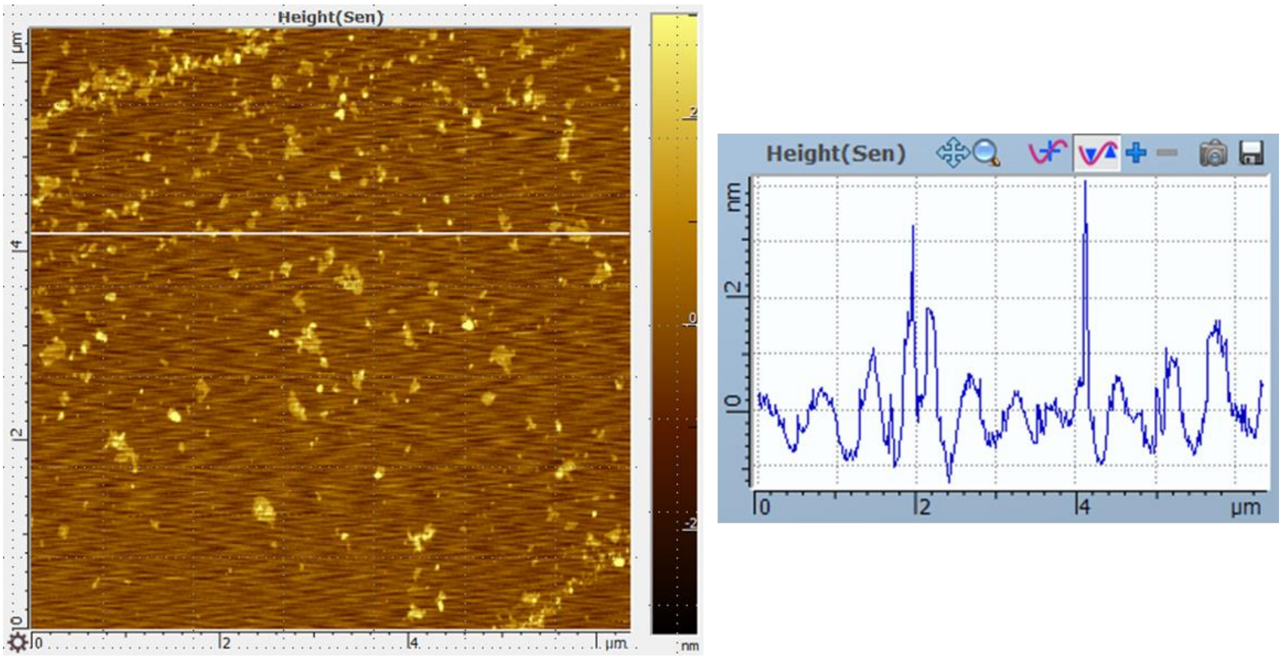

Figure 4.26 AFM images of monolayer functionalised graphene with small flakes sizes.

To summarise, the **crude PO-G** is a polydisperse material which is composited by partially oxidised graphene with different degree of exfoliation and functionalisation. Functionalised graphene with thickness of 4-200 nm can be spotted. With help of mild centrifuge, part of unreacted or thick GNP can be removed, however, according to AFM, TEM, and SRS analysis this process is not able to remove all those materials. The complex composition of the **crude PO-G** might be results of uneven oxidation due to the inefficient mixing and reflects the nature of a heterogenous reaction. On the other hand, part of those sediments can be converted to thinner and more dispersible material by probe-sonication. In addition, the probe-sonication can also produce thinner graphene 1-4 nm, which is rarely found in the sample without sonication. The I_D/I_G histogram of **PO-G 700 Dis** reflects the uniform oxidation level of the sample after the separation. Yet, the polydispersity problem of **PO-G 700 Dis** flake sizes has not been ameliorated compared to that of the **crude PO-G** after the process, since flakes with significantly different sizes and thickness can still be observed. The polydispersity of thickness can be only ascribed to inhomogeneous exfoliation or reaction, whereas the polydispersity of lateral size can also be ascribed to the polydispersity of the starting material. Even though monodisperse graphene can be achieved by a more complicated separation process, the yield of the corresponding separation can be minute and fruitless. Consequently, the **PO-G 700 Dis** is used for further characterisations and application.

4.3 Characterisation of the Separated Partially Oxidised Graphene

The degree of functionalisation of the **PO-G (PO-G 700 Dis)** is compared with that of GO and rGO. By comparing the I_D/I_G of the **PO-G** to that of GO (Figure 4.27), it can be found that the average I_D/I_G of the **PO-G** is less than that of GO, this indicates the **PO-G** is less functionalised than GO. This claim is further corroborated by analysing the I_{2D}/I_G distribution function of GO and **PO-G**. The average I_{2D}/I_G of **PO-G** was very close to that of pristine GNP (0.28 compared to 0.33), whereas the 2D peak of GO had totally disappeared due to the disruption of sp^2 domain of graphene. Comparing to rGO, the 2D band of **PO-G** is more recognisable, which means the sp^2 structure of **PO-G** is more retained than rGO. The retaining of sp^2 structure of graphene after partial oxidation was also proved by the UV-Vis spectra in (Figure 4.28). GO was characterised for its outstanding peaks at 230 nm for π-π * and 295 nm for n-π *. The peak at 230 nm will red shift to higher wavelength after the reduction and the shift depends on the degree of reduction. For the rGO reduced by hydrazine hydrate, the peak was observed at 270 nm, this normally represents the restoration of sp^2 domain of the graphene. The UV-Vis peak of **PO-G** was observed at 270 nm, this suggested that the sp^2 domain was not hugely disrupted as GO after the oxidation. The extinction coefficient of **PO-G** was determined by calibrating dispersion of **PO-G** with known concentration against corresponding absorbance at 660 nm. And ε=1105.6 L g^{-1} m^{-1} in water is found for **PO-G** (Section 6.1.4). Based on this value, the yield of **PO-G** per 1 mg **crude PO-G** is c.a. 0.25 mg. The dispersibility of the **PO-G** in water was monitored, and the dispersion can be stable at least in 25 hours (Figure 8.9 in Appendix 8.3.1).

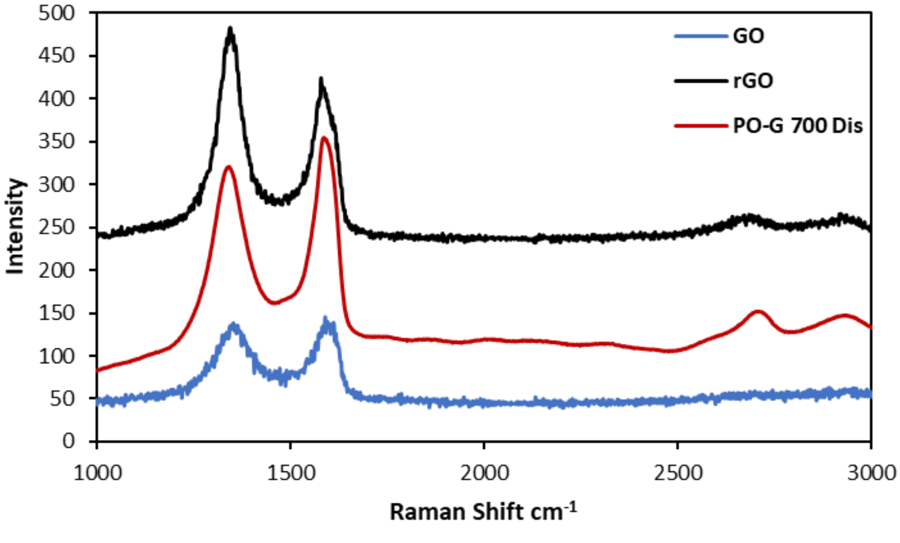

Figure 4.27 Raman spectrum of GO (blue), rGO (black), and ***PO-G 700 Dis*** *(red).*

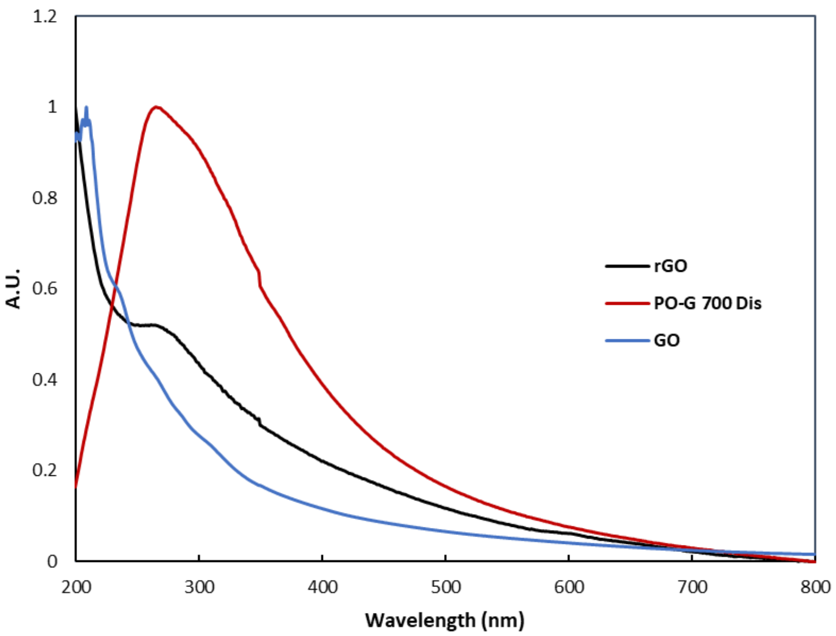

*Figure 4.28 UV-Vis spectrum of rGO (black), GO (blue), and **PO-G 700 Dis** (red).*

The degree of oxidation or functionalisation of **PO-G** is characterised by TGA. TGA curves of **pristine GNP, rGO, GO,** and **PO-G** were displayed in the (Figure 4.29**)**. As expected, the pristine GNP demonstrated a low weight loss (~1%) below 600 ℃. Similarly, the **rGO** also showed little overall weight loss (5%) due to loss of residual oxygen containing functional groups during the heating, no sharp weight loss is found in TGA curve of **rGO**. In contrast, **GO** exhibits a great global weight loss before 600 ℃ -- up to 38 % of the initial weight. This major weight loss consisted of two steps. The first step involved a sharp weight loss (25%) up to 250 ℃, which implies the decomposition of liable oxygen containing functional groups. The second step is smoother (10% weight loss), starts from 250 to 400 ℃, where the thermally more stable functional groups are cleaved from the graphitic structure. The partially oxidised sample (**PO-G**) has a very similar profile, however its weight loss from 200 to 300 ℃ was only ~ 5%, weight loss from 300-500 ℃ was 15% and overall weight loss was 27%, suggesting that much lower oxygen containing groups had been achieved by the partial oxidation. Comparing to TGA profiles of **GO** and **rGO**, TGA profile of **PO-G** is in an expected position, as it was in between the **rGO** and **GO** TGA curves.

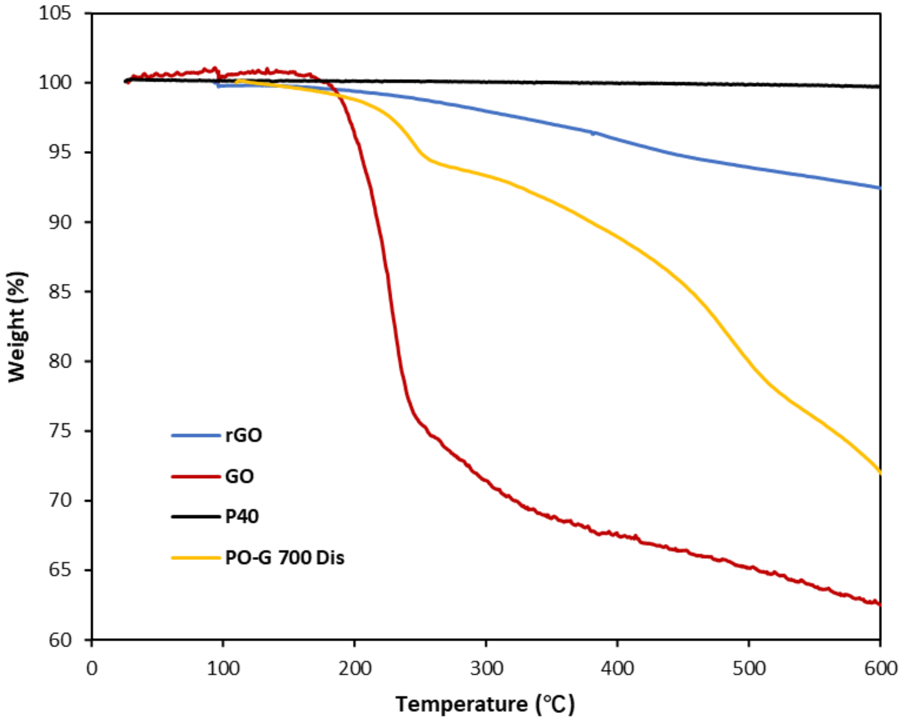

*Figure 4.29 TGA profile of rGO, GO, **PO-G 700 Dis**, and pristine **P40 GNP**.*

The **crude PO-G** is further characterised by XPS (Figure 4.30). Oxygen 1s and carbon 1s signal can both be spotted in the XPS scan spectrum. Residual fluorine was left on the sample due to using the PTFE membrane during isolation of SGICs. Oxygen content is found to be c.a. 7 at% in the **crude PO-G**. Given that the conversion rate of the **crude PO-G** to the **PO-G 700 Dis** is 25 wt%, the oxygen content of the **PO-G 700 Dis** is c.a. 13.5 at% and 17.2 wt%. The deconvolution of high-resolution C 1s (Figure 4.32) core level has resulted in 5 components: they are sp^2 carbon at 284.8 eV, C-C at 285.7 eV, C-O-C at 286.7 eV, COO- at 289.3 eV, and π-π* at 290 eV. The presence of π-π* shake up feature indicates the localisation of π electrons for the oxidised graphene. Comparing to C 1s of rGO (Figure 4.33), which is more carbonyl functionalised, the graphene derived from this partial oxidation is more epoxide functionalised. Moreover, the presence of trace sulphur (168.5 eV) can also be detected in the **crude PO-G**, which might suggest the presence of organosulfur groups or residual sulphate anions from the sulphate GICs.

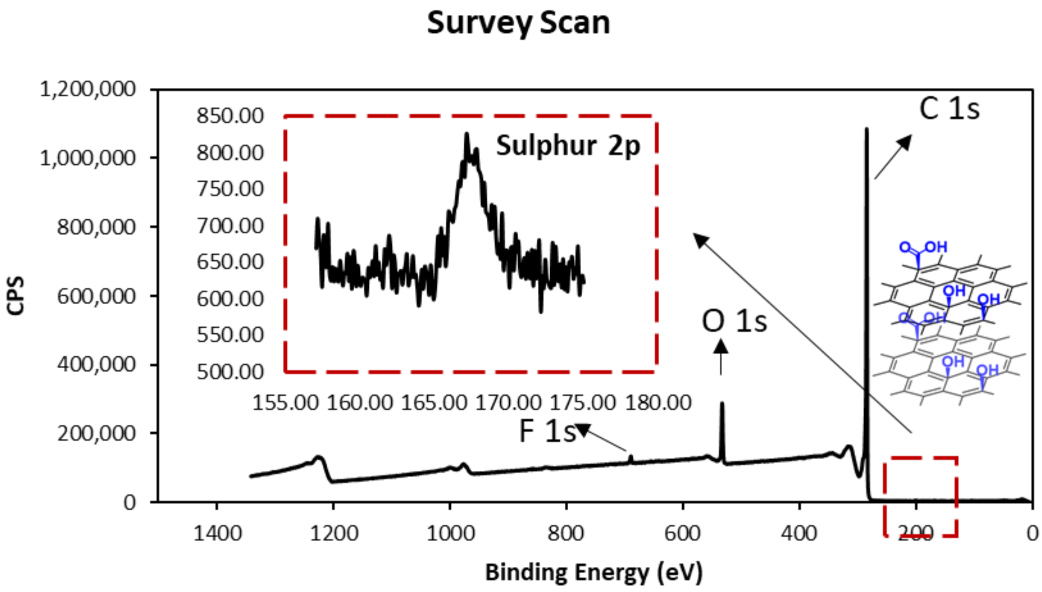

Figure 4.30 XPS survey scan of ***crude PO-G****.*

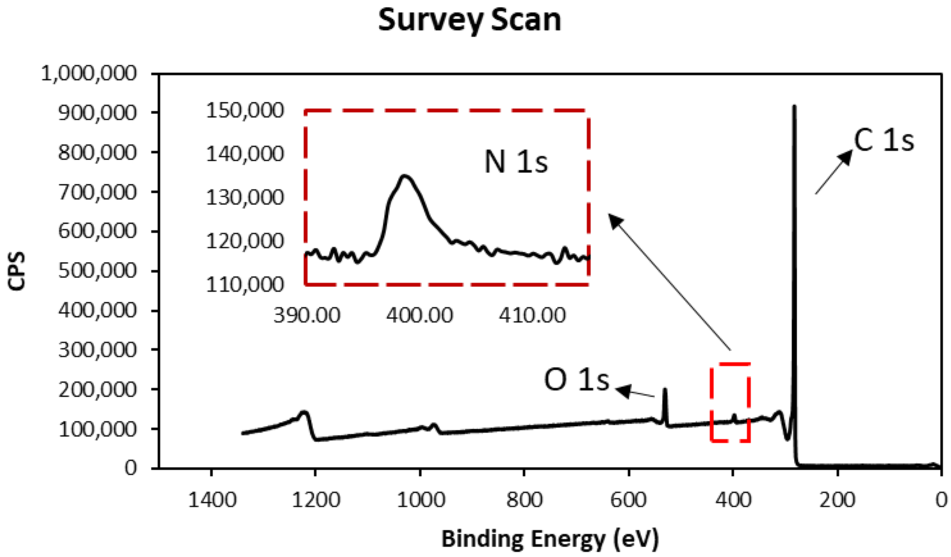

Figure 4.31 XPS survey scan of rGO, the presence of residual nitrogen comes from the reducing agent hydrazine.

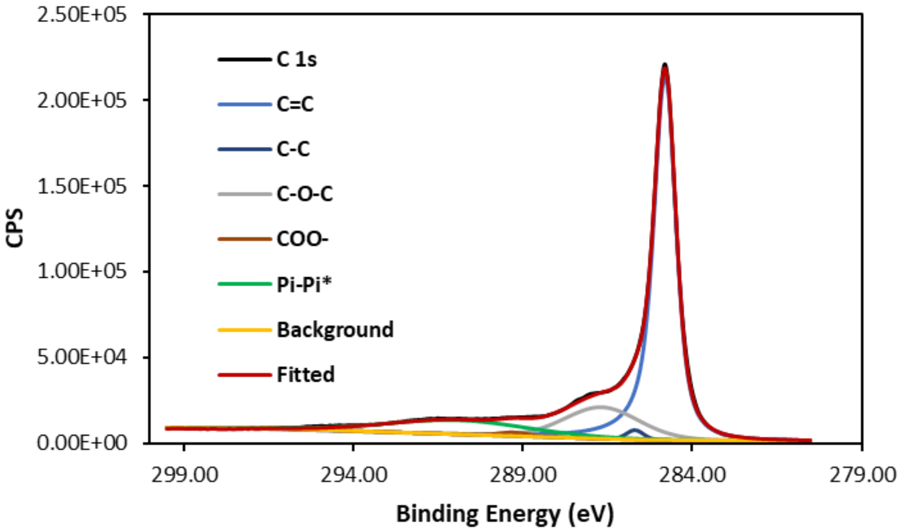

Figure 4.32 Deconvolution of C 1s peak for ***crude PO-G****.*

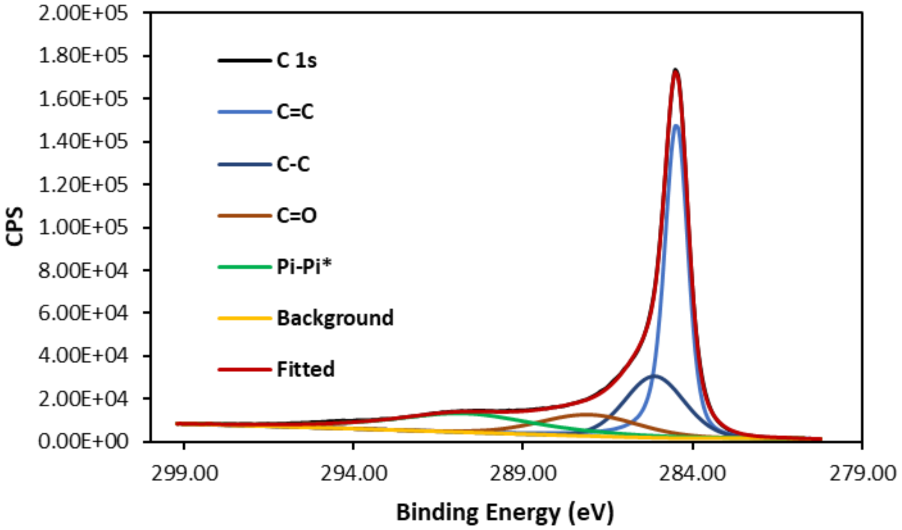

Figure 4.33 Deconvolution of C 1s peak for rGO.

It is well known that the graphene oxide is an insulator since its sp^2 electronic structure are heavily converted to sp^3 during the oxidation. In contrast, the partially oxidised graphene (**PO-G 700 Dis**) should be still conductive as its electronic structure was well retained during the oxidation.[168] The results are summarised in the Table 4.2. A thin cake of **PO-G 700 Dis** sample (20 mm diameter, ~0.3 mm thick) was prepared by vacuum filtration. The electrical resistance of the cake was measured by a four-point probe. It turns out that the electrical resistivity of the sample was 1.8×10^{-2} Ω·m (sheet resistance is 57.4 Ω/□) and its electrical conductivity was 86 S/m. Compared to the electrical conductivity of GNP, which is c.a. 7.3~7.7×10^{4} S/m, the electrical conductivity of **PO-G 700 Dis** is three orders of magnitudes less than that of the pristine GNP. The bulk electrical conductivity of the **crude PO-G**, however, is 9.1×10^{3} S/m, which is in the same order of the pristine GNP. This means the Mn (III) acetate dihydrate leads a mild oxidation so that the hydrophilic groups are added to the GNP and basal plane of graphene is preserved.

*Table 4.2 Electrical measurements of P40 pellet, **PO-G** cakes, and rGO films.*

Sample	Resistivity (Ω·m)	Sheet Resistance (Ω/□)	Electrical Conductivity (S/m)
rGO	-	(1.5 ± 0.2) x 10^{2} [169]	-
P40 GNP	1.4 x 10^{-5}	6.7 x 10^{-2}	(7.3 ± 0.4)x 10^{4}
PO-G 700 Dis	1.8 x 10^{-2}	57	86
Crude PO-G	1.1 x 10^{-4}	3.5 x 10^{-1}	9.1 x 10^{3}

4.4 Partial Oxidation in Other Solvents

When the oxidation is conducted in 1,2 DCE, the resulting oxidised material is composed of materials with different degree of functionalisation and unreacted starting material. The polydispersity of the product originates from the inefficient mixing during the reaction as SGIC has poor solubility and dispersibility in 1,2 DCE. Moreover, the degree of exfoliation can be limited due to the poor interaction between the as produced functionalised graphene and solvent. Therefore, a new solvent system must be developed to enhance the efficiency of the reaction and replacing the toxic 1,2 DCE. Two essential requirements must be met to be considered as a feasible solvent for the reaction. Candidates of appropriate solvent should be compatible with the radical reaction— avoid producing any explosive peroxide, this eliminates most of the oxygenated solvents, which will generate peroxide and pose safety issue to the reaction. Water could be a suitable solvent, yet the oxidant will be disproportionate in presence of water. The other requirement is the solvent should be able to disperse SGIC very well. Two solvents can satisfy those two requirements: ortho-dichlorobenzene and concentrated sulphuric acid. Same to 1,2 DCE, ODCB is a typical solvent which is usually used in radical reaction. In addition, ODCB is also a good solvent for graphene material, which makes ODCB a promising solvent to disperse SGIC and the oxidised graphene. The advantages of using concentrated sulphuric acid as solvent are stage-1 SGIC can be stabilised and SGIC can be uniformly dispersed. Sulphuric acid is also well known for its oxidising power, which makes it suitable for oxidation reaction. The reaction condition of the partial oxidation in concentrated sulphuric acid can be treated as modified Hummer method, where the strong oxidant permanganate is replaced by milder oxidant $Mn(OAc)_3$.

4.4.1 Organic Solvents

Partial oxidation of SGIC was delivered in ODCB and toluene. The SRS results (Figure 4.34) show that GNP remain unreacted in both solvents as I_D/I_G distributions stay unchanged. The profiles of I_D/I_G distributions are very similar to that with TEMPO as radical quencher. These results indicate ODCB and Toluene could inhibit the oxidation and not suitable to be used as solvents for partial oxidation of SGIC.

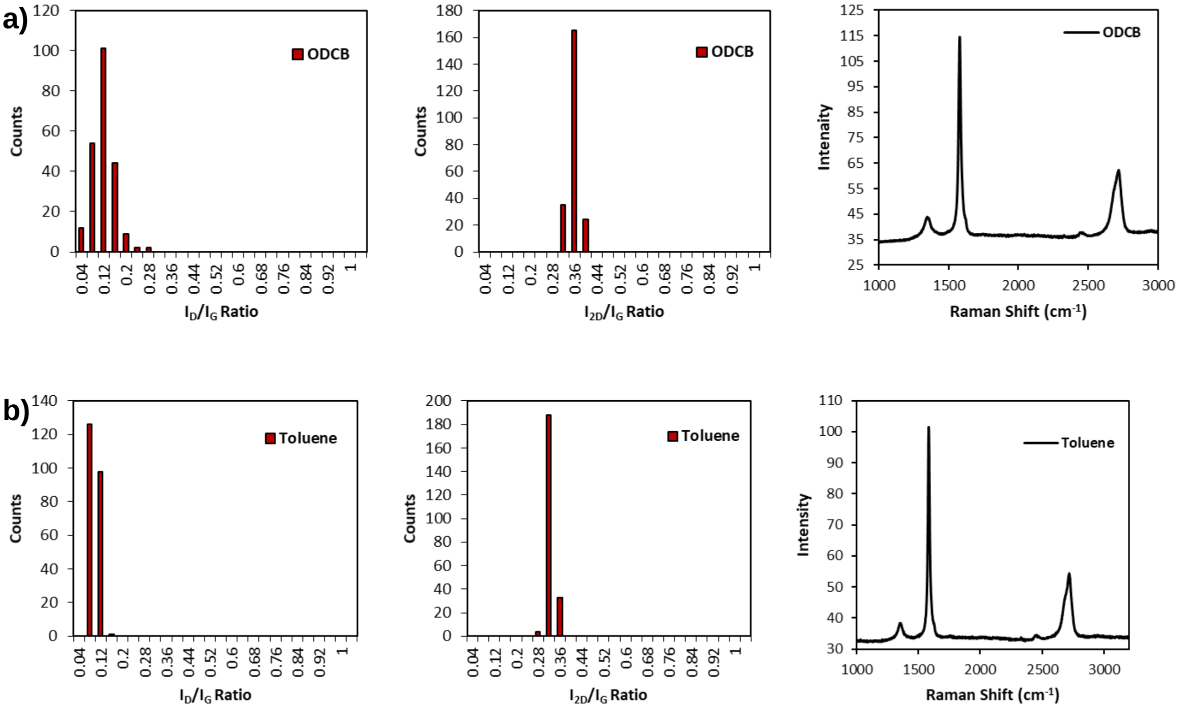

Figure 4.34 I_D/I_G, I_{2D}/I_G histograms, and average Raman spectrum of partial oxidation performed with ODCB (a) and Toluene (b) as solvents.

4.4.2 Partial Oxidation in Bulk Sulphuric Acid

The first problem of conducting partial oxidation in sulphuric acid is the amount of sulphuric acid (5 mL) for the formation of SGICs is too small to dissolve equimolar $Mn(OAc)_3$, in fact the mixture become very hard to stir upon addition of 0.2 grams of $Mn(OAc)_3$. Theoretically, more sulphuric acid is required to dissolve more $Mn(OAc)_3$. However, the stage of SGIC may change due to addition of more con. H_2SO_4. The stage of sulphate GICs in bulk sulphuric acid was studied by Raman spectrometer to understand its stability upon dilution of concentrated H_2SO_4.

As the Raman spectrum (Figure 4.35) after the dilution shows, stage 1 SGIC changed to mixture of higher stage SGIC after the dilution of 15 mL sulphuric acid. The stage remained, however, when 1 g persulphate was added into the diluted mixture.

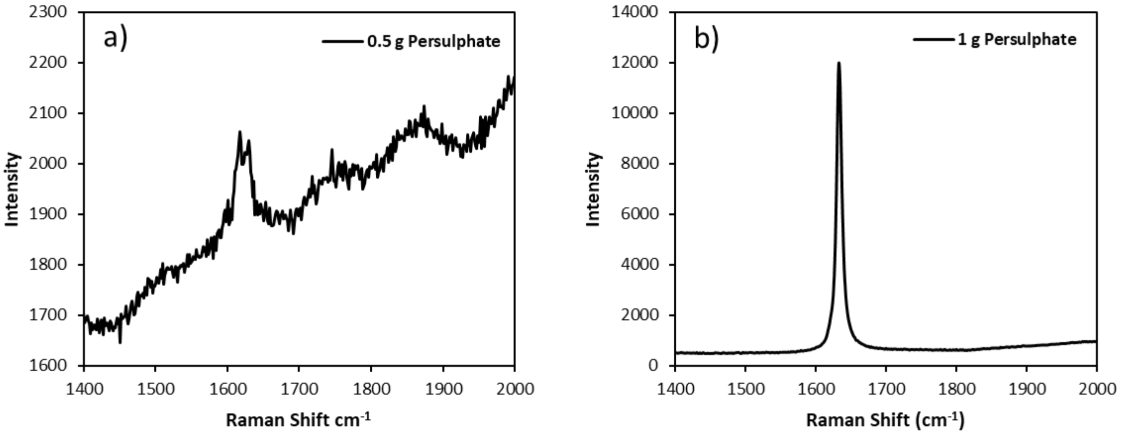

Figure 4.35 Raman spectrum of SGIC prepared by using 0.5 g (a) and 1g (b) potassium persulphate when 15 mL con. sulphuric acid was added.

The partial oxidation of Stage-1 SGIC was carried out as following steps: stage-1 SGIC was prepared by dissolving 1 g potassium persulphate into 20 mL concentrated sulphuric acid with 0.24 g P40 GNP. The preparation was complete after 1 hour of stirring. 2 g of anhydrous $Mn(OAc)_3$ and 200 µL water were added into the stage-1 SGIC and the mixture was heated to 85 ℃ for 3 hours. In the last hour, the temperature was brought to 95 ℃. The mixture was filtered through a glass frit after cooling and washed by copious water. In a 100 mL beaker, 0.1 g crude product was dispersed in 70 mL DI water. The dispersion was homogenised in a bath sonicator and then probe-sonicated for 30 minutes. The dispersion was then centrifuged at 700 rpm to remove the large flakes or aggregates and unreacted graphite. The supernatant was retained and filtered through an alumina membrane. The isolated solids were dried in vacuum oven (80 ℃) and labelled as **PO-G-BS**.

The processed **PO-G-BS** was studied by SRS (Figure 4.36). The distribution of I_D/I_G ratios is narrow indicating product with similar degree of oxidation was generated from the oxidation and the centrifuge processes. The distribution of I_{2D}/I_G ratios corroborated the products were homogenous in terms of oxidation degree, the retaining 2D band also indicates the preserved sp^2 structure of the graphene after the oxidation. The degree of exfoliation can be analysed by looking the I_{2D}/I_G vs position of 2D band plot. Though significant redshift can be spotted by comparing the *Pos* (2D) of P40 with that of **PO-G-BS**, the *Pos* (2D) of **PO-G** is more red-shifted. These suggest more exfoliated products can be formed when the reaction is heterogenous and small scaled. The results of AFM (Figure 4.37) reflect the same conclusion. By comparing the histograms of flake thickness for **PO-G** and **PO-G-BS**, **PO-G** was more exfoliated as 90% of the flakes were 1.4 nm - 6.9 nm thick, and 85% of flakes in **PO-G-BS** are 2.0-7.2 nm thick (Table 4.3 & Table 4.4). Conducting reaction in abundant sulphuric acid does not improve the homogeneity of thickness of the flakes. However, the reaction in sulphuric acid had led to more homogenous distribution of lateral size. Not surprisingly, oxidation in the bulk sulphuric acid had led to formation of flakes with smaller lateral size (0.05-0.2 microns, Figure 4.38) which can be found rarely in **PO-G**. This could be caused by the over-oxidation in the homogenous phase, where the hydroxyl radicals can move more freely.

The aiding ability of the oxidant $Mn(OAc)_3$ in terms of graphene oxidation and exfoliation can be revealed by comparing the AFM results of **PO-G** and **PO-G-BS** with those of **PO-W 1000**. The **PO-W 1000** was derived by processing the **crude PO-W** (section 4.2.1) with probe-sonication and 1000 rpm centrifugation. From the Table 4.3 and Table 4.4, it can be seen the **PO-G** and **PO-G-BS** generally have thinner flakes, this can be interpreted as the oxidation from the radicals helps the expansion of the SGIC interlayer and therefore facilitate the consequent exfoliation process during the reaction and probe-sonication. The resulting wider distribution of lateral size for **PO-G/PO-G-BS** also suggests the oxidation is more non-uniform (as the generation and attack of hydroxyl radicals would be more biased as it depends on the encountering of water and the oxidant) than the less powerful but abundant water.

According to AFM results (Figure 4.37), delivering oxidation in bulk sulphuric acid does improve the homogeneity of the lateral size of flakes comparing to oxidation in 1,2 DCE as more smaller flakes can be obtained due to more uniform reaction phase. This (Table 4.4) can be seen from the differences between the P10, P50, and P90 of **PO-G-BS** (0.18, 0.29, and 0.48 μm) and those of **PO-G** (0.17, 0.35, and 1.53 μm). Surprisingly, the **PO-G** sample has narrower distribution of flake thickness Though flakes still exist in different thickness and lateral size. Additionally, the oxidation extent has been improved as the yield has been increased significantly from 25% for **PO-G** to 70% for **PO-G-BS**.

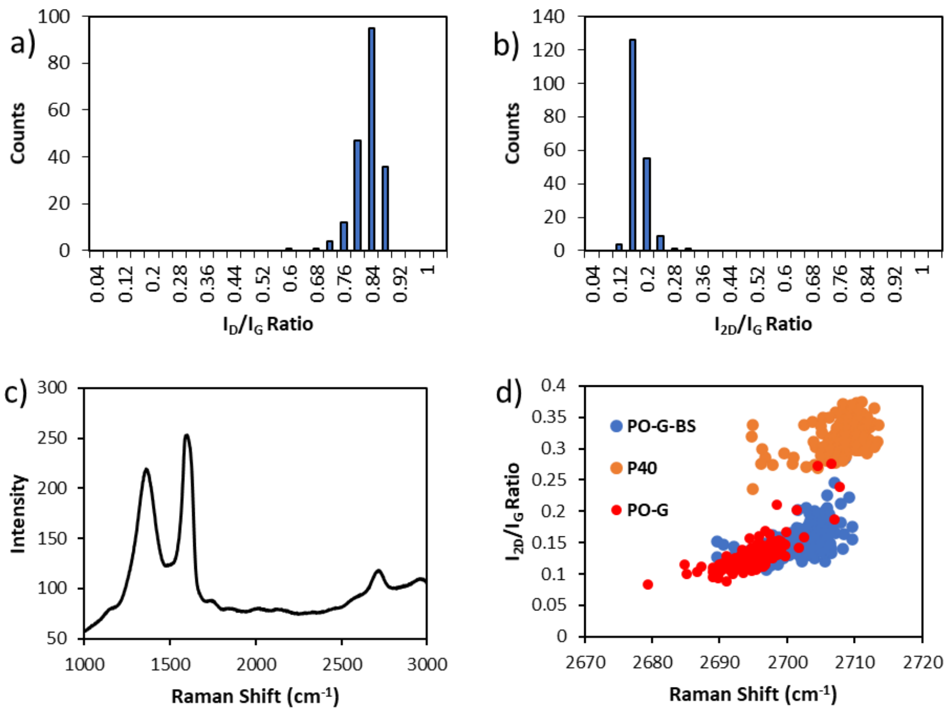

*Figure 4.36 I_D/I_G (a), I_{2D}/I_G (b) histograms, and average Raman spectrum (c) of **PO-G-BS**. I_{2D}/I_G vs 2D position plot (d) of **PO-G-BS**, **PO-G**, and pristine **P40 GNP**.*

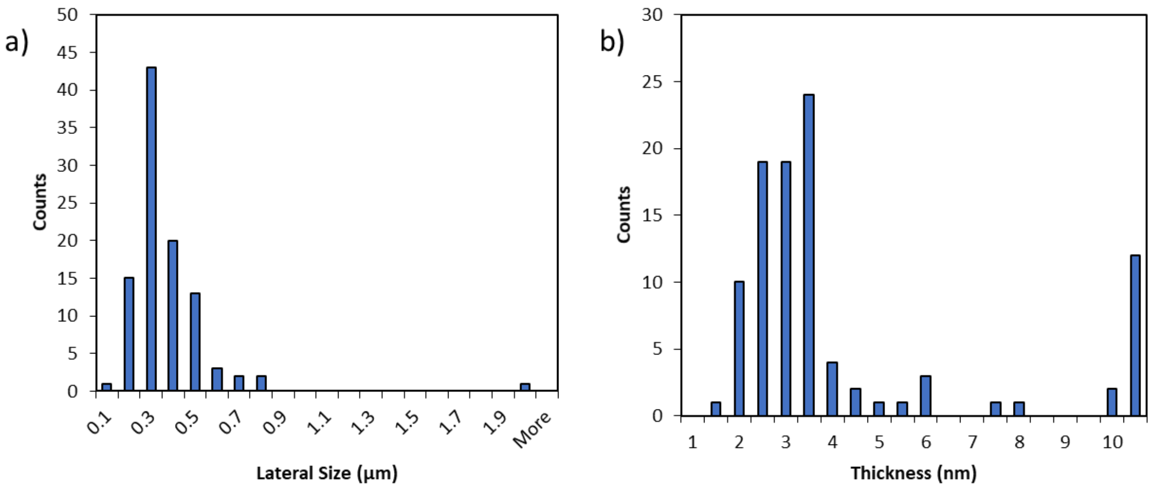

*Figure 4.37 Lateral size (a) and thickness (b) histograms of **PO-G-BS**.*

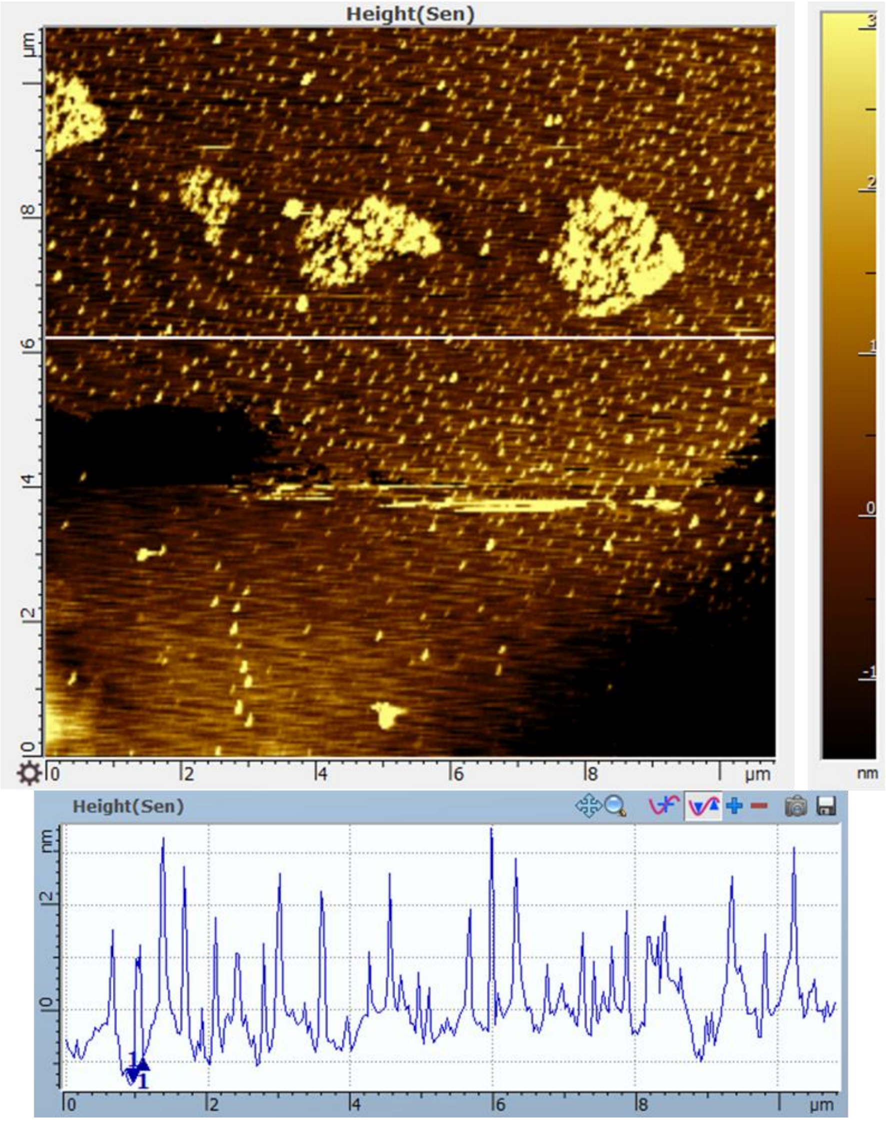

*Figure 4.38 The small flakes found in **PO-G-BS** sample.*

Overall, the feasibility of partial oxidation in other solvents including toluene, ODCB, and bulk con. sulphuric acid has been evaluated. The SRS studies indicate partial oxidation in organic solvents are inhibited, the reason could be the benzene-based solvent could act as radical quencher to stop the electron transfer between the oxidant and the water molecules. According to SRS results, when excessive con. sulphuric acid is used as solvent, **P40 GNP** will be oxidised into graphene materials which have almost the same degree of oxidation to **PO-G**. The AFM measurements suggest smaller flakes with uniform distribution were obtained via the reaction in the bulk acid, however those flakes have wider range of thickness. These results suggest both the homogeneity of lateral size and oxidation degree of the partial oxidised graphene has been improved by delivering partial oxidation in the bulk sulphuric acid.

Table 4.3 Flake thickness distribution analysis of ***crude PO-G****,* ***PO-G/PO-G 700 Dis****,* ***PO-G 300 Dis****,* ***PO-W 1000****, and* ***PO-G-BS****.*

Sample	10th Percentile nm	50th Percentile nm	90th Percentile nm	<Average Thickness> nm
crude PO-G	3.8	12	37.8	18.2
PO-G or PO-G 700 Dis	1.5	2.1	6.7	4
300 Dis	1.8	7.5	14.3	9.1
PO-W 1000	4.5	7.9	17.6	10.7
PO-G-BS	2	3.1	14.5	5.3

Table 4.4 Flake size distribution analysis of ***crude PO-G****,* ***PO-G/PO-G 700 Dis****,* ***PO-G 300 Dis****,* ***PO-W 1000****, and* ***PO-G-BS****.*

Sample	10th Percentile μm	50th Percentile μm	90th Percentile μm	<Average Lateral Size> μm
crude PO-G	0.16	0.53	1.13	0.66
PO-G/PO-G 700 Dis	0.17	0.35	1.53	1.53
300 Dis	0.26	0.41	0.69	0.64
PO-W 1000	0.18	0.26	0.36	0.27
PO-G-BS	0.18	0.29	0.48	0.33

4.5 Conclusion and Future Work

Exfoliation and partial oxidation of GNP have been achieved by using SGICs and the mild oxidant $Mn(OAc)_3$. A series of controlled experiments and condition optimisation reactions have been dedicated to find out the key factors affecting the completion of the oxidation and shed light on the mechanism of the process. It is shown that the synergic effect of water and plays a vital part in the oxidation. A conjectured radical pathway mechanism could be proposed, where the oxidant $Mn(OAc)_3$ mediates the oxidation by single electron transfer [170] to the water molecules to generate the hydroxyl and other radicals in the surrounding, the attack of hydroxyl and other radicals to the edge or basal plane of the sulphuric acid activated graphene layer leads to the exfoliation and oxidation of the GNP to the partially oxidised graphene. Contradictory results between SRS and dispersibility test arose (where high average I_D/I_G ratio does not always relate to good water dispersibility) when the PO-G deriving from different temperature and oxidation time were compared, which may indicate the formation of intermediate. The effect of temperature and oxidation time remains unclear, and further investigation on them could be the missing pieces to the whole jigsaw. The deeper understanding of mechanism of the process would be beneficial to control and enhance the current process.

The nature of the partial oxidation is supported by the relative low oxygen 13.5 at%, high electrical conductivity, and maintenance of 2D peak of the product comparing to that of GO. As compared with rGO, **PO-G** exhibits similar λ_{max} in UV-Vis and intermediate amount of weight loss (in between the rGO and GO) in the TGA. The crude product PO-G demonstrates good dispersibility in water as the stability of the dispersion can be over 12.5 hours. This property can be enhanced further to at least one month after the separation. The separation of **crude PO-G** reveals its complex composition. More few-layer graphene and even monolayer and bilayer graphene can be obtained through a relatively simple separation and sonication process. The efficiency and yield of the process can be further improved if the separation and sonication process was applied to the sediment and a final conversion rate of 25% (0.25 mg **PO-G** per 1 mg **crude PO-G**) can be achieved. The uniformity of the size and thickness of the resulted partially oxidised graphene was improved somewhat; however, it is still a material consisting of a range of flake sizes and thicknesses according to the pertaining AFM, TEM, and SRS studies. According to relevant studies [167,171], it is assumed that more complicated separation can afford more uniform product but with significant reduction on yield.

As variations in flake size and thickness of the graphene sample can result in limited performance in the lateral performance, efforts had been made to improve the uniformity of the **PO-G** sample. The polydispersity (non-uniformity) of the product can be ascribed to the heterogenous phase of the reaction due to the insolubility and un-dispersibility of SGICs and limited solubility of $Mn(OAc)_3$ in 1,2 DCE. Attempts of performing the oxidation in toluene, ODCB, and con. H_2SO_4 were made. It turned out the oxidation in toluene and ODCB was suppressed. This can be ascribed to the radical coupling to the solvents. On the other hand, partial oxidation can proceed in the con. H_2SO_4 by modifying the conditions of oxidation in 1,2 DCE and partially oxidised graphene with very similar quality can be produced. Since the reaction becomes more homogenous, more SGIC can be used for every batch and hence more yield. Additionally, uniformity of the flake sizes had been improved significantly, while the uniformity of flake thickness remained almost the same compared to that of PO-G after the process. However, small flakes and big flakes can still be spotted after the separation, which indicates the centrifugation employed was not sufficient. It seems that the graphene layer of the graphite undergoes uneven oxidative fission, or the **crude PO-G** are broken down by the probe-sonication to produce flakes with various size and thickness. To obtain more uniform PO-G, the lateral size of the starting material can be selected and controlled within a range by using sieves and the exfoliation can be done by replacing the probe-sonication with the less destructive shear mixer.

Chapter 5. Linear Viscoelastic Properties of Partially Oxidised Graphene/ Poly(methyl methacrylate) Nanocomposite

5.1 Introduction

Since its discovery in 2004, graphene has been regarded as a promising nano filler for composite fabrication due to its high surface area, outstanding tensile strength, and high electrical and thermal conductivity. With the addition of a small volumetric fraction of graphene, the macroscopic properties of various polymers can be enhanced hugely, and the resulting composite can demonstrate excellence in different applications. For example, graphene/epoxy resin[96,172–174], graphene/polyaniline[9,175–177], and graphene/polyurethane (PU)[178–181] composites demonstrate good barrier properties towards H_2O and O_2, and hence can be used as anticorrosion coatings. The graphene/polyaniline composite can be an ideal energy store since the specific capacitance and cycling life of the resulting capacitor are enhanced hugely according to the relevant studies. Incorporation of graphene into polypropylene (PP)[182], PU[180], poly(vinyl alcohol) (PVA)[183], polyimide[184], epoxy resin[173,185,186] etc. can result in significant improvement in terms of mechanical strength, thermal conductivity, and electrical conductivity. To achieve a better performance in the composite, high dispersibility of the graphene in the target polymer matrix is one of the critical factors. Since poor dispersibility of graphene will result in aggregation of graphene in the polymer which will decrease the surface area (aspect ratio) of the graphene and hence lead to poor reinforcing effects of the filler. As Long-Cheng Tang et al. suggested, the epoxy resin with highly dispersible rGO would have one or two orders of magnitude higher electrical conductivity than the epoxy resin with poorly dispersed rGO[165]. Good compatibility of graphene and polymer matrices can be achieved by employing chemical modification of the surface of the graphene[173,184,187–194]. Wan, Yan Jun et al. found the storage modulus of epoxy resin was improved significantly both in the glassy state and rubbery state by using silane functionalised graphene oxide compared to that of epoxy resin using graphene oxide at the same level of loading[195]. Mitra Yoonessi et al. reported the storage modulus of the polyimide composite has improved 20% by using surface modified filler compared to that with unmodified graphene[184]. Chih-Chun Teng et al. found that the thermal conductivity of the epoxy resin was enhanced 20% by using non-covalently functionalised pyrene-end poly(glycidyl methacrylate) Py-PGMA dispersed graphene compared to that with pristine graphene[194]. Moreover, different processing methodologies can make graphene nanocomposite have different levels of dispersion[165,177,180–182,196]. Hyunwoo Kim et al. concluded that the graphene would have different influences on the electrical and mechanical properties of the thermoplastic PU composite if the graphene/composite is fabricated by different processing techniques (in-situ polymerisation, melt compounding, and solvent blending)[181]. Therefore, understanding the state of dispersion of the graphene in the polymer matrices is important to help achieve better performance in the resulting composite.

Rheological measurements have been found to be an effective methodology to understand the effect of nano fillers on the microstructure of the polymer. In a Small Amplitude Oscillatory Shear (SAOS) test, the viscoelastic response of the composite will be linear, and the nanocomposite is assumed to be unchanged when the strain amplitude is sufficiently small. This linear region is extremely sensitive to the incorporation of the nano particles, where the viscoelastic properties of nanocomposite would change significantly according to the change of microscopic structure. More importantly, the dispersibility of graphene and other nano particles in the polymer matrices and the interaction between them can be elucidated by analysing the change of the linear viscoelasticity in the terminal region (low frequency). [8,11,197–200] Du. et al. found that the SWCNT/PMMA nanocomposite demonstrated the dependence of storage modulus G′ with frequency in the low frequency region weakens as the loading of SWCNT increased. This non-terminal behaviour is indicative of transition from liquid-like behaviour to solid, and the formation of a network in the polymer matrices. By examining the slope and the magnitude of G′ in low frequency region, the dispersibility of SWCNT in matrices can be evaluated.[201] By employing SAOS, Hengti Wang et al. are able to investigate the effect of surface modified silica nanoparticle on the poly(vinylidene fluoride) PVDF/poly(L-lactide) (PLLA) blend. The viscoelastic properties can be extracted from corresponding plots (Cole−Cole plot, van Gurp−Palmen plot, and the plot of $|\eta^*(\omega)|$ versus $|G^*(\omega)|$) and correlated to the evolution of the microscopic structure due to using nano silica with different modifications.[202] Qinghua Zhang et al. studied the dispersion state of MWCNT in polystyrene composite via oscillatory rheology. They found higher loading of the MWCNT and better dispersion in the polymer will result in better rheological performance for the composite.[203] In this chapter, the impact of surface functional groups of partially oxidised graphene and the impact of functionalised graphene on the microstructure of the graphene/PMMA composite will be investigated via linear rheological measurements.

5.2 Results & Discussion

5.2.1 Rheological Properties of Graphene Materials/PMMA Composite with Different Level of Loadings

The rheological properties of composites made from four different graphene materials (pristine P40 GNP—**PG**, partially oxidised graphene—**PO-G**, crude partially oxidised graphene—**crude PO-G**, and reduced graphene oxide—rGO alongside with pure PMMA) were characterised by SAOS tests. Master curves at a temperature of 200 ℃ showing the viscoelastic properties were generated by applying the time temperature superposition (TTS) theory of Williams−Landel−Ferry.[204]

5.2.1.1 P40 GNP

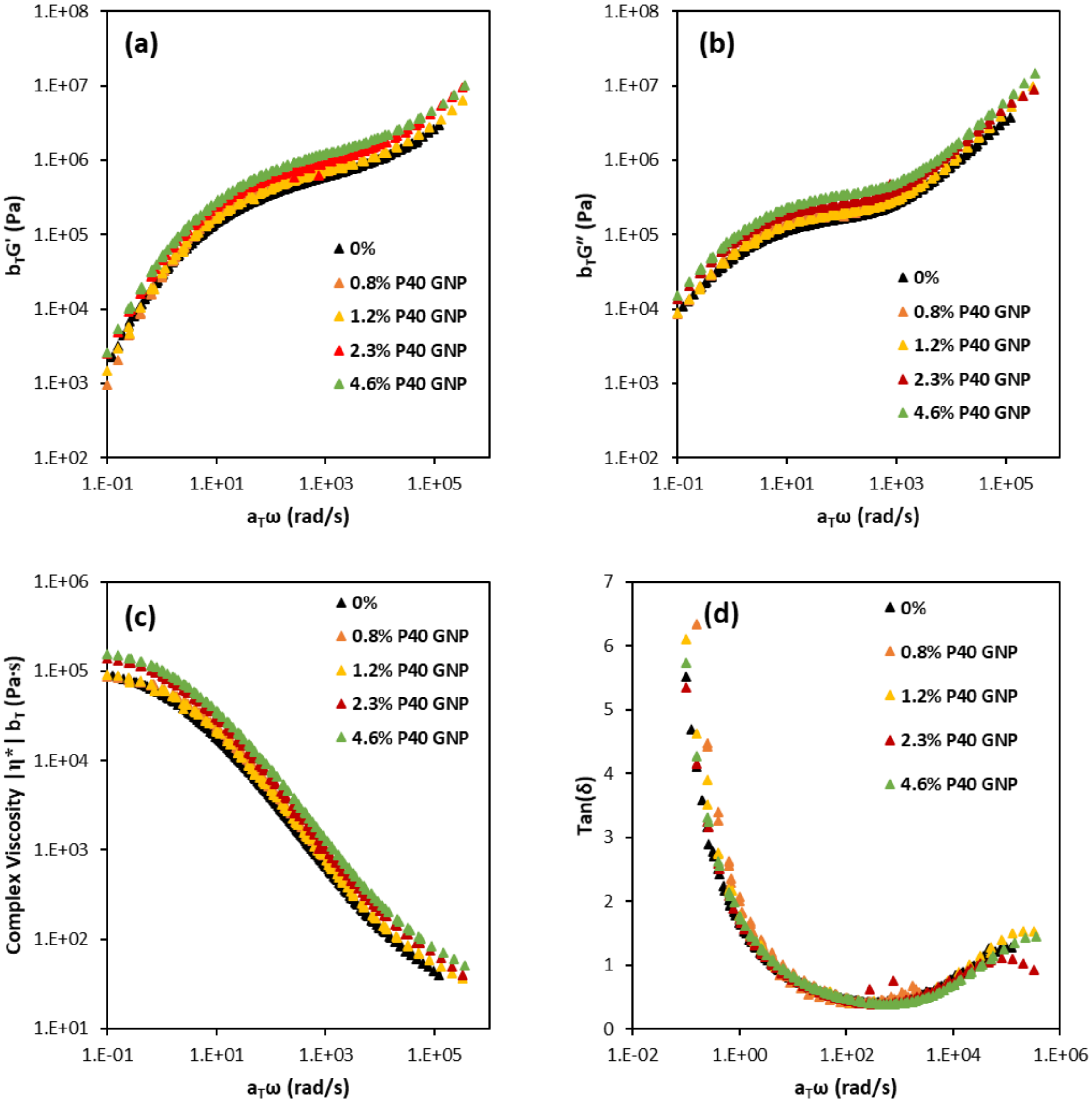

Figure 5.1 Master curves of PMMA composite filling with P40 GNP with various loading at the reference temperature 200 ℃: (a) G' storage modulus, (b) G" loss modulus, (c) |η| complex viscosity, and (d) Tan(δ) loss factor.*

Little change in the viscous and elastic properties of P40 GNP/PMMA composite could be realised when the loading of the composites was changed. As Figure 5.1 (a) and (b) shows, the storage modulus and loss modulus of P40 GNP/PMMA composites have stayed almost the same as compared to those of pure PMMA when the loading was varied from 0.8% to 4.6% vol. The storage moduli of all composites still demonstrate terminal behaviour in the low frequency region, this indicates viscous properties dominate in these composites. In addition, all the composites also exhibited almost identical profile for Tan(δ) as shown in Figure 5.1 (d). This suggested the composites are still liquid-like material at low frequency region. The flow behaviour of P40 GNP nanocomposites is further explored by plotting $|G^*(\omega)|$ against $|\eta^*(\omega)|$ Figure 5.2 (a). For any pure polymer, $|\eta^*(\omega)|$ has Newtonian plateau at low $|G^*(\omega)|$ values, which indicates the viscous property of the polymer in the low frequency ω region. In contrast, a sharp increase of $|\eta^*(\omega)|$ at low $|G^*(\omega)|$ values would be observed for a percolated nanocomposite. Hengti Wang et al. identified the reinforcing effect of the Janus grafted silica in the PVDF/PLLA blends by using the plotting $|G^*(\omega)|$ vs. $|\eta^*(\omega)|$ plot.[202] Similarly, Arun K. Kota et al. realised the formation of network structure for PS upon addition of MWCNT by using the same plot.[205] As can be seen from the plot, the curves of composites with 0.8% and 1.2% vol loading superpose with the curve of pure PMMA, which means the addition of 0.8% and 1.2% vol GNP did not increase the viscosity. A small increase in viscosity was realised when the loading was increased to 2.3% vol, and only marginal increase was found when the loading was increased from 2.3 to 4.6% vol. Since neither of the composites exhibited a sharp increase of $|\eta^*(\omega)|$ at low $|G^*(\omega)|$, P40 GNP exhibits poor interaction with the PMMA matrix.

The addition of 2.3% vol P40 GNP induced marginal improvement on complex viscosity of the resulting composites, suggesting the addition of P40 GNP enhanced the elastic property of the composite. The improvement of elastic property with the addition of more P40 GNP is more conspicuous to be noticed by constructing and analysing the Cole-Cole plot. In the Cole-Cole plot Figure 5.2 (c), the imaginary viscosity $\eta''(\omega)$ is plotted against dynamic viscosity $\eta'(\omega)$. Important information such as phase separation of the polymer blend or nanocomposite can be extracted from this plot. Typically, a semi-circular shape of the curve can be obtained by a miscible polymer system or well-dispersed filler. Any deviation from this shape can be ascribed to the existence of immiscible phases or formation of the network structure.[202,206,207] From the Cole-Cole plot of P40 GNP/PMMA composites, apparent semi-circle shape curves are retained for all composites, this confirms addition of P40 GNP in the PMMA had not induced any percolation. Instead, the radius of the semi-circular curve increased with the increasing loading of the P40 GNP, which confirmed the composite had become more resistant to flow as the loading increased.

The van Gurp-Palmen (vGP) plot, which plots phase angle $\delta_{(\omega)}$ against logarithmic complex modulus $|G^*(\omega)|$, is very sensitive to the time-temperature superposition and can be used to detect the gelation, change in entanglement, or percolation of the composite. Formation of network and polymer-filler entanglement will decrease the phase angle at low $|G^*(\omega)|$, which alternatively suggests the elastic response of the composite has been improved. Potentially, this indicates the formation of percolating PMMA-graphene network. As shown in the Figure

5.2 (b), with increasing concentration of P40 GNP, the phase angles of the composites stayed almost unchanged as compared to the phase angle of pure PMMA (80°), which indicates the P40 GNP had not induced formation of extended structure in PMMA. Overall, no microscopic evolution of the structure had happened to P40 GNP/PMMA composites, though marginal and limited improvement of the viscoelastic properties had been achieved with increasing loading of P40 GNP.

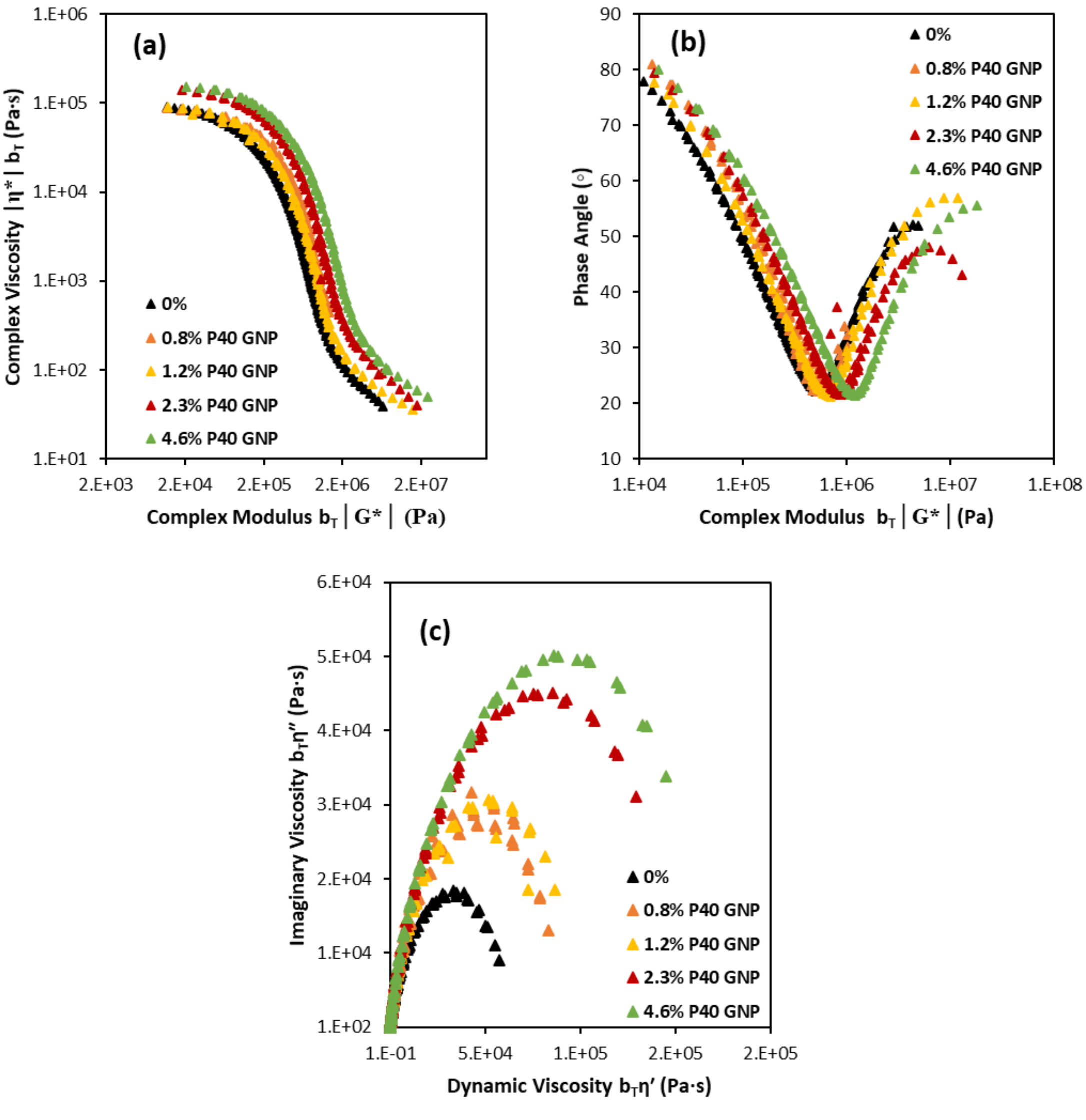

Figure 5.2 Advanced rheological plots of ***crude PO-G****/PMMA composite @ various loading: (a) complex modulus |G*(ω)| vs. complex viscosity |η *(ω)| , (b) van Gurp-Palman plots, and (c) Cole-Cole plots.*

5.2.1.2 Reduced Graphene Oxide

From the Figure 5.3 (a) and (b), a gradual increase of storage modulus and loss modulus can be spotted as the loading of rGO increases from 0.5% to 1.2 vol %, and the most noticeable increase can be spotted when 4.6 vol % of rGO was added. The slope of G′ in low ω region decreased for 4.6 vol % of rGO, the value of G′ (ω=0.1 rad/s) for 4.6 vol % of rGO increased by 23 times as compared to G′ (ω=0.1 rad/s) of pure PMMA. Those indicated the composite was more elastic with increasing loading of rGO. In Figure 5.3 (d), Tan(δ) had demonstrated the same result as the maximum of Tan(δ) decreased gradually with increasing concentration of rGO, which suggested the composites had become more elastic. However, the composites were still liquid-like in the terminal region. The Cole-Cole plot Figure 5.4 (c) shows that all samples do not deviate from the semi-circular shape, which indicates homogenous phase had been achieved by blending the PMMA and the rGO. The radius of the semi-circle increased with the increasing loading, which suggests elasticity of the PMMA had been improved by the favoured interaction between rGO and PMMA. From the van Gurp-Palmen (vGP) plot Figure 5.4 (b), the phase angle decreased significantly from 80° to 62° (ω=0.1 rad/s) as the loading was changed from 0 vol% to 4.6 vol%. The reduction of phase angle confirmed the enhanced elasticity of the composites and the development of microstructure. Unlike composites with other loadings, non-plateau behaviour of $|\eta^*(\omega)|$ at low $|G^*(\omega)|$ values for 4.6 vol% was observed from the $|\eta^*(\omega)|$ vs. $|G^*(\omega)|$ plot in Figure 5.5 (a), this anomaly also corresponds to development of some extended structure in the composite due to the improved rGO and PMMA interaction. Overall, the rGO does demonstrate better interaction with the PMMA and the elastic property of the composites has been improved accordingly with increased loading of the rGO; whereas with low level of loading, the improvement is limited. Some extended network starts to form as the loading is high, nevertheless, the development of the network is limited, and the composites are still viscous liquid material in the low frequency region.

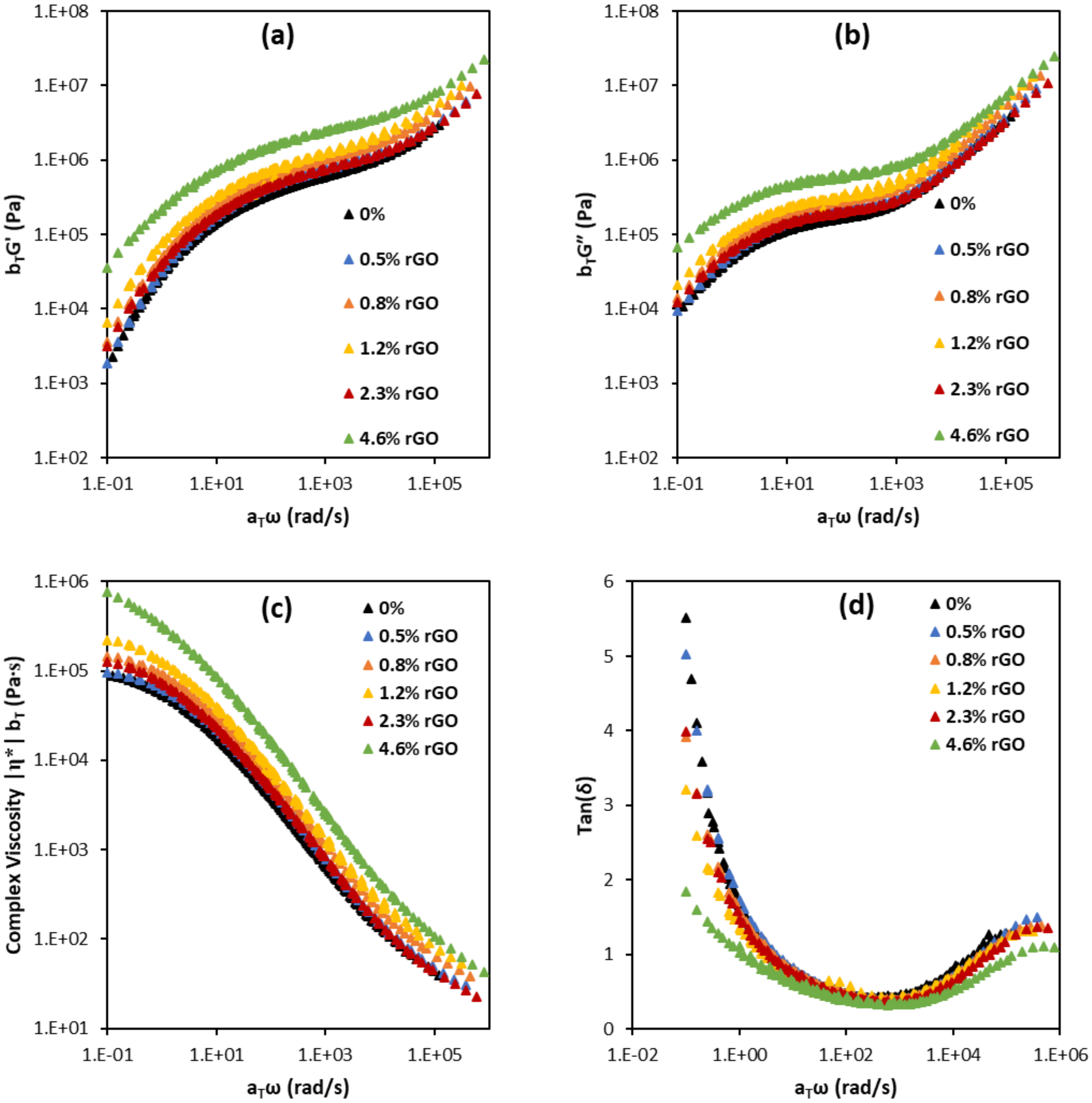

Figure 5.3 Master curves of PMMA composite filling with rGO with various loading at the reference temperature 200 ℃: (a) G' storage modulus, (b) G" loss modulus, (c) |η| complex viscosity, and (d) Tan(δ) loss factor.*

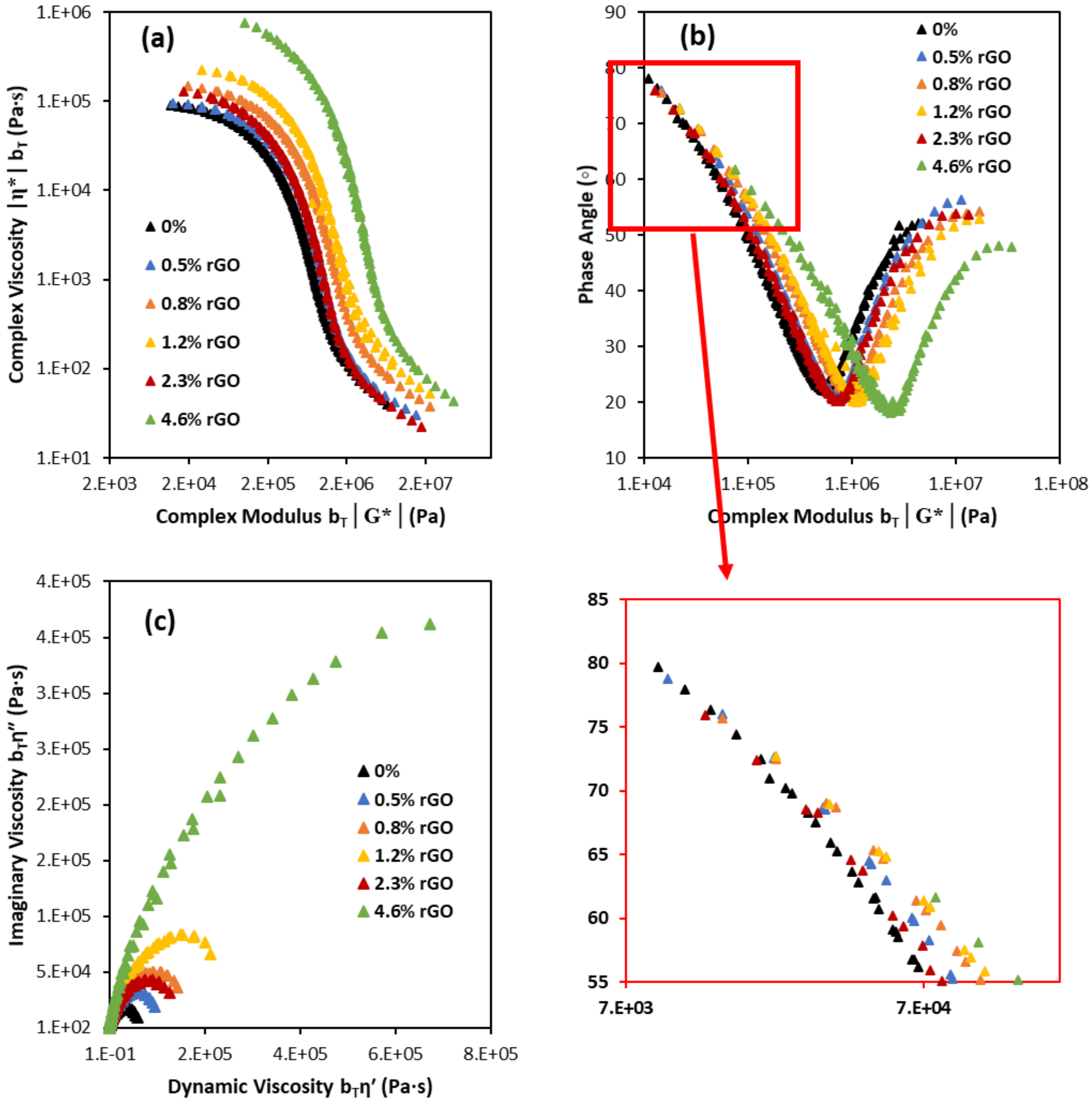

Figure 5.4 Advanced rheological plots of rGO/PMMA composite @ various loading: (a) complex modulus |G(ω)| vs. complex viscosity |η *(ω)| , (b) van Gurp-Palman plots, and (c) Cole-Cole plots. The inset of (b) magnifies the low frequency region, the points with lowest complex modulus corresponds to phase angle values @ ω=0.1 rad/s.*

5.2.1.3 Partially Oxidised Graphene

The same criteria were applied to examine the viscoelastic property of composite modified by using **PO-G**. The viscoelastic properties of **PO-G**/PMMA demonstrated clear concentration dependence. From the Figure 5.5 (a) and (b), the storage moduli G′ and loss modulus G″ of **PO-G**/PMMA composites increased with the increasing loading of the **PO-G**. Although G′ (ω=0.1 rad/s) increased as compared to the pure PMMA, G′ still showed terminal behaviour, which indicates the composites are still liquid. The |η *(ω)| vs reduced frequency plot Figure 5.5 (c) shows that the complex viscosity of the composites were increased with the increasing loading, which confirmed the addition of **PO-G** had improved the viscosity of the composites. It is worthy to notice the 2.3 vol% sample instead of 4.6 vol% had demonstrated the highest elastic response in those two plots. In Figure 5.5 (d), the Tan (δ) followed the similar trend, where a general decay of Tan (δ) could be related to the increase of loading and 2.3 vol% sample had shown the lowest value indicating the composites became more elastic after blending with the **PO-G**.

The three more advanced plots were employed to confirm if the addition of **PO-G** had changed the microscopic structure of the composites and evaluate the interaction between the filler and the PMMA. In the $|\eta^*(\omega)|$ vs. $|G^*(\omega)|$ plot Figure 5.6 (a), divergence instead of Newtonian plateau of the $|\eta^*(\omega)|$ had been observed at low $|G^*(\omega)|$ for all **PO-G**/PMMA samples, which suggests stronger interaction between the **PO-G** and the PMMA as the loading rose. The van Gurp-Palmen (vGP) plot Figure 5.6 (b) shows that the phase angles of 2.3 vol% sample (68°) and 4.6 vol% (73°) were lower than the phase angle of pure PMMA (80°) at low $|G^*(\omega)|$, the changes were indicative of the development of some degree of the extended network in the composite structure. The Cole-Cole plot Figure 5.6 (c) reveals the good miscibility between the PMMA and **PO-G**, as the plot shows all samples have semi-circular shape which suggests good miscibility of **PO-G** in PMMA. The bigger radius, on the other hand, is indicative of improved interaction between the PMMA and **PO-G**. Surprisingly, double loading of **PO-G** (4.6 vol%) did not lead to better rheological properties as compared to that of 2.3 vol% **PO-G**. The reason might be the big and thin (Table 5.1) graphene flakes could reaggregate to form thicker flakes during the preparation process when the concentration of **PO-G** in the solvent was doubled, which hence degrade the interaction between the flakes and the PMMA and have retarded effect on rheological performance of the resulting composite. A similar trend was observed in GO/PMMA composites, where the properties dropped off as the loading of GO increased.[208]

Overall, from the plots it can be seen that the elasticity of the composites can be improved by blending more **PO-G** generally, and only 4.6 vol% deviates the trend without a clear reason. The addition of **PO-G** did induce the formation of some extended network of the composites and favoured interaction was found between the **PO-G** and PMMA. However, the **PO-G**/PMMA composites are still typical viscous liquid material in the low frequency region, they have developed more reinforced structure than graphene composites.

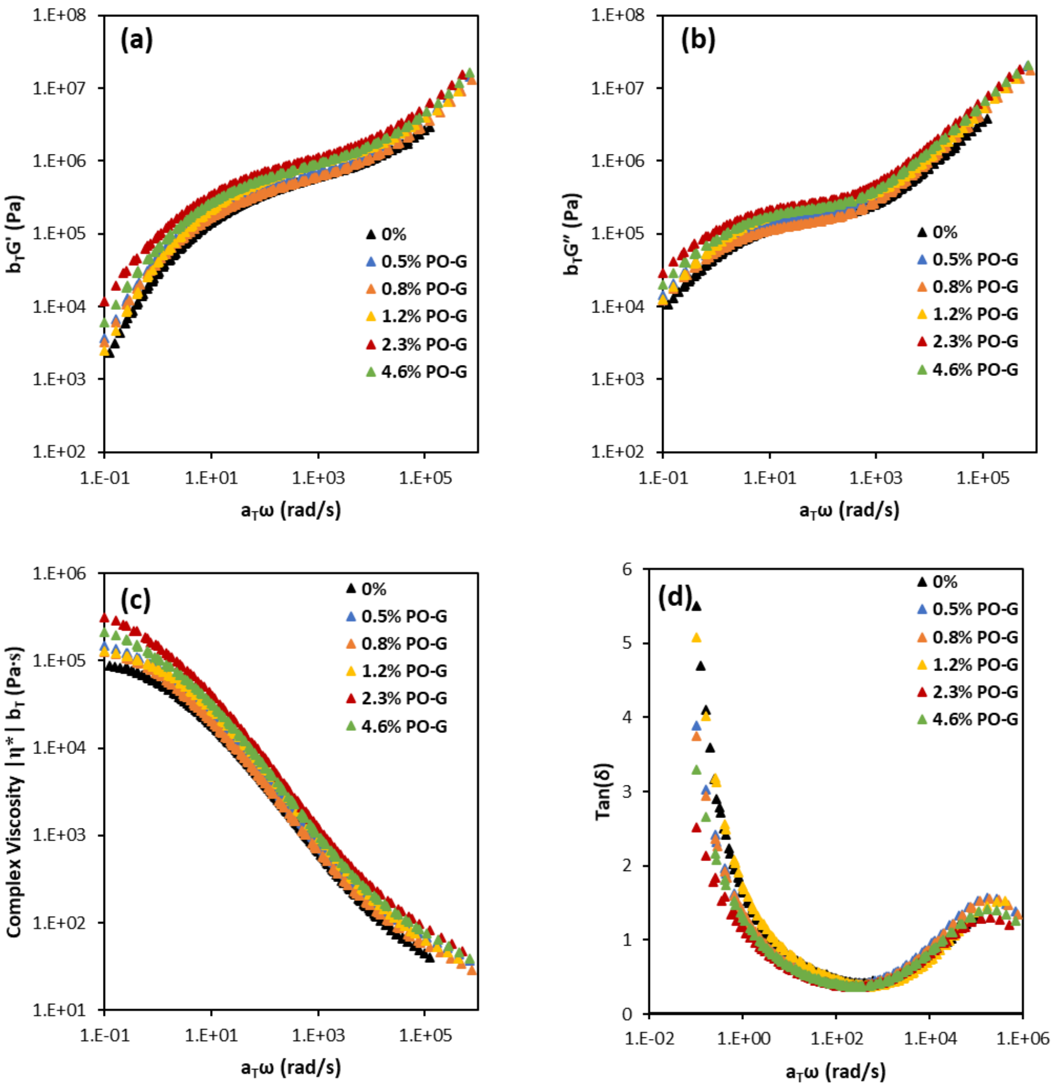

Figure 5.5 Master curves of PMMA composite filling with ***PO-G*** *with various loadings at the reference temperature 200 ℃: (a) G' storage modulus, (b) G" loss modulus, (c) |η*| complex viscosity, and (d) Tan(δ) loss factor.*

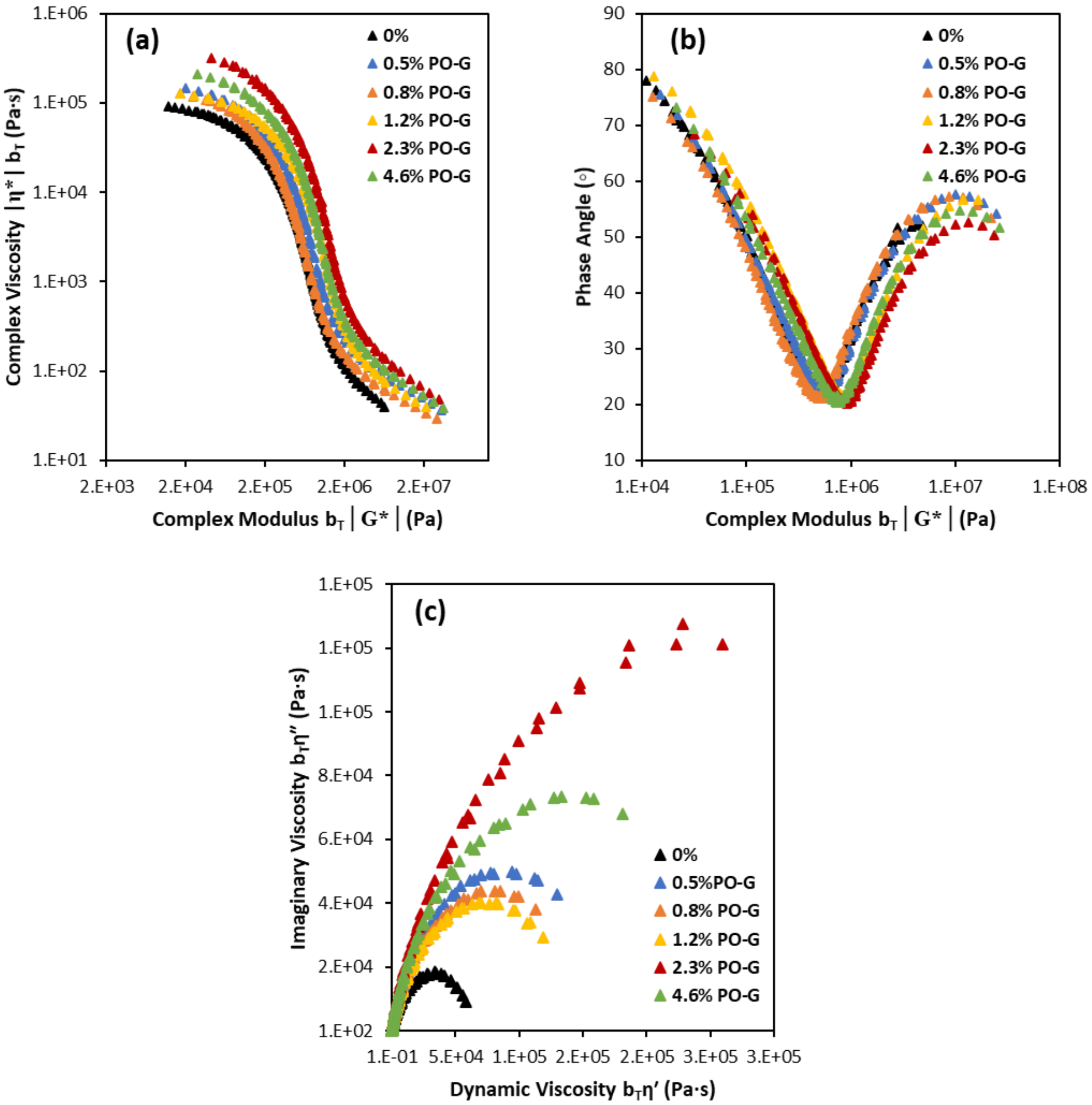

Figure 5.6 Advanced rheological plots of ***PO-G****/PMMA composite @ various loading: (a) complex modulus |G*(ω)| vs. complex viscosity |η *(ω)| , (b) van Gurp-Palman plots, and (c) Cole-Cole plots.*

5.2.2 Rheological Impact of Functionalised Graphene

To assess the effect of different fillers and functional groups, rheological properties of composites prepared by different filler with the same level of loading (2.3 vol% and 4.6 vol%) are put into the same plots. To help the comparison, flake dimensions of each graphene materials were studied by statistical AFM (Table 5.1 & Table 5.2). And the results are summarised in the table below.

Table 5.1 Lateral size measured by AFM of different graphene materials.

Sample	10th Percentile μm	50th Percentile μm	90th Percentile μm	<Average Lateral Size> μm
crude PO-G	0.16	0.53	1.13	0.66
PO-G/PO-G 700 Dis	0.17	0.35	1.53	1.53
rGO	0.12	0.14	0.17	0.15
P40 GNP (EX-P40)	0.16	0.20	0.27	0.22

Table 5.2 Thickness measured by AFM of different graphene materials.

Sample	10th Percentile nm	50th Percentile nm	90th Percentile nm	<Average Thickness> nm
crude PO-G	3.8	12	37.8	18.2
PO-G/PO-G 700 Dis	1.5	2.1	6.7	4
rGO	2.2	4.2	7.8	4.9
P40 GNP (EX-P40)	3.7	6.7	12.5	7.5

Figure 5.7 (a-d) illustrates the viscous and elastic properties of PMMA incorporated with 2.3 vol% of each graphene material. The different viscous and elastic response of **PO-G**/PMMA can be realised as compared with neat PMMA, P40 GNP/PMMA, and rGO/PMMA. As shown by Figure a, upon addition of **PO-G**, the G′ (ω) at low ω has increased by almost six times as compared to the pure PMMA (from 1590 Pa to 9065 Pa). In comparison, upon addition of **P40 GNP** and rGO, the G′ (ω) at low ω only has been improved marginally, suggesting incorporation of **PO-G** would lead to more elastic response. However, none of the filler including the **PO-G**/PMMA has demonstrated non-terminal behaviour as the G′(ω) of all the composites are still dependent on frequency at low ω, indicating none of the composites had developed percolated structure. Tan δ (ω) exhibits similar trend where addition of **PO-G** not only shifts the minimum of the Tan δ (ω) to lower value but also reduces the values of Tan δ (ω) in the low ω region. rGO has moderate effect, as loss factor Tan δ (ω) is decreased to 4 as compared to that (5.5) of neat PMMA. In contrast, addition of **P40 GNP** has little impact on the Tan δ (ω). For a filler showing reinforcing and network-forming effect, the | η*(ω)| value of the composite would be enhanced significantly at low ω region compared to that of the neat PMMA.[202] As shown in Figure 5.7 (c), incorporation of **PO-G** has increased the| η*(ω)| value slightly in the low ω region, and the |η*(ω)| is still frequency dependent, which indicates the **PO-G**/PMMA composite was more resistant to flow. In general, the master curves of G′(ω), G″(ω), | η*(ω)|, and Tan δ (ω) has shown the increased elastic response of **PO-G** and rGO/PMMA, and limited elastic improvement for **P40 GNP**/PMMA at 2.3 vol% loading. When the loading was increased to 4.6 vol%, as shown in Figure 5.9 (a-d), more pronounced

viscoelastic impact on the composite can be found for the rGO instead. As rGO/PMMA composite had shown distinctively high G′(ω), G″(ω), and |η*(ω)|, and low Tan δ $_{(\omega)}$ at low frequency region. More advanced plots have been employed to detect the interaction between the nano fillers and polymer matrices.

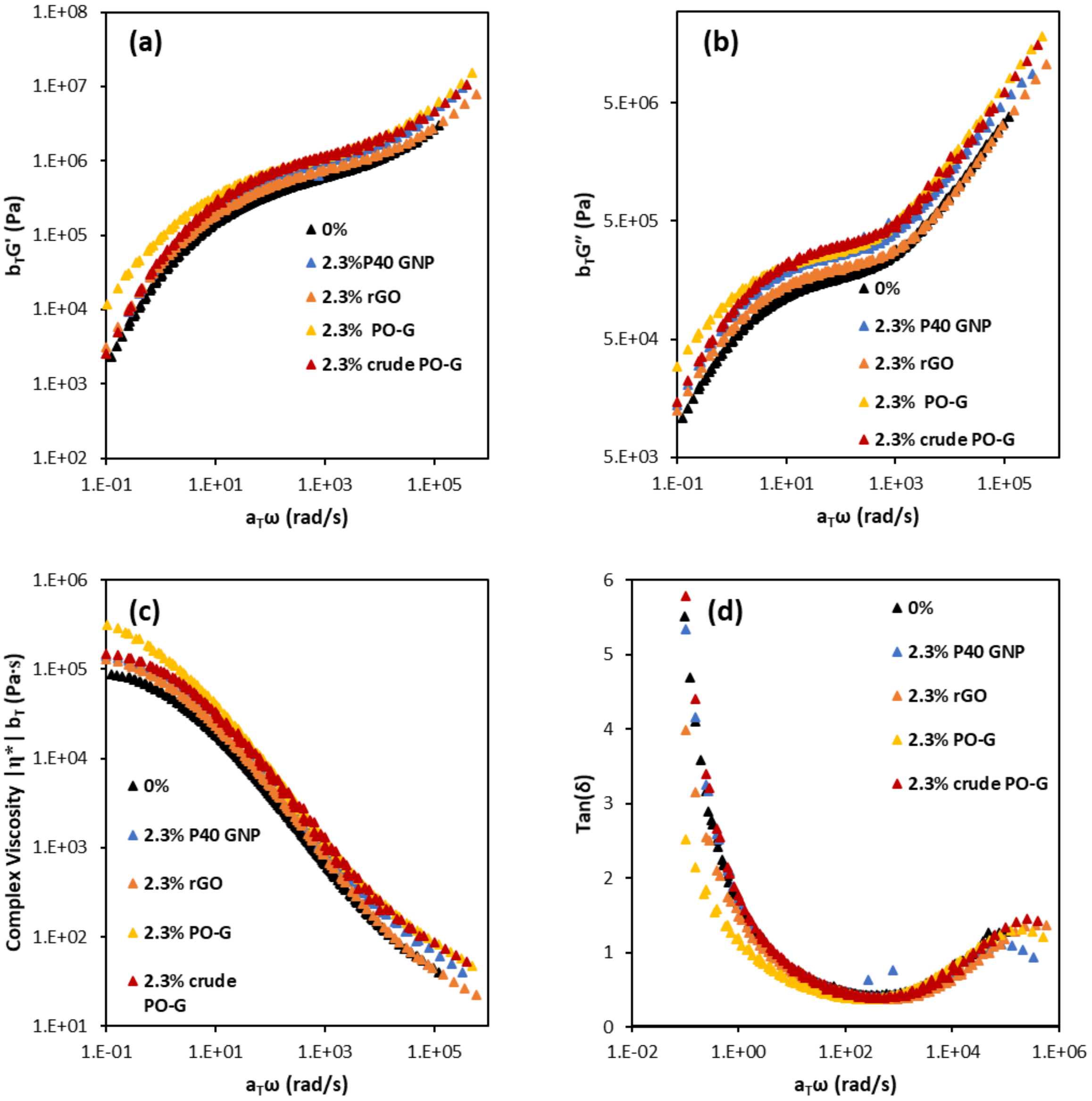

Figure 5.7 Master curves of PMMA composite filling with different kinds of graphene with 2.3 vol% loading at the reference temperature 200 ℃: (a) G′ storage modulus, (b) G″ loss modulus, (c) |η| complex viscosity, and (d) Tan(δ) loss factor.*

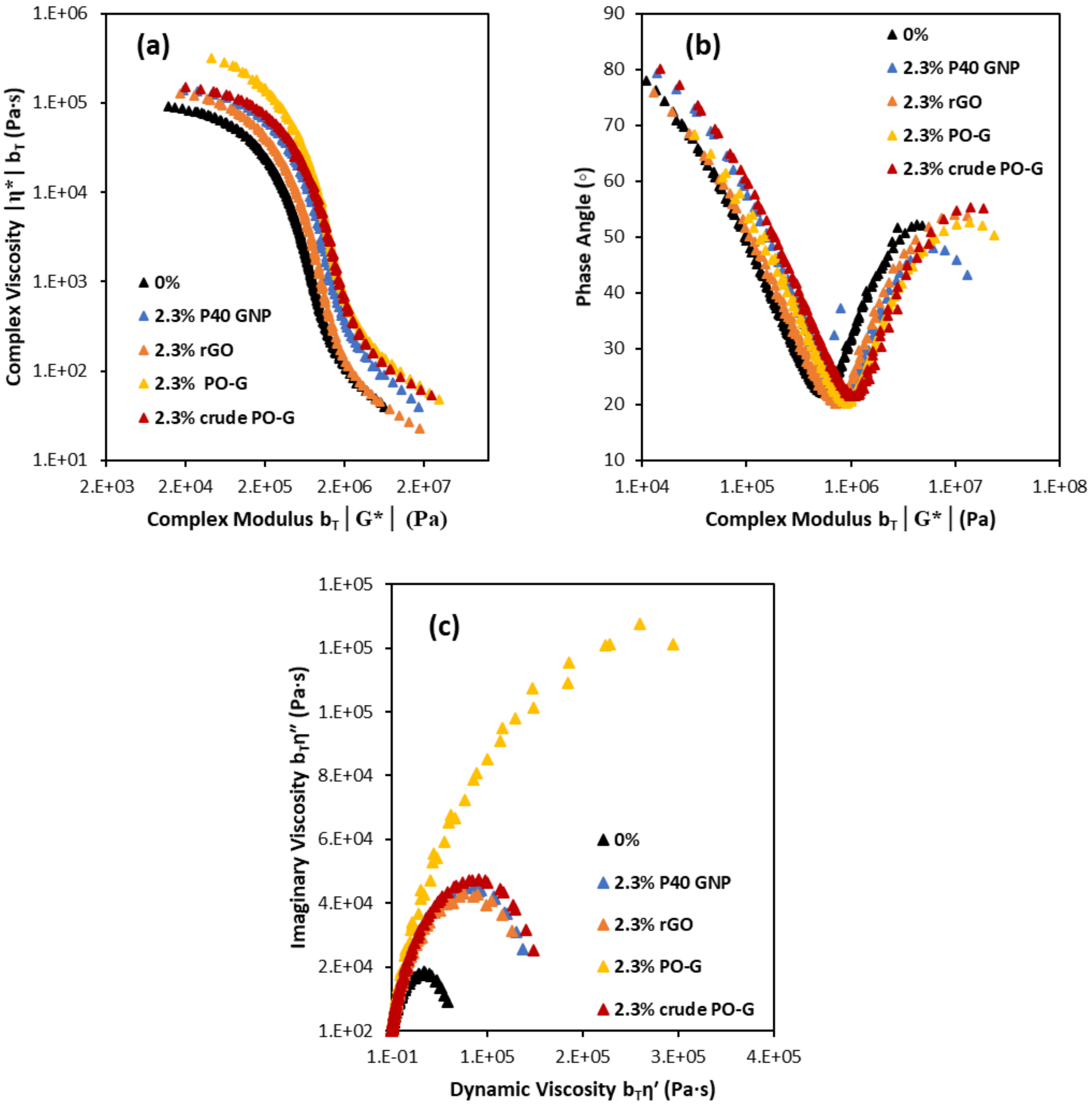

Figure 5.8 Advanced rheological plots of PMMA/Graphene composite @ 2.3 vol% loading: (a) complex modulus |G(ω)| vs. complex viscosity |η *(ω)| , (b) van Gurp-Palman plots, and (c) Cole-Cole plots.*

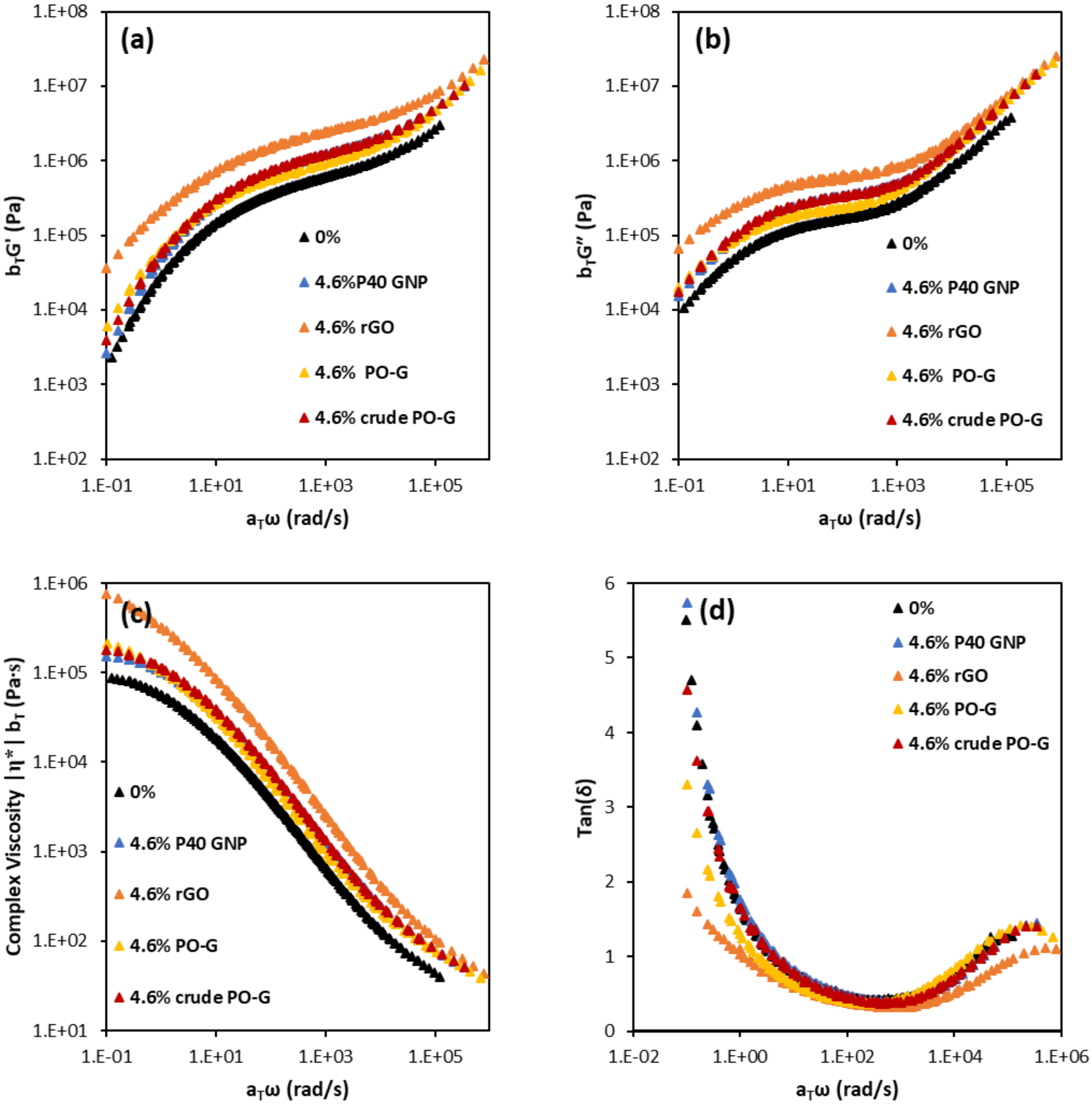

Figure 5.9 Master curves of PMMA composite filling with different kinds of graphene with 4.6 vol% loading at the reference temperature 200 ℃: (a) G' storage modulus, (b) G" loss modulus, (c) $|\eta^*|$ complex viscosity, and (d) Tan(δ) loss factor.

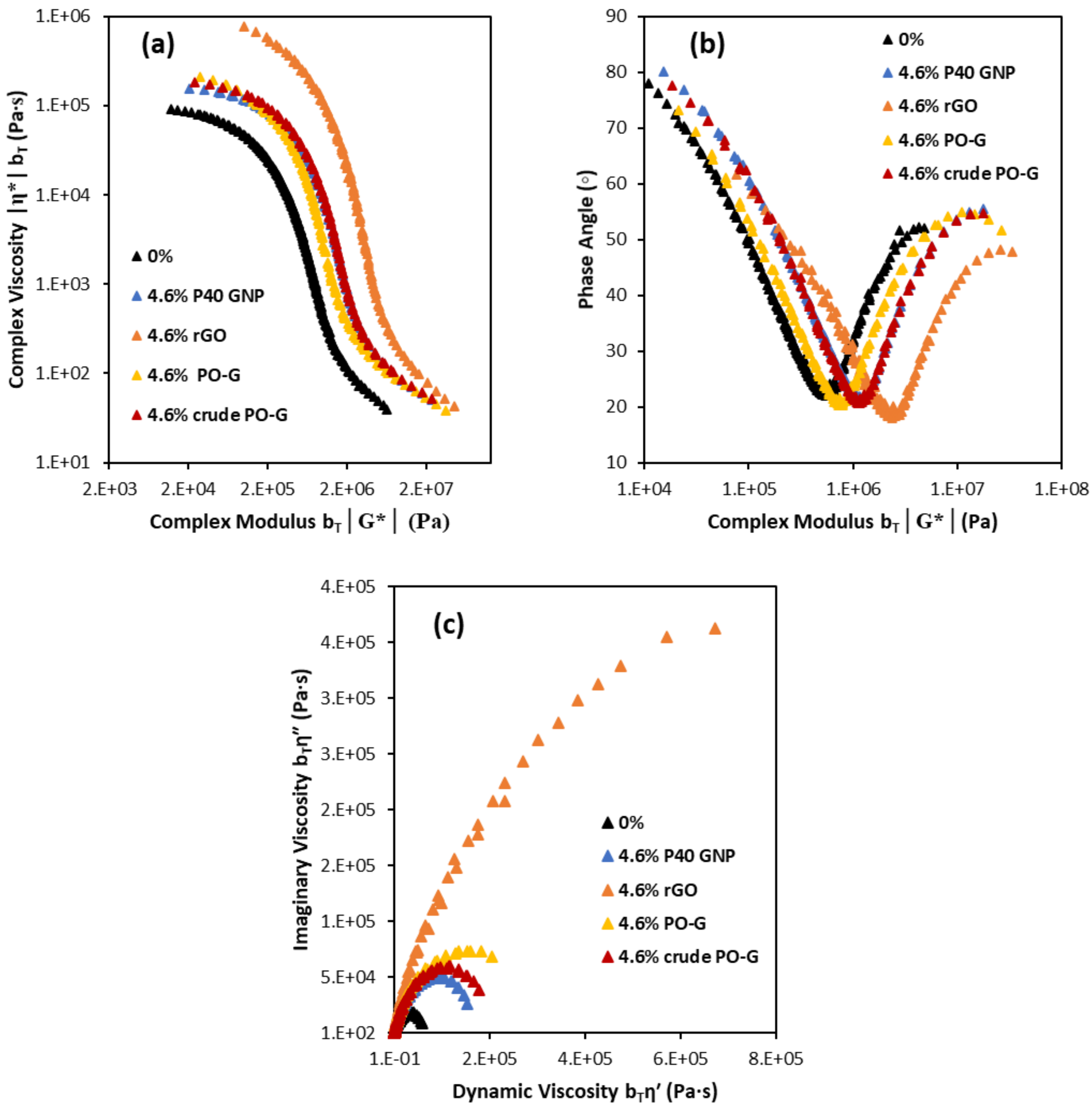

Figure 5.10 Advanced rheological plots of PMMA/Graphene composite @ 4.6 vol% loading: (a) complex modulus |G(ω)| vs. complex viscosity |η *(ω)| , (b) van Gurp-Palman plots, and (c) Cole-Cole plots.*

The network formation was investigated by the van Gurp-Palmen (vGP) plot. For the pure PMMA, the phase angle is close to 80° at low |G*(ω)| value, which corresponds to the liquid-like behaviour of the polymer. As shown in Figure 5.8 (b), almost no change of phase angle has been observed for the PMMA incorporated by (76°) rGO and pristine GNP (79°) at low |G*(ω)| region, suggesting both composites exhibit liquid property. The **PO-G**/PMMA not only demonstrated an obvious shift of the minima for phase angle to lower values, a marked decrease of $\delta_{(\omega)}$ at low |G*(ω)| has also been observed for the composite as the $\delta_{(\omega)}$ has reduced to 60°. This trend can be attributed to the improved compatibility of the functionalised **PO-G** and PMMA and formation of extended structure. Similar changes of phase angle were observed for rGO when the loading was increased to 4.6 vol% Figure 5.10 (b). The phase angle at low |G*(ω)| reduced to 60° and the minima of phase angle decreased to 18°, whereas other composites exhibited little changes. The changes of phase angles suggest 4.6 vol% loading of rGO has induced formation of extended network.

As can be seen from the Figure 5.8 (c), where the Cole-Cole plots of all composites with 2.3 vol% loading are included, P40 GNP, rGO and **PO-G** can be dispersed into PMMA with good homogeneity as the Cole-Cole plots of all composites have the same semi-circular shape but with larger radius. **PO-G**/PMMA composite has the largest radius among the three, this suggests significantly improved interaction was found for **PO-G** over rGO and P40 GNP at this loading level. In Figure 5.10 (c), strong interaction between rGO and PMMA was observed when the loading of filler was 4.6 vol%, whereas **PO-G** exhibited retarded effect on the composite. No phase separation was found for all composites at 4.6 vol% loading due to preservation of the semi-circle.

As shown in the Figure 5.8 (a), the rGO and **P40 GNP** nanocomposites (2.3 vol%) exhibit similar terminal behaviours compared to that of neat PMMA, which suggests both nanocomposites behave as viscous liquids. For the nanocomposite blended with **PO-G**, the Newtonian plateau for viscous liquid is lost, the |η *(ω)| diverges at low |G*(ω)| values instead. The restriction of the flow behaviour upon the addition of **PO-G** implies the stronger interaction between the nanomaterials and polymer matrices. In Figure 5.10 (a), stronger interaction was observed between rGO and the PMMA at 4.6 vol% loading, as the Newtonian plateau of |η *(ω)| was lost at low |G*(ω)| values.

Generally, the influences of the surface functional groups for the graphene on the linear viscoelastic properties of the corresponding nanocomposites have been explored by SAOS test. According to the detailed rheological study, the three kinds of fillers are all dispersible in the PMMA matrices. With the same amount of loading (2.3 vol%), the **PO-G** has demonstrated distinctive reinforcing effects to the polymer matrices among the three fillers, which induce the resulting composites to become more elastic at low ω values. In comparison to **PO-G**, the rGO has small impact and the pristine **P40 GNP** has limited impact on the viscoelastic properties of PMMA in the terminal region, in fact, the viscoelastic responses of the 2.3 vol% P40/PMMA have no remarkable difference compared to that of pure PMMA. It is worthy to notice the trend of viscoelastic properties when the loading is increased to 4.6 vol% rGO rather than **PO-G** demonstrates the most pronounced reinforcing effect in all composites. This can be explained by considering the dimensions of the two materials. By comparing the P10 (rGO= 2.2 nm, **PO-G**= 1.5 nm), P50 (rGO= 4.2 nm, **PO-G**= 2.1 nm), and P90 (rGO= 7.8 nm, **PO-G**= 6.7 nm) of thickness of both materials (Table 5.2), it can be seen that both materials have very similar thickness. The lateral size of rGO (Table 5.1), however, is significantly smaller than that of

PO-G (P10= 0.17 μm, P50= 0.35 μm, and P90= 1.53μm), as P10, P50, and P90 of rGO is only 0.12 μm, 0.14 μm, 0.17 μm. Higher concentration of materials are required for rGO to significantly induce the change on viscoelastic property of the composite. And it is also easier for the bigger material to bend or reaggregate into thicker flakes during the preparation, which in turn explains the retarding performance of the 4.6 vol% **PO-G**.[209]

5.2.3 Impact of Processing Methodology

As reported by relevant studies, nanocomposites derived from different processing procedures would possess different rheological properties.[19,165,177,180,182,196,210] In this study, both samples **PO-G** and **crude PO-G** were fabricated via solution blending. The **PO-G** sample was made by blending PMMA with centrifuged partially oxidised graphene (**PO-G 700 Dis**) in DMF, and the fabrication was done by stirring the dispersion overnight and precipitating the composite in abundant methanol; the other composite was made by blending the PMMA with crude partially oxidised graphene, the mixture was then subjected to probe-sonication after formation of a fine dispersion. The difference of the two materials is the flake dimensions and the dimension distributions. Recalling the AFM study in Chapter 4, the flakes of **PO-G** became thinner and smaller after the centrifuge as the percentage of flakes with z $\leq$4 nm was increased from 16% for **crude PO-G** to 72% **PO-G**, and the proportion of flakes with 1$\geq$ μm was reduced from 33% to 20% (Table 5.3). Same as the last section, the viscoelasticity of the two composites is evaluated by analysing the corresponding rheological measurements.

Table 5.3 Lateral sizes and thicknesses of ***PO-G 700 Dis*** *and* ***crude PO-G****.*

Sample	Average Lateral Size <x> (μm)	Thickness <z> (nm)	Percentage of Flakes z $\leq$ 4 nm (%)	Percentage of Flakes x $\geq$ 1 μm
PO-G 700 Dis	1	4	72%	20%
Crude PO-G	0.66	18.2	16%	33%

As shown in Figure 5.7 (a-d), **PO-G**/ PMMA sample with 2.3 vol% has demonstrated the most pronounced deviation from the pure PMMA, whereas the **crude PO-G** has exhibited small improvement as compared to the neat PMMA. This can be concluded from that the **PO-G** nanocomposites showed lower dependence of G′(ω) in low ω region, a more flattened Tan δ $_{(\omega)}$ in low ω region, and significantly higher |η *(ω)| in the low ω region. The interaction between the two fillers and the PMMA matrices were further elucidated by the more advanced plots vGP plot, Cole-Cole plot, and |G*(ω)| vs. |η *(ω)| plot. Significant reduction of the minimum phase angle and decrease of phase angle at lowest |G*(ω)| value have only been observed for **PO-G**/PMMA sample in the vGP plot, indicating that the addition of graphene without thicker flakes can lead to better reinforcing effect. In the Cole-Cole plot, the **PO-G** composite has appeared to retain the semi-circle shape and have a conspicuous bigger diameter, which are the signs of homogenous blending and strong interaction between the **PO-G** and the PMMA matrix; in contrast, blending of **crude PO-G** only produces semi-circular curve with smaller radius, which indicates uniform dispersion of the **crude PO-G** in the matrix and relatively weaker interaction with the matrix. Finally, **PO-G**/PMMA also displays a noticeable difference in the $|G^*(\omega)|$ vs. $|\eta^*(\omega)|$ plot, where divergence of $|\eta^*(\omega)|$ in the low $|G^*(\omega)|$ region appears. The loss of Newtonian plateau (which can still be seen in **PO-G**/PMMA) corroborates the improved interaction between the **PO-G** and the PMMA. When the loading is increased to 4.6 vol%, the viscoelastic performance of the **PO-G**/PMMA and the **crude PO-G**/PMMA composite are very close (Figure 5.9 and Figure 5.10), since re-aggregation of **PO-G** at higher concentration will result in thicker **PO-G**. For other concentrations, the **PO-G**/PMMA composites generally exhibited higher viscoelasticity than that of the **crude PO-G**/PMMA composites.

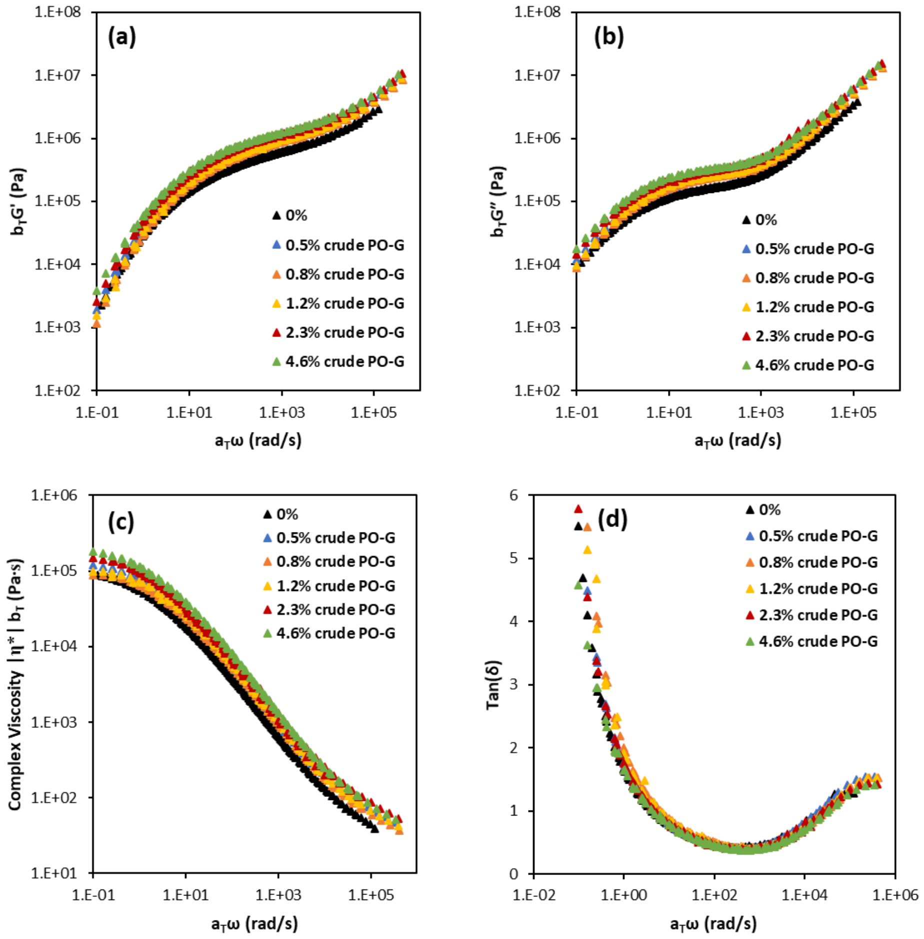

Figure 5.11 Master curves of PMMA composite filling with ***crude PO-G*** *with various loading at the reference temperature 200 ℃: (a) G' storage modulus, (b) G" loss modulus, (c) |η*| complex viscosity, and (d) Tan(δ) loss factor.*

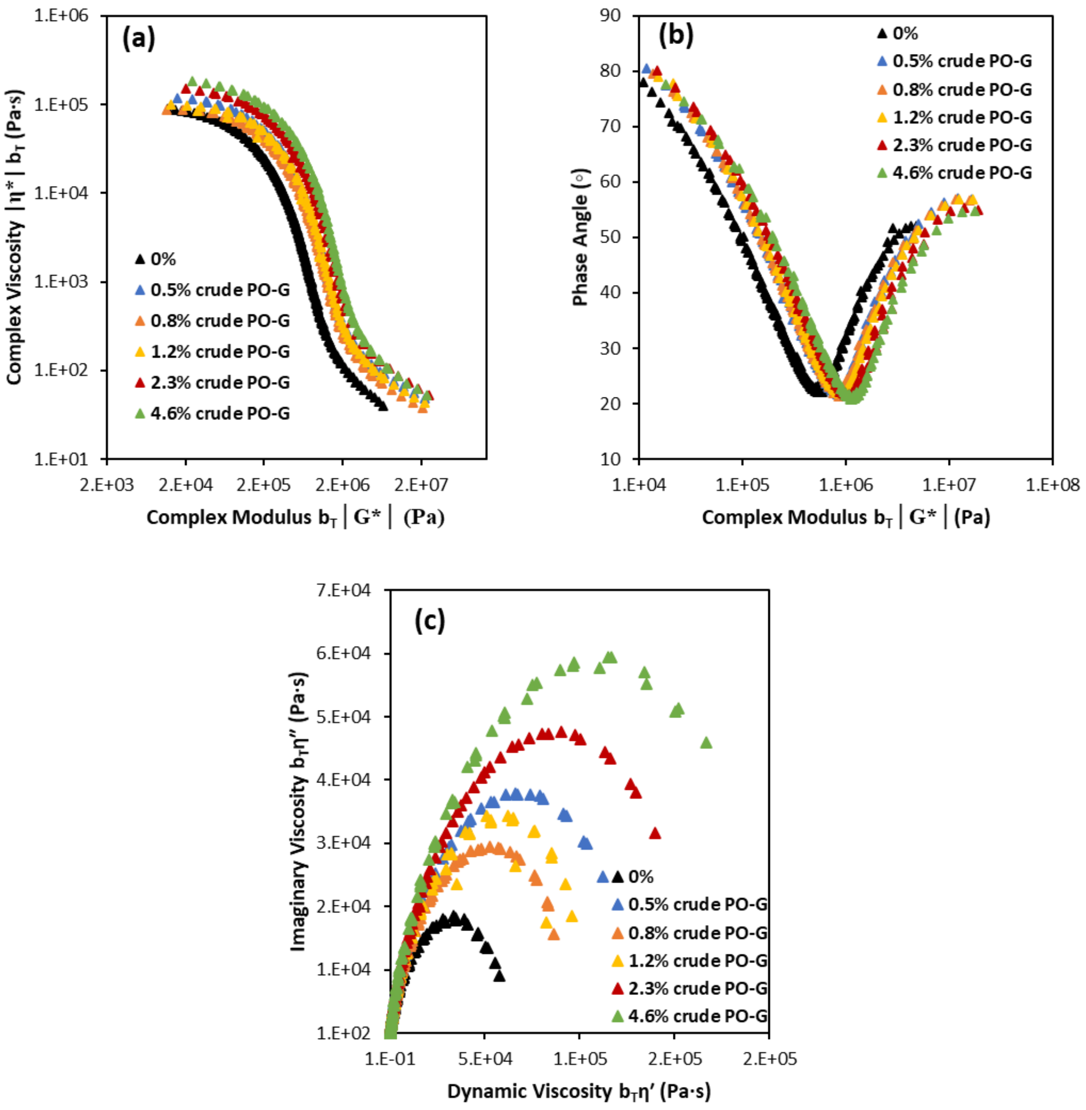

*Figure 5.12 Advanced rheological plots of **crude PO-G**/PMMA composite @ various loading: (a) complex modulus |G*(ω)| vs. complex viscosity |η *(ω)| , (b) van Gurp-Palman plots, and (c) Cole-Cole plots.*

In conclusion, the nanocomposite made by the separated graphene **PO-G** has shown more elasticity in rheological measurements than that fabricated by **crude PO-G**, which reveals a connected structure has been formed in the **PO-G**/PMMA composite due to the improved interaction between the more exfoliated flakes and the polymer matrix. Though **crude PO-G** and **PO-G** were synthesised by the same methodology, and the **crude PO-G** was also probe-sonicated during the preparation of the composites, the presence of large portions of thick materials in the **crude PO-G** induces agglomeration which reduces the available polymer-graphene interactions and hence degrades its reinforcing effect. Therefore, to have composites with better rheological performance, it is critical to remove the thick flakes and prevent agglomeration.

5.3 Conclusion

In this chapter, the viscoelastic properties of PMMA nanocomposites with three different kinds of graphene materials (**PO-G**, **P40 GNP**, and rGO) and loading levels were studied and analysed by rheology. It turns out all graphene materials disperse well in the PMMA matrix, where the addition of **P40 GNP** demonstrated no apparent reinforcing effect to the PMMA, and no network structure was probed in the resulting composites. With help of oxidation, the **PO-G** has exhibited improved interaction with the PMMA, and noticeable network development can be observed for the composite when the loading is 2.3 vol%. The induced viscoelastic change is comparable to the addition of rGO. The superior interaction between **PO-G** and PMMA comes from the functional groups and thin flake of the partially oxidised graphene. Other important physical properties such as thermal conductivity, electrical conductivity, and mechanical properties merit further investigation. In this study, it is also found that graphene material with thinner and larger flakes would have stronger interaction with the matrix and require less loading to improve the elasticity of the PMMA. Better understanding of the impact of the **PO-G** flakes dimensions can be achieved if more refined **PO-G** flakes are used in the future.

It is shown that aggregation of **PO-G** and rGO could lead to reduced interaction between the graphene materials and the PMMA. However, the reason behind it was still not fully understood. One of the reasons could be the re-aggregation of thin and large **PO-G** and rGO flakes during the preparation of the composites, where the over-concentrated **PO-G** dispersion was used. However, the effect of the amount of solvent used to prepare the composites on the aggregation of graphene fillers is not fully understood, and it can be an interesting area of future work. The aggregation can also happen when the composite solution was precipitated out in the anti-solvent. In this case, it is worthy to employ a combined rheometry and impedance spectroscopy to study the effect of shear rate on rheological and electrical properties of the composites are prepared by other processing methods. The introduction of shear force can see if the aggregated graphene can be broken-up and induce electrical or rheological changes.[19] Nevertheless, the study is a positive step towards to understanding the rheological effect of partially oxidised graphene on the PMMA.

Chapter 6. Experimental

6.1 Instrumentation

6.1.1 X-ray photoelectron spectroscopy

The XPS measurements were acquired in a Kratos Axis Nova XPS spectrometer with Al Kα X-Ray source at NEXUS in Newcastle University. The powder of sample was immobilised on a clean aluminium platen with carbon tape. The largest analysis area in this spectrometer (300x700 micron) was used in all the measurements. All the measurements were repeated at three different analysis positions with non-overlapping analysis areas. The charge compensation was done by aligning the maximum of C1s peak to 248.5 eV. The functional groups are identified by deconvolving and fitting the C1s peak with components defined by combination of Gaussian and Lorentzian functions. The asymmetric sp^2 component of graphitic material is fitted by Lorentzian Finite function. Touggard background is employed before every fitting. All the data analysis was done in Casaxps.Survey and scans were acquired with an energy resolution of 160 eV, and 0.4 eV steps, 100 ms dwell time and 2 sweeps.

6.1.2 Thermal Gravimetric analysis

The thermal behaviour of the samples was characterised by Perkin Elmer Pyris I. The measurement was carried out under helium. The samples were heated from room temperature to 110 ℃ in the first place. Held for 30 minutes at 110 ℃, and then the samples were heated to 800 ℃ with a heating rate of 10 ℃/mins.

6.1.3 Electrical Resistivity and Conductivity Measurement

The sheet resistance was measured directly from a thin cake of crude partially oxidised sample (**crude PO-G**). The cake was prepared by vacuum filtration of aqueous dispersions of the **crude PO-G** over PTFE membrane (0.2 um pore size). After filtration, the cake (20 mm diameter, 0.3 mm) with the membrane was transferred to a glass slide by heating for several hours so that the membrane can be peeled off freely. The thickness of the free-standing cake was measured by an electronic caliper. An average thickness was obtained by taking measurement on the different areas of the cake. For the pristine GNP sample, 20 mg samples were weighed out to prepare GNP pellets by a hydraulic press. The average thickness of the resulted pellet is around 0.2 mm and the diameter is 13 mm. The sheet resistance of **PO-G 700 Dis** was measured with the same approach. The electrical measurements were recorded using a Keithley 2602 Source Measure Unit (SMU) and a Guardian SRM232-PROBE-625-45-TC-R=10-FH 4-point, in-line probe head. The spacing between the 4-point probe is 1 mm. The voltage was swept between -1 to 1 V with a 150 points linear sweep, a compliance of 0.1 A and a sweep delay of 100 ms, and correction factors were applied to correct for the sample geometry. The electrical conductivity σ (S/cm) is derived from:

$$\sigma = \frac{1}{\rho}$$

where ρ is the volume resistivity Ω·cm, and can be calculated by the equation below:

$$\rho = \frac{\pi}{\ln{(2)}} \times \frac{V}{I} \times t \times k$$

where t is the sample thickness, k is the geometrical correction factor based on the ratio between the distance of probe inter spacing and the diameter of the sample, V/I is the sheet resistance and can be obtained from the measurement.

6.1.4 UV-Vis Spectroscopy

The UV-Vis spectroscopy was employed to determine the concentration of the dispersion. The UV-Vis spectra of the samples were recorded by an Anglient Technologies Cary 5000 UV-Vis-NIR spectrometer. The samples were contained in the thin quartz cuvettes (path length: 1mm) and the recording range is 200-1000 nm. The concentration of the dispersion was derived by using Beer Lambert Law (A=Ɛ·C·l, where C is the concentration in mg mL^{-1} and l is the light path which is 1 mm) and the absorbance at 660 nm. The extinction coefficient of PO-G 700 Dis is calculated from a standardised stock solution with concentration of 0.188 mg mL^{-1}. Other concentrations were created based on the starting concentration. The extinction coefficient (ε =1105.6 L g^{-1} m^{-1}) was determined by plotting absorbance against corresponding concentration. Similar process was applied to calculate the extinction coefficients of **EP-G** in different solvents (see Section 8.1.3).

6.1.5 Transmission electron Microscopy

Microscopy was conducted on a JOEL-2100 FEG TEM operated at 80 kV under high vacuum conditions. Samples for TEM were prepared by drop depositing onto holey or lacey carbon TEM grids (Cu, 300 mesh, SPI Supplies) a suspension of the material in the chosen solvent, prepared by 5 min bath sonication. Samples were dried in air before imaging and loaded into the TEM using a Gatan model 914 single tilt holder.

6.1.6 Scanning Electron Microscopy

Images were taken on a FEI Helios NanolabTM or SU70 Hitachi microscope operated in the range of 3 - 15 keV under high vacuum conditions. SEM samples were drop casted with a suspension of the material in the DCM on the pre-cleaned silicon. The dispersion was homogenised by 5 min of bath sonication (Ultrawave, U50, 30-40 kHz). Samples were air dried before imaging. Images were collected using a SE detector unless otherwise stated, where some images were collected using a YAG BSE detector. EDXS was collected using an Oxford Instruments EDXS system (INCA x-act LN2-free analytical Silicon Drift Detector), and the data analysis was performed on the proprietary INCA software.

6.1.7 Video of Dispersibility Test

A camera was set up to monitor the dispersibility of the graphene in corresponding solvents for 12.5 hours or 25 hours. 150 pictures were taken in total and the gap between each picture was 5 minutes or 10 minutes depending on the sample. All the dispersion was homogeniseld by bath sonication and shaking before filming. For PO-G series, the concentration of all dispersion was 1mg mL^{-1} and the samples were re-dispersed after purification but without further centrifuge unless otherwise specified. For EP-G series,

6.1.8 Raman Spectroscopy

Raman spectrum was recorded by using a Horiba LabRam Evolution High Resolution spectrometer with Nd:YAG laser (532nm, 2.33eV). Two approaches were employed to prepare samples for acquisition of Raman spectrum. Free powder of the carbon material was loaded on a clean silicon wafer and pressed against the wafer so that the surface is flattened. Alternatively, dispersion of graphitic material could be prepared, and a thin film of the material was obtained by vacuum filtration of the dispersion using a membrane. Statistical Raman Spectroscopy were then performed on an 80 μm × 80 μm area of the samples with a minimum of 225 spots by the same configuration of the spectrometer. All spectra were referenced to the Raman spectrum of a clean silicon wafer. For air sensitive potassium GICs, the acquisition was done by sealing the GICs with parafilm inside a curvette .

6.1.9 X-Ray Powder Diffraction

XRPD was conducted on a Bruker AXS d8 Advance x-ray powder diffractometer; the automated diffractometer operated at 40 kV and 40 mA, with flat-plane geometry, and using a Cu Kα1 X-ray source (λ = 1.5406 Å) or Mo-Ka1 X-ray source (λ = 0.7093 Å). The free powder of the graphitic sample was immobilised on a Vaseline covered glass plate. For the moisture sensitive potassium GICs, the sample was packed into a (diameter:1mm) capillary inside a N_2 filled glove box. The airtight of the capillary was achieved by sealing the opening with superglue. The powder diffraction pattern of potassium GICs was acquired by using Mo-Ka1 X-ray source.

6.1.10 Atomic Force Microscopy

AFM measurement was performed on a Scanning Probe Microscope (SPM) SmartSPM-1000 in tapping mode. The sample for AFM was prepared by drop-casting a diluted aqueous or

NMP dispersion of the graphitic material onto a piece of hydrophilic silicon wafer. The sample was left to dry slowly at 4 ℃ in a fridge over 24 hours. For the samples using NMP as solvent, IPA was used to washed off the NMP, and the sample was dried under a gentle stream of nitrogen. The hydrophilic silicon wafer was obtained by treating the silicon wafer with piranha solution overnight.

6.1.11 Rheology Measurements

Sample preparation: In an 8 mm diameter steel mould, 60 mg of the composite sample was annealed at 180° C for 20 minutes in a hydraulic press under a pressure of 5 tons.

Viscoelastic properties of the prepared samples were collected by using a TA Instruments' Discovery hybrid rheometer and an 8 mm parallel plate geometry. Frequency sweeps (0.1-100 rad/s and 5 points per decade) were performed at different temperatures, ranging from 140-200°C (10 °C steps) °C with 1% strain maximum. Master curves for the viscosity, elastic, and viscous modulus were obtained using the time-temperature superposition and the shift factors calculated according to the WLF (Williams-Landel-Ferry) model.

6.1.12 Calculation of Functionalisation Degree from TGA

The degree of functionalisation is calculated based on the sharp weight loss (from 200 to 600 ℃) which is obtained from TGA data of a sample. By assuming all the weight loss was contributed by one type of functionality, the molar ratio between the functionality and carbon atom can be derived by the equation below:

$$molar\ ratio\ of\ n_{FG}\colon n_{carbon} = \frac{W_{FG}}{M_{FG}}\colon\frac{100 - W_{FG}}{M_{carbon}}$$

Where W_{FG} is weight loss in the TGA; M_{FG} is molecular weight of the functional group; M_{carbon} is molecular weight of the carbon atoms. The functionalisation degree in atomic percentage, hence, can be calculated by the formula (note the molar amount can be directly converted to number of molecules and atoms by dividing the n_{FG} and n_{carbon} with the Avogadro Constant N_A):

$$Functionalisation\ Degree\ (at\%) = \left(\frac{n_{FG}}{n_{FG} + n_{carbon}} \times 100\right)\%$$

6.2 Materials and Synthesis

H_2SO_4 (>95%, Fisher Scientific UK), HCl (37%, Fisher Scientific, UK), P40 GNP (average lateral size: 10 μm, thickness 50-100 nm, Angstron Material), Graphite Flake (Mesh 325, 99%, Alfa Aesar), Graphite Flake (Mesh 80, Sigma Aldrich), Potassium chunk in mineral oil (98%, Sigma Aldrich), Epichlorohydrin, (99%, ACROS Organics), Manganese (III) acetate dihydrate

(97%, Sigma Aldrich), anhydrous Manganese (III) acetate (99%, purity checked by iodometric titration), Manganese permanganate (99%, ACROS Organics), $K_2S_2O_8$ ($\geq$ 99%, Sigma Aldrich), 1,2-Dichloroethane (99.8+%, ACROS Organics), (2,2,6,6-Tetramethylpiperidin-1-yl)oxyl TEMPO (98%, Sigma Aldrich), H_2O_2 27% w/w aqueous solution (Alfa Aesar), 4-iodophenylboronic acid (97%, ACROS Organics), 4-bromophenylboronic acid (97%, Alfa Aesar), 4-nitrophenylboronic acid (97%, ACROS Organics), 4-nitrobenzyl alcohol (99%, Sigma Aldrich), 4-methylbenzenesulfonyl chloride (99%, Sigma Aldrich), 4-iodoaniline (99%, ACROS Organics), THF (Tetrahydrofuran, 99%, Fisher Scientific), NMP (1-Methyl-2-pyrrolidone,99%, Sigma Aldrich), Acetic anhydride (99+%, ACROS Organics), GE Healthcare Whatman™ Nylon Membranes (pore size, 0.2 μm), Hydrophilic PTFE Membrane (pore size, 0.2 μm, Omnipore TM Membrane Filters), anodisc inorganic filter membrane (pore size, 0.2 μm ,Whatman®), Manganese(II) acetate tetrahydrate (99.99%, Sigma Aldrich). All the reagents were used without further purification unless specified otherwise.

6.2.1 Preparation of Graphenide from Stage-1 Potassium GICs

0.4g **F325** graphite or P40 GNP was heated at 120 ℃ for 2 hours in glovebox. The activated graphite was then mixed with a liquid alloy which was derived from mixing 0.163g potassium and 0.041g sodium. The mixture was heated to 200 ℃ for at least 4 hours until the colour of graphite turned to golden. 100 mL dry THF (dried by 4 Å molecular sieves for one week) was added to the mixture and the dispersion was probe-sonicated for 1 hour (250 W, 33% amplitude pulsed 5 sec on and 5 sec off). The sonicated dispersion was left to stir overnight, and then allowed to stand still for 5 hours. The supernatant was then subjected to centrifugation. The centrifugation was done at 2000 rpm for 20mins. The undissolved material was left behind and the clear dispersion, which contained dissolved graphenide was transferred to a sample vial.

6.2.2 Synthesis of Epoxy Functionalised Graphene (EP-G)

0.3 mL of epichlorohydrin was added into 40 mL graphenide solution. The mixture was left to stir overnight in the glovebox. The dispersion was collected by vacuum filtration on a nylon membrane (pore size: 0.2 μm). The solids were rinsed by copious distilled water and acetone and dried in a vacuum oven at 80 ℃ overnight.

6.2.3 Synthesis of Aniline Functionalised Graphene (Aniline-G)

40 mL graphenide solution was stirred with 0.2 mmol 4-iodoaniline overnight in the glovebox. The solids were collected by vacuum filtration on an inorganic alumina membrane (pore size: 0.2 μm). The solids were rinsed by copious acetone and distilled water and dried in a vacuum oven at 80 ℃ overnight.

6.2.4 Synthesis of 4-Nitrobenzyl Tosylates

The synthesis follows a known literature.[211] In detail, 0.33 mL NaOH aqueous solution (5M) was added to 20 mL THF where (0.153 g, 1.1 mmol) 4-nitrobenzyl alcohol was dissolved in a 50 mL round-bottom flask. To this mixture, 0.19 g, 1 mmol 4-methylbenzenesulfonyl chloride in 20 mL THF was added dropwise over 1 hour while the mixture was kept in an ice bath. After the addition, the mixture was allowed to stir for another three hours. The resulting precipitates were collected by vacuum filtration and then rinsed by water and dried in air for 2 hours. The solids were then recrystallised in methanol to give pure 4-nitrobenzyl tosylates, which is fluffy and pale-yellow crystal.

4-Nitrobenzyl Tosylates (MW=307.32 g/mol):150 mg (yield~50%) was obtained from 153 mg 4-nitrobenzyl alcohol. ^{1}H-NMR (400 MHz, DMSO, ppm):

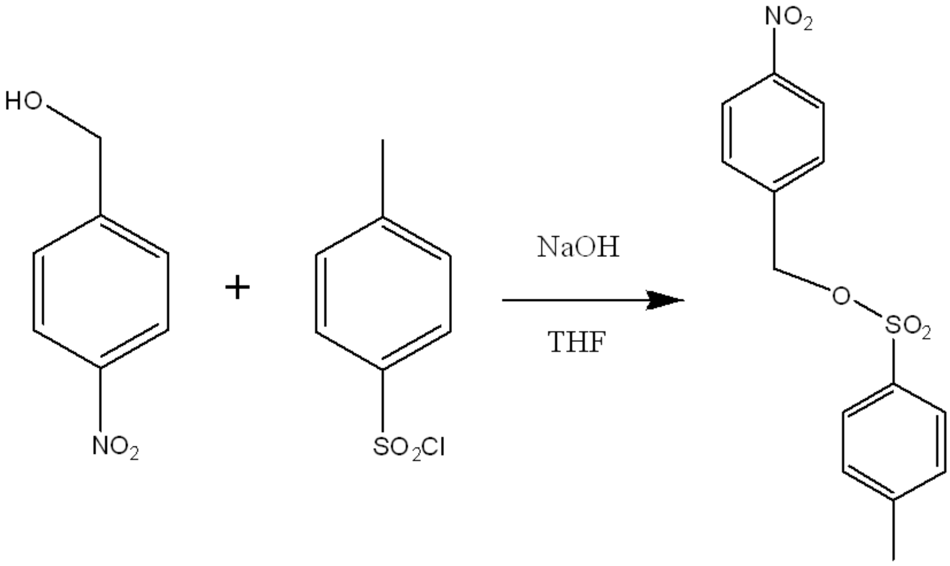

Scheme 6.1 Synthesis of 4-Nitrobenzyl Tosylates from 4-Nitrobenzyl Alcohol.

6.2.5 Synthesis of 4-Nitrobenzyl Functionalised Graphene (4-Nitrobenzyl-G)

40 mL graphenide solution was stirred with 0.2 mmol 4-nitrobenzyl tosylates overnight in the glovebox. The solids were collected by vacuum filtration on an inorganic alumina membrane (pore size: 0.2 μm). The solids were rinsed by copious acetone and distilled water and dried in a vacuum oven at 80 ℃ overnight.

6.2.6 Synthesis of Slowly Oxidised Graphenide

40 mL of potassium graphenide produced in 6.2.1 was left in atmosphere for two days. The black precipitates were collected by vacuum filtration with alumina membrane (pore size: 0.2

μm), the collected solids were washed repeatedly by DI water and acetone for at least 3 times. The washed solids were dried in vacuum oven (80 ℃) over overnight.

6.2.7 Preparation of Stock Dispersion for Extinction Coefficient Calculation

50 mg **EP-G** or **PO-G 700 Dis** were dispersed in 40 mL solvents in a bath sonicator. The uniform dispersion was added into a 50 mL volumetric cylinder and then diluted to 50 mL. 1 mg mL^{-1} stock dispersion was ready to use. Absorbance at 660 nm was recorded for the calculation.

6.2.8 Synthesis of Anhydrous Manganese (III) Acetate

The synthesis of anhydrous manganese (III) acetate follows a known method in a literature [212]. In detail, 34.6 g finely powdered anhydrous manganese (II) acetate and 7.9 g (0.2 mole) finely powdered $KMnO_4$ (0.05 mole) were dispersed in 150 mL glacial acetic acid. The resulted dispersion was shaken and transferred to a roller until all the solids had dissolved. The solution was then filtered through a fritted filter. The filtrate was heated to 75 ℃ for 2 hours after addition of 30 mL acetic anhydride. The $Mn(OAc)_3$ would slowly precipitate out when the mixture was cooled to room temperature and completely precipitate out after 24 hours' rest. The black solids were collected by a fritted glass Buchner funnel and rinsed with 100 mL warm glacial acetic acid to remove potassium acetate. The rinsed sample was then dried for at least 2 hours in *vacuo*. The anhydrous $Mn(OAc)_2$ was obtained by dehydrating $Mn(OAc)_2{\cdot}4H_2O$ *in vacuo* at 100 ℃.

6.2.9 Iodometric Titration

The iodometric titration was employed to check the amount of Mn(III) in the anhydrous $Mn(OAc)_3$ sample derived from a process in the literature. [212] In 50 mL nitrogen sparged distilled water, around 50 mg $Mn(OAc)_3$ sample was dissolved with 5 mL 2 M H_2SO_4 and 2 g KI. In an ice bath, the resulted solution was triply titrated with standard $Na_2S_2O_3$ solution (0.05102 M). As I_3^- species will be generated under the redox condition and hence turn the solution into straw-colour, the end point of the titration is the complete disappearance of the straw colour. To amplify the change of the endpoint, 20 mg mL^{-1} starch solution could be added into the solution. The amount of Mn^{3+} is calculated according to the redox equations below:

$$2Mn^{3+} + 3I^- \longrightarrow 2Mn^{2+} + I_3^-$$

$$2[S_2O_3]^{2-} + I_3^- \longrightarrow [S_4O_6]^{2-} + 3I^-$$

The results of titration are listed in the table below:

%Mn	$Na_2S_2O_3$ (mL)	$Mn(OAc)_3$ (mg)
25.8	4.92	53.3
25.4	4.95	54.4
25.7	4.82	52.4
%Mn for $Mn(OAc)_3$ = 23.7 %Mn for $Mn_3(OAc)_8OH$ [212] = 25.2		

6.2.10 Preparation of Stage-1 Sulphate GICs

To prepare the GIC, $K_2S_2O_8$ (0.5 g) was added to 95% H_2SO_4 (5 mL) with constant stirring. The mixing was accompanied by gas evolution from the partial decomposition of the persulfate anion. After the solution was clear, graphite (0.2g Mesh 80 Graphite flake or P40 GNP) was added to the solution and swirling was continued. The formation of the GIC was indicated by the appearance of the deep blue colour of the graphite. Complete intercalation was achieved in 6-8 h. The obtained mixture was then filtered by PTFE membrane (pore size: 0.2 μm) for 1 hour before reserving in a sample vial.

6.2.11 Functionalisation of Different Types of Graphite by 4-Iodophenylboronic Acid Derived Free Radical

For a typical reaction, in 20 mL 1,2 dichloroethane, 0.081g (0.3 mmol) manganese (III) acetate dihydrate , 0.004 g graphite, and 0.025g 4-iodophenylboronic acid (4-IPB, 0.1 mmol) were added. The mixture was stirred 6 hours at 80℃ oil bath. The obtained mixture was filtered through a nylon membrane (pore size: 0.2 μm). The solids were washed by 20 mL 3% H_2O_2 solution and 20 mL 0.5M HCl solution. The resulted dispersion was filtered through a nylon membrane (pore size: 0.2 μm). The obtained solids were washed by at least 200 mL water and 100 mL acetone. The cleaned solids were dried in a vacuum oven for at least 2 hours.

Mesh 80 Graphite, P40 GNP, and Mesh 325 Graphite Powder were used in this reaction scenario.

6.2.12 Functionalisation of Sulphate GICs by Different Phenylboronic Acids Derived Free Radical

The sulphate GICs obtained by Section 3.3.1 were used in this step. For a typical reaction, in 20 mL 1,2 dichloroethane, 0.081 g (0.3 mmol) manganese (III) acetate dihydrate, 0.0283 g

Mesh 80 sulphate GICs (0.0583 g for P40 Sulphate GICs), and 0.025 g 4-IPB (0.1 mmol) were added. The mixture was stirred 6 hours at 80℃ oil bath. The obtained mixture was filtered through a nylon membrane (pore size: 0.2 μm). The solids were washed by 20 mL 3% H_2O_2 solution and 20 mL 0.5M HCl solution. The resulted dispersion was filtered through a nylon membrane (pore size: 0.2 μm). The obtained solids were washed by at least 200 mL water and 100 mL acetone. The cleaned solids were dried in a vacuum oven for at least 2 hours.

In parallel experiments, 4-nitro-phenylboronic acid (4-NPB) and 4-bromo-phenylboronic acid (4-BPB) were used for each type of Sulphate GICs. Two controlled experiments were performed with presence of manganese (III) acetate dihydrate or 4-IPB only.

6.2.13 TEMPO Radical Quenching Reaction

A radical quencher reaction was performed by using P40 sulphate GICs. In detail, in 20 mL 1,2 dichloroethane, 0.081 g (0.3 mmol) manganese (III) acetate dihydrate , 0.0283 g Mesh 80 sulphate GICs (0.0483 g for P40 Sulphate GICs), 0.0312 TEMPO (0.2 mmol), and 0.025 g 4-IPB (0.1 mmol) were added. The obtained mixture was filtered through a nylon membrane (pore size: 0.2 μm). The solids were washed by 20 mL 3% H_2O_2 solution and 20 mL 0.5 M HCl solution. The resulted dispersion was filtered through a nylon membrane (pore size: 0.2 μm). The obtained solids were washed by at least 200 mL water and 100 mL acetone. The cleaned solids were dried in a vacuum oven at 80 ℃ for at least 2 hours.

6.2.14 Preparation of Partially Oxidised Graphene

For a standard condition to prepare partially oxidised graphite (**crude PO-G**), in 20 mL 1,2 dichloroethane, 0.081 g (1 eq. molar regard to amount sulphuric acid in SGIC) manganese (III) acetate dihydrate, 0.0581 g sulphate GIC (1 eq. molar) were added. The weight of sulphuric acid can be worked out roughly by weighing the SGICs and calculating the theoretical weight of stage-1 SGICs ($C_{24}H_5S_2O_8$) from the GNP used. Due to the hygroscopic nature of concentrated sulphuric acid, this value can only be estimated. The mixture was stirred 6 hours at 80 ℃ oil bath. The obtained mixture was filtered through a nylon membrane (pore size: 0.2 μm). The solids were washed by cold 20 mL 3% H_2O_2 solution and 20 mL 0.5 M HCl solution. The resulted dispersion was filtered through a nylon membrane (pore size: 0.2 μm). The obtained solids were washed by at least 200 mL water and 100 mL acetone. The cleaned solids were dried in a vacuum oven for at least 2 hours.

PO-W was prepared by replacing 1,2 dichloroethane with water and running the reaction without presence of $Mn(OAc)_3{\cdot}2H_2O$. **G-2** was prepared by running the standard condition without presence of $Mn(OAc)_3{\cdot}2H_2O$. **PO-WOM** was obtained by washing **G-2** with excessive water. **PO-M** was prepared by running the standard condition by replacing 1,2 dichloroethane with water.

For the parallel and control reactions, different temperature, reaction time, and molar ratio of sulphate GICs and Mn (III) acetate dihydrate were applied.

For the radical quenching reaction, equivalent amount of TEMPO (0.3 mmol) was added to the standard condition.

6.2.15 Separation of Partially Oxidised Graphene

The purified PO-G sample was re-dispersed in water by bath sonication, and then centrifuged at 300 rpm (11 rcf) to remove the less dispersible materials. The sediments after centrifugation was labelled as **300 SeD**. The supernatant was filtered, and the solids were dried and labelled as **300 Dis**.(Figure 6.1)

The 300 Sed sample was re-dispersed in 20 mL water and probe sonicated at (250W) for 0.5 hour. The resulted sample was labelled as **300 SeD AFPS**. The **crude PO-G** water dispersion was probe-sonicated at 250W for 0.5 hour and centrifuged at 700 rpm (65 rcf), the supernatant was filtered by a nylon membrane (pore size: 0.2 μm). The obtained solids were dried and labelled as **PO-G 700 Dis or PO-G**. To separate more **PO-G 700 Dis** sample, probe-sonication and centrifuge process was repeated for the sediment obtained by 700 rpm for two to three times.

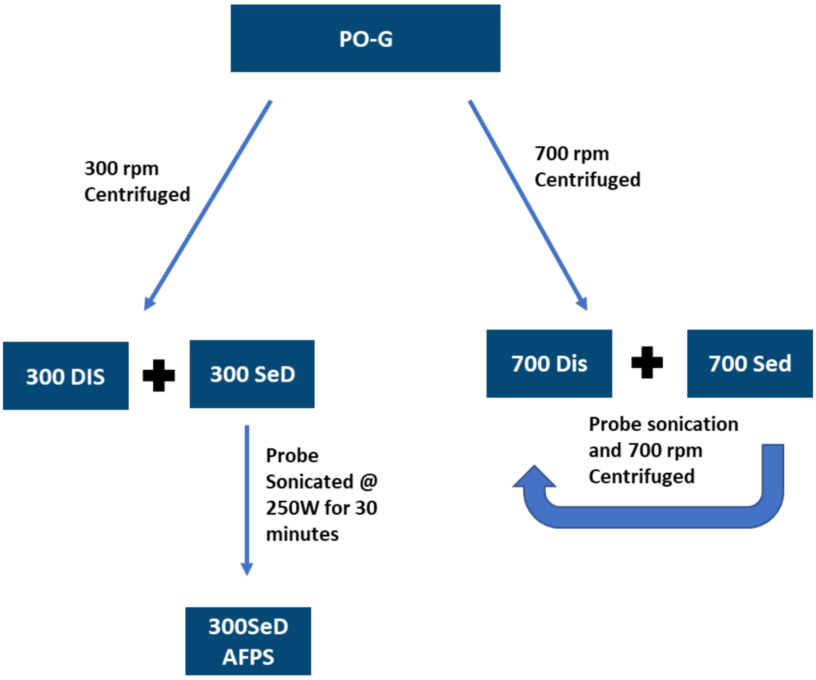

*Figure 6.1 Separation process for the **crude PO-G***

6.2.16 Preparation of Partially Oxidised Graphene in Organic Solvents

For a standard condition to prepare partially oxidised graphene, the solvent 1,2 DCE was replaced by ODCB and toluene.

6.2.17 Preparation of Partially Oxidised Graphene in Bulk Sulphuric Acid

The partial oxidation of Stage-1 SGIC was carried out as following steps: stage-1 SGIC was prepared by dissolving 1 g potassium persulphate into 20 mL concentrated sulphuric acid with 0.24 g P40 GNP. The preparation was complete after 1 hour of stirring. 2 g of anhydrous $Mn(OAc)_3$ and 200 μL water were added into the stage-1 SGIC and the mixture was heated to 85 ℃ for 3 hours. In the last hour, the temperature was brought to 95 ℃. The mixture was filtered through a glass frit after cooling to room temperature and washed by copious water. In a 100 mL beaker, 0.1 g crude product was dispersed in 70 mL DI water. The dispersion was homogenised in a bath sonicator and then probe-sonicated for 30 minutes. The dispersion was then centrifuged at 700 rpm to remove the large flakes or aggregates and unreacted graphite. The sediment was retained and subjected to repetitive sonication and centrifuge to yield more dispersible graphene. The combined supernatant was filtered through an alumina membrane (0.2 μm). The isolated solids were dried in vacuum oven (80 ℃) and labelled as **PO-G-BS**.

6.2.18 Preparation of Graphene Oxide

The graphite oxide was prepared by using modified Hummers method, where 5 g of graphite flake (mesh 325) was dissolved in 120 mL concentrated sulphuric acid. The mixture was cooled down to 0 ℃ and then 5 g of potassium permanganate was slowly added in with stirring so that the temperature of the mixture did not exceed 10 ℃. After addition of potassium permanganate,240 mL ice-cool water was added into the mixture slowly after the mixture was heated to 35 ℃ for 2 hours. The mixture was further diluted with 700 mL DI water and then washed by hydrogen peroxide (33%) and HCl (6 M) until effervescence stopped. The acidic mixture was washed by centrifuge until neutral. The washed graphite oxide was freeze-dried for 3 days.

50 mg of graphite oxide was dissolved in 50 mL DI water, the dispersion was probe-sonicated for 30 minutes (250 W, 33% amplitude, 5 s pulse). The exfoliated dispersion was centrifuged (1000 rpm) to remove aggregates and thick materials and the supernatant was retained for further use.

6.2.19 Hydrazine Reduced Graphene oxide

20 mL 1 mg mL^{-1} aqueous GO dispersion derived from **6.2.15** was probe sonicated and then refluxed with hydrazine monohydrate (34 μL) with stirring for 12 hours. The reduced graphene

oxide will precipitate out and the mixture was collected by vacuum filtration on a nylon membrane. The solids were washed by water and acetone repetitively and dried at 50 ℃ in a vacuum oven.

6.2.20 Exfoliated P40 GNP

1 mg mL^{-1} P40 GNP and NMP dispersion was prepared by dispersing 30 mg P40 GNP into 30 mL NMP. The dispersion was homogenised by bath sociation for 30 minutes. The dispersion was then subjected to probe-sonication for 30 minutes (250 W, 33% amplitude, 5s pulse). After sonication, the dispersion was centrifuged at 1000 rpm to remove large particles, the supernatant was filtered by alumina membrane (pore size: 0.2 μm) and the collected solid was washed thoroughly by acetone and IPA. The washed solids were dried in vacuum oven (100 ℃) overnight. The obtained products were labelled as **Ex-P40**.

6.2.21 Preparation of Hydrophilic Silicon Wafer

The silicon wafers were cleaned by wet tissue to remove any obvious stains and contaminates. The wafers were dried under nitrogen stream after being bath-sonicated in a mixture of water and IPA (50:50) for 30 minutes. The dried silicon wafers were immersed in piranha solution (concentrated H_2SO_4: 30% H_2O_2=3:1) overnight. The solution was added slowly to copious water in an ice bath and the silicon wafer was fished out and dried under nitrogen stream. The cleaned silicon wafers were stored in high purity water.

6.2.22 Preparation of Graphene/PMMA Nanocomposite

The **crude PO-G**, **P40 GNP**, **PO-G**, and rGO**/PMMA** samples were produced by the following procedures: PMMA (MW=87k, ρ= 1.19 g cm^{-3}) and graphene (**crude PO-G** and pristine **P40 GNP,** the density ρ_G is assumed to be 2.1 g cm^{-3}) [208] were dispersed in DMF by overnight stirring until all PMMA solids had been dissolved. The homogenous dispersion was then subjected to 30 minutes probe-sonication. The composite was obtained by precipitating dropwise into excessive methanol. The solids were stirred further in methanol for 30 minutes (250 W, pulse: 5 seconds and 5 seconds off) and stirred in fresh methanol for several hours before filtration. The filtered composites were dried in vacuum oven at 50 ℃ for several hours.

The **PO-G** or rGO/PMMA were produced by dispersing the **PO-G** or rGO and PMMA in 5 mL DMF by overnight stirring until all PMMA solids had been dissolved. The composite was obtained by precipitating dropwise into excessive methanol. The solids were stirred further in methanol for 30 minutes and stirred in fresh methanol for several hours before filtration. The filtered composites were dried in vacuum oven at 60 ℃ for several hours. The **PO-G** was obtained by following procedures: probe-sonicated aqueous dispersion of crude partially oxidised graphene for 30 minutes (250 W, pulse: 5 seconds and 5 seconds off) and centrifuged the dispersion at 300 rpm for 30 minutes. The FG was obtained by filtering the supernatant and drying the obtained solids.

Chapter 7. Reference

(1) Lee, C.; Wei, X.; Kysar, J. W.; Hone, J. Measurement of the Elastic Properties and Intrinsic Strength of Monolayer Graphene. *Science (80-.).* **2008**, *321* (5887), 385 LP – 388. https://doi.org/10.1126/science.1157996.

(2) Balandin, A. A.; Ghosh, S.; Bao, W.; Calizo, I.; Teweldebrhan, D.; Miao, F.; Lau, C. N. Superior Thermal Conductivity of Single-Layer Graphene. *Nano Lett.* **2008**, *8* (3), 902–907. https://doi.org/10.1021/nl0731872.

(3) Nair, R. R.; Blake, P.; Grigorenko, A. N.; Novoselov, K. S.; Booth, T. J.; Stauber, T.; Peres, N. M. R.; Geim, A. K. Fine Structure Constant Defines Visual Transparency of Graphene. *Science (80-.).* **2008**, *320* (5881), 1308 LP – 1308. https://doi.org/10.1126/science.1156965.

(4) Castro Neto, A. H.; Guinea, F.; Peres, N. M. R.; Novoselov, K. S.; Geim, A. K. The Electronic Properties of Graphene. *Rev. Mod. Phys.* **2009**, *81* (1), 109–162. https://doi.org/10.1103/RevModPhys.81.109.

(5) Lau, C. N.; Bao, W.; Velasco, J. Properties of Suspended Graphene Membranes. *Mater. Today* **2012**, *15* (6), 238–245. https://doi.org/10.1016/S1369-7021(12)70114-1.

(6) Kim, K. S.; Zhao, Y.; Jang, H.; Lee, S. Y.; Kim, J. M.; Kim, K. S.; Ahn, J. H.; Kim, P.; Choi, J. Y.; Hong, B. H. Large-Scale Pattern Growth of Graphene Films for Stretchable Transparent Electrodes. *Nature* **2009**, *457* (7230), 706–710. https://doi.org/10.1038/nature07719.

(7) Bulusheva, L. G.; Tur, V. A.; Fedorovskaya, E. O.; Asanov, I. P.; Pontiroli, D.; Riccò, M.; Okotrub, A. V. Structure and Supercapacitor Performance of Graphene Materials Obtained from Brominated and Fluorinated Graphites. *Carbon N. Y.* **2014**, *78*, 137–146. https://doi.org/10.1016/j.carbon.2014.06.061.

(8) Zhang, Y.; Sullivan, J. P.; Bose, A. Rheological and Microstructural Characterization of Aqueous Suspensions of Carbon Black and Reduced Graphene Oxide. *Colloids Surfaces A Physicochem. Eng. Asp.* **2020**, *592* (February), 124591. https://doi.org/10.1016/j.colsurfa.2020.124591.

(9) Wu, Q.; Xu, Y.; Yao, Z.; Liu, A.; Shi, G. Supercapacitors Based on Flexible Graphene/Polyaniline Nanofiber Composite Films. *ACS Nano* **2010**, *4* (4), 1963–1970. https://doi.org/10.1021/nn1000035.

(10) Tang, B.; Hu, G.; Gao, H.; Hai, L. Application of Graphene as Filler to Improve Thermal Transport Property of Epoxy Resin for Thermal Interface Materials. *Int. J. Heat Mass Transf.* **2015**, *85*, 420–429. https://doi.org/10.1016/j.ijheatmasstransfer.2015.01.141.

(11) Gao, C.; Zhang, S.; Wang, F.; Wen, B.; Han, C.; Ding, Y.; Yang, M. Graphene Networks with Low Percolation Threshold in Abs Nanocomposites: Selective Localization and Electrical and Rheological Properties. *ACS Appl. Mater. Interfaces* **2014**, *6* (15), 12252–12260. https://doi.org/10.1021/am501843s.

(12) Whitby, R. L. D. Chemical Control of Graphene Architecture: Tailoring Shape and Properties. *ACS Nano* **2014**, *8* (10), 9733–9754. https://doi.org/10.1021/nn504544h.

(13) Olabi, A. G.; Abdelkareem, M. A.; Wilberforce, T.; Sayed, E. T. Application of Graphene in Energy Storage Device – A Review. *Renew. Sustain. Energy Rev.* **2021**, *135* (June 2020), 110026. https://doi.org/10.1016/j.rser.2020.110026.

(14) Warda, M. Graphene Field Effect Transistors: A Review. **2020**, No. January.

(15) Choi, J. H.; Lee, J.; Byeon, M.; Hong, T. E.; Park, H.; Lee, C. Y. Graphene-Based Gas Sensors with High Sensitivity and Minimal Sensor-to-Sensor Variation. *ACS Appl. Nano Mater.* **2020**, *3* (3), 2257–2265. https://doi.org/10.1021/acsanm.9b02378.

(16) Hernandez, Y.; Nicolosi, V.; Lotya, M.; Blighe, F. M.; Sun, Z.; De, S.; McGovern, I. T.; Holland, B.; Byrne, M.; Gun’ko, Y. K.; Boland, J. J.; Niraj, P.; Duesberg, G.; Krishnamurthy, S.; Goodhue, R.; Hutchison, J.; Scardaci, V.; Ferrari, A. C.; Coleman, J. N. High-Yield Production of Graphene by Liquid-Phase Exfoliation of Graphite. *Nat. Nanotechnol.* **2008**, *3* (9), 563–568. https://doi.org/10.1038/nnano.2008.215.

(17) Khan, U.; O’Neill, A.; Lotya, M.; De, S.; Coleman, J. N. High-Concentration Solvent Exfoliation of Graphene. *Small* **2010**, *6* (7), 864–871. https://doi.org/10.1002/smll.200902066.

(18) Hamilton, C. E.; Lomeda, J. R.; Sun, Z.; Tour, J. M.; Barron, A. R. High-Yield Organic Dispersions of Unfunctionalized Graphene. *Nano Lett.* **2009**, *9* (10), 3460–3462. https://doi.org/10.1021/nl9016623.

(19) Boothroyd, S. C.; Johnson, D. W.; Weir, M. P.; Reynolds, C. D.; Hart, J. M.; Smith, A. J.; Clarke, N.; Thompson, R. L.; Coleman, K. S. Controlled Structure Evolution of Graphene Networks in Polymer Composites. *Chem. Mater.* **2018**, *30* (5), 1524–1531. https://doi.org/10.1021/acs.chemmater.7b04343.

(20) Khan, U.; O'Neill, A.; Lotya, M.; De, S.; Coleman, J. N. High-Concentration Solvent Exfoliation of Graphene. *Small* **2010**, *6* (7), 864–871. https://doi.org/10.1002/smll.200902066.

(21) Hernandez, Y.; Nicolosi, V.; Lotya, M.; Blighe, F. M.; Sun, Z.; De, S.; McGovern, I. T.; Holland, B.; Byrne, M.; Gun'ko, Y. K.; Boland, J. J.; Niraj, P.; Duesberg, G.; Krishnamurthy, S.; Goodhue, R.; Hutchison, J.; Scardaci, V.; Ferrari, A. C.; Coleman, J. N. High-Yield Production of Graphene by Liquid-Phase Exfoliation of Graphite. *Nat. Nanotechnol.* **2008**, *3* (9), 563–568. https://doi.org/10.1038/nnano.2008.215.

(22) Oyer, A. J.; Carrillo, J. M. Y.; Hire, C. C.; Schniepp, H. C.; Asandei, A. D.; Dobrynin, A. V.; Adamson, D. H. Stabilization of Graphene Sheets by a Structured Benzene/Hexafluorobenzene Mixed Solvent. *J. Am. Chem. Soc.* **2012**, *134* (11), 5018–5021. https://doi.org/10.1021/ja211225p.

(23) Xu, L.; McGraw, J. W.; Gao, F.; Grundy, M.; Ye, Z.; Gu, Z.; Shepherd, J. L. Production of High-Concentration Graphene Dispersions in Low-Boiling-Point Organic Solvents by Liquid-Phase Noncovalent Exfoliation of Graphite with a Hyperbranched Polyethylene and Formation of Graphene/Ethylene Copolymer Composites. *J. Phys. Chem. C* **2013**, *117* (20), 10730–10742. https://doi.org/10.1021/jp4008009.

(24) O'Neill, A.; Khan, U.; Nirmalraj, P. N.; Boland, J.; Coleman, J. N. Graphene Dispersion and Exfoliation in Low Boiling Point Solvents. *J. Phys. Chem. C* **2011**, *115* (13), 5422–5428. https://doi.org/10.1021/jp110942e.

(25) Lotya, M.; King, P. J.; Khan, U.; De, S.; Coleman, J. N. High-Concentration, Surfactant-Stabilized Graphene Dispersions. *ACS Nano* **2010**, *4* (6), 3155–3162. https://doi.org/10.1021/nn1005304.

(26) Lotya, M.; Hernandez, Y.; King, P. J.; Smith, R. J.; Nicolosi, V.; Karlsson, L. S.; Blighe, F. M.; De, S.; Zhiming, W.; McGovern, I. T.; Duesberg, G. S.; Coleman, J. N. Liquid Phase Production of Graphene by Exfoliation of Graphite in Surfactant/Water Solutions. *J. Am. Chem. Soc.* **2009**, *131* (10), 3611–3620. https://doi.org/10.1021/ja807449u.

(27) Uysal Unalan, I.; Wan, C.; Trabattoni, S.; Piergiovanni, L.; Farris, S. Polysaccharide-Assisted Rapid Exfoliation of Graphite Platelets into High Quality Water-Dispersible Graphene Sheets. *RSC Adv.* **2015**, *5* (34), 26482–26490. https://doi.org/10.1039/c4ra16947f.

(28) Some, S.; Kim, Y.; Hwang, E. H.; Yoo, H. J.; Lee, H. Binol Salt as a Completely Removable Graphene Surfactant. *Chem. Commun.* **2012**, *48* (62), 7732–7734. https://doi.org/10.1039/c2cc33916a.

(29) Park, S.; An, J.; Piner, R. D.; Jung, I.; Yang, D.; Velamakanni, A.; Nguyen, S. B. T.; Ruoff, R. S. Aqueous Suspension and Characterization of Chemically Modified Graphene Sheets. *Chem. Mater.* **2008**, *20* (21), 6592–6594. https://doi.org/10.1021/cm801932u.

(30) Stankovich, S.; Dikin, D. A.; Piner, R. D.; Kohlhaas, K. A.; Kleinhammes, A.; Jia, Y.; Wu, Y.; Nguyen, S. B. T.; Ruoff, R. S. Synthesis of Graphene-Based Nanosheets via Chemical Reduction of Exfoliated Graphite Oxide. *Carbon N. Y.* **2007**, *45* (7), 1558–1565. https://doi.org/10.1016/j.carbon.2007.02.034.

(31) Boukhvalov, D. W.; Katsnelson, M. I. Tuning the Gap in Bilayer Graphene Using Chemical Functionalization: Density Functional Calculations. *Phys. Rev. B - Condens. Matter Mater. Phys.* **2008**, *78* (8), 2–6. https://doi.org/10.1103/PhysRevB.78.085413.

(32) Zhang, H.; Bekyarova, E.; Huang, J. W.; Zhao, Z.; Bao, W.; Wang, F.; Haddon, R. C.; Lau, C. N. Aryl Functionalization as a Route to Band Gap Engineering in Single Layer Graphene Devices. *Nano Lett.* **2011**, *11* (10), 4047–4051. https://doi.org/10.1021/nl200803q.

(33) Niyogi, S.; Bekyarova, E.; Itkis, M. E.; Zhang, H.; Shepperd, K.; Hicks, J.; Sprinkle, M.; Berger, C.; Lau, C. N.; Deheer, W. A.; Conrad, E. H.; Haddon, R. C. Spectroscopy of Covalently Functionalized Graphene. *Nano Lett.* **2010**, *10* (10), 4061–4066. https://doi.org/10.1021/nl1021128.

(34) Martin, D. P.; Tariq, A.; Richards, B. D. O.; Jose, G.; Krasnikov, S. A.; Kulak, A.; Sergeeva, N. N. White Light Induced Covalent Modification of Graphene Using a Phenazine Dye. *Chem. Commun.* **2017**, *53*, 10715–10718. https://doi.org/10.1039/C7CC05158A.

(35) Novoselov, K. S.; Fal'Ko, V. I.; Colombo, L.; Gellert, P. R.; Schwab, M. G.; Kim, K. A Roadmap for Graphene. *Nature* **2012**, *490* (7419), 192–200. https://doi.org/10.1038/nature11458.

(36) Kim, S.; Zhou, S.; Hu, Y.; Acik, M.; Chabal, Y. J.; Berger, C.; De Heer, W.; Bongiorno, A.; Riedo, E. Room-Temperature Metastability of Multilayer Graphene Oxide Films. *Nat. Mater.* **2012**, *11* (6), 544–549. https://doi.org/10.1038/nmat3316.

(37) Eigler, S.; Dotzer, C.; Hirsch, A.; Enzelberger, M.; Müller, P. Formation and Decomposition of CO 2 Intercalated Graphene Oxide. *Chem. Mater.* **2012**, *24* (7), 1276–1282. https://doi.org/10.1021/cm203223z.

(38) Paci, J. T.; Belytschko, T.; Schatz, G. C. Computational Studies of the Structure, Behavior upon Heating and Mechanical Properties of Graphite Oxide. *J. Phys. Chem. C* **2007**, *111* (49), 18099–18111. https://doi.org/10.1021/jp075799g.

(39) Erickson, K.; Erni, R.; Lee, Z.; Alem, N.; Gannett, W.; Zettl, A. Determination of the Local Chemical Structure of Graphene Oxide and Reduced Graphene Oxide. *Adv. Mater.* **2010**, *22* (40), 4467–4472. https://doi.org/10.1002/adma.201000732.

(40) Becerril, H. A.; Mao, J.; Liu, Z.; Stoltenberg, R. M.; Bao, Z.; Chen, Y. Evaluation of Solution-Processed Reduced Graphene Oxide Films as Transparent Conductors. *ACS Nano* **2008**, *2* (3), 463–470. https://doi.org/10.1021/nn700375n.

(41) Huang, W.; Ptasinska, S. Functionalization of Graphene by Atmospheric Pressure Plasma Jet in Air or H 2 O 2 Environments. *Appl. Surf. Sci.* **2016**, *367*, 160–166. https://doi.org/10.1016/j.apsusc.2016.01.170.

(42) Englert, J. M.; Knirsch, K. C.; Dotzer, C.; Butz, B.; Hauke, F.; Spiecker, E.; Hirsch, A. Functionalization of Graphene by Electrophilic Alkylation of Reduced Graphite. *Chem. Commun.* **2012**, *48* (41), 5025–5027. https://doi.org/10.1039/c2cc31181j.

(43) Quintana, M.; Spyrou, K.; Grzelczak, M.; Browne, W. R.; Rudolf, P.; Prato, M. Functionalization of Graphene via 1,3-Dipolar Cycloaddition. *ACS Nano* **2010**, *4* (6), 3527–3533. https://doi.org/10.1021/nn100883p.

(44) Sharma, R.; Baik, J. H.; Perera, C. J.; Strano, M. S. Anomalously Large Reactivity of Single Graphene Layers and Edges toward Electron Transfer Chemistries. *Nano Lett.* **2010**, *10* (2), 398–405. https://doi.org/10.1021/nl902741x.

(45) Koehler, F. M.; Jacobsen, A.; Ensslin, K.; Stampfer, C.; Stark, W. J. Selective Chemical Modification of Graphene Surfaces: Distinction between Single- and Bilayer Graphene. *Small* **2010**, *6* (10), 1125–1130. https://doi.org/10.1002/smll.200902370.

(46) Knirsch, K. C.; Schäfer, R. A.; Hauke, F.; Hirsch, A. Mono- and Ditopic Bisfunctionalization of Graphene. *Angew. Chemie - Int. Ed.* **2016**, *55* (19), 5861–5864. https://doi.org/10.1002/anie.201511807.

(47) Englert, J. M.; Dotzer, C.; Yang, G.; Schmid, M.; Papp, C.; Gottfried, J. M.; Steinrück, H. P.; Spiecker, E.; Hauke, F.; Hirsch, A. Covalent Bulk Functionalization of Graphene. *Nat. Chem.* **2011**, *3* (4), 279–286. https://doi.org/10.1038/nchem.1010.

(48) Biswal, M.; Zhang, X.; Schilter, D.; Lee, T. K.; Hwang, D. Y.; Saxena, M.; Lee, S. H.; Chen, S.; Kwak, S. K.; Bielawski, C. W.; Bacsa, W. S.; Ruoff, R. S. Sodide and Organic Halides Effect Covalent Functionalization of Single-Layer and Bilayer Graphene. *J. Am. Chem. Soc.* **2017**, *139* (11), 4202–4210. https://doi.org/10.1021/jacs.7b00932.

(49) Quintana, M.; Montellano, A.; Del Rio Castillo, A. E.; Tendeloo, G. Van; Bittencourt, C.; Prato, M. Selective Organic Functionalization of Graphene Bulk or Graphene Edges. *Chem. Commun.* **2011**, *47* (33), 9330–9332. https://doi.org/10.1039/c1cc13254g.

(50) Zhu, H.; Huang, P.; Jing, L.; Zuo, T.; Zhao, Y.; Gao, X. Microstructure Evolution of Diazonium Functionalized Graphene: A Potential Approach to Change Graphene Electronic Structure. *J. Mater. Chem.* **2012**, *22* (5), 2063–2068. https://doi.org/10.1039/c1jm14862a.

(51) Fan, X.; Nouchi, R.; Tanigaki, K. Effect of Charge Puddles and Ripples on the Chemical Reactivity of Single Layer Graphene Supported by SiO2/Si Substrate. *J. Phys. Chem. C* **2011**, *115* (26), 12960–12964. https://doi.org/10.1021/jp202273a.

(52) Schäfer, R. A.; Weber, K.; Koleśnik-Gray, M.; Hauke, F.; Krstić, V.; Meyer, B.; Hirsch, A. Substrate-Modulated Reductive Graphene Functionalization. *Angew. Chemie - Int. Ed.* **2016**, *55* (47), 14858–14862. https://doi.org/10.1002/anie.201607427.

(53) Wang, Q. H.; Jin, Z.; Kim, K. K.; Hilmer, A. J.; Paulus, G. L. C.; Shih, C. J.; Ham, M. H.; Sanchez-Yamagishi, J. D.; Watanabe, K.; Taniguchi, T.; Kong, J.; Jarillo-Herrero, P.; Strano, M. S. Understanding and Controlling the Substrate Effect on Graphene Electron-Transfer Chemistry via Reactivity Imprint Lithography. *Nat. Chem.* **2012**, *4* (9), 724–732. https://doi.org/10.1038/nchem.1421.

(54) Gao, G.; Liu, D.; Tang, S.; Huang, C.; He, M.; Guo, Y.; Sun, X.; Gao, B. Heat-Initiated Chemical Functionalization of Graphene. *Sci. Rep.* **2016**, *6*, 1–8. https://doi.org/10.1038/srep20034.

(55) Liu, D.; He, M.; Huang, C.; Sun, X.; Gao, B. Fermi-Level Dependence of the Chemical Functionalization of Graphene with Benzoyl Peroxide. *J. Phys. Chem. C* **2017**, *121* (19), 10546–10551. https://doi.org/10.1021/acs.jpcc.7b01520.

(56) Zhang, X.; Luo, D.; Zhang, H.; Hwang, D. Y.; Park, S. O.; Li, B. W.; Biswal, M.; Jiang, Y.; Huang, Y.; Kwak, S. K.; Bielawski, C. W.; Ruoff, R. S. Effect of Copper Substrate Surface Orientation on the Reductive Functionalization of Graphene. *Chem. Mater.* **2019**. https://doi.org/10.1021/acs.chemmater.9b01729.

(57) Park, M. J.; Choi, H.-H.; Park, B.; Lee, J. Y.; Lee, C.-H.; Choi, Y. S.; Kim, Y.; Yoo, J. M.; Lee, H.; Hong, B. H. Enhanced Chemical Reactivity of Graphene by Fermi Level Modulation. *Chem. Mater.* **2018**, acs.chemmater.8b01614. https://doi.org/10.1021/acs.chemmater.8b01614.

(58) Tahara, K.; Kubo, Y.; Lindner, B.; Hashimoto, S.; Hirose, S.; Brown, A.; Hirsch, B.; Daukiya, L.; De Feyter, S.; Tobe, Y. Steric and Electronic Effects of Electrochemically Generated Aryl Radicals on Grafting of the Graphite Surface. *Langmuir* **2019**, *35* (6), 2089–2098. https://doi.org/10.1021/acs.langmuir.8b03339.

(59) Friedrich, J. F.; Hidde, G.; Lippitz, A.; Unger, W. E. S. Plasma Bromination of Graphene for Covalent Bonding of Organic Molecules. *Plasma Chem. Plasma Process.* **2014**, *34* (3), 621–645. https://doi.org/10.1007/s11090-013-9509-x.

(60) Sarkar, S.; Bekyarova, E.; Niyogi, S.; Haddon, R. C. Diels-Alder Chemistry of Graphite and Graphene: Graphene as Diene and Dienophile. *J. Am. Chem. Soc.* **2011**, *133* (10), 3324–3327. https://doi.org/10.1021/ja200118b.

(61) Hossain, M. Z.; Shimizu, N. In Situ Functionalization of Graphene with Reactive End Group through Amine Diazotization. *J. Phys. Chem. C* **2017**, *121* (45), 25223–25228. https://doi.org/10.1021/acs.jpcc.7b08454.

(62) Peng, C.; Xiong, Y.; Liu, Z.; Zhang, F.; Ou, E.; Qian, J.; Xiong, Y.; Xu, W. Bulk Functionalization of Graphene Using Diazonium Compounds and Amide Reaction. *Appl. Surf. Sci.* **2013**, *280*, 914–919. https://doi.org/10.1016/j.apsusc.2013.05.094.

(63) Tristant, D.; Wang, Y.; Gerber, I.; Monthioux, M.; Pénicaud, A.; Puech, P. Optical Signatures of Bulk and Solutions of KC8 and KC24. *J. Appl. Phys.* **2015**, *118* (4), 1–6. https://doi.org/10.1063/1.4927291.

(64) Dimiev, A.; Bachilo, S. M.; Saito, R.; Tour, J. M. Reversible Formation of Ammonium Persulfate/Sulfuric Acid Graphite Intercalation Compounds and Their Peculiar Raman Spectra—Supporting Information. 1–5.

(65) Botas, C.; Álvarez, P.; Blanco, P.; Granda, M.; Blanco, C.; Santamaría, R.; Romasanta, L. J.; Verdejo, R.; López-Manchado, M. A.; Menéndez, R. Graphene Materials with Different Structures Prepared from the Same Graphite by the Hummers

and Brodie Methods. *Carbon N. Y.* **2013**, *65*, 156–164. https://doi.org/10.1016/j.carbon.2013.08.009.

(66) You, X.; Yang, S.; Li, J.; Deng, Y.; Dai, L.; Peng, X.; Huang, H.; Sun, J.; Wang, G.; He, P.; Ding, G.; Xie, X. Green and Mild Oxidation: An Efficient Strategy toward Water-Dispersible Graphene. *ACS Appl. Mater. Interfaces* **2017**, *9* (3), 2856–2866. https://doi.org/10.1021/acsami.6b13703.

(67) Au, H.; Rubio, N.; Shaffer, M. S. P. Brominated Graphene as a Versatile Precursor for Multifunctional Grafting. *Chem. Sci.* **2018**, *9* (1), 209–217. https://doi.org/10.1039/C7SC03455E.

(68) Jung, J. H.; Park, C. H.; Ihm, J. A Rigorous Method of Calculating Exfoliation Energies from First Principles. *Nano Lett.* **2018**, *18* (5), 2759–2765. https://doi.org/10.1021/acs.nanolett.7b04201.

(69) Catheline, A.; Vallés, C.; Drummond, C.; Ortolani, L.; Morandi, V.; Marcaccio, M.; Iurlo, M.; Paolucci, F.; Pénicaud, A. Graphene Solutions. *Chem. Commun.* **2011**, *47* (19), 5470. https://doi.org/10.1039/c1cc11100k.

(70) Farmer, D. B.; Roksana, G. M.; Perebeinos, V.; Lin, Y. M.; Tuievski, G. S.; Tsang, J. C.; Avouris, P. Chemical Doping and Electron-Hole Conduction Asymmetry in Graphene Devices. *Nano Lett.* **2009**, *9* (1), 388–392. https://doi.org/10.1021/nl803214a.

(71) Abiman, P.; Wildgoose, G. G.; Compton, R. G. A Mechanistic Investigation into the Covalent Chemical Derivatisation of Graphite and Glassy Carbon Surfaces Using Aryldiazonium Salts. *J. Phys. Org. Chem.* **2008**, *21* (6), 433–439. https://doi.org/10.1002/poc.1331.

(72) Combellas, C.; Jiang, D. E.; Kanoufi, F.; Pinson, J.; Podvorica, F. I. Steric Effects in the Reaction of Aryl Radicals on Surfaces. *Langmuir* **2009**, *25* (1), 286–293. https://doi.org/10.1021/la8025792.

(73) Combellas, C.; Kanoufi, F.; Pinson, J.; Podvorica, F. I. Sterically Hindered Diazonium Salts for the Grafting of a Monolayer on Metals. *J. Am. Chem. Soc.* **2008**, *130* (27), 8576–8577. https://doi.org/10.1021/ja8018912.

(74) Greenwood, J.; Phan, T. H.; Fujita, Y.; Li, Z.; Ivasenko, O.; Vanderlinden, W.; Van Gorp, H.; Frederickx, W.; Lu, G.; Tahara, K.; Tobe, Y.; Uji-I, H.; Mertens, S. F. L.; De Feyter, S. Covalent Modification of Graphene and Graphite Using Diazonium

Chemistry: Tunable Grafting and Nanomanipulation. *ACS Nano* **2015**, *9* (5), 5520–5535. https://doi.org/10.1021/acsnano.5b01580.

(75) Xia, Z.; Leonardi, F.; Gobbi, M.; Liu, Y.; Bellani, V.; Liscio, A.; Kovtun, A.; Li, R.; Feng, X.; Orgiu, E.; Samorì, P.; Treossi, E.; Palermo, V. Electrochemical Functionalization of Graphene at the Nanoscale with Self-Assembling Diazonium Salts. *ACS Nano* **2016**, *10* (7), 7125–7134. https://doi.org/10.1021/acsnano.6b03278.

(76) Shih, C. J.; Wang, Q. H.; Jin, Z.; Paulus, G. L. C.; Blankschtein, D.; Jarillo-Herrero, P.; Strano, M. S. Disorder Imposed Limits of Mono- and Bilayer Graphene Electronic Modification Using Covalent Chemistry. *Nano Lett.* **2013**, *13* (2), 809–817. https://doi.org/10.1021/nl304632e.

(77) Li, W.; Li, Y.; Xu, K. Azidated Graphene: Direct Azidation from Monolayers, Click Chemistry, and Bulk Production from Graphite. *Nano Lett.* **2020**, *20* (1), 534–539. https://doi.org/10.1021/acs.nanolett.9b04267.

(78) Zhang, X.; Han, M.; Chen, S.; Bao, L.; Li, L.; Xu, W. Azo Addition to Exfoliated Graphene: A Facile and High Yield Route to Functionalized Graphene. *RSC Adv.* **2013**, *3* (39), 17689–17692. https://doi.org/10.1039/c3ra42591f.

(79) Craciun, M. F.; Russo, S.; Yamamoto, M.; Tarucha, S. Tuneable Electronic Properties in Graphene. *Nano Today* **2011**, *6* (1), 42–60. https://doi.org/10.1016/j.nantod.2010.12.001.

(80) García-Rodeja, Y.; Solà, M.; Fernández, I. Understanding the Reactivity of Planar Polycyclic Aromatic Hydrocarbons: Towards the Graphene Limit. *Chem. - A Eur. J.* **2016**, *22* (30), 10572–10580. https://doi.org/10.1002/chem.201600900.

(81) Daukiya, L.; Mattioli, C.; Aubel, D.; Hajjar-Garreau, S.; Vonau, F.; Denys, E.; Reiter, G.; Fransson, J.; Perrin, E.; Bocquet, M. L.; Bena, C.; Gourdon, A.; Simon, L. Covalent Functionalization by Cycloaddition Reactions of Pristine Defect-Free Graphene. *ACS Nano* **2017**, *11* (1), 627–634. https://doi.org/10.1021/acsnano.6b06913.

(82) Georgakilas, V.; Bourlinos, A. B.; Zboril, R.; Steriotis, T. A.; Dallas, P.; Stubos, A. K.; Trapalis, C. Organic Functionalisation of Graphenes. *Chem. Commun.* **2010**, *46* (10), 1766–1768. https://doi.org/10.1039/b922081j.

(83) Zhang, X.; Hou, L.; Cnossen, A.; Coleman, A. C.; Ivashenko, O.; Rudolf, P.; Van Wees, B. J.; Browne, W. R.; Feringa, B. L. One-Pot Functionalization of Graphene

with Porphyrin through Cycloaddition Reactions. *Chem. - A Eur. J.* **2011**, *17* (32), 8957–8964. https://doi.org/10.1002/chem.201100980.

(84) Wang, A.; Yu, W.; Xiao, Z.; Song, Y.; Long, L.; Cifuentes, M. P.; Humphrey, M. G.; Zhang, C. A 1,3-Dipolar Cycloaddition Protocol to Porphyrin-Functionalized Reduced Graphene Oxide with a Push-Pull Motif. *Nano Res.* **2015**, *8* (3), 870–886. https://doi.org/10.1007/s12274-014-0569-x.

(85) Cunha, E.; Ren, H.; Lin, F.; Kinloch, I. A.; Sun, Q.; Fan, Z.; Young, R. J. The Chemical Functionalization of Graphene Nanoplatelets through Solvent-Free Reaction. *RSC Adv.* **2018**, *8* (58), 33564–33573. https://doi.org/10.1039/C8RA04817G.

(86) Uceta, H.; Vizuete, M.; Carrillo, J. R.; Barrejón, M.; Fierro, J. L. G.; Prieto, M. P.; Langa, F. Cycloaddition of Nitrile Oxides to Graphene: A Theoretical and Experimental Approach. *Chem. - A Eur. J.* **2019**, *25* (64), 14644–14650. https://doi.org/10.1002/chem.201903105.

(87) Barrejón, M.; Gómez-Escalonilla, M. J.; Fierro, J. L. G.; Prieto, P.; Carrillo, J. R.; Rodríguez, A. M.; Abellán, G.; López-Escalante, M. C.; Gabás, M.; López-Navarrete, J. T.; Langa, F. Modulation of the Exfoliated Graphene Work Function through Cycloaddition of Nitrile Imines. *Phys. Chem. Chem. Phys.* **2016**, *18* (42), 29582–29590. https://doi.org/10.1039/c6cp05285a.

(88) Zhang, X.; Browne, W. R.; Feringa, B. L. Preparation of Dispersible Graphene through Organic Functionalization of Graphene Using a Zwitterion Intermediate Cycloaddition Approach. *RSC Adv.* **2012**, *2* (32), 12173–12176. https://doi.org/10.1039/c2ra22440b.

(89) Hammouri, M.; Jha, S. K.; Vasiliev, I. First-Principles Study of Graphene and Carbon Nanotubes Functionalized with Benzyne. *J. Phys. Chem. C* **2015**, *119* (32), 18719–18728. https://doi.org/10.1021/acs.jpcc.5b04065.

(90) García, D.; Rodríguez-Pérez, L.; Herranz, M. A.; Peña, D.; Guitián, E.; Bailey, S.; Al-Galiby, Q.; Noori, M.; Lambert, C. J.; Pérez, D.; Martín, N. A C60-Aryne Building Block: Synthesis of a Hybrid All-Carbon Nanostructure. *Chem. Commun.* **2016**, *52* (40), 6677–6680. https://doi.org/10.1039/c5cc10462a.

(91) Zhong, X.; Jin, J.; Li, S.; Niu, Z.; Hu, W.; Li, R.; Ma, J. Aryne Cycloaddition: Highly Efficient Chemical Modification of Graphene. *Chem. Commun.* **2010**, *46* (39), 7340–7342. https://doi.org/10.1039/c0cc02389b.

(92) Zhong, X.; Yu, H.; Zhuang, G.; Li, Q.; Wang, X.; Zhu, Y.; Liu, L.; Li, X.; Dong, M.; Wang, J. G. Pyridyne Cycloaddition of Graphene: External Active Sites for Oxygen

Reduction Reaction. *J. Mater. Chem. A* **2014**, *2* (4), 897–901. https://doi.org/10.1039/c3ta13449k.

(93) Magedov, I. V.; Frolova, L. V.; Ovezmyradov, M.; Bethke, D.; Shaner, E. A.; Kalugin, N. G. Benzyne-Functionalized Graphene and Graphite Characterized by Raman Spectroscopy and Energy Dispersive X-Ray Analysis. *Carbon N. Y.* **2013**, *54* (Cvd), 192–200. https://doi.org/10.1016/j.carbon.2012.11.025.

(94) Zan, W. Chemical Functionalization of Graphene by Carbene Cycloaddition: A Density Functional Theory Study. *Appl. Surf. Sci.* **2014**, *311* (2), 377–383. https://doi.org/10.1016/j.apsusc.2014.05.071.

(95) Chua, C. K.; Ambrosi, A.; Pumera, M. Introducing Dichlorocarbene in Graphene. *Chem. Commun.* **2012**, *48* (43), 5376–5378. https://doi.org/10.1039/c2cc31936e.

(96) Hu, Z.; Song, C.; Shao, Q.; Li, J.; Huang, Y. One-Step Functionalization of Graphene by Cycloaddition of Diarylcarbene and Its Application as Reinforcement in Epoxy Composites. *Compos. Sci. Technol.* **2016**, *135*, 21–27. https://doi.org/10.1016/j.compscitech.2016.09.008.

(97) Sainsbury, T.; Passarelli, M.; Naftaly, M.; Gnaniah, S.; Spencer, S. J.; Pollard, A. J. Covalent Carbene Functionalization of Graphene: Toward Chemical Band-Gap Manipulation. *ACS Appl. Mater. Interfaces* **2016**, *8* (7), 4870–4877. https://doi.org/10.1021/acsami.5b10525.

(98) Choi, J.; Kim, K. J.; Kim, B.; Lee, H.; Kim, S. Covalent Functionalization of Epitaxial Graphene by Azidotrimethylsilane. *J. Phys. Chem. C* **2009**, *113* (22), 9433–9435. https://doi.org/10.1021/jp9010444.

(99) Liu, L. H.; Lerner, M. M.; Yan, M. Derivitization of Pristine Graphene with Well-Defined Chemical Functionalities. *Nano Lett.* **2010**, *10* (9), 3754–3756. https://doi.org/10.1021/nl1024744.

(100) Liu, L. H.; Yan, M. Simple Method for the Covalent Immobilization of Graphene. *Nano Lett.* **2009**, *9* (9), 3375–3378. https://doi.org/10.1021/nl901669h.

(101) Plachinda, P.; Evans, D.; Solanki, R. Electrical Conductivity of PFPA Functionalized Graphene. *Solid. State. Electron.* **2013**, *79*, 262–267. https://doi.org/10.1016/j.sse.2012.08.009.

(102) Park, J.; Jayawardena, H. S. N.; Chen, X.; Jayawardana, K. W.; Sundhoro, M.; Ada, E.; Yan, M. A General Method for the Fabrication of Graphene-Nanoparticle Hybrid

Material. *Chem. Commun.* **2015**, *51* (14), 2882–2885. https://doi.org/10.1039/c4cc07936a.

(103) Liu, L.-H.; Nandamuri, G.; Yan, M. Electrical Properties of Covalently Immobilized Single-Layer Graphene Devices. *J. Nanosci. Nanotechnol.* **2011**, *11*, 1288–1292. https://doi.org/10.1166/jnn.2011.3886.

(104) Faghani, A.; Donskyi, I. S.; Fardin Gholami, M.; Ziem, B.; Lippitz, A.; Unger, W. E. S.; Böttcher, C.; Rabe, J. P.; Haag, R.; Adeli, M. Controlled Covalent Functionalization of Thermally Reduced Graphene Oxide To Generate Defined Bifunctional 2D Nanomaterials. *Angew. Chemie - Int. Ed.* **2017**, *56* (10), 2675–2679. https://doi.org/10.1002/anie.201612422.

(105) Gholami, M. F.; Lauster, D.; Ludwig, K.; Storm, J.; Ziem, B.; Severin, N.; Böttcher, C.; Rabe, J. P.; Herrmann, A.; Adeli, M.; Haag, R. Functionalized Graphene as Extracellular Matrix Mimics: Toward Well-Defined 2D Nanomaterials for Multivalent Virus Interactions. *Adv. Funct. Mater.* **2017**, *27* (15). https://doi.org/10.1002/adfm.201606477.

(106) Park, J.; Jayawardena, H. S. N.; Chen, X.; Jayawardana, K. W.; Sundhoro, M.; Ada, E.; Yan, M. A General Method for the Fabrication of Graphene-Nanoparticle Hybrid Material. *Chem. Commun.* **2015**, *51* (14), 2882–2885. https://doi.org/10.1039/c4cc07936a.

(107) Bahçeci Sertkol, S.; Esat, B.; Momchilov, A. A.; Burak Yılmaz, M.; Sertkol, M. An Anthraquinone-Functionalized Reduced Graphene Oxide as Electrode Material for Rechargeable Batteries. *Carbon N. Y.* **2017**, *116*, 154–166. https://doi.org/10.1016/j.carbon.2017.02.005.

(108) Cai, M.; Thorpe, D.; Adamson, D. H.; Schniepp, H. C. Methods of Graphite Exfoliation. *J. Mater. Chem.* **2012**, *22* (48), 24992–25002. https://doi.org/10.1039/c2jm34517j.

(109) Yoon, G.; Seo, D. H.; Ku, K.; Kim, J.; Jeon, S.; Kang, K. Factors Affecting the Exfoliation of Graphite Intercalation Compounds for Graphene Synthesis. *Chem. Mater.* **2015**, *27* (6), 2067–2073. https://doi.org/10.1021/cm504511b.

(110) Dresselhaus, M. S.; Dresselhaus, G. Intercalation Compounds of Graphite. *Adv. Phys.* **1981**, *30* (2), 139–326. https://doi.org/10.1080/00018738100101367.

(111) Englert, J. M.; Vecera, P.; Knirsch, K. C.; Schäfer, R. A.; Hauke, F.; Hirsch, A. Scanning-Raman-Microscopy for the Statistical Analysis of Covalently Functionalized Graphene. *ACS Nano* **2013**, *7* (6), 5472–5482. https://doi.org/10.1021/nn401481h.

(112) Chakraborty, S.; Chattopadhyay, J.; Guo, W.; Billups, W. E. Functionalization of Potassium Graphite. *Angew. Chemie - Int. Ed.* **2007**, *46* (24), 4486–4488. https://doi.org/10.1002/anie.200605175.

(113) Pénicaud, A.; Drummond, C. Deconstructing Graphite: Graphenide Solutions. *Acc. Chem. Res.* **2013**, *46* (1), 129–137. https://doi.org/10.1021/ar300141s.

(114) Abellán, G.; Schirowski, M.; Edelthalhammer, K. F.; Fickert, M.; Werbach, K.; Peterlik, H.; Hauke, F.; Hirsch, A. Unifying Principles of the Reductive Covalent Graphene Functionalization. *J. Am. Chem. Soc.* **2017**, *139* (14), 5175–5182. https://doi.org/10.1021/jacs.7b00704.

(115) Hof, F.; Schäfer, R. A.; Weiss, C.; Hauke, F.; Hirsch, A. Novel Λ3-Iodane-Based Functionalization of Synthetic Carbon Allotropes (SCAs) - Common Concepts and Quantification of the Degree of Addition. *Chem. - A Eur. J.* **2014**, *20* (50), 16644–16651. https://doi.org/10.1002/chem.201404662.

(116) Knirsch, K. C.; Hof, F.; Lloret, V.; Mundloch, U.; Hauke, F.; Hirsch, A. Topology-Driven Reductive Silylation of Synthetic Carbon Allotropes. *J. Am. Chem. Soc.* **2016**, *138* (48), 15642–15647. https://doi.org/10.1021/jacs.6b09487.

(117) Vecera, P.; Holzwarth, J.; Edelthalhammer, K. F.; Mundloch, U.; Peterlik, H.; Hauke, F.; Hirsch, A. Solvent-Driven Electron Trapping and Mass Transport in Reduced Graphites to Access Perfect Graphene. *Nat. Commun.* **2016**, *7*. https://doi.org/10.1038/ncomms12411.

(118) Vecera, P.; Chacón-Torres, J. C.; Pichler, T.; Reich, S.; Soni, H. R.; Görling, A.; Edelthalhammer, K.; Peterlik, H.; Hauke, F.; Hirsch, A. Precise Determination of Graphene Functionalization by in Situ Raman Spectroscopy. *Nat. Commun.* **2017**, *8* (May). https://doi.org/10.1038/ncomms15192.

(119) Jiang, C.; Peng, Z.; De Los Reyes, C.; Young, C. C.; Tsentalovich, D. E.; Jamali, V.; Ajayan, P. M.; Tour, J. M.; Pasquali, M.; Martí, A. A. Increased Solubility and Fiber Spinning of Graphenide Dispersions Aided by Crown-Ethers. *Chem. Commun.* **2017**, *53* (9), 1498–1501. https://doi.org/10.1039/c6cc09623a.

(120) Hou, H. L.; Merino, J. P.; Criado, A.; Hirsch, A.; Prato, M. The Reactivity of Reduced Graphene Depends on Solvation. *2D Mater.* **2019**, *6* (2), 3–9. https://doi.org/10.1088/2053-1583/aafd9b.

(121) Hou, H. L.; Dasler, D.; Hauke, F.; Hirsch, A. Reductive Functionalization of Graphenides With Nickel(II) Porphyrin Diazonium Compounds. *Phys. Status Solidi - Rapid Res. Lett.* **2017**, *11* (11), 1–5. https://doi.org/10.1002/pssr.201700306.

(122) McAllister, M. J.; Li, J. L.; Adamson, D. H.; Schniepp, H. C.; Abdala, A. A.; Liu, J.; Herrera-Alonso, M.; Milius, D. L.; Car, R.; Prud'homme, R. K.; Aksay, I. A. Single Sheet Functionalized Graphene by Oxidation and Thermal Expansion of Graphite. *Chem. Mater.* **2007**, *19* (18), 4396–4404. https://doi.org/10.1021/cm0630800.

(123) Dimiev, A. M.; Tour, J. M. Mechanism of Graphene Oxide Formation. *ACS Nano* **2014**, *8* (3), 3060–3068. https://doi.org/10.1021/nn500606a.

(124) Mkhoyan, K. A.; Contryman, A. W.; Silcox, J.; Stewart, D. A.; Eda, G.; Mattevi, C.; Miller, S.; Chhowalla, M. Atomic and Electronic Structure of Graphene-Oxide. *Nano Lett.* **2009**, *9* (3), 1058–1063. https://doi.org/10.1021/nl8034256.

(125) Gómez-Navarro, C.; Meyer, J. C.; Sundaram, R. S.; Chuvilin, A.; Kurasch, S.; Burghard, M.; Kern, K.; Kaiser, U. Atomic Structure of Reduced Graphene Oxide. *Nano Lett.* **2010**, *10* (4), 1144–1148. https://doi.org/10.1021/nl9031617.

(126) Shao, G.; Lu, Y.; Wu, F.; Yang, C.; Zeng, F.; Wu, Q. Graphene Oxide: The Mechanisms of Oxidation and Exfoliation. *J. Mater. Sci.* **2012**, *47* (10), 4400–4409. https://doi.org/10.1007/s10853-012-6294-5.

(127) Xu, Y.; Sheng, K.; Li, C.; Shi, G. Highly Conductive Chemically Converted Graphene Prepared from Mildly Oxidized Graphene Oxide. *J. Mater. Chem.* **2011**, *21* (20), 7376–7380. https://doi.org/10.1039/c1jm10768b.

(128) Tian, S.; Sun, J.; Yang, S.; He, P.; Wang, G.; Di, Z.; Ding, G.; Xie, X.; Jiang, M. Controllable Edge Oxidation and Bubbling Exfoliation Enable the Fabrication of High Quality Water Dispersible Graphene. *Sci. Rep.* **2016**, *6* (April), 1–8. https://doi.org/10.1038/srep34127.

(129) Kim, S.; Lee, J. Y.; Yoon, T. H. Few-Layer-Graphene with High Yield and Low Sheet Resistance: Via Mild Oxidation of Natural Graphite. *RSC Adv.* **2017**, *7* (57), 35717–35723. https://doi.org/10.1039/c7ra06042d.

(130) Eigler, S.; Enzelberger-Heim, M.; Grimm, S.; Hofmann, P.; Kroener, W.; Geworski, A.; Dotzer, C.; Röckert, M.; Xiao, J.; Papp, C.; Lytken, O.; Steinrück, H. P.; Müller, P.; Hirsch, A. Wet Chemical Synthesis of Graphene. *Adv. Mater.* **2013**, *25* (26), 3583–3587. https://doi.org/10.1002/adma.201300155.

(131) Eigler, S. Graphite Sulphate - A Precursor to Graphene. *Chem. Commun.* **2015**, *51* (15), 3162–3165. https://doi.org/10.1039/c4cc09381j.

(132) Seiler, S.; Halbig, C. E.; Grote, F.; Rietsch, P.; Börrnert, F.; Kaiser, U.; Meyer, B.; Eigler, S. Effect of Friction on Oxidative Graphite Intercalation and High-Quality Graphene Formation. *Nat. Commun.* **2018**, *9* (1), 1–9. https://doi.org/10.1038/s41467-018-03211-1.

(133) Liu, F.; Wang, C.; Sui, X.; Riaz, M. A.; Xu, M.; Wei, L.; Chen, Y. Synthesis of Graphene Materials by Electrochemical Exfoliation: Recent Progress and Future Potential. *Carbon Energy* **2019**, *1* (2), 173–199. https://doi.org/10.1002/cey2.14.

(134) Tian, S.; Yang, S.; Huang, T.; Sun, J.; Wang, H.; Pu, X.; Tian, L.; He, P.; Ding, G.; Xie, X. One-Step Fast Electrochemical Fabrication of Water-Dispersible Graphene. *Carbon N. Y.* **2017**, *111*, 617–621. https://doi.org/10.1016/j.carbon.2016.10.044.

(135) Sarkar, S.; Bekyarova, E.; Haddon, R. C. Reversible Grafting of α-Naphthylmethyl Radicals to Epitaxial Graphene. *Angew. Chemie - Int. Ed.* **2012**, *51* (20), 4901–4904. https://doi.org/10.1002/anie.201201320.

(136) Wang, H. S.; Tian, S. Y.; Yang, S. W.; Wang, G.; You, X. F.; Xu, L. X.; Li, Q. T.; He, P.; Ding, G. Q.; Liu, Z.; Xie, X. M. Anode Coverage for Enhanced Electrochemical Oxidation: A Green and Efficient Strategy towards Water-Dispersible Graphene. *Green Chem.* **2018**, *20* (6), 1306–1315. https://doi.org/10.1039/c7gc03345a.

(137) Bergbreiter, D. E.; Killough, J. M. Reactions of Potassium-Graphite. *J. Am. Chem. Soc.* **1978**, *100* (7), 2126–2134. https://doi.org/10.1021/ja00475a025.

(138) Weitz, I. S.; Rabinovitz, M. The Application of C8K for Organic Synthesis: Reduction of Substituted Naphthalenes. *J. Chem. Soc. Perkin Trans. 1* **1993**, No. 1, 117–120. https://doi.org/10.1039/p19930000117.

(139) Lalancette, J.-M.; Rollin, G.; Dumas, P. Metals Intercalated in Graphite. I. Reduction and Oxidation. *Can. J. Chem.* **1972**, *50* (18), 3058–3062. https://doi.org/10.1139/v72-485.

(140) Dasler, D.; Schäfer, R. A.; Minameyer, M. B.; Hitzenberger, J. F.; Hauke, F.; Drewello, T.; Hirsch, A. Direct Covalent Coupling of Porphyrins to Graphene. *J. Am. Chem. Soc.* **2017**, *139* (34), 11760–11765. https://doi.org/10.1021/jacs.7b04122.

(141) Bepete, G.; Hof, F.; Huang, K.; Kampioti, K.; Anglaret, E.; Drummond, C.; Pénicaud, A. ”Eau de Graphene” from a KC8graphite Intercalation Compound Prepared by a Simple Mixing of Graphite and Molten Potassium. *Phys. Status Solidi - Rapid Res. Lett.* **2016**, *10* (12), 895–899. https://doi.org/10.1002/pssr.201600167.

(142) Wang, Y.; Huang, K.; Derré, A.; Puech, P.; Rouzière, S.; Launois, P.; Castro, C.; Monthioux, M.; Pénicaud, A. Conductive Graphene Coatings Synthesized from Graphenide Solutions. *Carbon N. Y.* **2017**, *121*, 217–225. https://doi.org/10.1016/j.carbon.2017.05.073.

(143) Purewal, J. Hydrogen Adsorption by Alkali Metal Graphite Intercalation Compounds. *Calif. Inst. Technol. PhD Thesis* **2010**, *2010*, 168.

(144) Eichinger, G.; Besenhard, J. O. High Energy Density Lithium Cells: Part II. Cathodes and Complete Cells. *J. Electroanal. Chem. Interfacial Electrochem.* **1976**, *72* (1), 1–31. https://doi.org/https://doi.org/10.1016/S0022-0728(76)80072-1.

(145) Chacón-Torres, J. C.; Wirtz, L.; Pichler, T. Manifestation of Charged and Strained Graphene Layers in the Raman Response of Graphite Intercalation Compounds. *ACS Nano* **2013**, *7* (10), 9249–9259. https://doi.org/10.1021/nn403885k.

(146) Hasdeo, E. H.; Nugraha, A. R. T.; Dresselhaus, M. S.; Saito, R. Breit-Wigner-Fano Line Shapes in Raman Spectra of Graphene. *Phys. Rev. B - Condens. Matter Mater. Phys.* **2014**, *90* (24). https://doi.org/10.1103/PhysRevB.90.245140.

(147) Chacón-Torres, J. C.; Pichler, T. Defect Modulated Raman Response of KC 8 Single Crystals. *Phys. Status Solidi Basic Res.* **2011**, *248* (11), 2744–2747. https://doi.org/10.1002/pssb.201100135.

(148) Qiu, T.; Yang, J. G.; Bai, X. J.; Wang, Y. L. The Preparation of Synthetic Graphite Materials with Hierarchical Pores from Lignite by One-Step Impregnation and Their Characterization as Dye Absorbents. *RSC Adv.* **2019**, *9* (22), 12737–12746. https://doi.org/10.1039/c9ra00343f.

(149) Pénicaud, A.; Drummond, C. Deconstructing Graphite: Graphenide Solutions. *Acc. Chem. Res.* **2013**, *46* (1), 129–137. https://doi.org/10.1021/ar300141s.

(150) Denis, P. A. Organic Chemistry of Graphene: The Diels-Alder Reaction. *Chem. - A Eur. J.* **2013**, *19* (46), 15719–15725. https://doi.org/10.1002/chem.201302622.

(151) Farquhar, A. K.; Fitchett, C. M.; Dykstra, H. M.; Waterland, M. R.; Brooksby, P. A.; Downard, A. J. Diels-Alder Reaction of Anthranilic Acids: A Versatile Route to Dense Monolayers on Flat Edge and Basal Plane Graphitic Carbon Substrates. *ACS Appl. Mater. Interfaces* **2016**, *8* (35), 23389–23395. https://doi.org/10.1021/acsami.6b07727.

(152) Silva, A. M. G.; Lacerda, P. S. S.; Tomé, A. C.; Neves, M. G. P. M. S.; Silva, A. M. S.; Cavaleiro, J. A. S.; Makarova, E. A.; Lukyanets, E. A. Porphyrins in 1,3-Dipolar Cycloaddition Reactions. Synthesis of New Porphyrin-Chlorin and Porphyrin-Tetraazachlorin Dyads. *J. Org. Chem.* **2006**, *71* (22), 8352–8356. https://doi.org/10.1021/jo0611770.

(153) Rani, J. R.; Lim, J.; Oh, J.; Kim, J. W.; Shin, H. S.; Kim, J. H.; Lee, S.; Jun, S. C. Epoxy to Carbonyl Group Conversion in Graphene Oxide Thin Films: Effect on Structural and Luminescent Characteristics. *J. Phys. Chem. C* **2012**, *116* (35), 19010–19017. https://doi.org/10.1021/jp3050302.

(154) Dimiev, A. M.; Bachilo, S. M.; Saito, R.; Tour, J. M. Reversible Formation of Ammonium Persulfate/Sulfuric Acid Graphite Intercalation Compounds and Their Peculiar Raman Spectra. *ACS Nano* **2012**, *6* (9), 7842–7849. https://doi.org/10.1021/nn3020147.

(155) Iwata, Y.; Tanaka, Y.; Kubosaki, S.; Morita, T.; Yoshimi, Y. A Strategy for Generating Aryl Radicals from Arylborates by Using Organic Photoredox Catalysis: Photo-Meerwein Type Arylations of Electron-Deficient Alkenes. *Chem. Commun.* **2018**, *54* (50), 1257–1260. https://doi.org/10.1039/C7CC09140K.

(156) Yan, G.; Yang, M.; Wu, X. Synthetic Applications of Arylboronic Acid via an Aryl Radical Transfer Pathway. *Org. Biomol. Chem.* **2013**, *11* (46), 7999. https://doi.org/10.1039/c3ob41851k.

(157) Dickschat, A.; Studer, A. Radical Addition of Arylboronic Acids to Various Olefins under Oxidative Conditions. *Org. Lett.* **2010**, *12* (18), 3972–3974. https://doi.org/10.1021/ol101818k.

(158) Demir, A. S.; Reis, Ö.; Emrullahoglu, M. Generation of Aryl Radicals from Arylboronic Acids by Manganese(III) Acetate: Synthesis of Biaryls and Heterobiaryls. *J. Org. Chem.* **2003**, *68* (2), 578–580. https://doi.org/10.1021/jo026466c.

(159) Chen, C. F.; Park, C. H.; Boudouris, B. W.; Horng, J.; Geng, B.; Girit, C.; Zettl, A.; Crommie, M. F.; Segalman, R. A.; Louie, S. G.; Wang, F. Controlling Inelastic Light Scattering Quantum Pathways in Graphene. *Nature* **2011**, *471* (7340), 617–620. https://doi.org/10.1038/nature09866.

(160) Liu, D.; Liu, C.; Li, H.; Lei, A. Direct Functionalization of Tetrahydrofuran and 1,4-Dioxane: Nickel-Catalyzed Oxidative C(Sp3)-H Arylation. *Angew. Chemie - Int. Ed.* **2013**, *52* (16), 4453–4456. https://doi.org/10.1002/anie.201300459.

(161) Chilkoti, A.; Ratner, B. D. X-Ray Photoelectron Spectroscopy of Iodine-Doped Nonconjugated Polymers. *Chem. Mater.* **1993**, *5* (6), 786–792. https://doi.org/10.1021/cm00030a012.

(162) Hai-Fang, W.; Xiao-Yong, D.; Jing, W.; Xing-Fa, G.; Geng-Mei, X.; Zu-Jin, S.; Zhen-Nan, G.; Yuan-Fang, L.; Yu-Liang, Z. XPS Study of C- I Covalent Bond on Single-Walled Carbon Nanotubes (SWNTs). *Acta Physico - Chimica Sinica*. 2004, pp 673–675.

(163) Lud, S. Q.; Steenackers, M.; Jordan, R.; Bruno, P.; Gruen, D. M.; Feulner, P.; Garrido, J. A.; Stutzmann, M. Chemical Grafting of Biphenyl Self-Assembled Monolayers on Ultrananocrystalline Diamond. *J. Am. Chem. Soc.* **2006**, *128* (51), 16884–16891. https://doi.org/10.1021/ja0657049.

(164) Hunger, R.; Jaegermann, W.; Merson, A.; Shapira, Y.; Pettenkofer, C.; Rappich, J. Electronic Structure of Methoxy-, Bromo-, and Nitrobenzene Grafted onto Si(111). *J. Phys. Chem. B* **2006**, *110* (31), 15432–15441. https://doi.org/10.1021/jp055702v.

(165) Tang, L. C.; Wan, Y. J.; Yan, D.; Pei, Y. B.; Zhao, L.; Li, Y. B.; Wu, L. Bin; Jiang, J. X.; Lai, G. Q. The Effect of Graphene Dispersion on the Mechanical Properties of Graphene/Epoxy Composites. *Carbon N. Y.* **2013**. https://doi.org/10.1016/j.carbon.2013.03.050.

(166) Davies, G. Some Aspects of the Chemistry of Manganese(III) in Aqueous Solution. *Coord. Chem. Rev.* **1969**, *4* (2), 199–224. https://doi.org/10.1016/S0010-8545(00)80086-7.

(167) Green, A. A.; Hersam, M. C. Emerging Methods for Producing Monodisperse Graphene Dispersions. *J. Phys. Chem. Lett.* **2010**, *1* (2), 544–549. https://doi.org/10.1021/jz900235f.

(168) Morimoto, N.; Kubo, T.; Nishina, Y. Tailoring the Oxygen Content of Graphite and Reduced Graphene Oxide for Specific Applications. *Sci. Rep.* **2016**, *6*, 4–11. https://doi.org/10.1038/srep21715.

(169) Edwards, R. S. Synthesis of Graphene Platelets A Thesis Submitted for the Partial Fulfilment of the Requirement for the By. **2015**.

(170) Snider, B. B. Manganese(III)-Based Oxidative Free-Radical Cyclizations. *Chem. Rev.* **1996**, *96* (1), 339–364. https://doi.org/10.1021/cr950026m.

(171) Backes, C.; Paton, K. R.; Hanlon, D.; Yuan, S.; Katsnelson, M. I.; Houston, J.; Smith, R. J.; McCloskey, D.; Donegan, J. F.; Coleman, J. N. Spectroscopic Metrics Allow in Situ Measurement of Mean Size and Thickness of Liquid-Exfoliated Few-Layer Graphene Nanosheets Support. *Nanoscale* **2016**, *8* (7), 4311–4323. https://doi.org/10.1039/c5nr08047a.

(172) Bello, R. H.; Coelho, L. A. F.; Becker, D. Role of Chemical Funcionalization of Carbon Nanoparticles in Epoxy Matrices. *J. Compos. Mater.* **2018**, *52* (4), 449–464. https://doi.org/10.1177/0021998317709082.

(173) Duan, W.; Chen, Y.; Ma, J.; Wang, W.; Cheng, J.; Zhang, J. High-Performance Graphene Reinforced Epoxy Nanocomposites Using Benzyl Glycidyl Ether as a Dispersant and Surface Modifier. *Compos. Part B Eng.* **2020**, *189* (February), 107878. https://doi.org/10.1016/j.compositesb.2020.107878.

(174) Yu, B.; Shi, Y.; Yuan, B.; Qiu, S.; Xing, W.; Hu, W.; Song, L.; Lo, S.; Hu, Y. Enhanced Thermal and Flame Retardant Properties of Flame-Retardant-Wrapped Graphene/Epoxy Resin Nanocomposites. *J. Mater. Chem. A* **2015**, *3* (15), 8034–8044. https://doi.org/10.1039/c4ta06613h.

(175) Chang, C. H.; Huang, T. C.; Peng, C. W.; Yeh, T. C.; Lu, H. I.; Hung, W. I.; Weng, C. J.; Yang, T. I.; Yeh, J. M. Novel Anticorrosion Coatings Prepared from Polyaniline/Graphene Composites. *Carbon N. Y.* **2012**, *50* (14), 5044–5051. https://doi.org/10.1016/j.carbon.2012.06.043.

(176) Yan, J.; Wei, T.; Shao, B.; Fan, Z.; Qian, W.; Zhang, M.; Wei, F. Preparation of a Graphene Nanosheet/Polyaniline Composite with High Specific Capacitance. *Carbon N. Y.* **2010**, *48* (2), 487–493. https://doi.org/10.1016/j.carbon.2009.09.066.

(177) Wang, H.; Hao, Q.; Yang, X.; Lu, L.; Wang, X. Effect of Graphene Oxide on the Properties of Its Composite with Polyaniline. *ACS Appl. Mater. Interfaces* **2010**, *2* (3), 821–828. https://doi.org/10.1021/am900815k.

(178) Cui, J.; Xu, J.; Li, J.; Qiu, H.; Zheng, S.; Yang, J. A Crosslinkable Graphene Oxide in Waterborne Polyurethane Anticorrosive Coatings: Experiments and Simulation. *Compos. Part B Eng.* **2020**, *188* (February), 107889. https://doi.org/10.1016/j.compositesb.2020.107889.

(179) Zhang, F.; Liu, W.; Liang, L.; Wang, S.; Shi, H.; Xie, Y.; Yang, M.; Pi, K. The Effect of Functional Graphene Oxide Nanoparticles on Corrosion Resistance of Waterborne Polyurethane. *Colloids Surfaces A Physicochem. Eng. Asp.* **2020**, *591* (December 2019). https://doi.org/10.1016/j.colsurfa.2020.124565.

(180) Wang, X.; Hu, Y.; Song, L.; Yang, H.; Xing, W.; Lu, H. In Situ Polymerization of Graphene Nanosheets and Polyurethane with Enhanced Mechanical and Thermal Properties. *J. Mater. Chem.* **2011**, *21* (12), 4222–4227. https://doi.org/10.1039/c0jm03710a.

(181) Kim, H.; Miura, Y.; MacOsko, C. W. Graphene/Polyurethane Nanocomposites for Improved Gas Barrier and Electrical Conductivity. *Chem. Mater.* **2010**, *22* (11), 3441–3450. https://doi.org/10.1021/cm100477v.

(182) Song, P.; Cao, Z.; Cai, Y.; Zhao, L.; Fang, Z.; Fu, S. Fabrication of Exfoliated Graphene-Based Polypropylene Nanocomposites with Enhanced Mechanical and Thermal Properties. *Polymer (Guildf).* **2011**, *52* (18), 4001–4010. https://doi.org/10.1016/j.polymer.2011.06.045.

(183) Zhao, X.; Zhang, Q.; Chen, D.; Lu, P. Enhanced Mechanical Properties of Graphene-Based Polyvinyl Alcohol Composites. *Macromolecules* **2010**, *43* (5), 2357–2363. https://doi.org/10.1021/ma902862u.

(184) Yoonessi, M.; Shi, Y.; Scheiman, D. A.; Lebron-Colon, M.; Tigelaar, D. M.; Weiss, R. A.; Meador, M. A. Graphene Polyimide Nanocomposites; Thermal, Mechanical, and High-Temperature Shape Memory Effects. *ACS Nano* **2012**, *6* (9), 7644–7655. https://doi.org/10.1021/nn302871y.

(185) Pathak, A. K.; Borah, M.; Gupta, A.; Yokozeki, T.; Dhakate, S. R. Improved Mechanical Properties of Carbon Fiber/Graphene Oxide-Epoxy Hybrid Composites. *Compos. Sci. Technol.* **2016**. https://doi.org/10.1016/j.compscitech.2016.09.007.

(186) Naebe, M.; Wang, J.; Amini, A.; Khayyam, H.; Hameed, N.; Li, L. H.; Chen, Y.; Fox, B. Mechanical Property and Structure of Covalent Functionalised Graphene/Epoxy Nanocomposites. *Sci. Rep.* **2014**. https://doi.org/10.1038/srep04375.

(187) Ramanathan, T.; Abdala, A. A.; Stankovich, S.; Dikin, D. A.; Herrera-Alonso, M.; Piner, R. D.; Adamson, D. H.; Schniepp, H. C.; Chen, X.; Ruoff, R. S.; Nguyen, S. T.; Aksay, I. A.; Prud'Homme, R. K.; Brinson, L. C. Functionalized Graphene Sheets for Polymer Nanocomposites. *Nat. Nanotechnol.* **2008**, *3* (6), 327–331. https://doi.org/10.1038/nnano.2008.96.

(188) Fang, M.; Wang, K.; Lu, H.; Yang, Y.; Nutt, S. Covalent Polymer Functionalization of Graphene Nanosheets and Mechanical Properties of Composites. *J. Mater. Chem.* **2009**, *19* (38), 7098–7105. https://doi.org/10.1039/b908220d.

(189) Bao, C.; Guo, Y.; Song, L.; Kan, Y.; Qian, X.; Hu, Y. In Situ Preparation of Functionalized Graphene Oxide/Epoxy Nanocomposites with Effective Reinforcements. *J. Mater. Chem.* **2011**, *21* (35), 13290–13298. https://doi.org/10.1039/c1jm11434d.

(190) Yang, H.; Li, F.; Shan, C.; Han, D.; Zhang, Q.; Niu, L.; Ivaska, A. Covalent Functionalization of Chemically Converted Graphene Sheets via Silane and Its Reinforcement. *J. Mater. Chem.* **2009**, *19* (26), 4632–4638. https://doi.org/10.1039/b901421g.

(191) Song, S. H.; Park, K. H.; Kim, B. H.; Choi, Y. W.; Jun, G. H.; Lee, D. J.; Kong, B. S.; Paik, K. W.; Jeon, S. Enhanced Thermal Conductivity of Epoxy-Graphene Composites by Using Non-Oxidized Graphene Flakes with Non-Covalent Functionalization. *Adv. Mater.* **2013**. https://doi.org/10.1002/adma.201202736.

(192) Kim, J.; Cha, J.; Chung, B.; Ryu, S.; Hong, S. H. Fabrication and Mechanical Properties of Carbon Fiber/Epoxy Nanocomposites Containing High Loadings of Noncovalently Functionalized Graphene Nanoplatelets. *Compos. Sci. Technol.* **2020**, *192* (December 2019), 108101. https://doi.org/10.1016/j.compscitech.2020.108101.

(193) Vasileiou, A. A.; Kontopoulou, M.; Docoslis, A. A Noncovalent Compatibilization Approach to Improve the Filler Dispersion and Properties of Polyethylene/Graphene Composites. *ACS Appl. Mater. Interfaces* **2014**, *6* (3), 1916–1925. https://doi.org/10.1021/am404979g.

(194) Teng, C. C.; Ma, C. C. M.; Lu, C. H.; Yang, S. Y.; Lee, S. H.; Hsiao, M. C.; Yen, M. Y.; Chiou, K. C.; Lee, T. M. Thermal Conductivity and Structure of Non-Covalent Functionalized Graphene/Epoxy Composites. *Carbon N. Y.* **2011**, *49* (15), 5107–5116. https://doi.org/10.1016/j.carbon.2011.06.095.

(195) Wan, Y. J.; Gong, L. X.; Tang, L. C.; Wu, L. Bin; Jiang, J. X. Mechanical Properties of Epoxy Composites Filled with Silane-Functionalized Graphene Oxide. *Compos. Part A Appl. Sci. Manuf.* **2014**, *64*, 79–89. https://doi.org/10.1016/j.compositesa.2014.04.023.

(196) Bose, S.; Kuila, T.; Uddin, M. E.; Kim, N. H.; Lau, A. K. T.; Lee, J. H. In-Situ Synthesis and Characterization of Electrically Conductive Polypyrrole/Graphene Nanocomposites. *Polymer (Guildf).* **2010**, *51* (25), 5921–5928. https://doi.org/10.1016/j.polymer.2010.10.014.

(197) Liu, D.; Li, W.; Zhang, N.; Huang, T.; Yang, J.; Wang, Y. Graphite Oxide-Driven Miscibility in PVDF/PMMA Blends: Assessment through Dynamic Rheology Method. *Eur. Polym. J.* **2017**, *96* (111), 232–247. https://doi.org/10.1016/j.eurpolymj.2017.09.018.

(198) Kim, H.; Macosko, C. W. Processing-Property Relationships of Polycarbonate/Graphene Composites. *Polymer (Guildf).* **2009**, *50* (15), 3797–3809. https://doi.org/10.1016/j.polymer.2009.05.038.

(199) Ghelichi, M.; Taheri Qazvini, N.; Jafari, S. H.; Khonakdar, H. A.; Reuter, U. Nanoclay Dispersion in a Miscible Blend: An Assessment through Rheological Analysis. *J. Polym. Res.* **2012**, *19* (3), 8–10. https://doi.org/10.1007/s10965-012-9830-8.

(200) Okolieocha, C.; Beckert, F.; Herling, M.; Breu, J.; Mülhaupt, R.; Altstädt, V. Preparation of Microcellular Low-Density PMMA Nanocomposite Foams: Influence of Different Fillers on the Mechanical, Rheological and Cell Morphological Properties. *Compos. Sci. Technol.* **2015**, *118*, 108–116. https://doi.org/10.1016/j.compscitech.2015.08.016.

(201) Du, F.; Scogna, R. C.; Zhou, W.; Brand, S.; Fischer, J. E.; Winey, K. I. Nanotube Networks in Polymer Nanocomposites: Rheology and Electrical Conductivity. *Macromolecules* **2004**, *37* (24), 9048–9055. https://doi.org/10.1021/ma049164g.

(202) Wang, H.; Yang, X.; Fu, Z.; Zhao, X.; Li, Y.; Li, J. Rheology of Nanosilica-Compatibilized Immiscible Polymer Blends: Formation of a “Heterogeneous Network” Facilitated by Interfacially Anchored Hybrid Nanosilica. *Macromolecules* **2017**, *50* (23), 9494–9506. https://doi.org/10.1021/acs.macromol.7b02143.

(203) Zhang, Q.; Fang, F.; Zhao, X.; Li, Y.; Zhu, M.; Chen, D. Use of Dynamic Rheological Behavior to Estimate the Dispersion of Carbon Nanotubes in Carbon

Nanotube/Polymer Composites. *J. Phys. Chem. B* **2008**, *112* (40), 12606–12611. https://doi.org/10.1021/jp802708j.

(204) Williams, M. L.; Landel, R. F.; Ferry, J. D. The Temperature Dependence of Relaxation Mechanisms in Amorphous Polymers and Other Glass-Forming Liquids. *J. Am. Chem. Soc.* **1955**, *77* (14), 3701–3707. https://doi.org/10.1021/ja01619a008.

(205) Kota, A. K.; Cipriano, B. H.; Duesterberg, M. K.; Gershon, A. L.; Powell, D.; Raghavan, S. R.; Bruck, H. A. Electrical and Rheological Percolation in Polystyrene/MWCNT Nanocomposites. *Macromolecules* **2007**, *40* (20), 7400–7406. https://doi.org/10.1021/ma0711792.

(206) Bazli, L.; Khavandi, A.; Boutorabi, M. A.; Karrabi, M. Correlation between Viscoelastic Behavior and Morphology of Nanocomposites Based on SR/EPDM Blends Compatibilized by Maleic Anhydride. *Polymer (Guildf).* **2017**, *113*, 156–166. https://doi.org/10.1016/j.polymer.2017.02.057.

(207) Joshi, M.; Butola, B. S.; Simon, G.; Kukaleva, N. Rheological and Viscoelastic Behavior of HDPE/Octamethyl-POSS Nanocomposites. *Macromolecules* **2006**, *39* (5), 1839–1849. https://doi.org/10.1021/ma051357w.

(208) Weir, M. P.; Johnson, D. W.; Boothroyd, S. C.; Savage, R. C.; Thompson, R. L.; King, S. M.; Rogers, S. E.; Coleman, K. S.; Clarke, N. Distortion of Chain Conformation and Reduced Entanglement in Polymer-Graphene Oxide Nanocomposites. *ACS Macro Lett.* **2016**, *5* (4), 430–434. https://doi.org/10.1021/acsmacrolett.6b00100.

(209) Young, R. J.; Li, Z.; Liu, M.; Kinloch, I. A. Mechanisms of Mechanical Reinforcement by Graphene and Carbon Nanotubes in Polymer Nanocomposites. *Nanoscale* **2020**, 2228–2267. https://doi.org/10.1039/c9nr06952f.

(210) Kim, H.; Kobayashi, S.; Abdurrahim, M. A.; Zhang, M. J.; Khusainova, A.; Hillmyer, M. A.; Abdala, A. A.; MacOsko, C. W. Graphene/Polyethylene Nanocomposites: Effect of Polyethylene Functionalization and Blending Methods. *Polymer (Guildf).* **2011**, *52* (8), 1837–1846. https://doi.org/10.1016/j.polymer.2011.02.017.

(211) Yang, Y.; Voak, A.; Wilkinson, S. R.; Hu, L. Design, Synthesis, and Evaluation of Potential Prodrugs of DFMO for Reductive Activation. *Bioorganic Med. Chem. Lett.* **2012**, *22* (21), 6583–6586. https://doi.org/10.1016/j.bmcl.2012.09.005.

(212) Hessel, L. W. Manganic Acetate in Anhydrous Acetic Acid: Preparation, Structure and Some Oxidation Reactions. **1968**.

Chapter 8. Appendix

8.1 Supporting Information for Chapter 2

8.1.1 H^1 NMR Data

4-Nitrobenzyl alcohol: H^1NMR (400 MHz, d_6-acetone, ppm) δ 8.25 (d,2H), δ 7.55 (d,2H), δ 4.8 (s,2H).

p-toluenesulphonyl chloride: H^1NMR (400 MHz, d_6-DMSO, ppm) δ 7.95 (d,2H), δ 7.45 (d,2H), δ 2.5 (s,3H).

4-nitrobenzyl tosylate: : H^1NMR (400 MHz, d_6-DMSO, ppm) δ 8.25 (d,2H), δ 7.9 (d,2H), δ 7.45 (d,2H), δ 7.3 (d,2H), δ 5.2 (s,2H), δ 2.5 (s,3H).

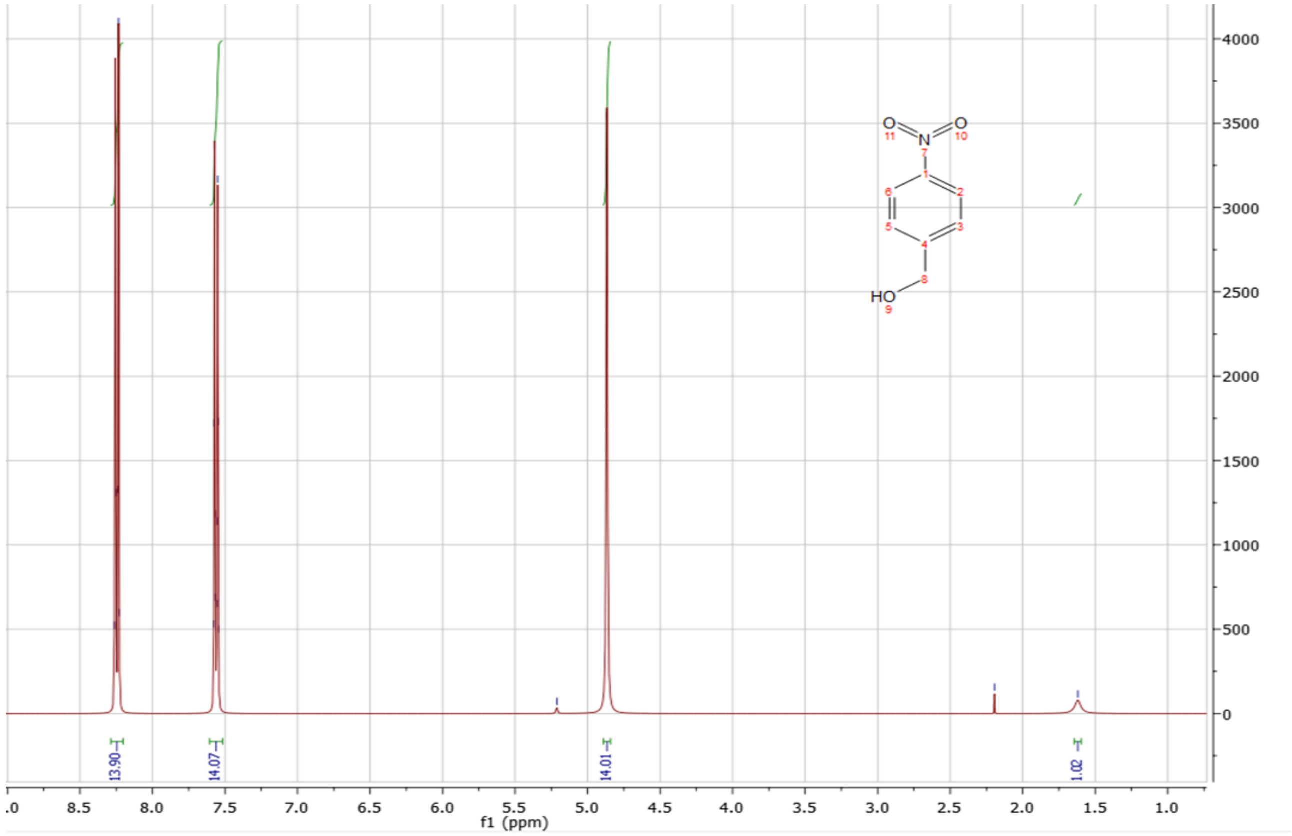

Figure 8.1 H^1NMR of 4-nitrobenzyl alcohol

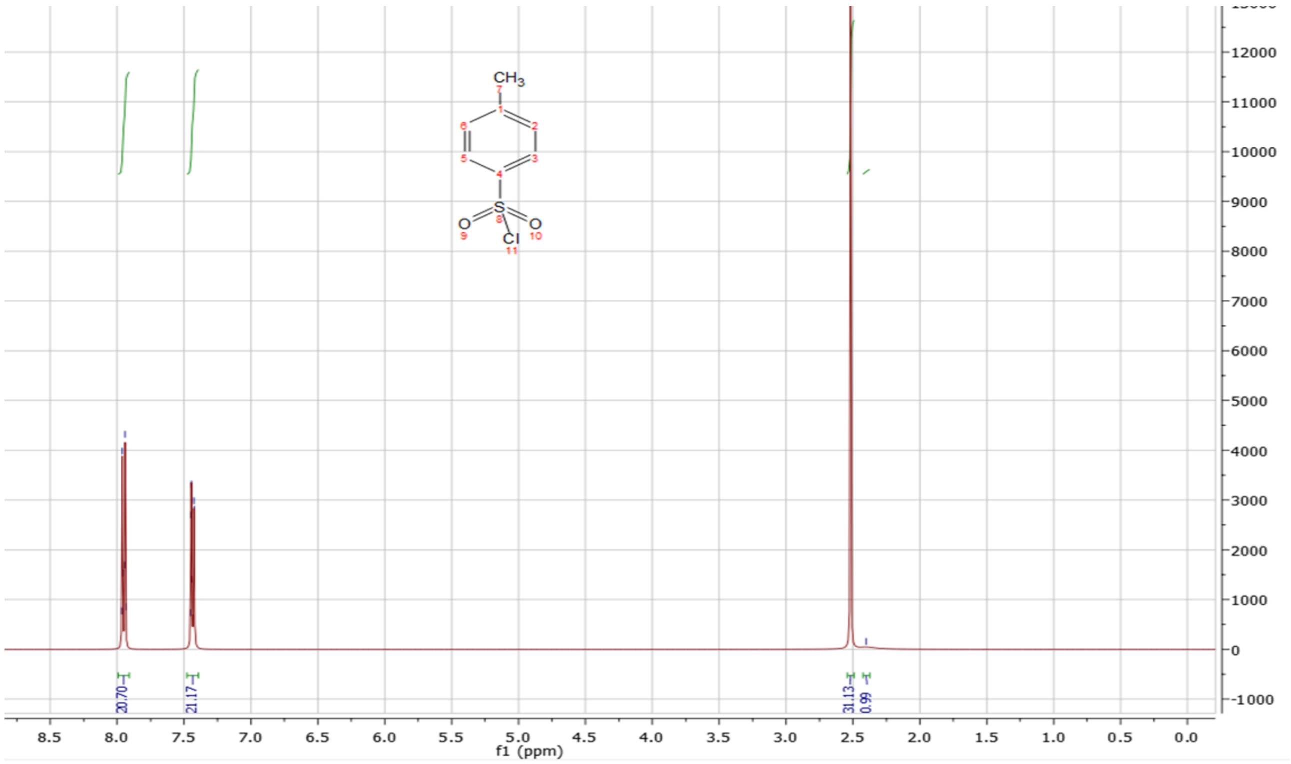

Figure 8.2 H^{1}NMR of p-toluenesulphonyl chloride

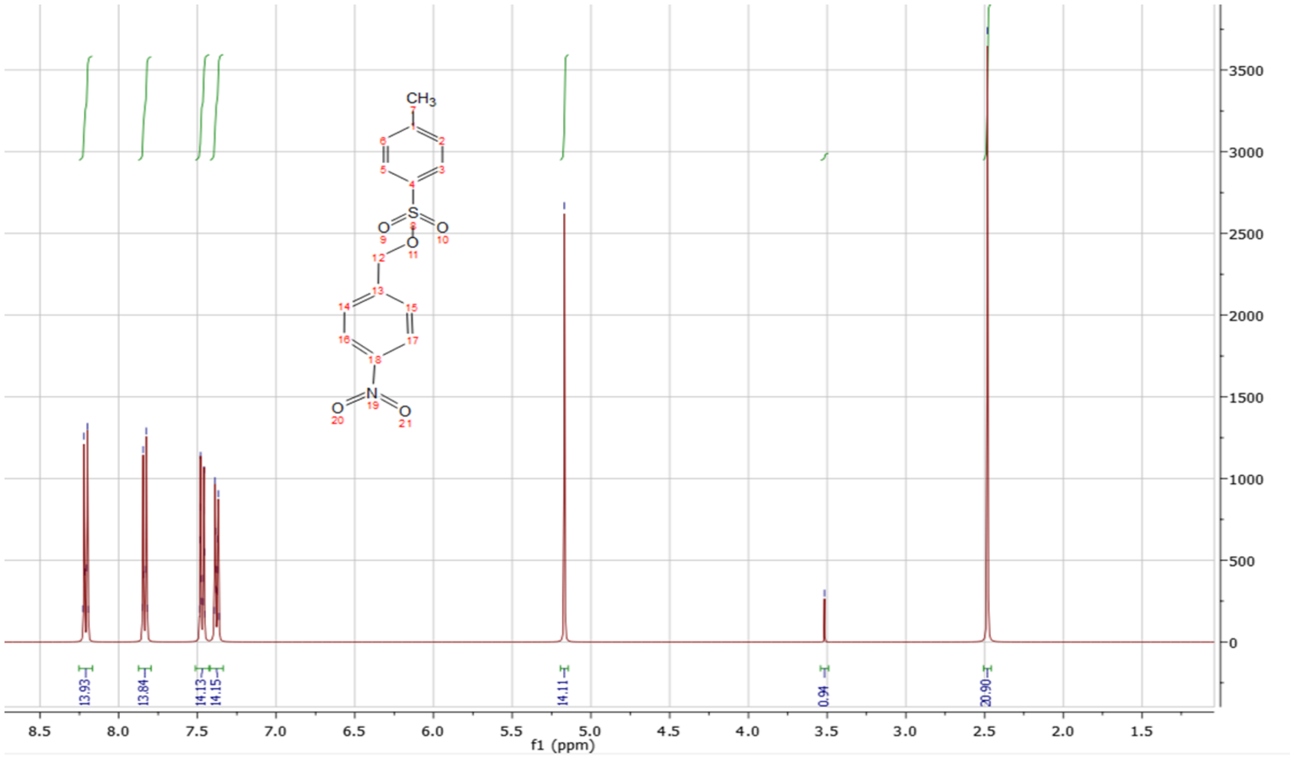

Figure 8.3 H^{1}NMR of 4-nitrobenzyl tosylate

8.1.2 AFM Images of the Functionalised Graphene

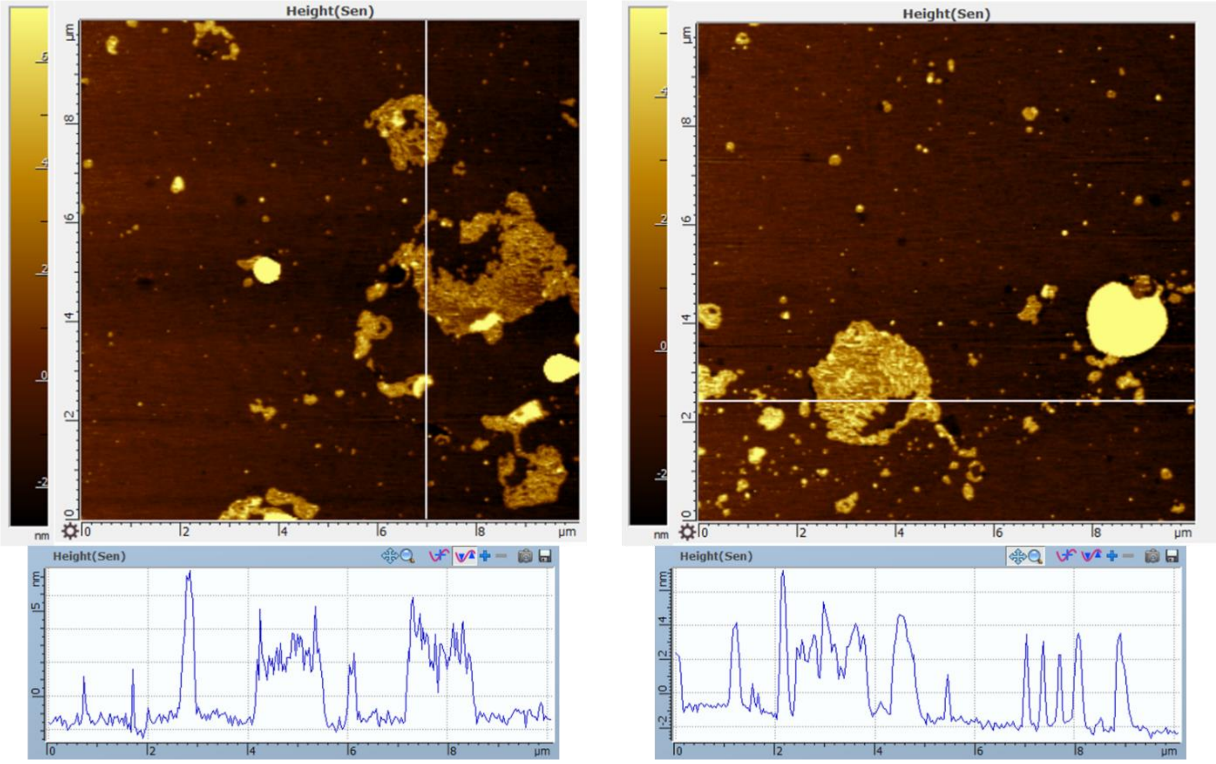

Figure 8.4 AFM images and height profiles of ***Aniline-G*** *flakes*

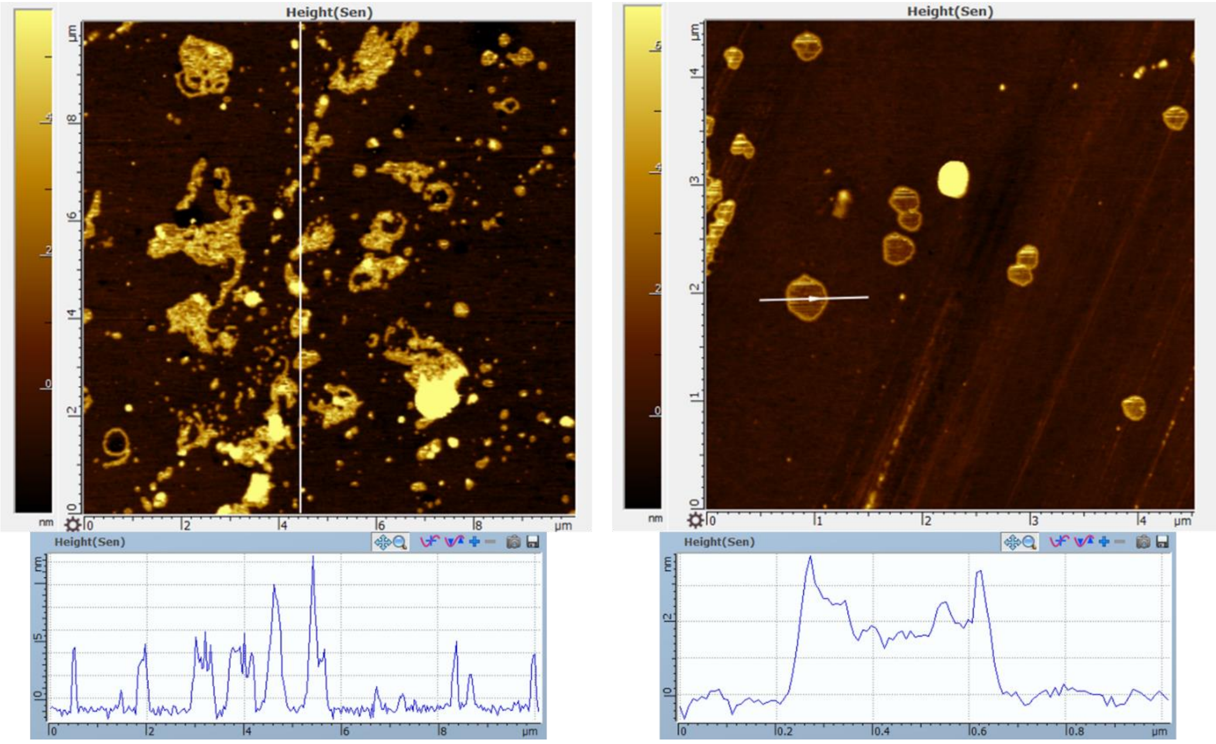

Figure 8.5 AFM images of ***Aniline-G*** *flakes*

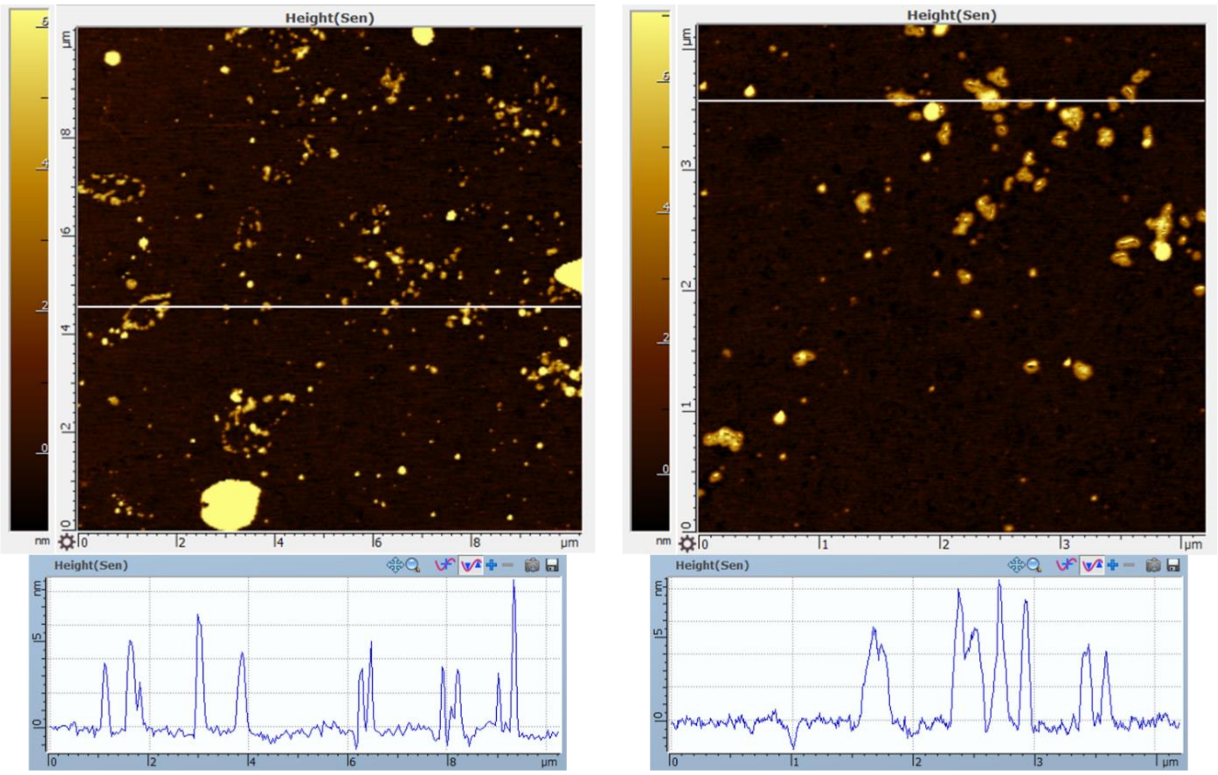

Figure 8.6 AFM images and height profiles of **EP-G** flakes

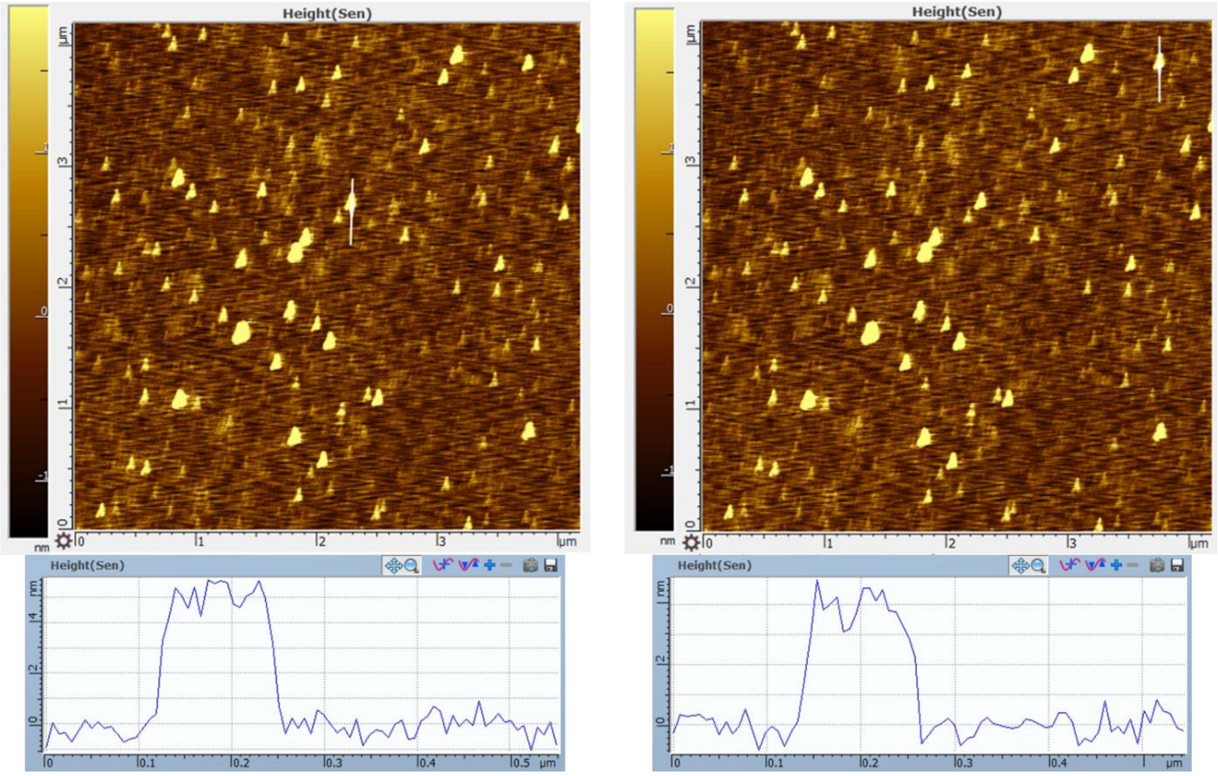

Figure 8.7 AFM image and height profiles of different **4-Nitrobenzyl-G** flakes

8.1.3 UV-Vis Calibration Curve of Extinction Coefficients for EP-G

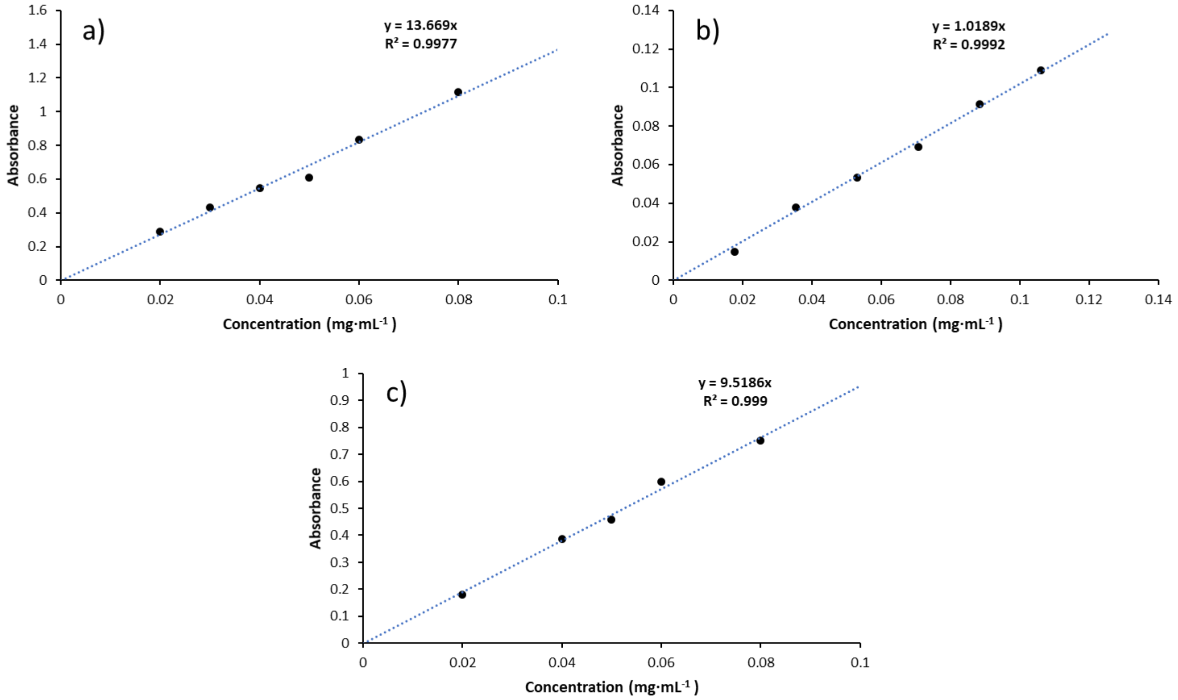

*Figure 8.8 UV-Vis calibration plot of **EP-G** in (a) IPA, (b) acetone, and (c) ethanol.*

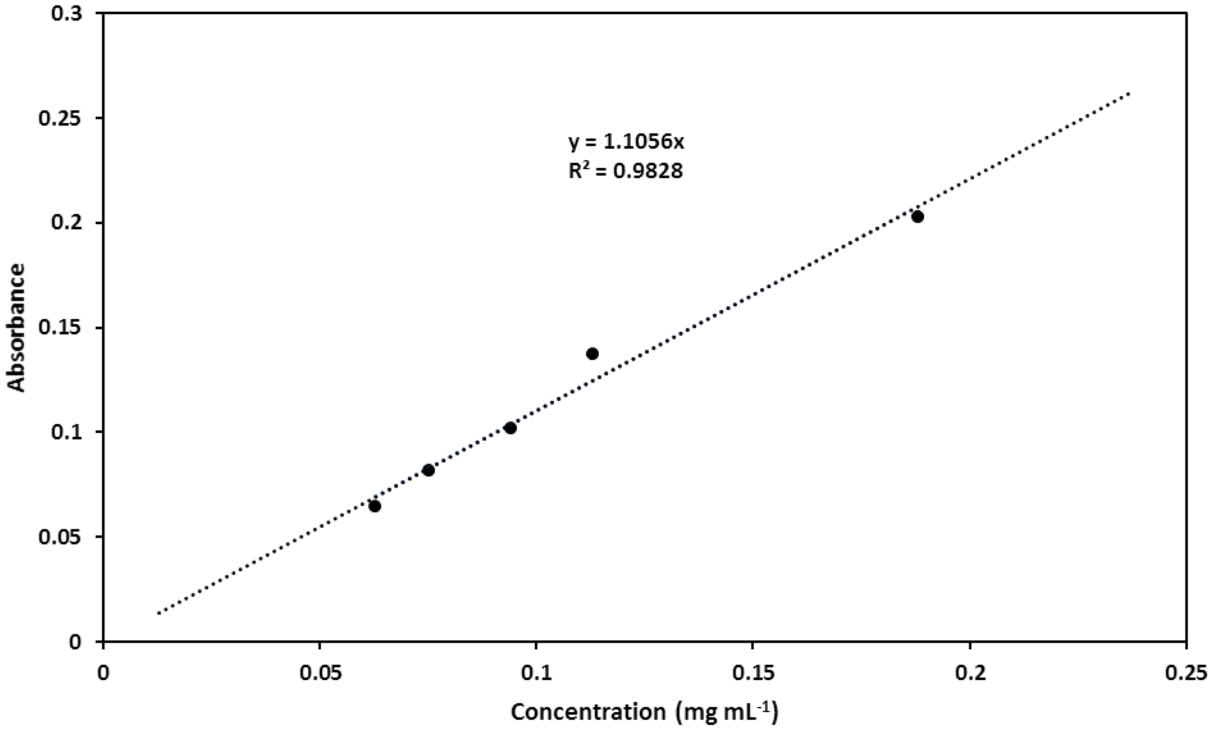

*Figure 8.9 UV-Vis calibration plot of **PO-G 700 Dis**.*

8.1.4 Other Data

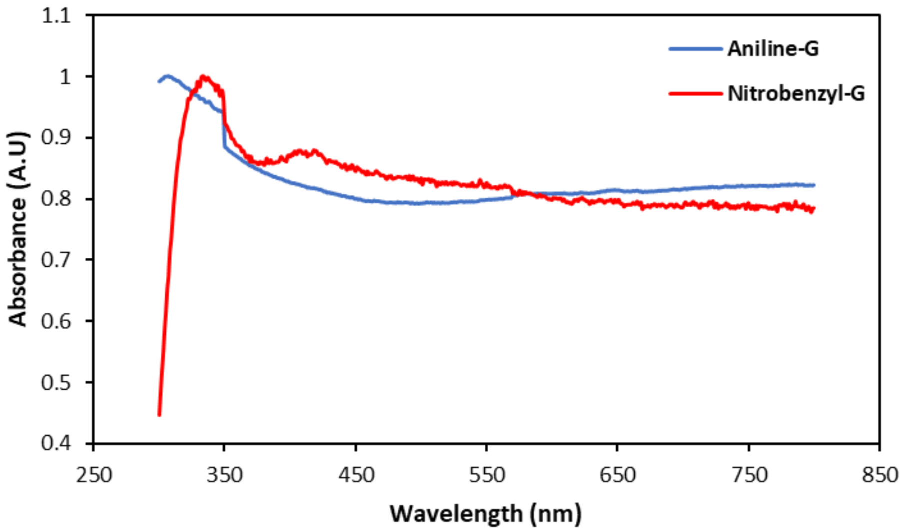

Figure 8.10 UV-Vis spectra of ***Aniline-G*** *(blue) and Nitrobenzyl-G (red) in NMP*

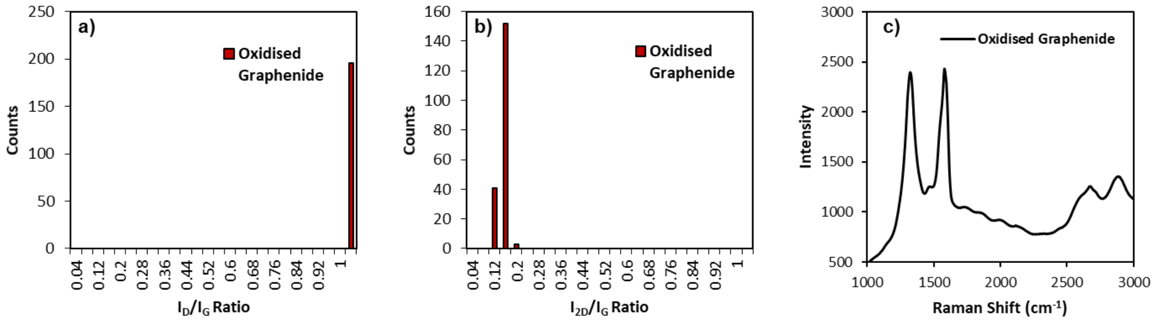

Figure 8.11 I_D/I_G (a) and I_{2D}/I_G (b) histograms, and average Raman spectrum (c) of the oxidised graphene derived from slow oxidation of the graphenide in atmosphere.

8.2 Supporting Information for Chapter 3

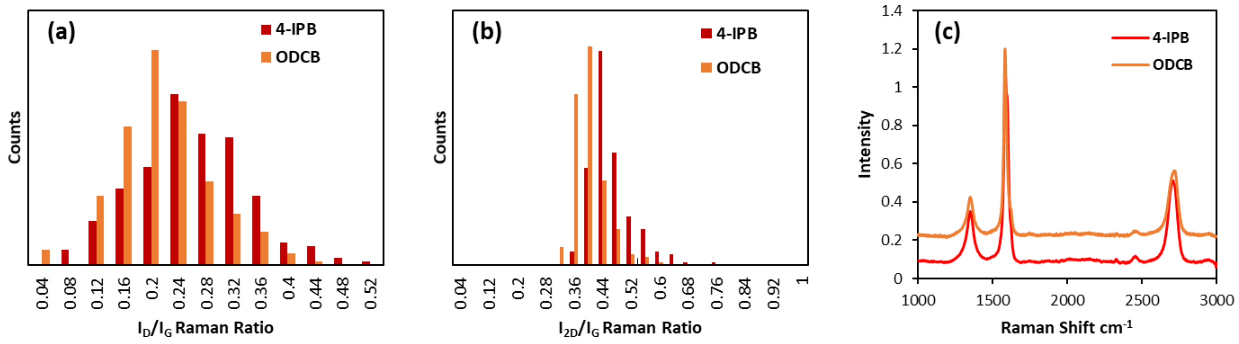

Figure 8.12 (a) I_D/I_G and I_{2D}/I_G (b) histograms, and (c) Raman spectra of P40 SGICs functionalised by 4-IPB and by the radical in the ODCB.

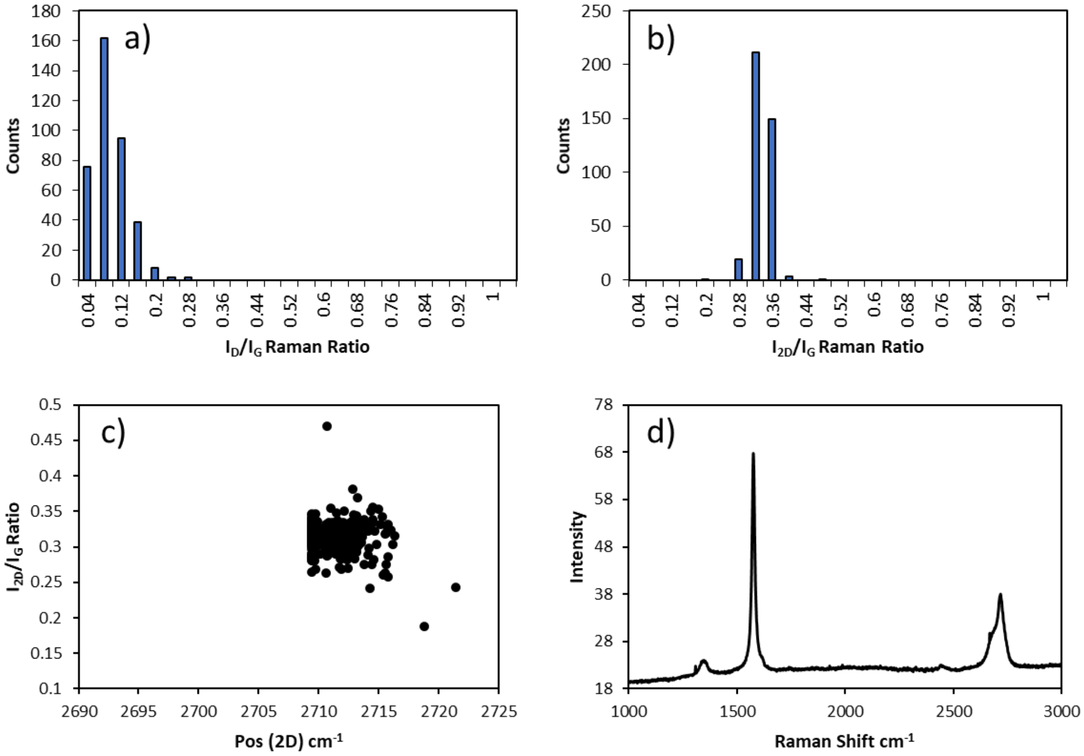

Figure 8.13 (a) I_D/I_G and I_{2D}/I_G (b) histograms, (c) I_{2D}/I_G vs Pos (2D) plot, and Raman spectra of ***M80*** *Graphite.*

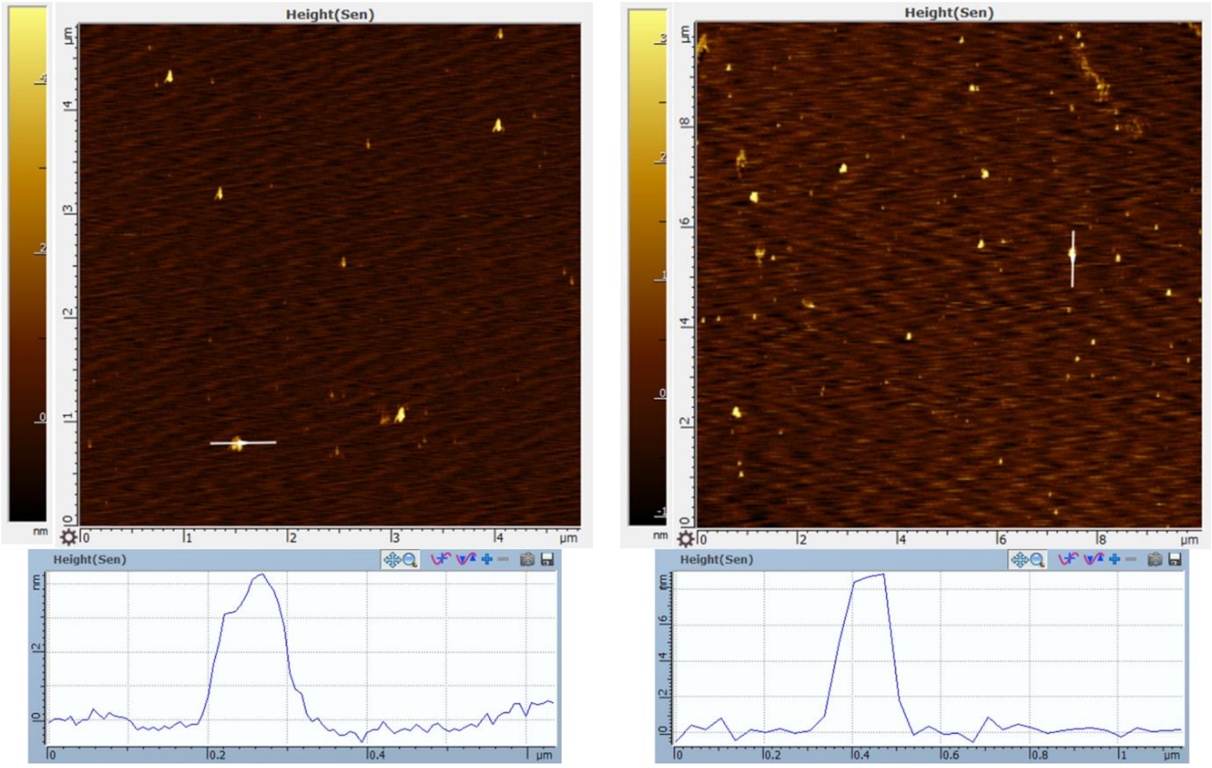

Figure 8.14 AFM images and height profiles of ***4-IPG***

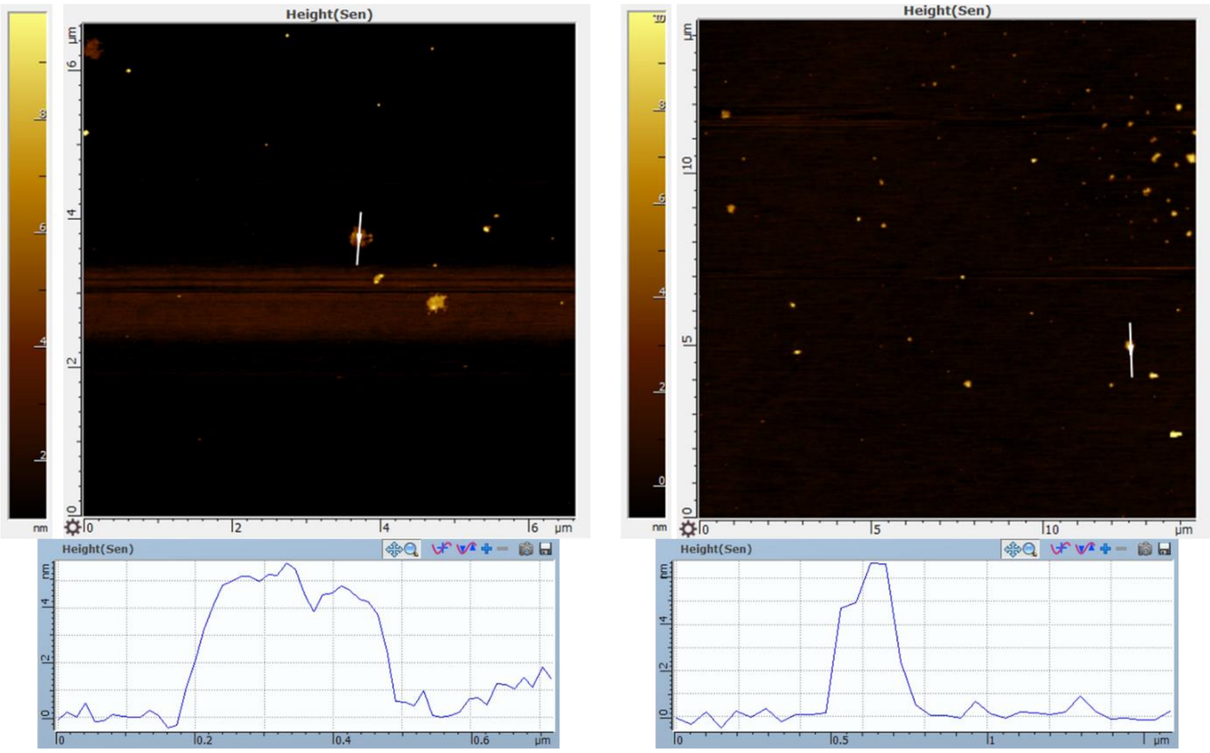

Figure 8.15 AFM images and measurements of ***4-BPG***

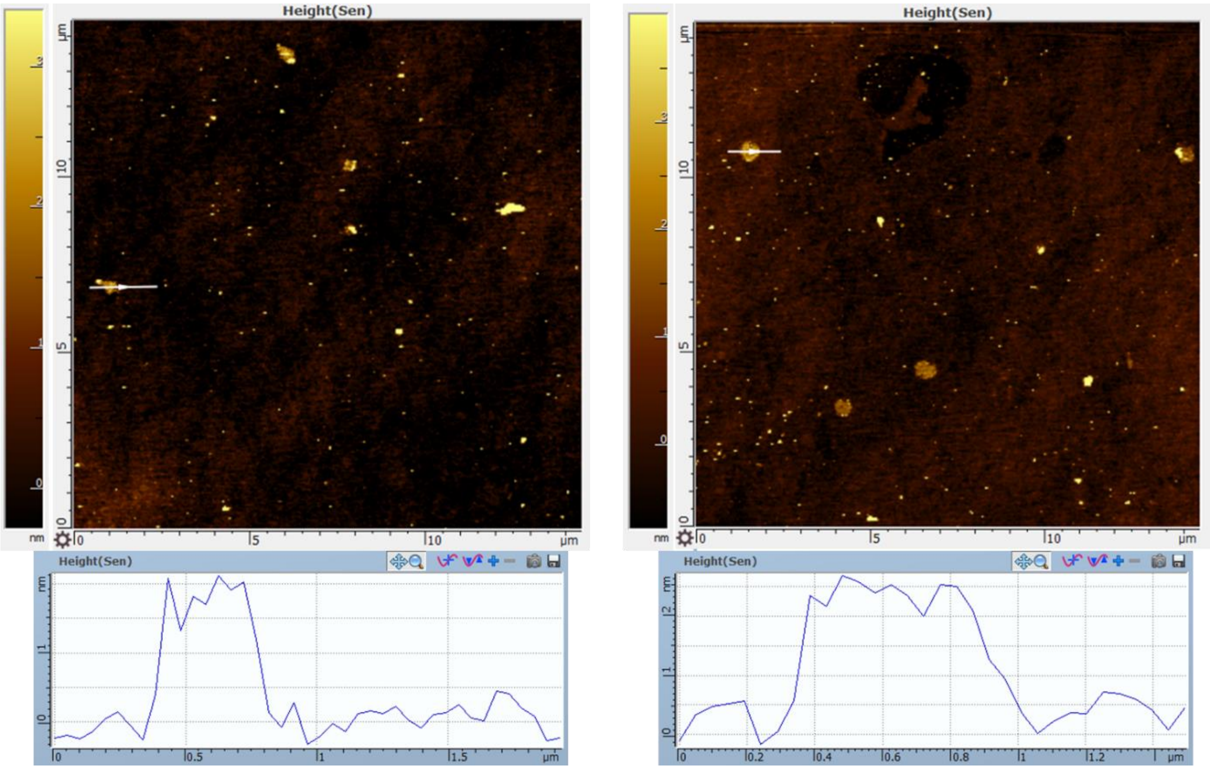

Figure 8.16 AFM images and height profiles of ***4-NPG***

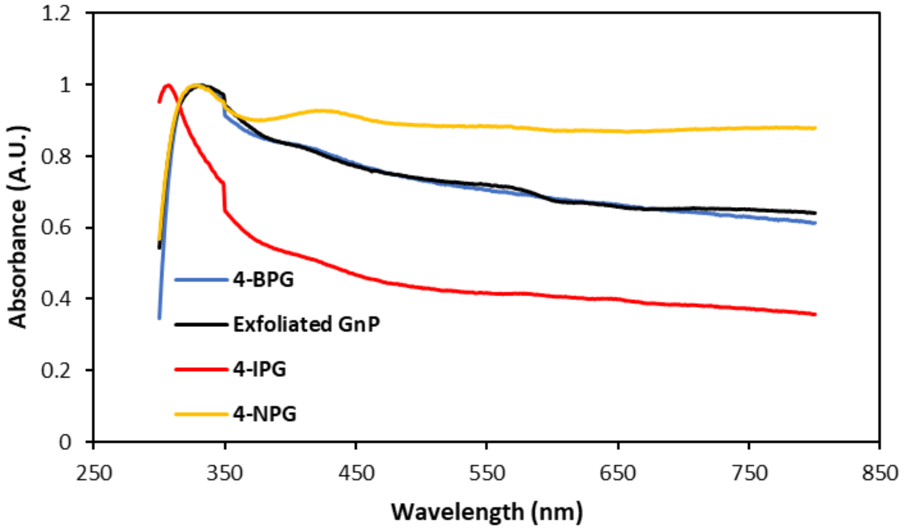

Figure 8.17 UV-vis spectra of aryl-functionalised graphene and exfoliated GNP in NMP

8.3 Supporting Information for Chapter 4

8.3.1 Crude PO-G

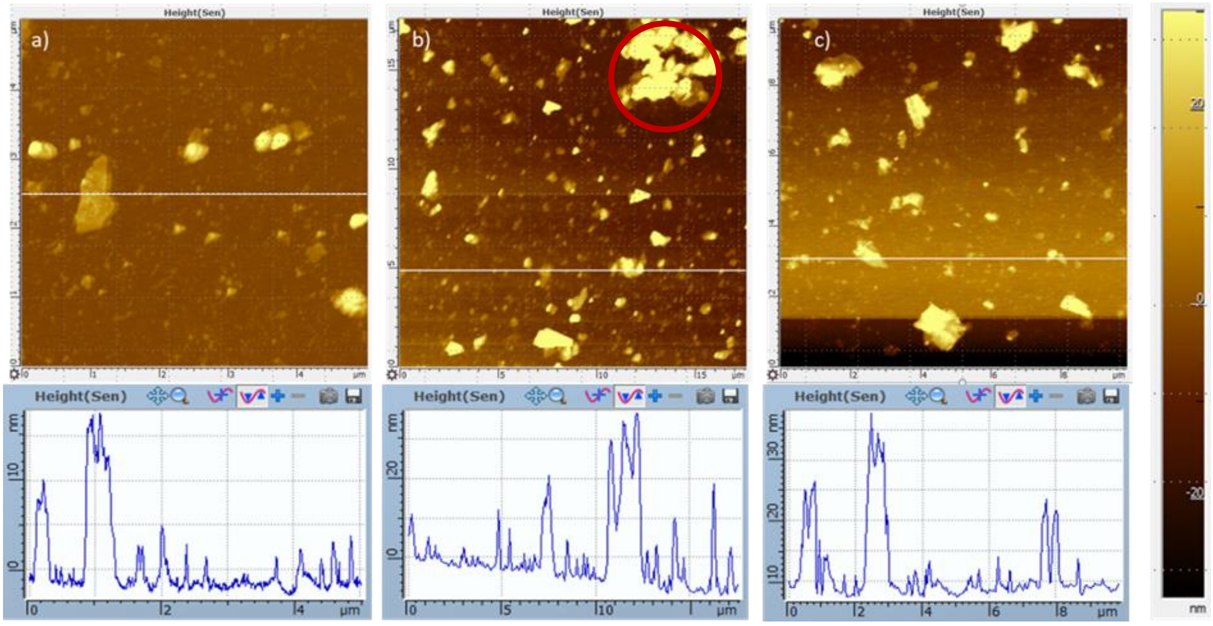

Figure 8.18 (a) (b) (c) AFM images show the lateral size and thickness of the ***crude PO-G****; GNP undergoes incomplete exfoliation can be spotted in (b), highlighted by the red circle.*

8.3.2 Centrifuged PO-W

The **PO-W** (derived by heating the isolated SGICs with water) was also exfoliated by probe-sonication (250W, 33% amplitude, 5 s pulse) and separated further by centrifuging at 1000 rpm. The supernatant was subjected to characterisation of AFM and SRS.

According to SRS results (Figure 8.21), the average I_D/I_G ratio of **PO-W 1000 Dis** (I_D/I_G= 0.39) is lower than that of **PO-G 700 Dis** (I_D/I_G= 0.89). In addition, the average I_{2D}/I_G ratio of **PO-G 700 Dis** (I_{2D}/I_G= 0.13) is significantly lower than that of **PO-W 1000 Dis** (I_{2D}/I_G= 0.4). These results indicate the **PO-G 700 Dis** is more functionalised (oxidised) than the **PO-W 1000 Dis**. Moreover, the **PO-G 700 Dis** is more exfoliated than the **PO-W 1000 Dis** since the average *Pos* (2D) of **PO-G 700 Dis** (2694.9 cm^{-1}) is less than that of **PO-W 1000 Dis** (2706.9 cm^{-1}). The **PO-G 700 Dis** has 90% of graphene ≤ 6.9 nm (Figure 8.21), which is significantly higher than the percentage of (56% ≤ 7 nm) **PO-W 1000 Dis** according to the results of statistical AFM. Overall, graphene is more oxidised and more exfoliated by the assistance of $Mn(OAc)_3$.

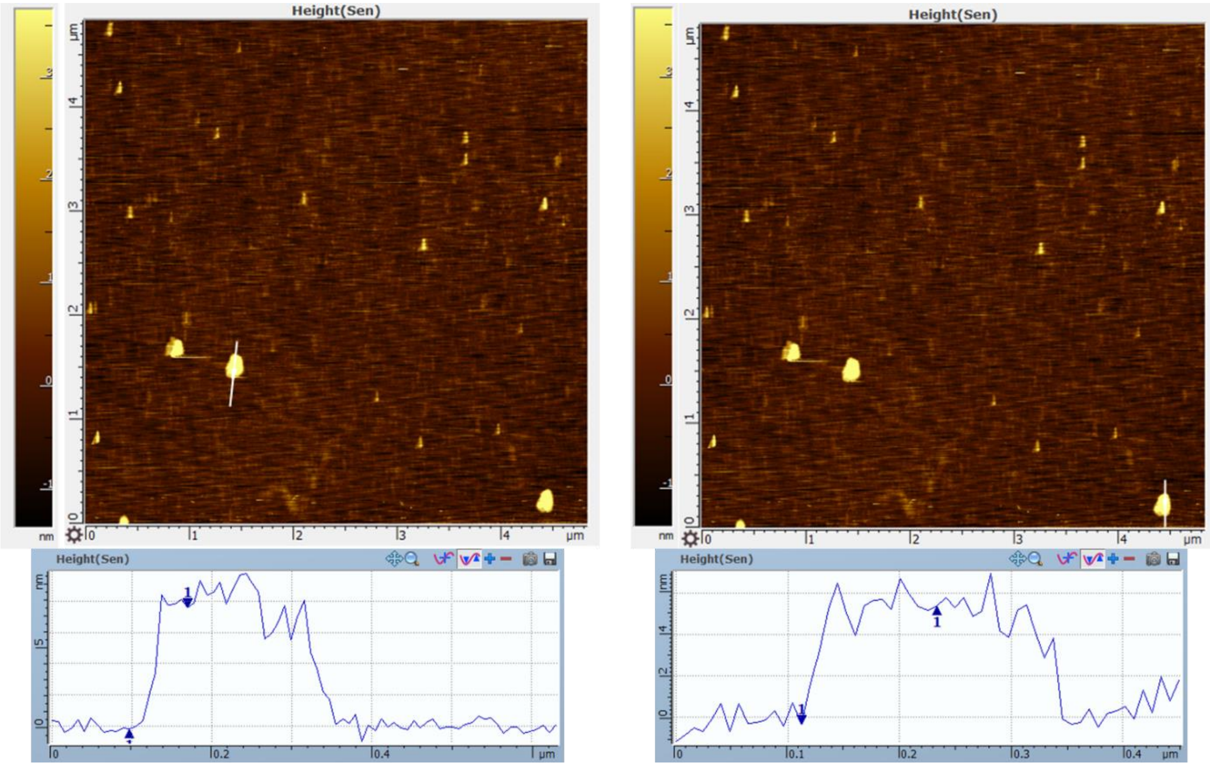

Figure 8.19 AFM image and height profiles of different graphene flakes from the ***PO-W 1000 Dis*** *sample.*

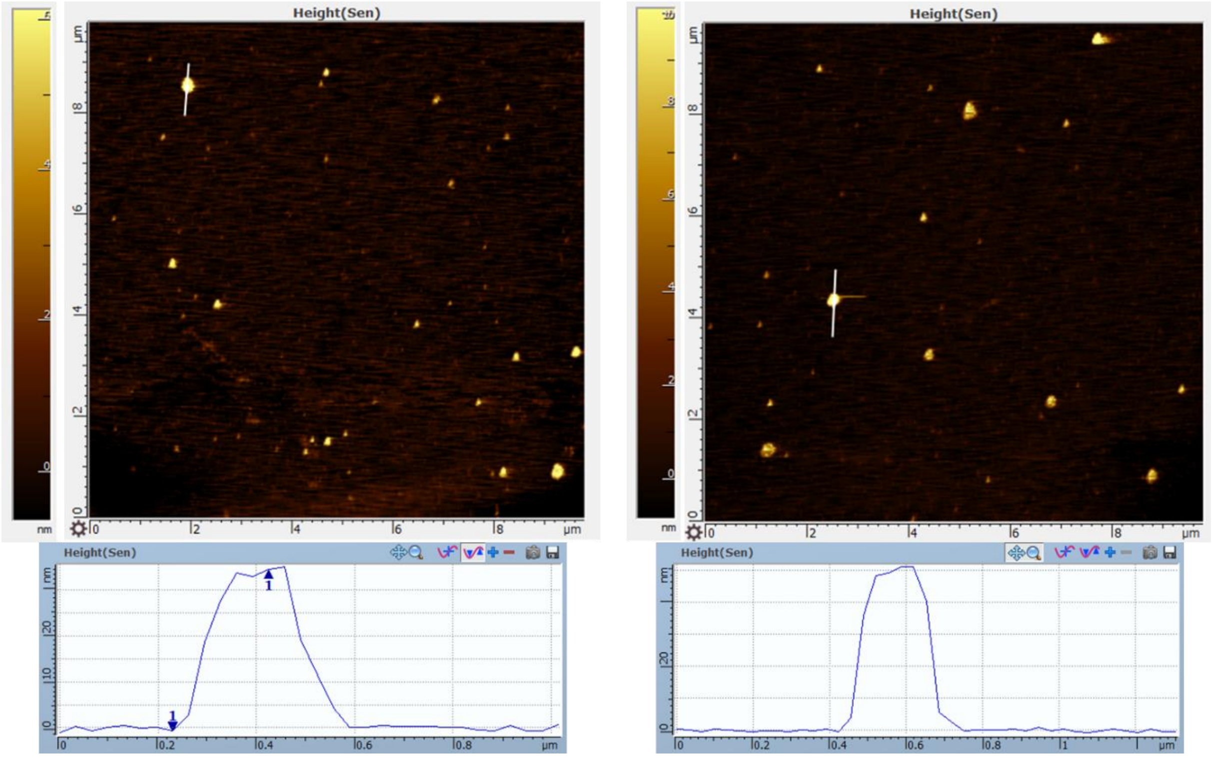

Figure 8.20 AFM images and height profiles of graphene flakes from the ***PO-W*** *sample.*

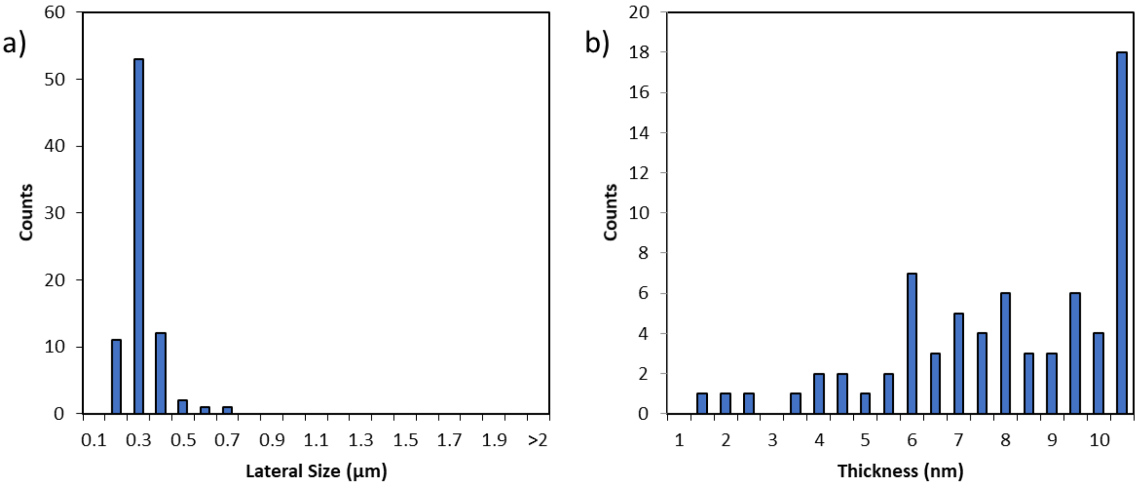

Figure 8.21 Lateral size (a) and thickness (b) histograms of ***PO-W 1000 Dis****.*

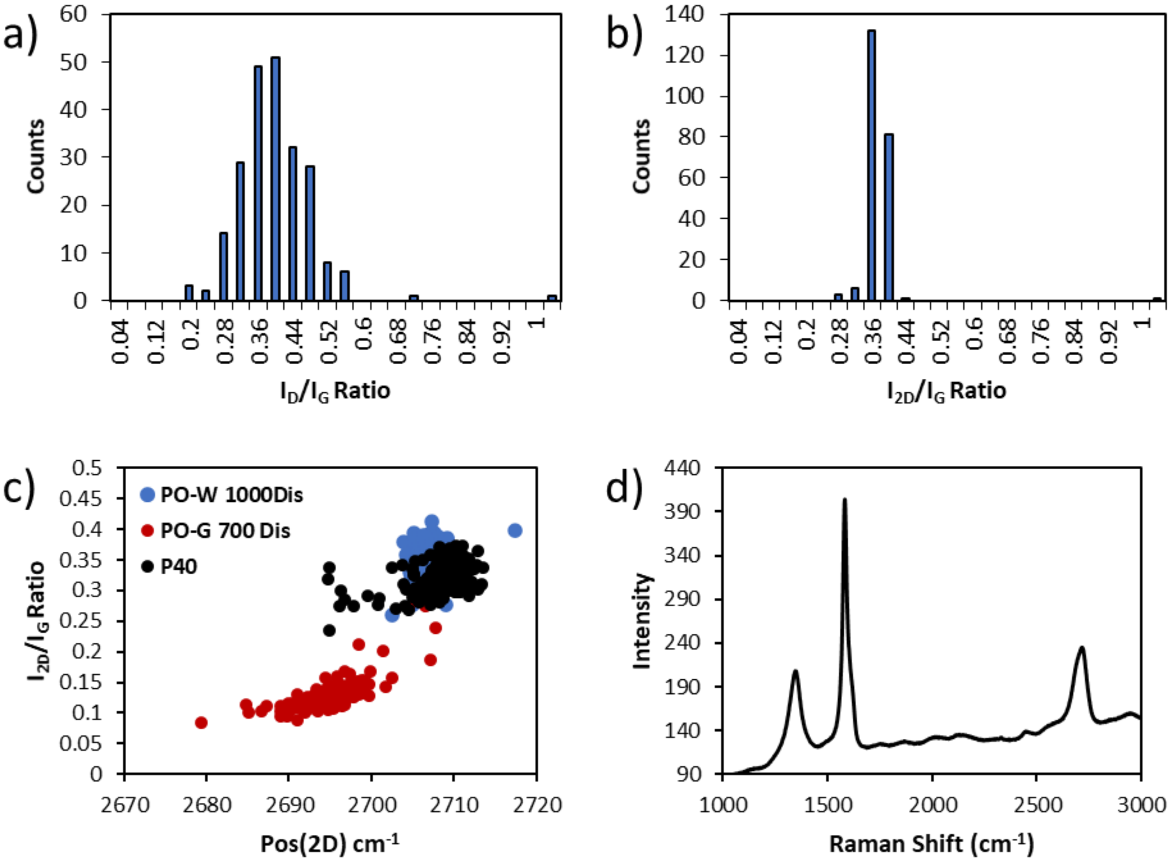

Figure 8.22 (a) I_D/I_G and I_{2D}/I_G (b)histograms, (c) I_{2D}/I_G vs Pos (2D) plot, and (d) Raman spectrum of ***PO-W 1000 Dis*** *graphene.*

8.3.3 Exfoliated P40 GNP

The P40 GNP was processed according to the procedure 6.2.20 and the obtained product was call **EX-P40**. The SRS results (Figure 8.24) show that the average I_D/I_G ratio **EX-P40** increased slightly from 0.11 (**P40 GNP**) to 0.17 due to defects created by probe-sonication. The average I_{2D}/I_G ratio also increased from 0.33 (**P40 GNP**) to 0.45, though the position of 2D band did not exhibit apparent shift. These results still suggest the exfoliation of the GNP after probe-sonication. AFM results (Figure 8.23) are consistent with the SRS results, as the average lateral size was decreased from 10 μm to 0.22 μm and thickness was reduced from 50-100 nm to 7.46 nm after the processing. Overall, **P40 GNP** became thinner and smaller after probe-sonication.

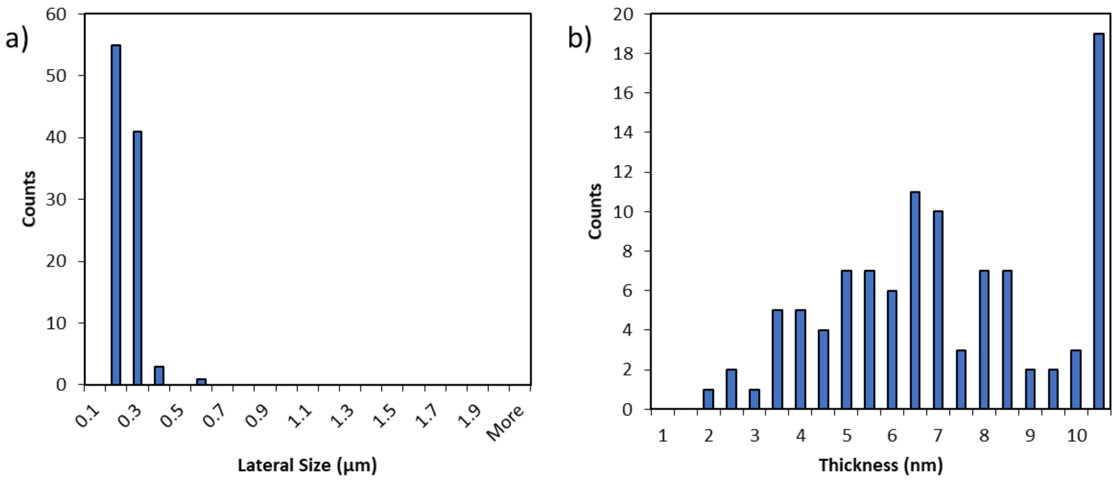

Figure 8.23 Lateral size (a) and thickness (b) histograms of ***EX-P40.***

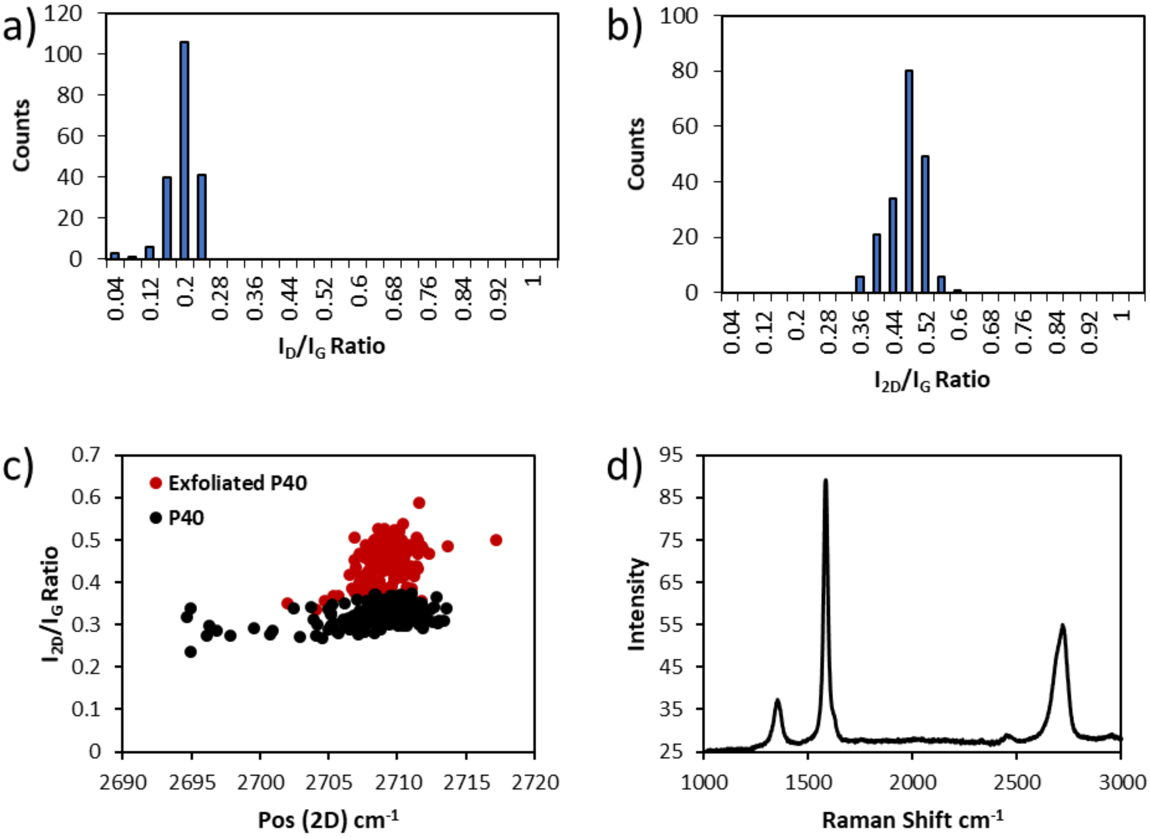

Figure 8.24 (a) I_D/I_G *and* I_{2D}/I_G *(b) histograms, (c)* I_{2D}/I_G *vs Pos (2D) plot, and (d) Raman spectrum of* ***EX- P40****.*

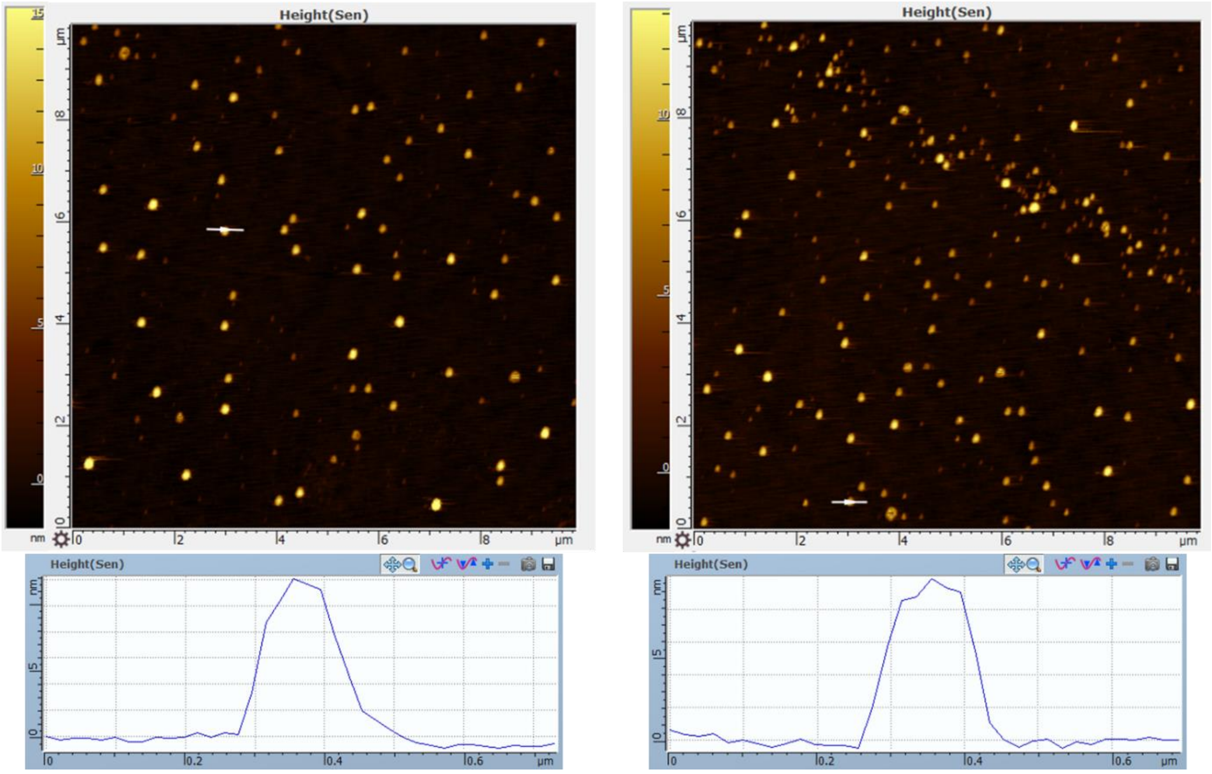

Figure 8.25 AFM images and measurements of graphene flakes from the ***EX-P40*** *sample.*

8.3.4 Reduced Graphene Oxide

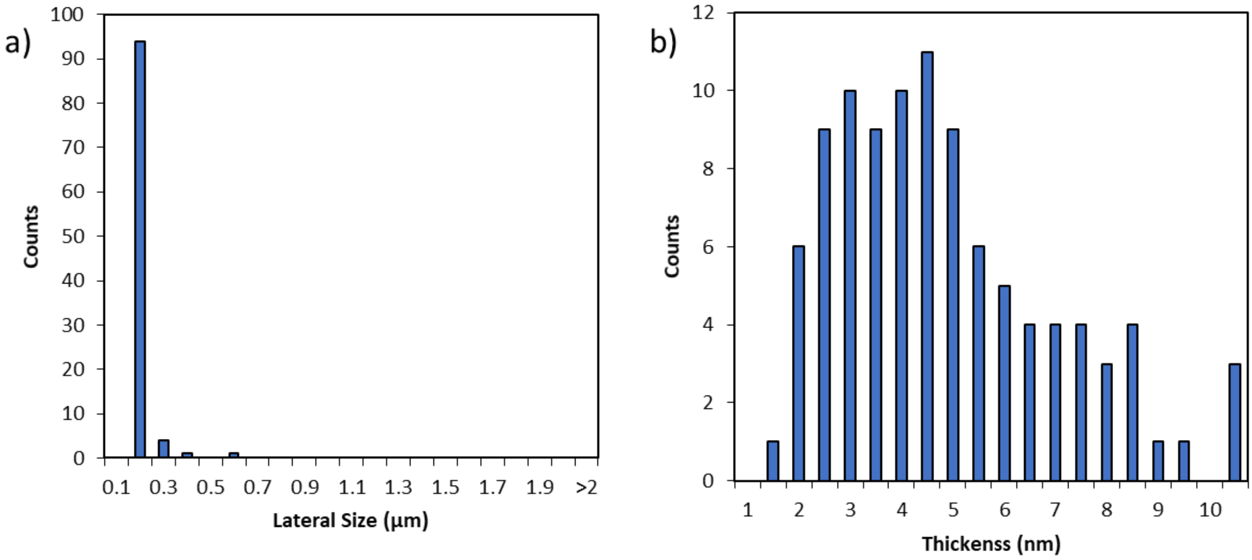

Figure 8.26 Lateral size (a) and thickness (b) histograms of rGO sample

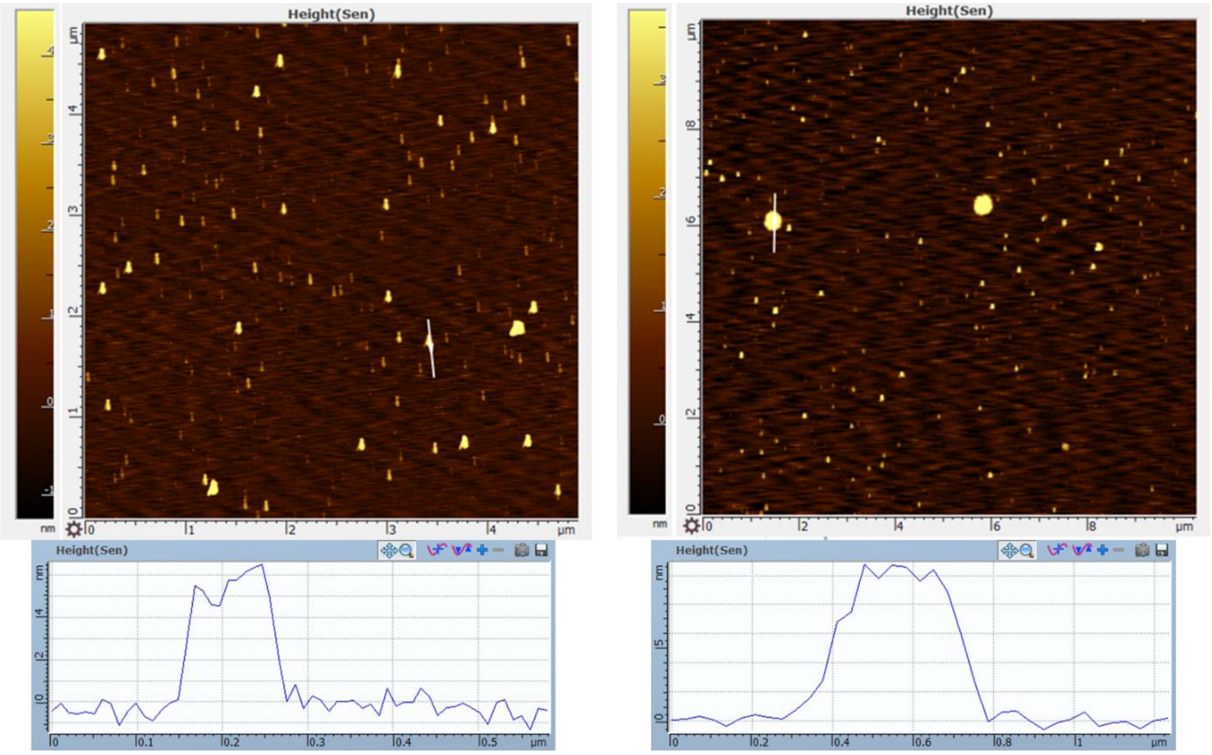

Figure 8.27 AFM images and measurements of graphene flakes from the rGO sample.

8.3.5 AFM of PO-G-BS

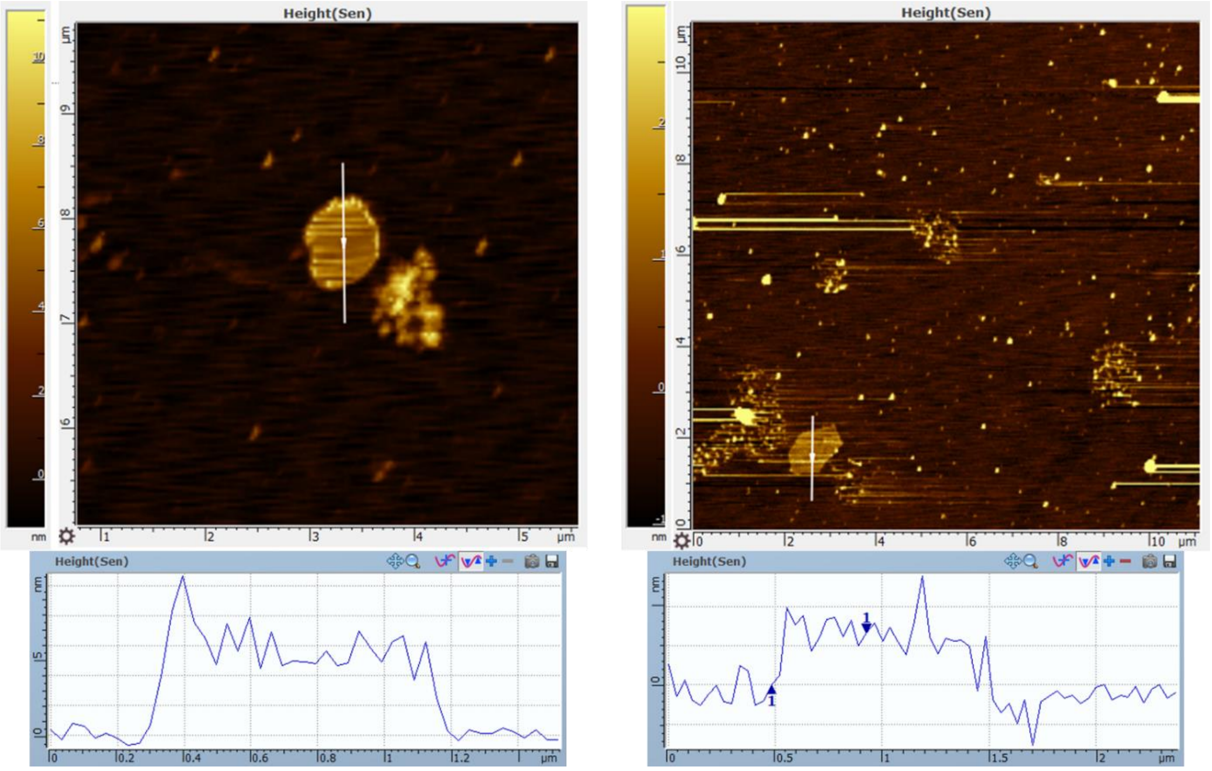

Figure 8.28 AFM images and measurements of graphene flakes from the ***PO-G-BS*** *sample.*

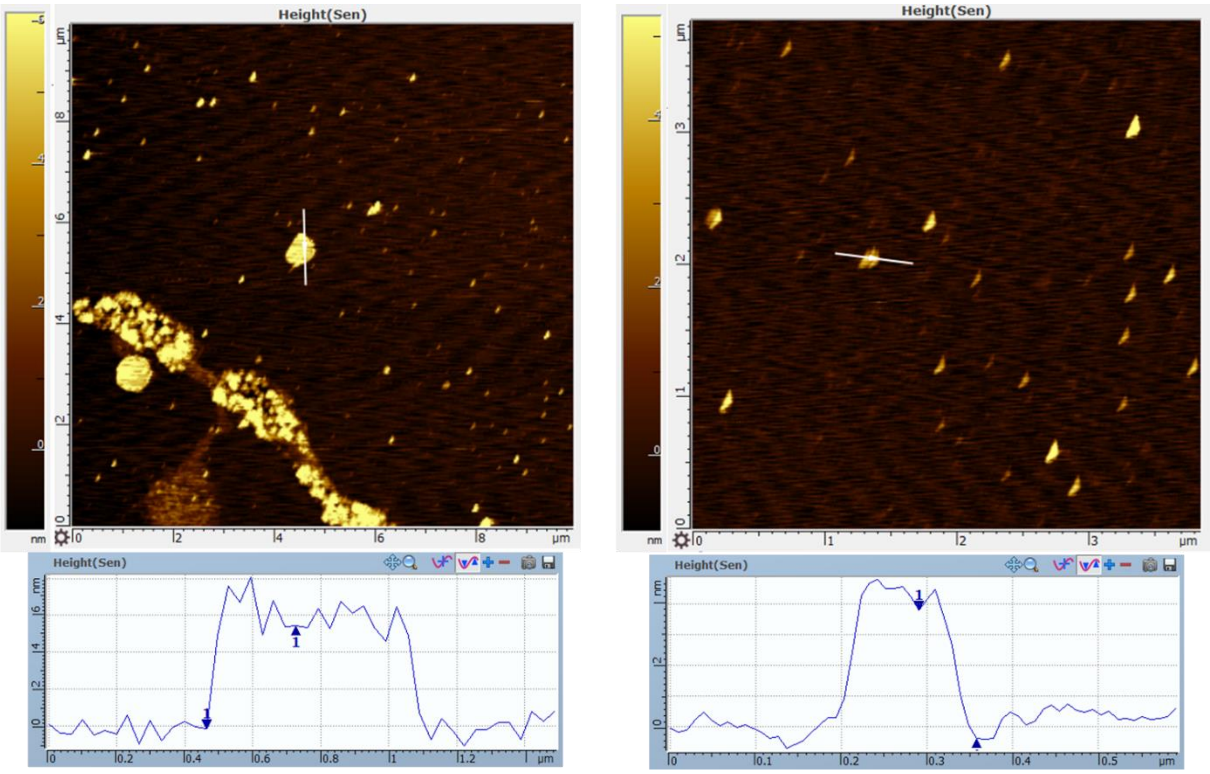

Figure 8.29 AFM images and measurements of graphene flakes from the ***PO-G-BS*** *sample.*

8.4 Dispersibility Video

The original videos (labelled with corresponding figure number) are submitted with the thesis in separate files.

8.4.1.1 PO-G Series

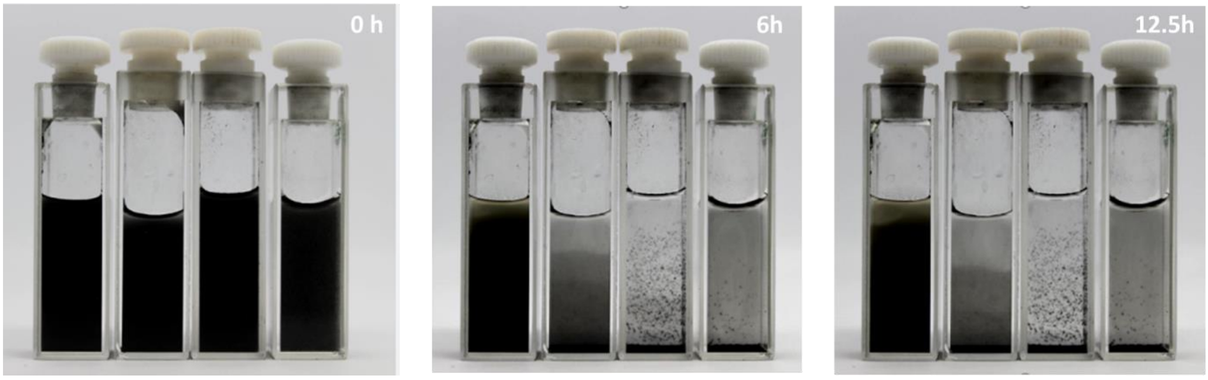

Figure 8.30 In each picture from left to right: aqueous dispersion of ***crude PO-G****,* ***crude PO-W****,* ***crude PO-M****, and* ***PO-WOM****. Picture from left to right represents the dispersibility state at the beginning of the test, in the middle of the test, and the end of the test.*

*Figure 8.31 In each picture from left to right: aqueous dispersion of **crude PO-G**, **P40 GNP**, **crude PO-G** derived by 6 vol% water, and **crude PO-G** (H_2SO_4: $Mn(OAc)_3{\cdot}2H_2O$=2:1). Picture from left to right represents the dispersibility state at the beginning of the test, in the middle of the test, and the end of the test.*

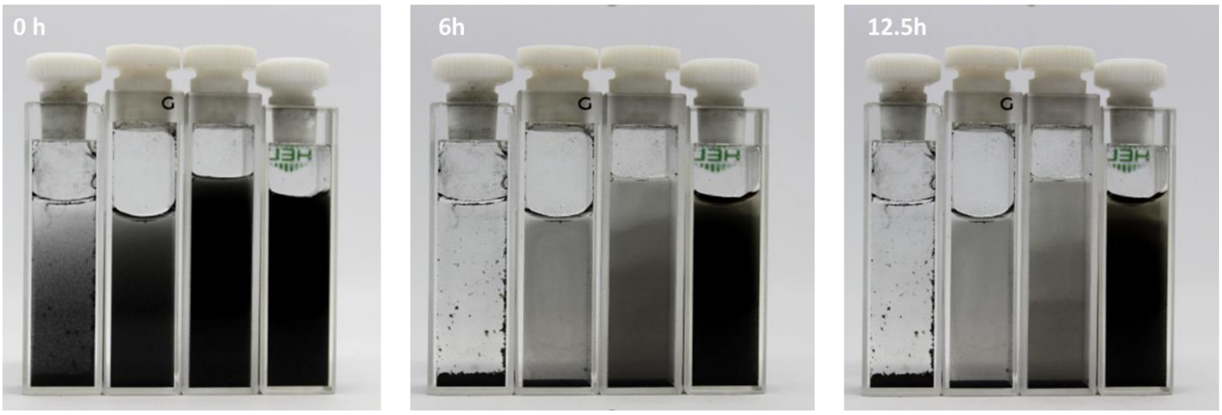

*Figure 8.32 In each picture from left to right: aqueous dispersion of **crude PO-G** (60 ℃), **crude PO-G** (40 ℃), **crude PO-G** (oxidation of 3 hours), and **crude PO-G** (oxidation of 12 hours). Picture from left to right represents the dispersibility state at the beginning of the test, in the middle of the test, and the end of the test.*

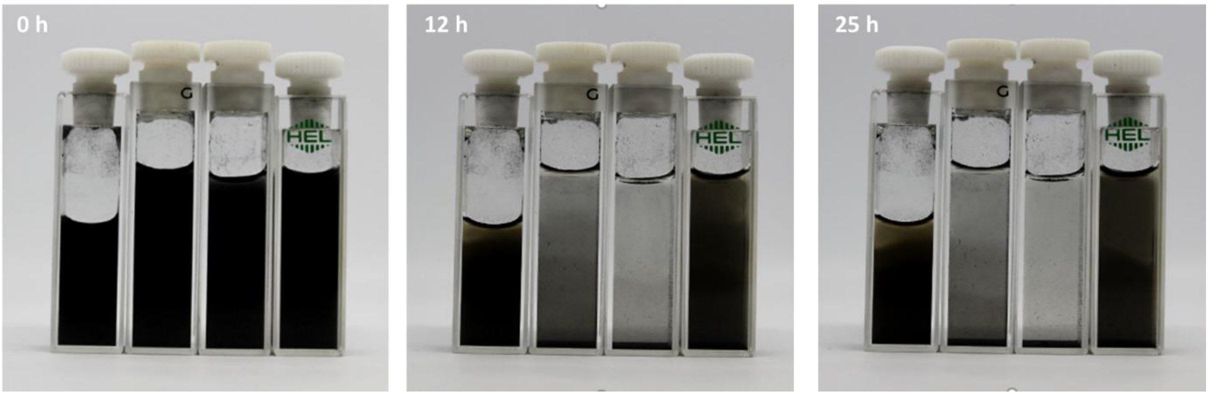

*Figure 8.33 In each picture from left to right: aqueous dispersion of **crude PO-G**, **crude PO-G** (oxidation of 18 hours), **crude PO-G** (H_2SO_4: $Mn(OAc)_3{\cdot}2H_2O$=4:1), and **crude PO-G** (oxidation of 12 hours). Picture from left to right represents the dispersibility state at the beginning of the test, in the middle of the test, and the end of the test.*

*Figure 8.34 In each picture from left to right: aqueous dispersion of **crude PO-G**, **crude PO-G** (addition of 0 vol% water during the reaction), **crude PO-G** (addition of 1 vol% water during the reaction), and **crude PO-G** (addition of 2 vol% water during the reaction). Picture from left to right represents the dispersibility state at the beginning of the test, in the middle of the test, and the end of the test.*

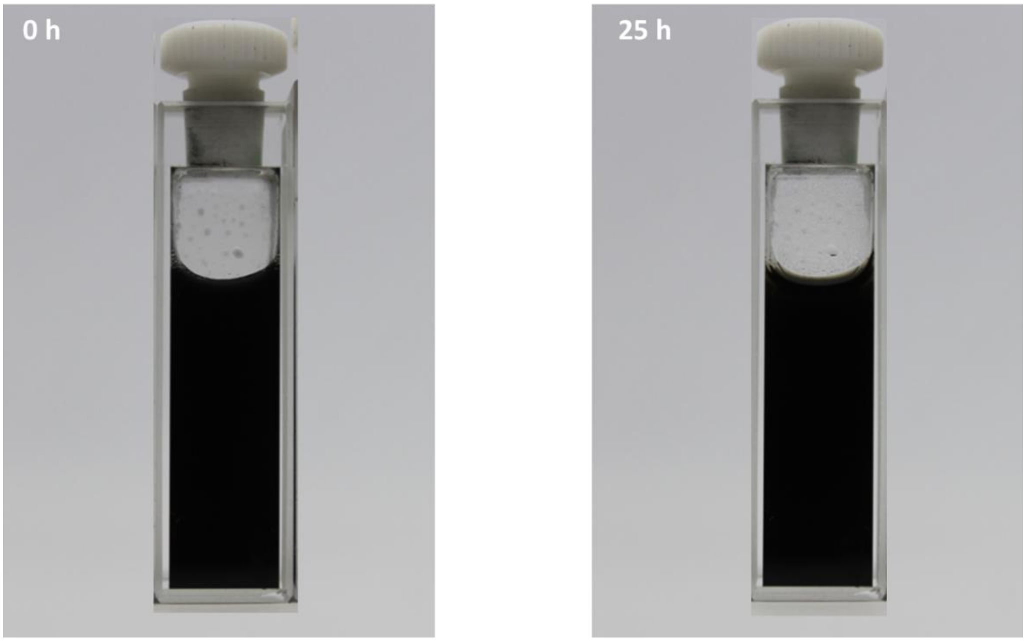

*Figure 8.35 Dispersibility of **PO-G 700 Dis** in water over 25 hours (the photo was cut from the other photo where other uninterested samples were included).*

Figure 8.36 Dispersibility of ***PO-G 700 Dis*** *in water (0.5 mg mL^{-1}) from 0 (left) to1 month (right). (Pictures no video)*

8.4.1.2 EP-G Series

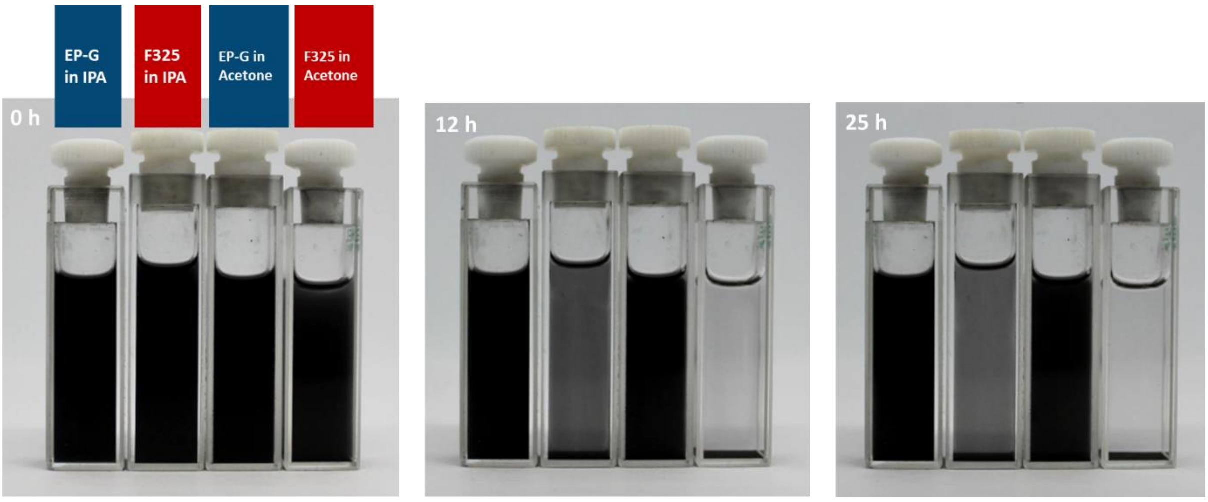

Figure 8.37 Comparison of dispersibility of ***EP-G*** *and* ***F325*** *in IPA and acetone over 25 hours.*

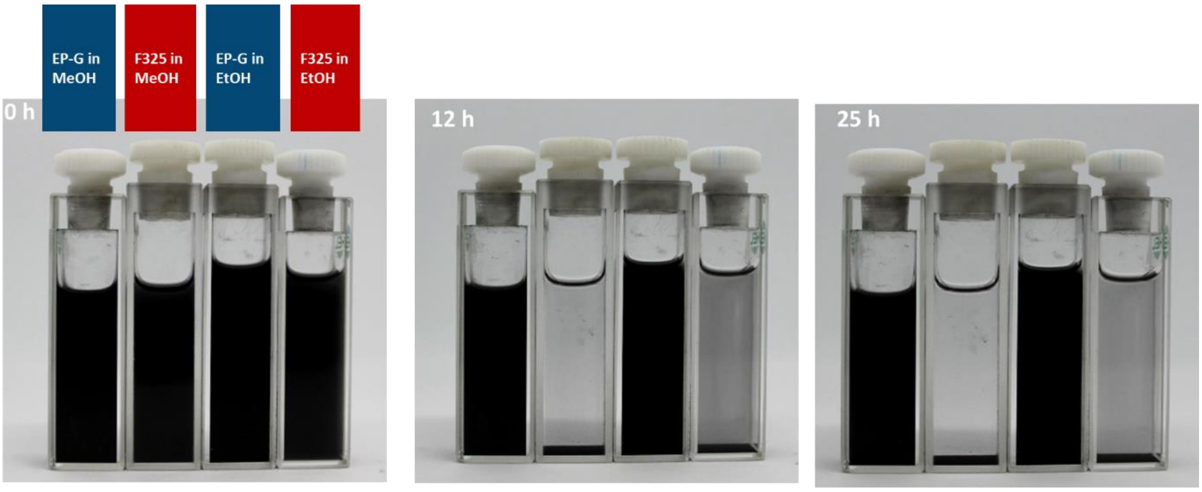

Figure 8.38 Comparison of dispersibility of ***EP-G*** *and* ***F325*** *in methanol and ethanol over 25 hours.*

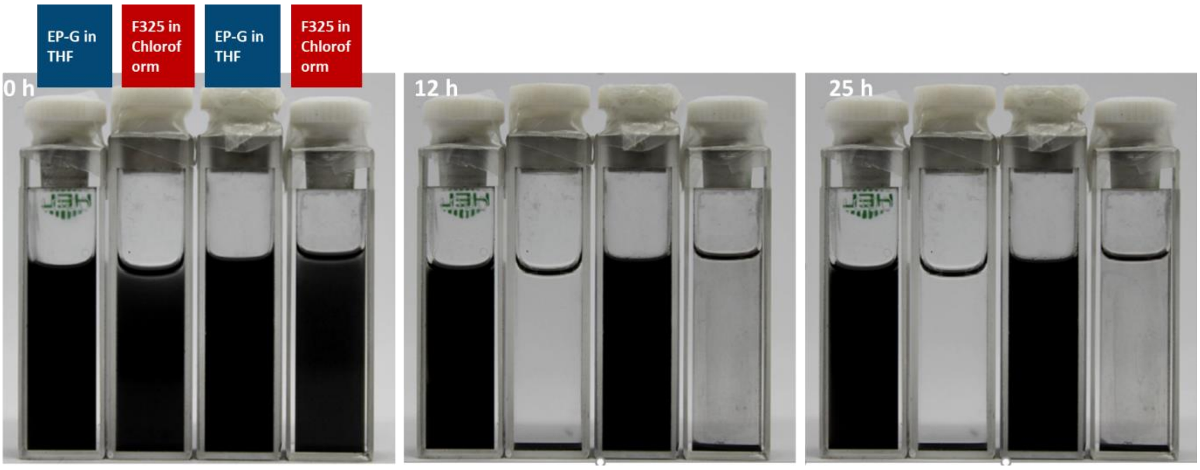

*Figure 8.39 Comparison of dispersibility of **EP-G** and **F325** in THF and chloroform over 25 hours.*